The evaporation of multiple sessile droplets

Joseph James Kilbride

A thesis submitted in partial fulfilment of the requirements of Nottingham Trent University for the degree of Doctor of Philosophy.

4th February 2024

Department of Physics and Mathematics
School of Science and Technology
Nottingham Trent University

Contents

Abstract

The evaporation of multiple droplets is an interesting and abundant phenomena in nature and industry and as a result has many applications. Most research to this point has focused on studying the isolated case but in reality it is rare for droplets to evaporate on their own. Droplets evaporating in close proximity to each other interact and their dynamics are influenced by this. To study them the evaporation rates must be extracted from each droplet in the array. Traditionally for isolated droplets the volume and evaporation rate has been established by imaging the droplet from the side and measuring its profile, however for multiple sessile droplets in two dimensional arrays not all droplets can be seen simultaneously. A solution to this is to image the arrays from the top but without knowing the droplet heights or contact angles, the volumes cannot be established. In addition to this, it is difficult to dispense droplets repeatably and accurately before they evaporate. Both these challenges have prevented authors from conducting careful experimental investigations of the evaporation. Because of this, theoretical work has moved ahead of experimental work, with several recent analytical models for the evaporation being proposed [1, 2]. In this thesis a technique is developed, validated and optimised to image the droplets simultaneously (chapter 2). Experimental data is then taken for multiple droplets and compared to these analytical models evaluating their performance and demonstrating their limitations. It is found that the theory works well for small arrays of droplets (chapter 3) but cannot capture the dynamics of large arrays or arrays on heated substrates (chapter 4). Exhaled breath droplets are then investigated and it is found that whilst the array is evaporating the larger droplets grow due to the Kelvin effect [3]. The diffusive theory is modified to account for this and a simple mean field model is proposed, capturing the experimental array dynamics well (chapter 5). Finally, direct numerical simulations (DNS) of multiple droplets are conducted and it is shown that the model qualitatively captures the droplet evaporation rates (chapter 6). These simulations make future investigations of the vapour and thermal dynamics of the arrays possible, which are challenging to image and measure experimentally.

Dedication

I would like to dedicate this work to my family Caroline, Dominic and Jessica whose love and support led me to completing this PhD. Also, my girlfriend Chloé who put up with me obsessing over multiple droplets. Without her I would not have made it this far. I am also dedicating this work to the loving memory of my grandparents Mary and Philip Kilbride and Sandy and Alan Roman.

Acknowledgements

I would like to acknowledge the contributions of my collaborators Prof. Howard Stone, Dr. Hassan Masoud, Azmaine Iqtidar, Dr. Andrew Edwards and Kieran Fagg. As well as Nottingham Trent University and the Santander Becas award for funding the project.

I would like to thank Prof. Prashant Valluri and Dr David Scott whose knowledge and insightful discussions helped improve the computational aspects of my work. I am very grateful to Prash and David for the opportunity to spend two months at the university of Edinburgh during my second year. The computational training they provided during this period and after, was incredibly valuable.

Also, thank you to Dr Fouzia Ouali for her legendary Workshop classes in the first year of my undergraduate in 2015. And for her supervision during my first research project in 2017. Both these occasions made a big impact on my academic progression. Without her continued help during the PhD project, my experiments would not have been as productive.

Lastly I wish to thank Dr David Fairhurst, who I am especially grateful to. Dave's supervision and ideas immeasurably improved the quality of my work. The various opportunities he afforded, guided me to be the researcher I have become. The many enjoyable hours discussing the physics of the project helped make the last three years some of the most enjoyable of my life.

Publications

The publications from the work within this thesis (and those still in preparation at the time of writing) are listed here:

Reference	Corresponding chapters	Status
Edwards et al. 2021 [4]	3	Published
Kilbride et al. 2023 [5]	2 and 3	Published
Iqtidar et al. 2023 [6]	3	Published
Kilbride et al. (tbc)	4	In preparation
Kilbride et al. (tbc)	5	In preparation

Nomenclature

Acronyms

CA	Constant contact angle (evaporation mode)
CCD	Charge couple device
CR	Constant contact radius (evaporation mode)
DI	Diffuse Interface
DOF	Depth of field
FFT	Fast fourier transform
FOV	Field of view
LHS	Left hand side
MFT	Mean field theory
PD	Pattern Distortion
PSM	Point source method
RHS	Right hand side
RH	Relative humidity (%)

Arrays

N	Number of droplets
R	Radius (of array)
r_c	Radial distance from centre (of array)

s Inter-droplet separation (centre to centre)

Droplet

$\left(\frac{dV}{dt}\right)^*$ Isolated volumetric evaporation rate

τ Droplet evaporation lifetime

θ Equilibrium contact angle (always in radians, unless stated otherwise.)

a Base radius

h Height

j Interfacial flux

M Magnification

r Radius of curvature

r_k Kelvin radius

T Temperature

V Volume

Liquid

γ Surface tension

μ Dynamic viscosity

ν Kinematic viscosity

ρ Density

Other symbols

κ Thermal conductivity

λ Wavelength

L Length scale

M_w Molar mass

T_s Substrate temperature

Constants

g Gravitational acceleration

R_g Ideal gas constant

Gas

ϕ Fractional relative humidity

ϕ_{sat} Saturation fraction (for interfacial curvature r, at temperature T)

c Concentration

c_∞ Saturation concentration (for flat interface $r \to \infty$, at temperature T)

c_{amb} Ambient concentration

c_{sat} Saturation concentration

D Diffusion coefficient

Chapter 1

Introduction

Evaporating multiple droplets are abundant in nature (e.g. raindrops, sweat on skin, clouds and condensation from warm air) and industry (e.g. spray coating, ink-jet printing, surface patterning and evaporative cooling) so understanding their dynamics has many potential applications. There are many studies on the evaporation of droplets in isolation [7], however there is much less work on how they evaporate collectively. Despite this, droplets almost always appear in groups (arrays) and their individual evaporation is no longer sufficient to explain their dynamics.

Multiple droplet evaporation has attracted recent public interest due to the coronavirus COVID-19 pandemic. The droplets exhaled within breath contain and transport the viruses. It is thought that the droplet carrying the virus extends its survival time [8] and therefore understanding and enhancing the multiple droplet evaporation is key to reducing transmission.

The evaporation of isolated droplets gives rise to many interesting secondary effects, for example its evaporative flux controls the internal flow. When the droplet also contains non-volatile solute, this flow leads to its transport and famously to the coffee ring effect [9]. In ink-jet printing these rings are seen as undesirable as they aim to build images from a series of homogeneous circular stains left behind by the ink-droplets after it evaporates. Multiple droplet evaporation can be used to influence the evaporative flux and therefore represents a method in which the internal flow could be controlled. By placing sacrificial droplets around an evaporating ink droplet, it is possible that the shape of the stain could be adapted and the resolution of the printers could be enhanced. This has been shown to be possible by Pradhan and Panigrahi [10], with the data shown to agree well with theory

developed by Wray et al. [11].

Multiple droplets are also formed by drop-wise condensation. This process is important for the formation of clouds [12]. Understanding how the growth of cloud droplets are influenced by inter-droplet interactions has applications in cloud seeding and in meteorological predictions of precipitation. Fuel injection systems also study multiple droplets as they evaporate, in order to optimise engine efficiency [13]. Droplets are also used to enhance efficiency in industrial processes, using them to cool hot components [14]. These applications make multiple droplet research important.

In the remaining sections of this chapter the important physics relevant to this thesis is explained. The existing work on the subject of multiple droplets is presented to put the thesis in is research context.

1.1 Diffusion

Physical quantities (such as temperature and concentration) often vary spatially across solids, liquids and gases. In many cases these quantities spread over time often until they become completely homogeneous. This spreading is called diffusion and it originates from asymmetric collisions between molecules. An example of a spatially varying quantity of this sort might be concentration in binary gas mixtures. If you open a bottle of perfume after some time the perfume can be smelt a distance away from the lid and therefore must have been transported. Just after the lid has been opened the concentration of perfume molecules around it increases, whilst far away from the lid the number of molecules is zero, giving rise to a gradient. Because of this gradient, molecules of perfume are more likely to collide with other perfume molecules from the direction in which the gradient is larger. This increased probability results in a net movement of the molecules away from the container. At a continuum level this movement is described by Fick's law [15]

$$\mathbf{j} = -D(c,T)\nabla c \tag{1.1}$$

where $\mathbf{j}$ is a mass flux ($kg\,s^{-1}\,m^{-2}$), c is the concentration of the diffusing substance and T is temperature. The magnitude of $\mathbf{j}$ depends on the specific substance and is captured by the diffusion coefficient, D which can be a function of both c and T. The change in the value of c at a specific point in space is described by the diffusion equation and depends

on the divergence of the flux ($\nabla \cdot \mathbf{j}$)

$$\frac{\partial c}{\partial t} = -\nabla \cdot (D(c,T)\nabla c). \tag{1.2}$$

In cases where D is weakly dependent on c and the diffusion can be considered isothermal (constant T) eq. 1.2 can be simplified to

$$\frac{\partial c}{\partial t} = -D\nabla^2 c. \tag{1.3}$$

It is also the case that heat diffuses in the same way and c can be replaced by T in eq. 1.3. A good empirical fit to the variation of D with temperature for some quantities is given by

$$D(T) = D(0)(1 + 0.007T) \tag{1.4}$$

over $-10 < T(^{\circ}\mathrm{C}) < 50$ [16]. Where $D(0)$ is a coefficient specific to the diffusing quantity (see table 1.1).

Quantity	$D(0)$ ($\mathrm{m^2 s^{-1}}$)
water vapour	2.12×10^{-5}
heat	1.89×10^{-5}

Table 1.1: The quantity specific diffusion coefficient, taken from Monteith and Unsworth 2013 [16].

1.2 Convection

Flow within a fluid is referred to a convection. The extent to which a fluid is influenced by convection compared to diffusion is given by the Peclet number (Pe) defined as

$$\mathrm{Pe} = \frac{UL}{D}, \tag{1.5}$$

where U is the characteristic velocity and L is a characteristic length scale. When convection is caused by external movement (*i.e.* a fan or a door closing in a room), this is called forced convection. Convection can also be caused by, density differences within the fluid leading to flow caused by gravity, which is called natural convection. A parcel of less dense fluid will be displaced if it is beneath a parcel with higher density. This is because

gravity exerts a stronger force on the dense parcel, causing a flow which circulates them around each other. Regions of circulating flow are called convection cells and the upward and downward motion of the less and more dense parcels (respectively) are referred to as convective plumes [17]. Density differences ($\Delta\rho$) in fluids are often caused by variations in temperature or composition. In these cases the convective flow has to compete with the viscous dissipation of the parcels moving through the liquid which acts to prevent the development of convective cells. Therefore the amount of gravitational potential energy (GPE) must be enough to overcome the viscous dissipation. An example of where convection is observed is above evaporating bodies of water (like oceans or lakes), as humid air is less dense than dry air. The arrows in fig. 1.1 depict the cells and plumes which can form over evaporating liquids. The Pe can be used to characterise both or a combination of natural and forced convection. When a system is dominated by natural convection the Pe can be written in a more specific form as the Grashof number (Gr), defined as

$$\mathrm{Gr} = \frac{\Delta\rho}{\rho}\frac{gR^3}{\nu^2} = \frac{\text{buoyancy forces}}{\text{viscous forces}}. \tag{1.6}$$

Where R is a length scale which depends on the geometry of the system, ν is the kinematic viscosity and ρ is the density of the bulk. This dimensionless number describes this competition between gravity and viscosity. Convection can also be mediated by diffusion, for example consider a plume consisting of a higher concentration of a less dense fluid. As it rises, diffusion acts to increase its density, as it generates a mass flux between the plume and the surrounding fluid. If the timescale for this diffusion is comparable to that of the convective flow the amount of GPE obtained will be reduced as their densities will equilibrate.

Taller cells will provide the most GPE but will also have greater diffusive flux, due to the larger vertical contact area between the adjacent plumes. Shorter plumes however will suffer from greater dissipation relative to the amount of GPE. Therefore, the rate of diffusion influences the size and shape of the convective plumes [18]. The ratio of the momentum diffusivity or viscosity (ν) to the mass diffusivity (D) is called the Schmidt number (Sc)

$$\mathrm{Sc} = \frac{\nu}{D}. \tag{1.7}$$

In systems in which convection is predominantly mediated by diffusion (and not viscous

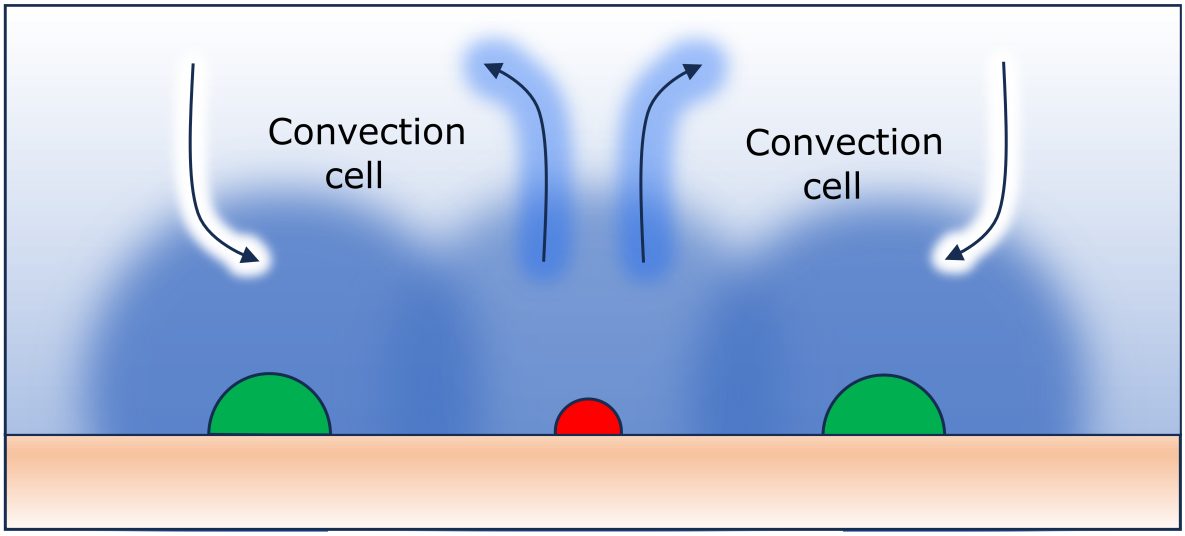

Figure 1.1: Diagram of the convection cells and plumes which can form above liquid or heated surfaces. The arrows represent a flow caused by convective plumes.

dissipation), the Gr can by multiplied by Sc resulting in the Rayleigh number (Ra)

$$\mathrm{Ra} = \frac{\Delta\rho R^3 g}{\mu D}, \tag{1.8}$$

noting that $\mu = \nu\rho$. The Ra therefore compares the buoyancy driven natural convection to the mass diffusion in the system. Eq. 1.8 predicts that convective transport is enhanced for large length scales and variations in density.

In this thesis 'convection' is used to refer to natural convection and 'advection' refers to forced convection.

1.3 Droplet geometry

The geometry of droplets which form on surfaces is characterised by an equilibrium contact angle (θ) which measures the internal angle between the substrate and the tangent to the interface at the contact line labelled in fig. 1.2. The value for θ can be calculated according to the 'Young' equation

$$\cos(\theta) = \frac{\gamma_{SG} - \gamma_{SL}}{\gamma_{LG}} \tag{1.9}$$

and is dependent on the three surface energies (γ) between the substrate (S), liquid (L), gas (G). These surface energies can be considered as forces acting to move the contact line.

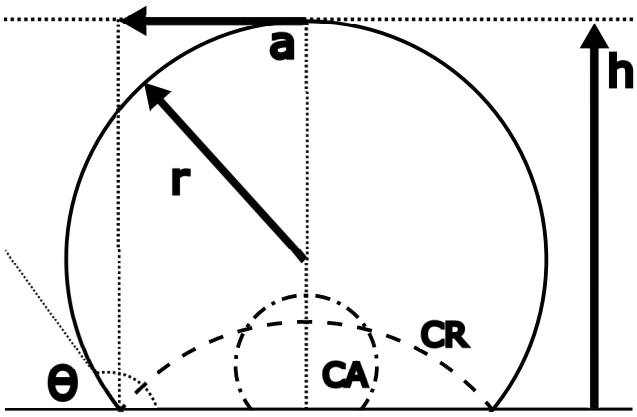

Figure 1.2: Droplet diagram showing the radius of curvature (r), base radius (a), height (h) and contact angle (θ) of two droplets which are evaporating in CA and CR mode.

Therefore if γ_{SG} is dominant or γ_{LG} is large, then the contact line gets pulled outward leading to very small contact angles and eventually liquid films. These substrates are referred to as 'hydrophilic' because of the equilibrium contact angle formed by water and correspond to the range $0 \leq \theta < \pi/2$ radians. Hydrophobic substrates with dominant γ_{SL}, refer to substrates which result in contact angles between $\pi/2 \leq \theta \leq \pi$ radians.

A static droplet's shape is determined by a balance between the (Laplace) pressure built inside the droplet and the hydrostatic pressure caused by gravity. The ratio of these forces is the Bond number (Bo)

$$\mathrm{Bo} = \frac{\Delta\rho g h^2}{\gamma_{LG}}. \tag{1.10}$$

The length scale which balances these forces (*i.e.* Bo = 1) is named the capillary length ($\lambda_c = \sqrt{\gamma_{LG}/\Delta\rho g}$). When the height of the droplets (h) is much less than λ_c and surface tension dominates (Bo $\ll$ 1), surface tension acts to minimise the surface area of the interface and as such the shape is spherically capped. For larger droplets with $h \gg \lambda_c$, gravity dominates (Bo $\gg$ 1) and droplets become puddles, flattened in the centre.

The volume of a spherical cap (V) is well known and is related to a number of geometric measurements, namely the base radius (a), radius of curvature (r) as well as the previously mentioned h and θ. Knowledge of any two of these measurements provides a complete description. In chapter 2 of this thesis the most commonly measured parameters are a and h, the expression relating these to V is

$$V = \frac{\pi}{6}(3a^2h + h^3). \tag{1.11}$$

In chapter 4 and 5 the most commonly measured parameters are θ and r, the expression relating these to V is

$$V = \frac{\pi}{3} r^3 (2 + \cos\theta)(1 - \cos\theta)^2. \tag{1.12}$$

1.4 Evaporation

When a liquid is evaporating there is a phase change happening at the interface. Molecules which obtain enough energy are able to overcome the energy potential created by the inter-molecular attractions which maintain the liquid. The energy to facilitate evaporation is called the latent heat of vaporisation and is supplied as heat from the surroundings. When the liquid is contained within a low-pressure environment the evaporation is largely limited by the supply of latent heat. At low-pressure it is therefore possible for evaporation to consume all of the available latent heat, reducing the liquid's temperature until it is cold enough to freeze. The Hertz-Knudsen relation [19] describes the maximum molar flux ($\mathrm{mol\,m^{-2}s^{-1}}$) from the interface

$$j_M = \frac{p_0 - p}{\sqrt{2\pi M R_g T}} \tag{1.13}$$

where M_w is the molar mass, R_g is the universal gas constant, p_0 is the vapour pressure of the liquid and p is the surrounding gas pressure, with $p = 0$ corresponding to a perfect vacuum. In many cases however liquids evaporate at standard temperatures and atmospheres, and evaporation becomes inhibited by the surrounding gas. The vapour molecules exiting at the interface (vaporising) will collide with the gas molecules, moving in a random walk. Some of these molecules will re-enter the liquid (condensing). Once the interface region becomes saturated the number of molecules vaporising and condensing will be equal and a dynamic equilibrium is reached, with the volume of the liquid not changing [20]. If the surrounding gas is unsaturated a concentration gradient exists normal to the interface, leading to diffusion (governed by eq. 1.3 discussed in section 1.1). This diffusion acts to reduce the saturation at the interface, lowering the number of condensing molecules and increasing the number of vaporising molecules until the saturation equilibrium is reached again. In general it is assumed that the interface is always at saturation and the net amount of molecular flux across the interface is that which sustains this [21].

This saturation concentration (c_∞) is given by the ideal gas law

$$c_\infty = \frac{p_{sat} M_w}{R_g T} \tag{1.14}$$

where p_{sat} is the saturation vapour pressure, which can be calculated with the semi-empirical Antoine equation

$$p_{sat} = 10^{A - \frac{B}{C+T}}. \tag{1.15}$$

A, B and C are tabulated, empirically obtained constants for a specific liquid. The values for water for $0 \leq T(^\circ\mathrm{C}) \leq 100$ are given in table. 1.4.

Both c_∞ and p_∞ are used interchangeably to quantify the volatility of a liquid.

A	B	C
8.07131	1730.63	233.426

Table 1.2: Antoine coefficients for water.

1.5 Isolated Droplet Evaporation

The evaporation rates of sessile isolated droplets of low volatility liquids (*e.g.* water) at standard pressure and temperature are well described by existing theory. These rates have been shown to be limited by diffusive transport of its vapour into the surrounding environment. The concentration of vapour surrounding a droplet is therefore governed by eq. 1.3 (as described in section 1.1). If the timescale for diffusion (L^2/D) is small in comparison to the lifetime of the droplet, the evaporation can be assumed to be quasi-steady. This means that the the concentration (c) does not vary in time and $\frac{\partial c}{\partial t} = 0$. Substituting this into eq. 1.3 shows the vapour concentration is given by the Laplace equation

$$\nabla^2 c = 0. \tag{1.16}$$

The exact solution to eq. 1.16 around an equi-convex lens was solved by N.N Lebedev [22] as an electrostatics problem. Jackson showed that close to the contact line this flux (j), radially over the interface (r_c) of the lens (droplet) varies with its contact angle [23],

$$j \propto (a^2 - r_c^2)^{\frac{\pi}{2(\pi-\theta)}-1}. \tag{1.17}$$

This function predicts: at $\theta = \pi/2$ radians, homogeneous flux on the interface; between $0 < \theta < \pi/2$ radians, enhanced flux near the contact line ($r_c \to a$); and between $\pi/2 < \theta < \pi$ radians, suppressed flux near the contact line [24]. Integrating j over the surface of the droplet gives the total volumetric evaporation rate ($m^3 s^{-1}$) according to the diffusion limited model [25]

$$\rho_l \frac{dV_T}{dt} = a\pi D c_\infty (\phi_{sat} - \phi) f(\theta), \tag{1.18}$$

where $\phi = c_{amb}/c_\infty$ is the fractional ambient humidity at $r_c = \infty$. ϕ_{sat} is saturation fraction at the interface. $f(\theta)$ is a function representing the effect of the substrate which depends on the contact angle. Several simplified expressions for $f(\theta)$ have been proposed [25–27], one example which is continuous and defined over $0 \leq \theta \leq \pi$ radians is

$$f(\theta) = \frac{2}{\sqrt{1 + \cos\theta}}, \tag{1.19}$$

as reported by Hu, Wu, and Liu [28] [1]

1.5.1 Thermal effects and internal flow

As discussed in section 1.4 liquids require latent heat to evaporate, which is sourced from its environment and the liquid itself. In this section the flux over a droplet's interface was described to be in general non-uniform and therefore the amount of latent heat required to sustain this lead to differential cooling on the interface. Due to the low thermal conductivity (κ) of gases (for air $\kappa \approx 26 \times 10^{-3}\,\mathrm{W\,m^{-1}K^{-1}}$) [30]) in comparison to solids (for glass $\kappa \approx 1\,\mathrm{W\,m^{-1}K^{-1}}$) [31]), heat is largely supplied by conduction from the substrate. The rate at which the latent heat can be transported to different points on the interface depends on the conductivity of the droplet (for water $\kappa = 0.586\,\mathrm{W\,m^{-1}K^{-1}}$) [32]) and the height of the droplet interface over which it must be conducted. The conduction distance and the non-uniform evaporative flux are both dependent on the contact angle. For flat droplets, the difference in height at the apex and near the contact line is similar but the evaporative flux is pronounced near the contact line and therefore the cooling should be greatest in this region. For droplets with higher contact angles ($\theta > \pi/2$) the temperature should be lowest near the apex, because it is both furthest from the substrate and also the region with the largest flux.

[1] After the submission of this thesis Wray and Moore published a more accurate expression to eq. 1.19 [29], which could be used in future work.

The flow inside droplets has been studied in detail by many authors, for example Deegan et al. [9] who showed that the coffee ring effect is caused by radial outward flow as a result of a pinned contact line. Further theoretical work has since been carried out modelling these flows more generally [2, 33]. In addition to flow driven by evaporation, the variations in flux leads to further considerations. For example, the surface tension (γ) of the droplet depends on temperature and the non-uniform cooling on the surface can therefore result in Marangoni flows. This is discussed in detail by Ristenpart et al. [34], connecting these flows to the temperature profiles and shapes of the droplets. Marangoni flows can also be generated by different components with dissimilar volatilities, binary droplets of this sort have very complex flow patterns due to both Marangoni effects and density driven flow [35, 36].

1.6 Condensation

As described in section 1.4, air can become saturated with the vapour which evaporates from a liquid. This occurs when the amount of vapour molecules condensing reaches a dynamic equilibrium with those vaporising. The specific equilibrium condensation depends on its temperature (see eq. 1.14). If saturated air is cooled quickly the amount of vapour within the air is greater than the equilibrium. Air in this state is referred to as supersaturated. This often occurs near to a cold surface, which will cool the immediately adjacent air, leading to condensation onto the surface. This continues until the concentration is reduced and equilibrium is restored. The condensation can either be film-wise or drop-wise which depends on the specific properties of the surface and the contact angle the liquid forms onto it (described by eq. 1.9). Typically, impurities on the substrate act as nucleation sites for droplet condensation [37]. Arrays of these droplets of $\sim \mu$m size over a surface are often referred to as breath figures and there is much work on the formation and applications of them, see the book by Rodríguez-Hernández and Bormashenko [38]. The growth of a single droplet due to a supersaturated environment can be predicted by eq. 1.18 where $(\phi_{sat} - \phi) < 0$. In drop-wise condensation the growth of each droplets can also be due to water absorption onto the substrate, coalescence of adjacent droplets or by direct droplet deposition from the air [39–41].

1.7 The Kelvin effect

Liquid interfaces which are sufficiently curved have a higher vapour pressure than flat interfaces. A molecule at a curved interface has fewer neighbouring molecules than at a flat interface. Therefore the inter-molecular forces exerted and the latent heat required to vaporise it are less. As a result of this, there is an increased amount of molecules escaping and the concentration of vapour molecules at the interface must be greater, before the dynamic equilibrium between condensation and vaporisation is re-balanced. The increase in saturation concentration at the interface due to its curvature, is called the Kelvin effect [42]. The reverse is also true, with concave interfaces having lower saturation concentration.

For clouds to form, droplets must be able to grow from pure vapour due to condensation. However the vapour pressure over droplets with a small radius of curvature (r) will have large vapour pressures and will therefore not be stable in saturation conditions. Non-volatile impurities (solute) can aid in the process of droplet growth, by reducing the vapour pressure of these small droplets and acting as nucleation sites [43]. This is called the Raoult effect.

The Raoult effect and the Kelvin effect can be combined [44] to show how the ratio of the vapour pressure of droplets of different radii ($p(r)$) to p_{sat} varies and is given by

$$\frac{p(r)}{p_\infty} = \exp\left(\frac{r_k}{r} - \frac{3nM}{4\pi\rho_l r^3}\right). \tag{1.20}$$

Where $r_k = 2M\gamma/RT\rho_l$ is the Kelvin radius, n is the number of moles of solute and $p(r)/p_\infty = \phi_{sat}$ in eq. 1.18. The first term in the brackets represents the Kelvin effect and the second the Raoult effect.

1.8 Multiple droplets

When droplets evaporate within an array they do not evaporate as the sum of their isolated constituents, instead they evaporate with group dynamics each influencing their neighbours and altering their individual evaporation rates. There are several possible ways in which droplets in close proximity could influence one another including thermally, through precursor films or by changing local vapour concentrations.

1.8.1 Diffusive evaporation

For sessile isolated droplets of low volatility liquids (*e.g.* water) at standard pressure and temperature, it has been reported that the superimposition of the vapour fields surrounding each droplet is a significant part of these interactions [45–49]. In these cases the evaporation is found to be diffusion limited and the local increase in vapour concentration near the interface due to the presence of neighbours, is found to slow the evaporation rate compared to the isolated case. This is because vapour mutually diffuses into the regions of air between the droplets, leading to it becoming saturated. Therefore the rate limiting process for phase change at the interface is the time it takes for the vapour to be diffused away and for 'space' to be created near the interface for molecules to escape the liquid. This is often called the 'Shielding effect' as multiple droplets shield the evaporation of their neighbours. Similar diffusive interactions have also been observed for the case of dissolution [50–53]. A series of analytical models have been proposed to capture the dynamics of these vapour interactions [1, 45, 54, 55]. A specific description of each model is given in the following sections (1.8.3, 1.8.4 and 1.8.5).

Multiple droplet evaporation is also investigated in reverse, in drop-wise condensation literature, the formation and dynamics of which, are described in section 1.6. Similar diffusive interactions are observed for multiple droplet condensation, as droplets in close proximity do not grow as fast due to local depletion of the vapour around the droplets [56–58].

1.8.2 Convective evaporation

In addition to diffusion, natural convection has also been observed by Carrier et al. [45] and Kelly-Zion et al. [59] to enhance the evaporation rate of droplets. Kelly-Zion et al. placed single flat droplets of different R on pinned aluminium surfaces and measured their evaporation. Carrier et al. conducted experiments with filled beakers of water also at different length scales (R). Both authors found a transition in which evaporation rate increased from $\frac{dV}{dt} \propto R^1$ to $\frac{dV}{dt} \propto R^{>1}$. They both attributed this enhanced evaporation to natural convection of the vapour and showed the transition is predicted by Ra. The effect of natural convection above dissolving liquid droplets was reported by Laghezza et al. [51], who conducted experiments and simulations, showing that this enhanced evaporation can overcome the diffusive shielding effect and enhance the droplet evaporation in the array,

to even greater than that of the isolated case. Dietrich et al. [60] experimentally imaged the flow around dissolving droplets finding the formation of a convective plume above the droplets transporting the dissolving liquid away from them. A theoretical expression was derived by Dollet and Boulogne [61] to describe the enhanced evaporation as a result of the formation of a single plume by separating the droplet into an edge and intermediate zone. The edge has a similar flux to that of an isolated droplet (see eq. 1.17). In the intermediate zone the formation of a slender boundary layer with flow towards the centre of the droplet is assumed and a flux in this region is given as

$$j = \frac{D(c_{sat} - c_{amb})Gr^{1/5}}{R^{3/5}(R - r_c)^{2/5}}. \tag{1.21}$$

Simulations conducted by Chong et al. [53] demonstrated that these plumes also appear above droplets dissolving, with individual plumes merging into one.

1.8.3 Carrier et al

Carrier et al. [45] developed an analytical model for the evaporation of an array of droplets. The authors noticed that the combined vapour concentration field around multiple droplet has similarities to that of a single droplet. The inter-droplet regions will quickly saturate and in the centre of the array, the evaporation will largely be governed by diffusion of vapour above and at the edge of the array. Therefore the evaporative flux is similar to that of a single flat 'superdroplet' which spans over the entire array. The flux over its surface is therefore predicted by eq. 1.17 with $\theta = 0$, giving

$$j \propto (R^2 - r_c^2)^{-1/2}. \tag{1.22}$$

This simplification allows the authors to combine the individual droplet contributions and derive an approximate expression, characterising the total evaporation rate of an array of N droplets with individual base radius a as a single 'superdroplet' with radius R, as

$$\frac{dV}{dt} = \frac{4\rho_l \pi N a c_{sat} R}{R + \pi N a}. \tag{1.23}$$

It is important to note that this expression doesn't give evaporation rates for the individual droplets, but does give a prediction for the entire array.

1.8.4 Diffusive interactions of flat droplets

Fabrikant [54] proposed an analytical model for the diffusive transport of a species through a porous membrane. An expression for the flux through each pore is derived, affected by the number and size of the neighbouring pores. Wray, Duffy, and Wilson [1] recognised the similarity of the problem to that of multiple droplets, then applied this model to predicting the evaporation of flat sessile droplets (no contact angle). Successfully re-deriving the Fabrikant expression and comparing to the experiments of Khilifi et al. [62]. The theory models the shielding effect caused by the diffusive vapour fields which form around each of the individual droplets (as described in section 1.5). Because of the use of the Laplace equation the theory assumes that the vapour is quasi-static and that the transient time is too short to influence the evaporation. For the theory these transient transitions occur instantly, both for the initially development of the vapour and when a droplets disappears within the array. The evaporation rate of a kth droplet is the evaporation of the same droplet in isolation $\left(\frac{dV}{dt}\right)^*$ reduced by its interactions with its neighbours as

$$\left(\frac{dV}{dt}\right)_{\mathrm{k}} = \left(\frac{dV}{dt}\right)^*_{\mathrm{k}} - \sum_{\substack{\mathrm{n}=1 \\ \mathrm{n}\neq\mathrm{k}}}^{N} \left(\frac{dV}{dt}\right)_{\mathrm{n}} \psi_{\mathrm{kn}}, \tag{1.24}$$

where the last term is the summation of the interactions of the kth droplet with the nth over the N droplets in the array. These interactions depend on the evaporation rate of the nth droplet and $\psi_{0,\mathrm{kn}}$ given as

$$\psi_{kn} = \frac{2}{\pi} \arcsin\left(\frac{a_k}{s_{kn}}\right), \tag{1.25}$$

containing the influence of the base radius (a) and separation between kth and nth droplets (s_{kn}).

1.8.5 Diffusive interactions of spherical cap droplets

An alternative but similar approach to Wray et al [1] is that of Masoud et al [55] who redrived some of Fabrikant later work [63]. The model can be written in the same form as eq. 1.24 but differs in its calculation of the interaction term (ψ_{kn}). The model still captures the diffusion limited interactions but extends to droplets with $\theta > 0$. To do this the interaction term is instead inferred from the spherical cap vapour concentration field

around the kth droplet in isolation. Evaluating it at a distance s_{kn} from the centre of the kth droplet to the centre of the nth droplet. The value of the evaluated point in the concentration field is given by

$$\psi_{\mathrm{kn}} = 4I_1 \frac{a_{\mathrm{n}}}{s_{\mathrm{kn}}} + (I_1 + 4I_2) \frac{a^3(s_{\mathrm{kn}}^2 - 3h_{\mathrm{k}}^2)}{s_{\mathrm{kn}}^5} \tag{1.26}$$

where I_1 and I_2 are integrals defined as

$$I_1 = \int_0^\infty \left[1 + \frac{\cosh\left((2\pi - \theta)\tau\right)}{\cosh\left(\theta\tau\right)}\right]^{-1} d\tau \tag{1.27}$$

and

$$I_2 = \int_0^\infty \left[1 + \frac{\cosh((2\pi - \theta)\tau)}{\cosh(\theta\tau)}\right]^{-1} \tau^2 d\tau. \tag{1.28}$$

For both the Wray et al and Masoud et al models eq. 1.24 can be written in matrix form as

$$\left[\frac{dV}{dt}\right] \Psi = \left[\frac{dV}{dt}\right]^*, \tag{1.29}$$

where $\left[\frac{dV}{dt}\right]^*$ is a $N \times 1$ matrix with elements equal to the known isolated evaporation rates of each droplet. Ψ is an $N \times N$ matrix with the element at k, n representing the interaction of the kth droplet with the nth.

For both forms of the interaction term the diagonal elements equal unity, and the off diagonal elements are calculated by eq. 1.25 or 1.26 for the Fabrikant-Wray et al and for the Masoud et al models respectively. $\left[\frac{dV}{dt}\right]$ is an $N \times 1$ matrix with elements equal to the unknown evaporation rates of each droplet in the array. By inverting Ψ the system of equations can be solved for the N unknown evaporation rates accounting for the diffusive interactions.

$$\left[\frac{dV}{dt}\right] = \left[\frac{dV}{dt}\right]^* \Psi^{-1}. \tag{1.30}$$

Therefore by specifying the droplet positions and radii, eq. 1.30 allows for general predictions of the individual evaporation rates for any arbitrary configuration of multiple droplets. The matrix of isolated values $\left[\frac{dV}{dt}\right]^*$ can be measured or theoretically predicted by eq. 1.18.

The models of Carrier et al. [45], Fabrikant-Wray, Duffy, and Wilson [1, 54] and Masoud, Howell, and Stone [55] are compared against repeatedly in this thesis and will be henceforth be referred to as the Carrier et al, Wray et al and Masoud et al models

respectively.

It is also noticed that a similar model, published before that of Wray et al and Masoud et al was developed by Annamalai, Ryan, and Chandra [64] who used a point source method (PSM), treating each droplet as a vapour point source to obtain a similar expression for the interaction term in eq. 1.25. They found good agreement with a full calculation of the problem. These PSM models are widely used in the field of fuel combustion [65]. Future work utilising these models will be discussed further in chapter 7, section 7.6.

1.9 One-sided model

In addition to diffusion limited evaporation other models exist to describe evaporation with phase change being the rate limiting process. These models are referred to as the one-sided models [66] and are important when diffusion becomes fast enough to no longer limit the rate at which molecules can escape the surface. In this case the evaporative flux over the interface of a droplet depends on the amount of heat supplied to the interface and therefore the interfacial temperature. This model is applicable to droplets on heated substrates, for evaporation into low pressure environments and when the liquid is contaminated with solute which increases the latent heat of vaporisation [67, 68].

Chapter 2

The Pattern Distortion technique

To capture the evaporation dynamics and characterise the droplet-droplet interactions, the size of each droplet in an array must be measured throughout the evaporation process. The most common method when studying isolated droplets is a side camera which captures images of the droplet's profile. Calibrated measurements of the radius and height in these images provide enough information to calculate a volume assuming the droplet is radially symmetric (has a circular contact line) and is a spherical cap. For multiple droplets (specifically 2D arrays) side cameras are unable to image every droplet, as central droplets are obscured by those at the edge. Top cameras have been used to view droplets simultaneously however on their own they provide no information about the droplet's height (or equivalently contact angle). Global evaporation rates for the entire array can be measured with a mass balance but cannot resolve individual droplets and is incapable of studying droplet-droplet interactions.

Clearly these limitations demonstrate the need for a new technique which is suited to experimental multiple droplet research. This chapter explains the development, validation and optimisation of a new 'Pattern Distortion' (PD) technique, which does not suffer from the aforementioned restrictions.

The technique is a top camera approach which treats droplets as liquid lenses and relies on geometrical optics to relate its optical properties to its shape. A situation where this effect can be observed is when raindrops land on phone screens. The droplet acts as a lens and the embedded pixels act as the object imaged by this lens. The different images which are formed by various droplets geometries in this situation can be seen in fig. 2.1. Qualitatively it can be observed that the image which forms is very sensitive to the lens

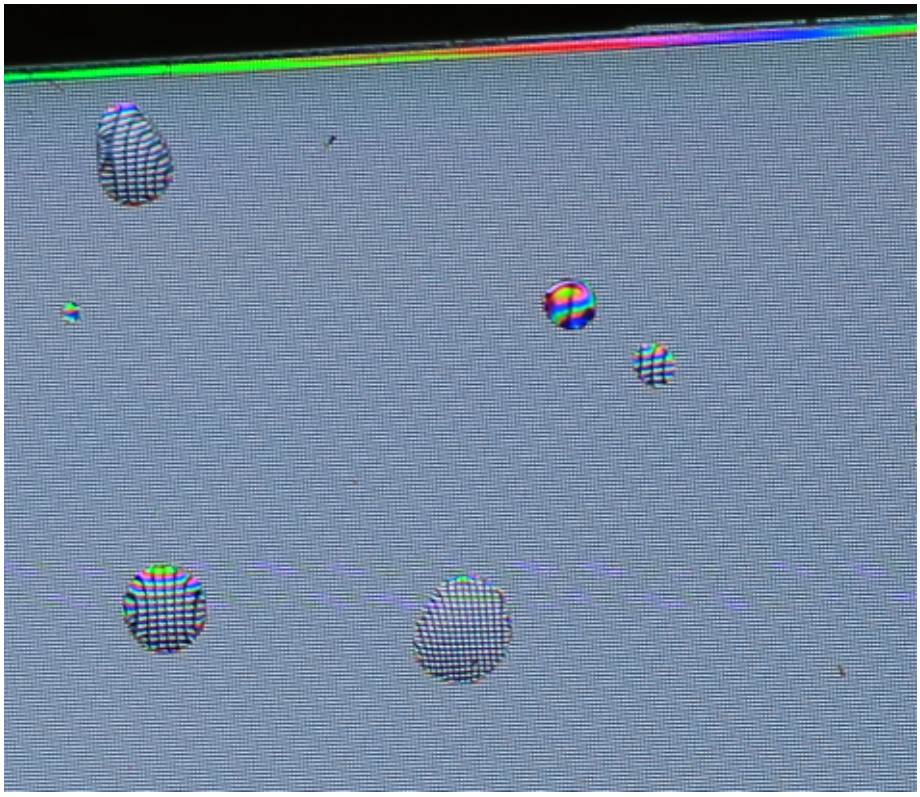

Figure 2.1: iPhone 11 phone screen with different shaped water droplets forming images of the underlying pixels.

which created it and the magnification of the pixels is largest in the smallest droplets. The aim of this chapter is to understand the connection of a spherical cap droplet geometry and the resulting image formed.

2.1 Matrix transfer optics

In order to quantify how the magnification by a droplet is related to its geometry we apply an optical transfer matrix method. The method traces paraxial rays through an optical system by combining matrices corresponding to how they propagate through it. One such matrix describes translation events through a uniform medium of thickness d and can be described by the matrix

$$\begin{pmatrix} 1 & d \\ 0 & 1 \end{pmatrix} \tag{2.1}$$

The rays can also refract at curved interfaces between two refractive indices n_i and n_f, which is model by the matrix

$$\begin{pmatrix} 1 & 0 \\ \frac{n_i - n_f}{r n_f} & \frac{n_i}{n_f} \end{pmatrix}. \tag{2.2}$$

Where r is the radius of curvature of the interface, which is negative if it is concave. When the interface is flat $r \to \infty$ and the bottom left element of matrix. 2.2 becomes nil. The matrices 2.1 and 2.2 can be used individually to describe single events or consecutively to describe composite optical systems. In either case the matrix (matrices) acts as an operator (χ) mapping points in the object plane to points in the image plane. The height (y_{obj}) and angle (ϕ_{obj}) of each ray in the object plane with respect to the optical axis is transformed by χ to the final height (y_{im}) and angle (ϕ_{im}) in the image plane as follows

$$\begin{pmatrix} y_{im} \\ \phi_{im} \end{pmatrix} = \chi \begin{pmatrix} y_{obj} \\ \phi_{obj} \end{pmatrix} = \begin{pmatrix} \chi_{11} & \chi_{12} \\ \chi_{21} & \chi_{22} \end{pmatrix} \begin{pmatrix} y_{obj} \\ \phi_{obj} \end{pmatrix}. \tag{2.3}$$

By multiplying out eq. 2.3 you obtain

$$y_{im} = \chi_{11} y_{im} + \chi_{12} \phi_{obj}, \tag{2.4}$$

for the final height of the ray and

$$\phi_{im} = \chi_{21} y_{obj} + \chi_{22} \phi_{obj}, \tag{2.5}$$

for the final angle of the ray. If χ is a single translation (eq. 2.1), then by substitution eq. 2.4 becomes

$$y_{im} = y_{obj} + d\phi_{obj}, \tag{2.6}$$

where the small angle approximation has been used such that $\phi_{obj} \approx \tan(\phi_{obj}) = \frac{y_{obj} - y_{im}}{d}$, and eq. 2.5 becomes

$$\phi_{im} = 0 + \phi_{obj}. \tag{2.7}$$

In other words the height of the ray can change but its angle of propagation remains the same. Equally, if eq. 2.2 is substituted in the same way (representing a single refraction), $y_{obj} = y_{im}$ and the angle changes according to Snell's law. Making the paraxial approximation here means that the width of the lens (or collection of lenses in the case of multiple

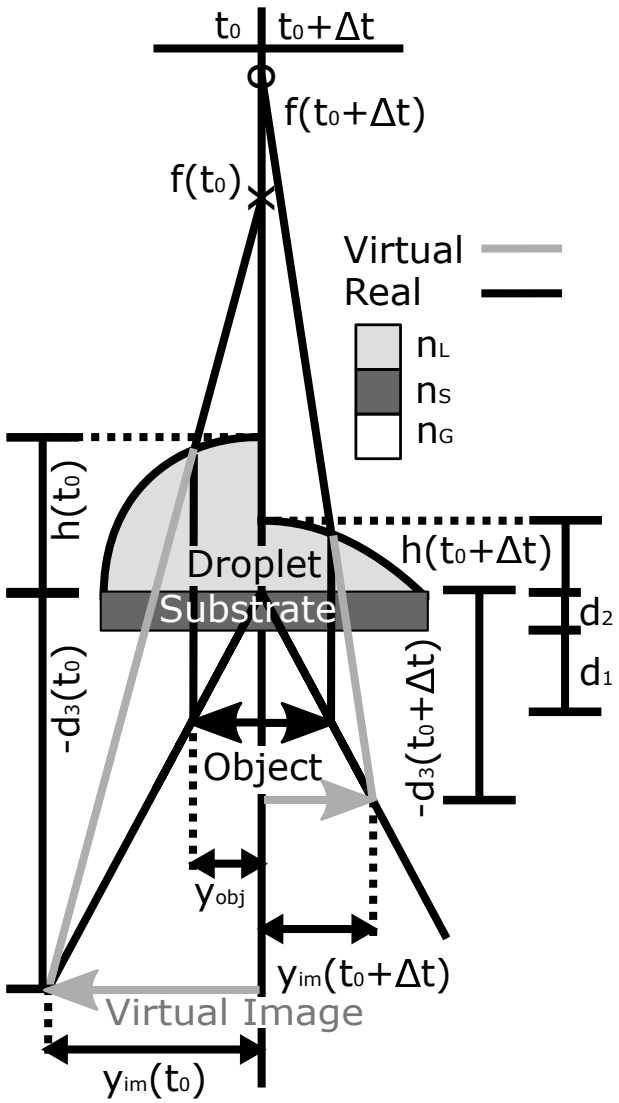

Figure 2.2: Diagram tracing real (black) and virtual (grey) ray paths from the pattern (d_1, n_G), through the substrate (d_2, n_S) and droplet (h,n_L), to the (virtual) image plane (d_3), for a time t_0 (left) and $t_0 + \Delta t$ (right, of the optical axis). y_{im} is the height of the image formed and f is the focal point of the droplet.

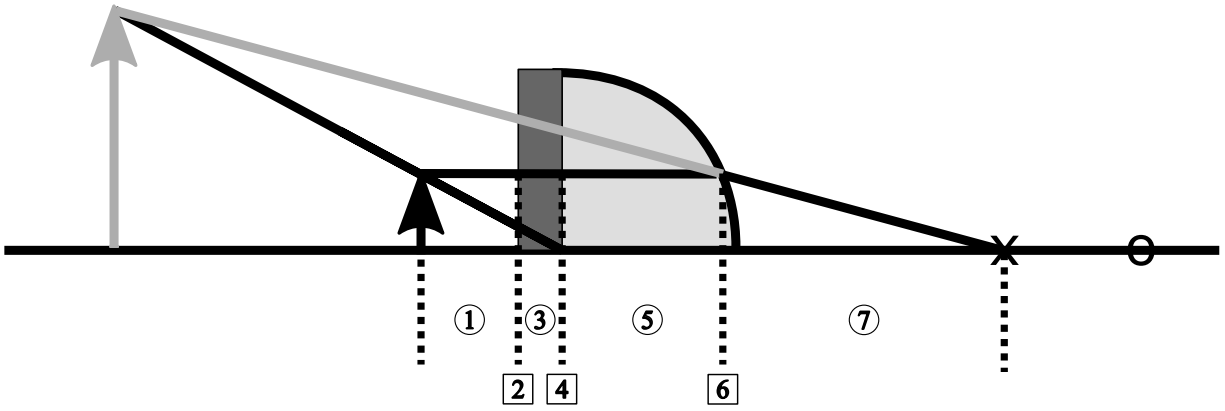

Figure 2.3: Replotting the LHS of fig. 2.2 with numbered translation (circled) and refraction (squared) events of the paraxial rays.

droplets) must be sufficiently small compared to the perpendicular distance to the imaging camera. For our sessile droplet optical system χ in eq. 2.3 is a series of refractions and translations (see fig. 2.2). The rays of light originate from a point on the object plane then undergo four translations and three refractions, namely:

1. Transfer a distance, d_1 through the air beneath the substrate.
2. Refract from the air of refractive index, n_G into the substrate of refractive index, n_S.
3. Transfer through the substrate of thickness, d_2.
4. Refract from the substrate into the liquid of refractive index, n_L.
5. Transfer through the droplet of height, h.
6. Refract at the droplet interface of radius of curvature r, back into the air.
7. Transfer through air to the image plane at position, d_3.

For clarity the LHS of fig. 2.2 has been replotted in fig.2.3 with the translations and refractions numbered corresponding to the above list. These seven events result in the

following seven matrices,

$$\chi = \begin{pmatrix} 1 & d_3 - h \\ 0 & 1 \end{pmatrix} \begin{pmatrix} 1 & 0 \\ \frac{n_L - n_G}{r n_G} & \frac{n_L}{n_G} \end{pmatrix} \begin{pmatrix} 1 & h \\ 0 & 1 \end{pmatrix} \begin{pmatrix} 1 & 0 \\ 0 & \frac{n_S}{n_L} \end{pmatrix} \begin{pmatrix} 1 & d_2 \\ 0 & 1 \end{pmatrix} \begin{pmatrix} 1 & 0 \\ 0 & \frac{n_G}{n_S} \end{pmatrix} \begin{pmatrix} 1 & d_1 \\ 0 & 1 \end{pmatrix} = \begin{pmatrix} \chi_{11} & \chi_{12} \\ \chi_{21} & \chi_{22} \end{pmatrix}. \tag{2.8}$$

Here n_G, n_S, n_L denote the refractive indices of the gas, substrate and liquid respectively. Matrix multiplication of eq. 2.8 reduces χ to a single 2×2 matrix describing how points in the object plane (y_{obj}) are mapped onto the image plane (y_{im}). In order for an image to form, all rays from the object plane must come to a single point on the image plane. Therefore, the final height of each ray on the image plane y_{im} cannot depend on the initial angle of the rays at the object plane ϕ_{obj}. Consequently at the position where the image is formed the element χ_{12} is equal to zero. For our situation of seven matrices this leads to

$$\chi_{12} = d_1 + (d_3 - h)\left[\frac{(n_L - n_G)(d_1 + \frac{h n_G}{n_L} + \frac{d_2 n_G}{n_S})}{r n_G} + 1\right] + \frac{h n_G}{n_L} + \frac{d_2 n_G}{n_S} = 0. \tag{2.9}$$

Rearranging, results in an expression for the position of the image plane (d_3)

$$d_3 = h - \left[\frac{r n_G \left(\frac{d_1}{n_G} + \frac{h}{n_L} + \frac{d_2}{n_S}\right)}{(n_L - n_G)\left(\frac{d_1}{n_G} + \frac{h}{n_L} + \frac{d_2}{n_S}\right) + r}\right]. \tag{2.10}$$

For thick lenses under the paraxial approximation the image plane is measured from the principle point of the interface which forms the image. For the spherical cap (plano-convex) droplet (lens) the principle point of the curved interface lies at the apex and so the image distance is $d_3 - h$. Recognising this, eq. 2.10 can be written into the form of a standard lens equation

$$\left(\frac{n_G - n_L}{n_G}\right)\frac{1}{r} = \frac{1}{d_3 - h} + \frac{1}{n_G\left(\frac{d_1}{n_G} + \frac{h}{n_L} + \frac{d_2}{n_S}\right)}. \tag{2.11}$$

Where the LHS can be shown to be the plano-convex $1/f$ from the Lens-maker's equation. The term χ_{11} in eq. 2.8 represents the linear magnification of the system and

$$\frac{y_{im}}{y_{obj}} = \chi_{11} = M = \frac{(d_3 - h)(n_L - n_G)}{r n_G} + 1. \tag{2.12}$$

Eq. 2.10 can be used to substitute for the unknown d_3, which after rearrangement yields an expression relating M to the radius of curvature of the droplet's interface in terms of known distances d_1 and d_2 and refractive indices n_L, n_G and n_S,

$$M = \frac{r n_G}{r n_G - \left(d_1 + \frac{h n_G}{n_L} + \frac{d_2 n_G}{n_S}\right)(n_G - n_L)}. \tag{2.13}$$

If the droplet is undistorted by gravity *i.e.* $Bo \ll 1$, its shape can be considered a spherical cap and r can be related to the height, h and base radius, a by

$$r = -\frac{h^2 + a^2}{2h}. \tag{2.14}$$

By substituting into eq. 2.13

$$M = \frac{h^2 + a^2}{(2n-1)h^2 - 2nlh + a^2}, \tag{2.15}$$

where

$$n = \frac{n_G}{n_L} \tag{2.16a}$$

$$l = \frac{n_L - n_G}{n}\left(\frac{d_1}{n_G} + \frac{d_2}{n_S}\right). \tag{2.16b}$$

The term l has units of length and captures the various optical and geometric parameters of the setup. This definition also simplifies the form of eq. 2.15.

By expressing h in terms of the contact angle (θ), eq. 2.15 can be rewritten as

$$M = \frac{\tan^2\left(\frac{\theta}{2}\right) + 1}{(2n-1)\tan^2\left(\frac{\theta}{2}\right) - 2n\left(\frac{l}{a}\right)\tan\left(\frac{\theta}{2}\right) + 1}. \tag{2.17}$$

In fig. 2.4, eq. 2.17 is used to plot the calculated values of M for a range of l/a and θ values, which can be used to optimise the experimental setup to provide the largest sensitivity to changes in the droplet's shape. The white region represents high magnifi-

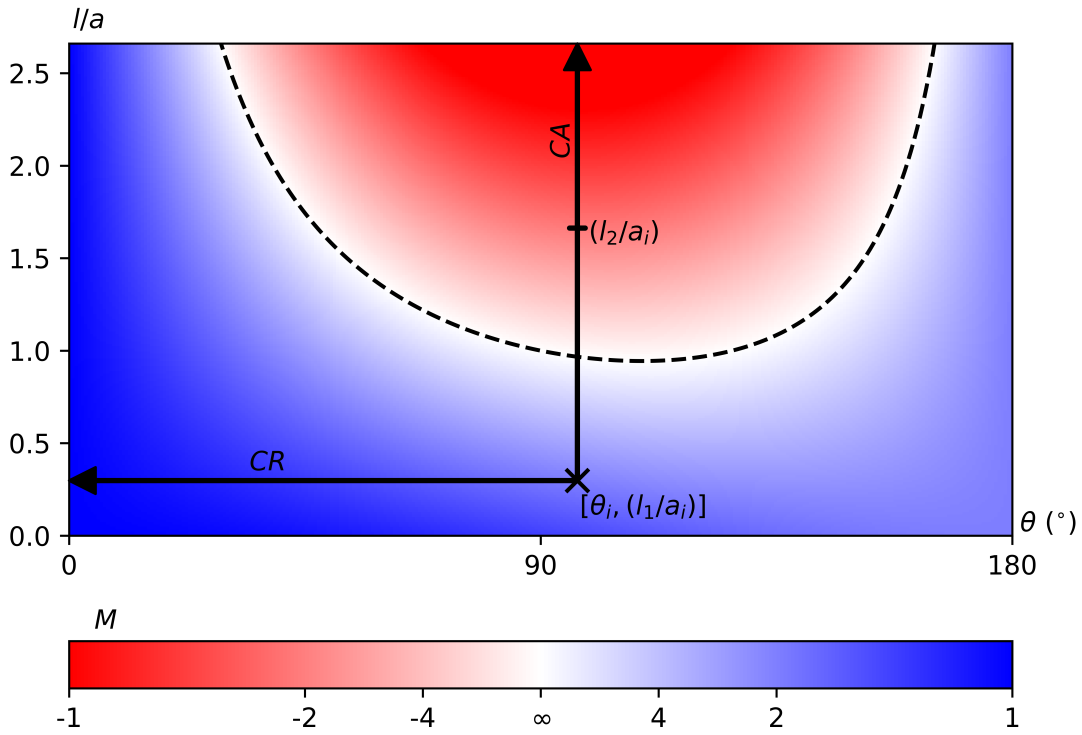

Figure 2.4: The magnification M mapped over θ and l/a. Dashed line indicates $M = \infty$. The black cross at $[\theta_i, (l_1/a_i)]$ indicates the approximate initial position of the droplets in fig. 2.7 and 2.8 (in section 2.3), the vertical and horizontal lines show the evolution of M for CA and CR evaporation respectively.

cation, with the black dashed line indicating an infinitely magnified image, determined mathematically by setting the denominator in eq. 2.17 equal to zero. The length-scale l emerges as the radius of a droplet with contact angle $\theta = 90°$ that forms an image with infinite magnification.

2.2 Image processing

To extract the magnification from the top images, a MATLAB circle detection script (available at: `https://doi.org/10.6084/m9.figshare.26587522.v1`) was written to place a region of interest (ROI) over the central portion of each droplet and measure the median diameter of the dots inside the droplet in each frame. The size of this region is chosen based on the following considerations: if the region is made too big the magnification of the distorted dots at the edge lead to increased certainty in the measured diameter and consequently the height. Additionally magnifications will vary across this ROI due to the fact the interface is curved therefore an average of the magnification would give an

average height of the interface within the ROI. Determining the volume of a spherical cap requires the height at the apex and so for larger ROI the volume can be made artificially smaller. Within these considerations the largest ROI is optimum as it provides averages to be taken to reduce uncertainty in determination of dot sizes.

The raw images are made binary by performing an Otsu threshold and inverting. The MATLAB function `bwconncomp` is used to find connected pixel components (the dots) in the image. This function detects a component if eight or more black pixels in the binary image are connected by their edges or corners. The `regionprops` function is then called to extract positional information for each component as well as a radius, calculated by fitting an ellipse and averaging its minor and major axes. Trigonometry is then used to extract only the components which lie completely within the ROI specified by the user. The median or mean radii of the detected dots is computed and the process is repeated across each frame. Fig. 2.5 shows an example of a raw (left) and processed (middle) image along with the corresponding feature extraction (right) determined by the code. The median dot radius for each frame is divided by the median radius in the final frame (when the droplet has evaporated), to calculate M. The mean also returns similar values and has a statistical advantage in images with minimal noise and artefacts but the median was used in this case because it is found to be less susceptible to uncertainty caused by misdetections.

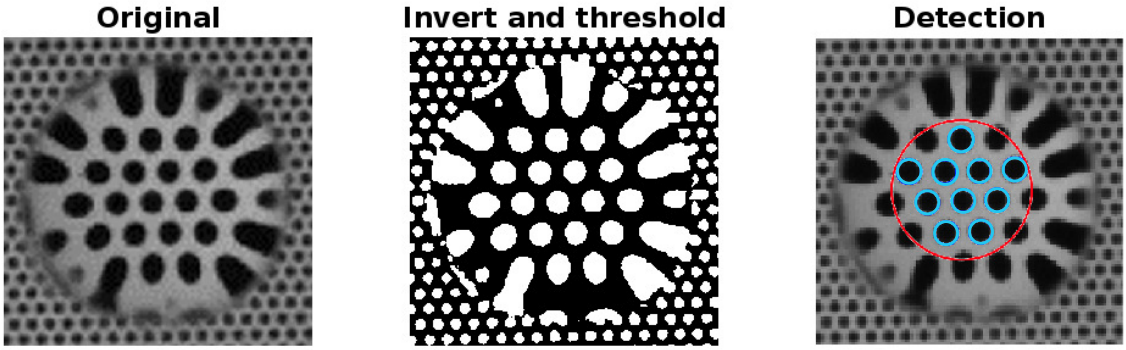

Figure 2.5: An example of the image processing and dot detection process used to determine the magnification in each frame of the Pattern Distortion data. In the right panel the blue circles represents dots detected within the ROI indicated by the red circle.

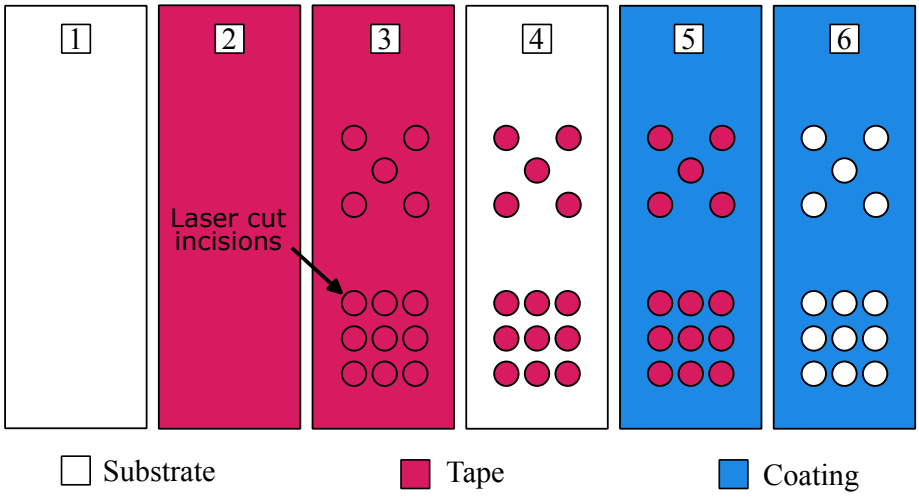

Figure 2.6: A method for selectively hydrophobising a surface by using laser cut tape to mask the substrate before coating.

2.3 Validation

In order to validate the technique, a single high resolution repeating hexagonal dot pattern is used as the object. Alternatively, single features could be placed under each droplet however this requires careful alignment such that they are placed directly under the apexes of each droplet. For this reason a repeating pattern is used, ensuring there is always a feature near the centre of the droplet. The pattern is purchased from JD Photo Data and is manufactured by printing chrome dots lithographically on soda-lime glass (item: SL12) with a diameter of $100.0 \pm 0.4\,\mu$m and a pitch of $150\,\mu$m with a cumulative accuracy of $\pm 2\,\mu$m over 70.7 mm. To ensure the droplets maintain a known circular base radius throughout evaporation, the contact line is pinned. To achieve this, a clean glass slide in ($n_S = 1.46$) is covered with polyimide tape and a 10 W UV 355 nm (TRUMPF, SCIII10SL) laser is used to make circular incisions in the tape. The outer part of the tape is then removed and the slide is hydrophobised by spray coating with Glaco Mirror Coat Zero [SOFT99], baked for 12 mins at 50°C and left then to cure for 10 mins at room temperature. Finally, the remaining circular pieces of tape are removed, revealing uncoated hydrophilic glass regions, surrounded by the hydrophobic coating. See fig. 2.6 for a diagram of this process. Controlling the size and position of these circular incisions means bespoke templates can be created which pin the location and contact lines of the droplets for approximately 80% of their drying time.

De-ionised (DI) water was produced with an 18 MΩcm PURELAB Chorus 1 ELGA system. A DI water droplet ($n_L = 1.33$) with $a = 1.06 \pm 0.04$ mm, $\theta \approx 97°$ and $V_0 \approx 3\,\mu$L

is deposited by hand into the hydrophilic region of the prepared substrate of thickness $d_2 = 1.05 \pm 0.01\,\text{mm}$ with the pattern placed directly beneath ($d_1 = 0\,\text{mm}$). To prevent air currents the droplets were contained within an acrylic box ($W = 722\,\text{mm}$, $H = 510\,\text{mm}$, $D = 473\,\text{mm}$) with an ambient fractional humidity (RH) of $38 \pm 5\%$ and temperature (T) of $22.9 \pm 1.0°\text{C}$. Images are taken simultaneously by a top camera with a $\times 0.3$ rectilinear lens and side camera with a $\times 4$ objective lens to measure the magnification and height respectively. The magnification is extracted as described in section 2.2. By rearranging eq. 2.15 the quadratic can be solved for the two roots and M is converted to a height, h. The appropriate root can be determined by knowing if the image is virtual/real, as the positive root is the larger/smaller value of h,

$$h = \frac{Mnl \pm \sqrt{(Mnl)^2 - a^2(M(2n-1)-1)(M-1)}}{M(2n-1)-1}. \tag{2.18}$$

The height determined from top camera magnification and eq. 2.18 (h_{top}) is plotted against the height measured directly by a side camera (h_{side}) in fig. 2.7. The grey region represents the variation in h_{top} within the uncertainty of the measured base radius. The uncertainty in the base radius comes from the technique which is used to pin the droplets contact line and is therefore not a limit of Pattern Distortion itself. If this pinning technique was improved, the uncertainty in the measurement of height would be set by the measurement of the size of the dots within the resolution limits of the camera. Therefore it is possible to more accurately determine h (or equivalently θ). Regardless, the data agrees well with the black line ($h_{top} = h_{side}$), confirming the Pattern Distortion (PD) technique's ability to capture the shape of the droplet from its magnification.

To further validate the PD technique the same method was applied to a three-droplet line. In fig. 2.8 h_{top} is plotted against h_{side} for the left (L, blue), middle (M, green) and right (R, red) droplets with initial base radii of $a_L = 0.99 \pm 0.03\,\text{mm}$, $a_M = 1.03 \pm 0.04\,\text{mm}$ and $a_R = 0.98 \pm 0.05\,\text{mm}$ respectively, and a centre to centre separation of $s = 4a$. For this multiple droplet system the PD data again agrees closely with the side camera heights for the blue and red series. The slight non-circularity of the middle droplet's contact line results in the topology of the liquid interface diverging from a spherical shape. As a result, the imaged dots become marginally distorted which causes the minor discrepancy seen in the green series and highlights the sensitivity of the method to the shape of the contact line. The extension to non-circular contact lines and non-spherical droplets is discussed in

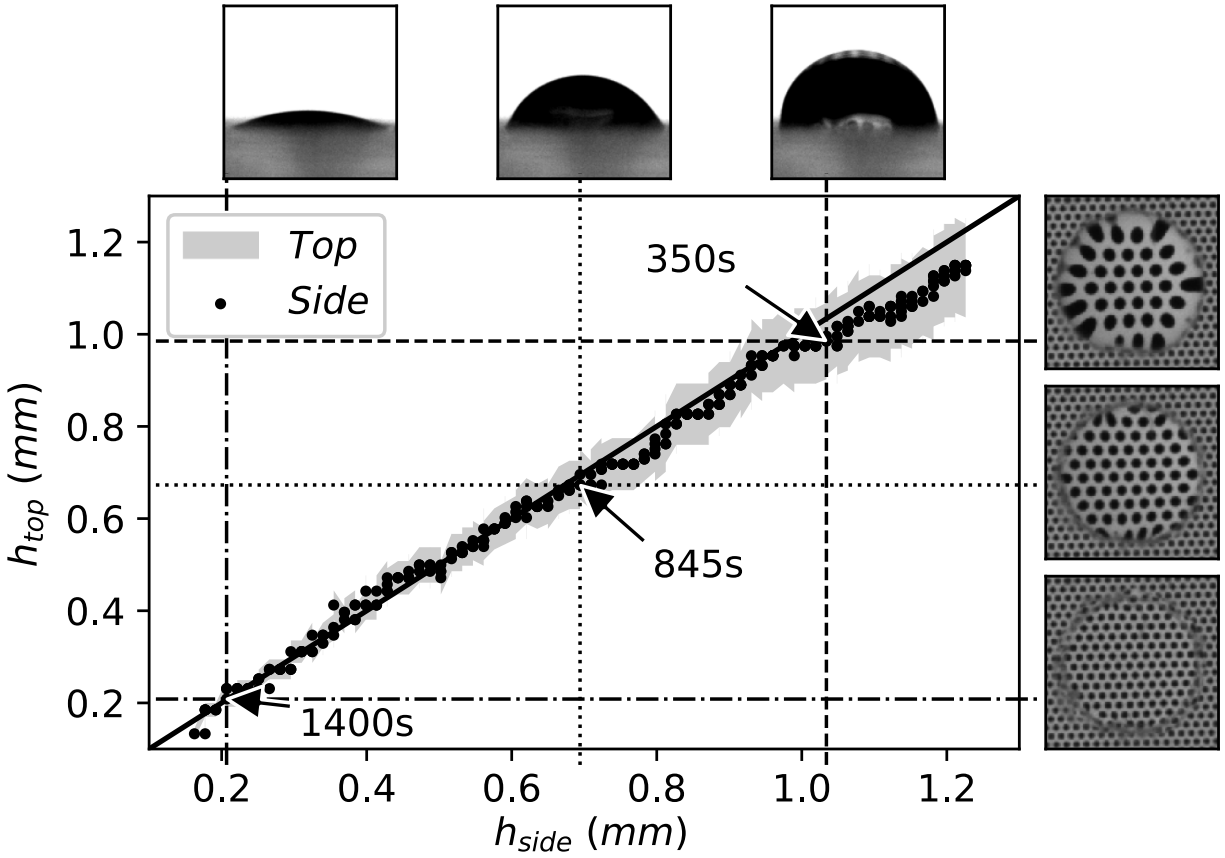

Figure 2.7: Height determined by the top camera (h_{top}) by substitution of M into eq. 2.18 against side camera height (h_{side}) for an isolated droplet. The surrounding insets show three top and side frames during evaporation. The shaded regions are the variation in h_{top} due to the uncertainty in the base radius (a).

section 2.5.4. By plotting the data in this way the difference in evaporation rate cannot be seen however the middle droplet took 11% longer ($\sim 200\,\mathrm{s}$) to evaporate.

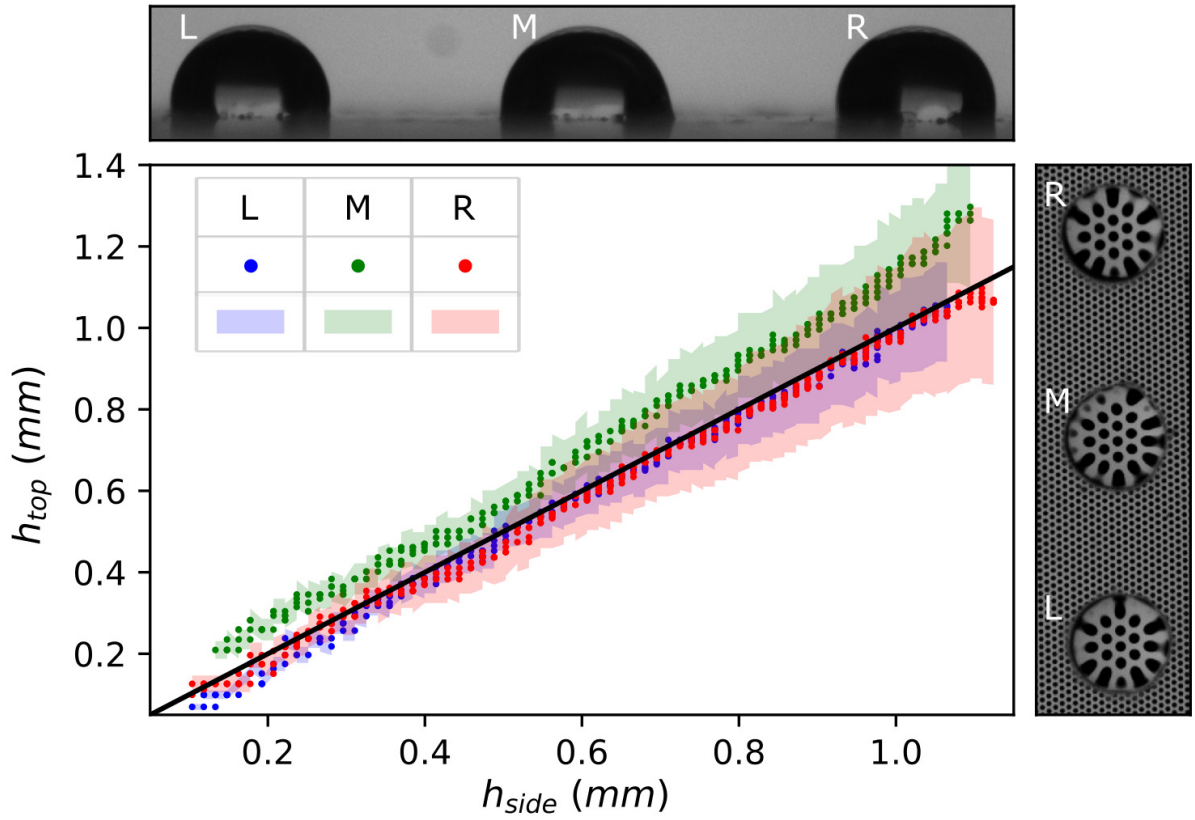

Figure 2.8: Height determined by the top camera (h_{top}) by substitution of M into eq. 2.18 against side camera height (h_{side}) for a three droplet line with the left (L), middle (M) and right (R) coloured blue, green and red respectively. The surrounding insets show the first experimental frames from the top and side cameras. The filled regions are the variation in h_{top} due to the uncertainty in the base radius (a).

The uncertainty due to the paraxial approximation is $< 1\%$ for these experiments. The ratio of the distance of the droplet from the centre of the FOV and the distance of the camera from the substrate was 1/10. This ratio must remain small for the paraxial approximation to be valid.

2.4 Optimisation

To experimentally measure the magnification, an object placed beneath each droplet must be imaged from above using a fixed top-down camera. For repeating patterns the maximum absolute magnification $|M^+|$ should be chosen such that each droplet has at least one

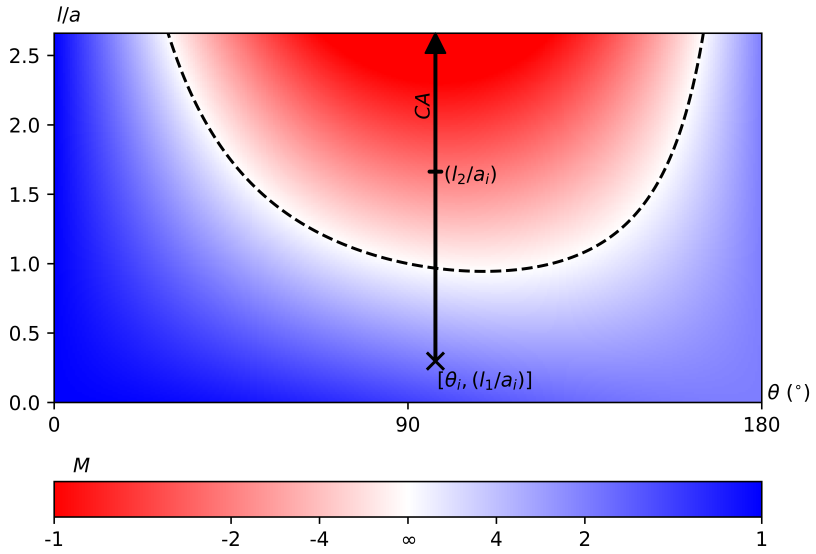

Figure 2.9: Repeating fig. 2.4 highlighting CA evaporation trajectories.

measurable dot initially within the analysed region of interest (ROI). This is because the magnification generally decreases monotonically during evaporation and will ensure one or more dot is always visible. The ROI should be centred on the droplet apex avoiding the distorted features near the contact line. The values d_1 (the gap beneath the substrate) and d_2 (the thickness of the substrate), contained within the parameter l, can be used to manipulate the initial magnification. The sign of M^+ corresponds to whether a real (inverted) or virtual (upright) image is formed and makes it possible to prevent droplets crossing the dashed line in fig. 2.4, when the magnification will become too large to be analysed. The choice of which side of the dashed line an experiment should start is determined by the droplet's mode of evaporation: for a constant contact radius (CR), evaporation trajectories move from right to left on fig. 2.4 from an initial coordinate $[\theta_i, l_1/a_i]$. To avoid crossing into the red region, l can be selected to place the droplet in the blue region (forming a virtual image). It can also be utilised to ensure monotonic variation in magnification. For a constant contact angle (CA), evaporation will result in an upward trajectory and therefore a better choice of l on fig. 2.4 is l_2 commencing in the red region (forming a real image). Fig. 2.4 (repeated in fig. 2.9) allows optimal design of the experimental setup, tailored to specific droplet geometries.

2.4.1 Magnification change due to image plane movement

An important experimental consideration is the movement of the image plane, located at $d_3(t)$, along the optical axis during evaporation. This movement can lead to the image of the dots shifting outside the depth of field (DOF) of the CCD camera. The resulting blur in the image makes identifying the size of each droplet ambiguous and gives rise to an uncertainty in M. To investigate the effect of the dot edge becoming de-focused, the variation in dot diameter ϵ was measured as it was translated a distance δ from the focal plane of the CCD camera. Fig. 2.10 shows δ plotted against $\epsilon/\epsilon_{\delta=0}$. To compare this to how far the image plane moves as the droplet lens changes shape, the maximum displacement of d_3 for a droplet evaporating in CR mode with $a = 1\,\text{mm}$, for initial contact angles $\theta_0 = 90°, 145°$ and $165°$ is also plotted. It can be seen from the position of the blue bars that for higher values of θ_0, it is important to ensure that the dot pattern is perfectly in-focus midway through evaporation, in order to minimise the uncertainty overall. The blue bars are therefore centred on $\delta = 0$ and positioned horizontally at the point of intersection with the de-focusing curve of the lens (black data points). The x-axis intercept indicated by the dotted blue lines therefore represent the uncertainty in M due to the movement of the image plane. For the droplets used in this chapter and thesis, this corresponds to a variation of $\approx 4\%$.

The movement of the image plane formed by the droplets is the object which is imaged by the camera. When an object is moved on the optical axes of a standard lens its magnification changes due to the angular nature of the FOV. Again for large contact angles this may become significant and lead to uncertainty in measuring M and therefore determining the droplet geometry. Telecentric lenses provide the possibility of eliminating the uncertainty due to this effect as they are insensitive to this movement of the image plane. These lenses use carefully placed apertures to capture only rays of light which are parallel to the optical axis. Because of this they do not have an angular field of view and therefore objects moving along the optical axis do not change size [69]. Telecentricity could therefore be utilised to eliminate this. Lenses of this sort also tend to have large usable DOFs addressing the de-focusing discussed in section 2.5.3.

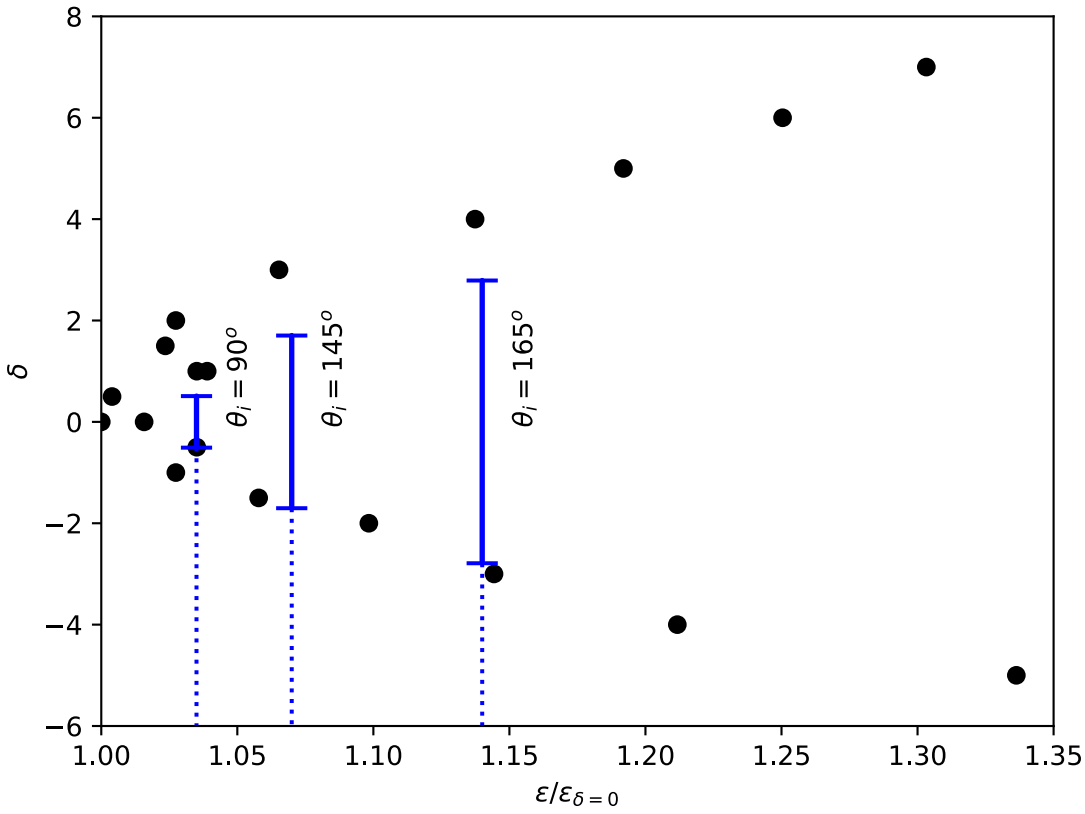

Figure 2.10: Variation in normalised dot diameter ($\epsilon/\epsilon_{\delta=0}$) translated a distance δ from the imaging plane of the CCD camera. The blue bars represent the range of movement in the image plane, for complete evaporation from three initial contact angles (θ_i). The bars are positioned horizontally to encompass the maximum magnification data point within this range when centred vertically at $\delta = 0$. The increase in M due to de-focusing is therefore indicated by the dashed lines.

2.5 Extensions and other applications

This section lists some possible extensions of the technique which have not been the focus of this project but represent future directions to improve it, as well as additional applications which Pattern Distortion could be applied to.

2.5.1 Liquid lenses

In addition to evaporation experiments, fig. 2.11 can assist the design of adaptive liquid lenses. Much of the existing research in this area focuses on methods of controlling the position of liquid interfaces, known as actuation techniques (see Zhu et al. [70] for a review) but not the effect this control has on the optical properties. The theory can predict the range of magnifications which can be achieved by different liquid lens geometries. The curved solid lines plot the magnification by liquid lenses of constant volume (CV) whose shape is controlled by means of actuation techniques (*e.g.* electro-wetting). The curve CV_1 represents the possible values for a droplet with $V = 3.0\,\mu\mathrm{L}$ and $l_1 = 0.32\,\mathrm{mm}$, which are the experimental values of the droplets presented within this chapter. The second curve (CV_2) illustrates the possible magnifications for a smaller lens of $V = 0.1\,\mu\mathrm{L}$, which is capable of forming both real and virtual images.

2.5.2 Bubbles and composite lenses

When dispensing droplets it was noticed that occasionally a bubble can get trapped within the droplet and has an interesting effect on the magnification. This represents a composite lens system with different shaped optical components and refractive indices. Recent work has shown liquid composite lenses can be effective at adaptively forming images [71]. By making a slight modification to the matrices in eq. 2.8 we are able to use the PD technique to determine the size of a bubble trapped at the apex of a droplet. To do this the matrices in eq. 2.8 need to be adapted. The distances in the first and third translation matrices are adjusted by the diameter of the bubble ($2r_B$) and the radius of curvature in the second refraction matrix is now $+r_B$ due to the bubble's concave surface, rather than the convex

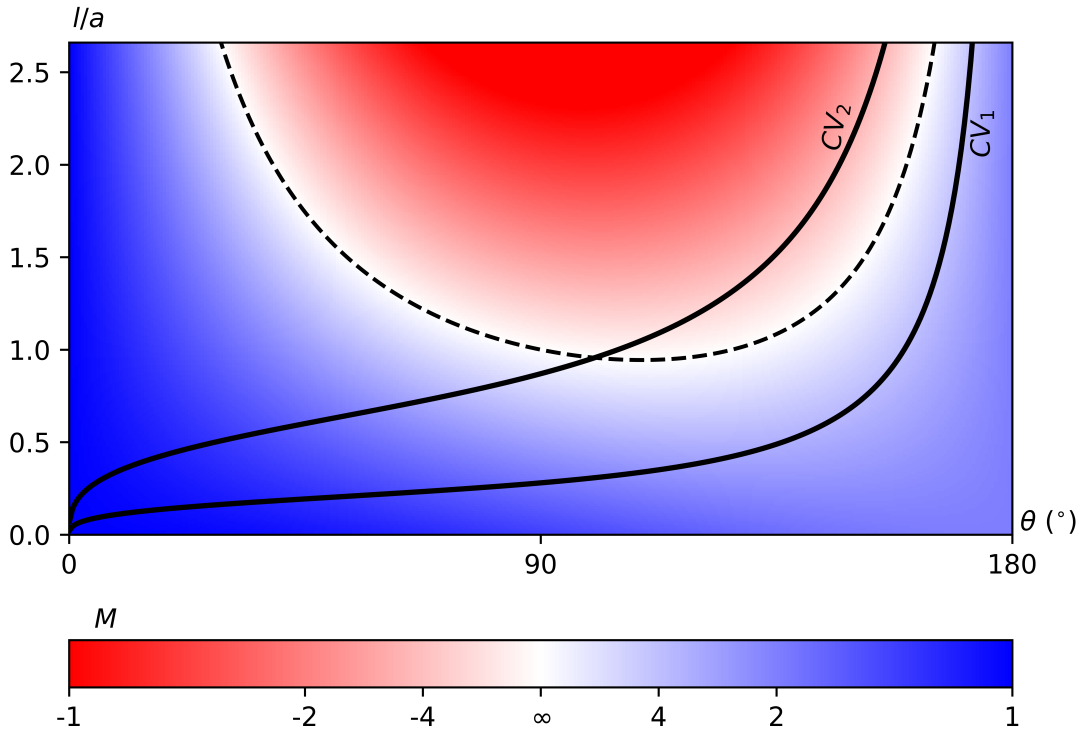

Figure 2.11: The magnification M mapped over θ and l/a. Dashed line indicates $M = \infty$. The curved lines indicate the magnifications which can be traversed by an actuated liquid lens of constant volume $CV_1 = 10\mu L$ and $CV_2 = 0.1\mu L$.

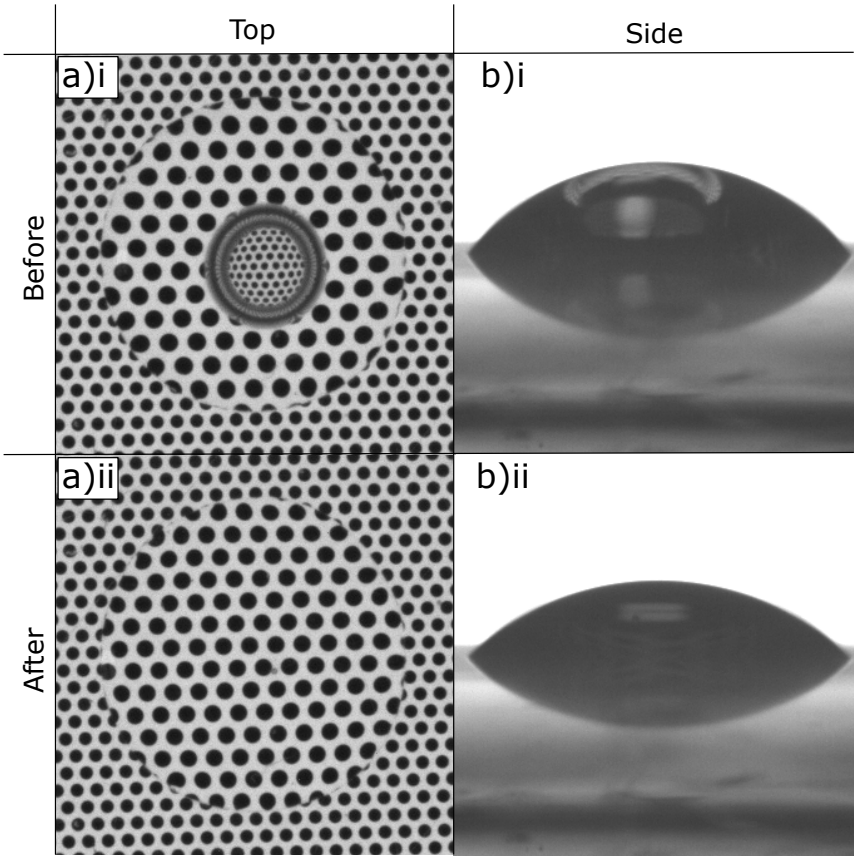

Figure 2.12: a) Top and b) side camera images of a droplet-bubble composite lens i) before and ii) after popping.

surface of the droplet $-r$.

$$\chi = \begin{pmatrix} 1 & d_3 - h + 2r_B \\ 0 & 1 \end{pmatrix} \begin{pmatrix} 1 & 0 \\ \frac{n_L - n_G}{r_B n_G} & \frac{n_L}{n_G} \end{pmatrix} \begin{pmatrix} 1 & h - 2r_B \\ 0 & 1 \end{pmatrix} \begin{pmatrix} 1 & 0 \\ 0 & \frac{n_S}{n_L} \end{pmatrix} \begin{pmatrix} 1 & d_2 \\ 0 & 1 \end{pmatrix} \begin{pmatrix} 1 & 0 \\ 0 & \frac{n_G}{n_S} \end{pmatrix} \begin{pmatrix} 1 & d_1 \\ 0 & 1 \end{pmatrix} = \begin{pmatrix} \chi_{11} & \chi_{12} \\ \chi_{21} & \chi_{22} \end{pmatrix} \tag{2.19}$$

The upper surface of the bubble was omitted as it was assumed to be uniform and thin thus having an insignificant effect on the optics. As a result mathematically the rays refract at the lower interface of the bubble and then translate directly to the image plane. An equation relating M to r_B was then derived as described previously. To create the droplet-bubble composite liquid lens, a droplet of DI water with a volume of $1.3\,\mu$L was deposited onto a clear acrylic substrate of thickness $d_2 = 0.8 \pm 0.01\,$mm and refractive index $n_S = 1.489$. A bubble of air was then injected inside the droplet using a pipette. The droplet-bubble was recorded simultaneously with top (fig. 2.12 a) and side (fig. 2.12 b) cameras until the bubble popped.

To calculate its size the magnification of dots is first measured just outside the bubble ($M = 1.39 \pm 0.01$) to obtain the height of the droplet, $h = 0.76 \pm 0.04$ mm by substituting into eq. 2.18. Then by analysing the reduced magnification ($M = 0.56 \pm 0.08$) (in fig. 2.12 a), caused by the concave lower interface of the bubble we calculate a predicted value for its radius of curvature of $r_B = 0.29 \pm 0.06$ mm, entirely from top camera measurements. If the bubble is assumed spherical this value can be verified by using a side camera to infer r_B. To do this we measure the change in volume of the droplet just before (fig. 2.12 b i) and just after the bubble pops (fig. 2.12 b ii), yielding $r_B = 0.35 \pm 0.12$ mm. Comparing these two values demonstrates the PD technique can successfully be applied to composite lenses as well as to measure and study bubbles. Fig. 2.12 a also shows how the precision in the technique can be significantly enhanced for applications which do not require a large field of view when a higher magnification lens is used.

Because of the measurement of magnification adjacent to the droplet these dots are not at the apex and the associated height is therefore slightly lower than the actual value. This error will become larger, as the bubble size or the droplet's contact angle increases and will eventually become a limitation. Another challenge is the image formed just outside the bubble and dots inside the bubble being formed at different positions. This leads to an uncertainty in determining M.

The theory also assumes that the bubble is located exactly at the apex of the droplet which is not always easy to ensure as can be seen in fig 2.12. This could have been caused by the substrate not being completely flat, or the presence of smaller bubbles preventing free movement to the apex.

Because of these measurement uncertainties further experimental provisions would need to be made to minimise these values and improve the accuracy of the determined r.

2.5.3 Reducing error due to de-focussing

As discussed in section 2.4 the changing geometry of evaporating liquid lenses means that the focal length of the lens is changing. Because of this the image distance (d_3) changes during evaporation and the image is formed in different places. If this movement is significant it can move outside of the lenses DOF and the resulting de-focused image leads to an uncertainty in the measurement of M. This is most apparent with droplets with large θ. The easiest solution to this problem is to ensure that the lens used has a

sufficient DOF to avoid significant de-focusing however this may be costly and difficult for certain droplet geometries. One alternative suggestion for extending the technique to avoid/reduce the uncertainty caused by motion of the image plane is to calibrate the effect of de-focusing on the measurement of magnification for the droplets and lens used experimentally. A technique for resolving the size of image features which are out of focus is described by Sharma et al. [72] which might make it possible to address this issue.

2.5.4 Non-spherical interfaces

Currently the technique has only addressed spherically shaped droplets which is a valid assumption for water droplets with approximately $h < 1.5\,\text{mm}$. Above this the interface becomes distorted by gravity and flattens in the centre. Expressions exist which describe the shape of these gravity flatten droplets [73–75] which could in principle be substituted in to the theory in place of eq. 2.14. The problem is that magnification is not sensitive to the h alone when the interface is flat. One possible solution would be to interpret the image formed at the very edge of the droplet which always remains curved. This would likely require considerations of the distortions which occur this close to the edge of the lens.

Another possible extension would be to surfaces which do not have axial symmetry but do have a dimension in which the curvature is spherically capped. For example a rivulet has an almost infinite r in its direction of flow and magnification in this direction would be minimal however perpendicular to this, the curvature may be a circular cap (again depending on the associated Bo number). The magnification could then be extracted from this perpendicular dimension alone and the height profile in the direction of the flow could be determined. This 1D magnification extraction could also be used to determine multiple radii of curvature of droplets with certain non-circular contact line shapes. For example an ovular contact line would distort the circular dot features into ovals and extraction of the magnification in the major and minor axes separately could be related to the equivalent major and minor axis of the ellipsoidal cap droplet.

Other surfaces which have a complex 2D topology would require a different method to resolve the height variation. One such method which attempts this is Wildeman [76].

2.5.5 Measuring evaporating binary droplet composition

Because the Pattern Distortion technique relies on the optical properties of the lens like the refractive index of the liquid (n_L), M depends on this property as can be seen in eq. 2.13. Because of this the refractive index must be constant and known in order for the geometry to be determined. However if the value of n_L is not known (for example if the droplet has multiple volatile components) then it may be possible to use the technique's sensitivity to n_L in a different way, to measure the variation in concentration during evaporation. To do this the geometry of the lens would need to be established by other means (i.e. side cameras/mass balances). Once this geometry is known eq. 2.13 can be solved for n_L. To test the sensitivity of M to this parameter consider a single binary droplet with known components of unknown concentration with different refractive indices. With a side camera capturing its geometry and a top camera taking Pattern Distortion measurements of the magnification through the droplet. The possible ranges of θ and a can be assumed and magnifications of first (M_1) and second (M_2) components in pure form can be calculated. If the refractive index of for the binary mixture (n_L) lies between n_1 and n_2 [77], the maximum variation is $|\Delta M| = |M_1 - M_2|$. The expected value of n_L for different concentrations can also be predicted theoretically using the mixing rules [78] or determined experimentally [79]. $|\Delta M|$ is plotted for two different binary mixtures of water-ethanol ($M_1 = M_{water}$, $M_2 = M_{ethanol}$) and water-propylene glycol ($M_1 = M_{water}$, $M_2 = M_{PG}$) against θ in fig. 2.13. It can be seen that greater differences in M are observed for the water-PG mixture because of the greater distinction in refractive index. The different series represent different value of l/a. The graph shows that for low contact angles ($\theta < 150°$) ΔM varies monotonically and is enhanced at high θ or by increasing l/a.

The challenge of the method will be measuring the variation in magnification with high enough accuracy as the changes will be very small. In order to achieve this sensitivity, l/a will have to be increased which practically means changing the optical setup distances d_1 and d_2 (again see fig. 2.2). Increasing this parameter can result in the magnification becoming too large for the pattern to be viewed inside the droplet. In this case a smaller pattern would be required which would be difficult to make. Additionally because of the large sensitivity to M required, high magnification lenses will be needed limiting the FOV and number of viewable droplets.

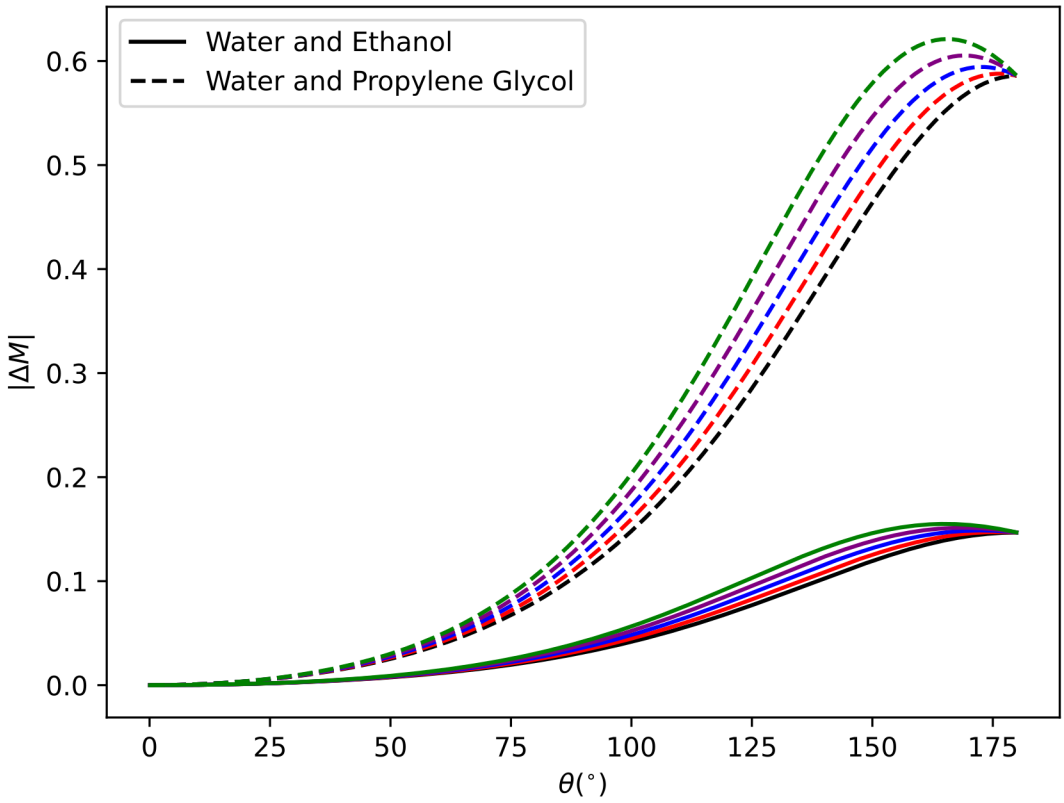

Figure 2.13: Absolute magnification difference ($|\Delta M|$) between pure water ($n_{water} = 1.33$) and two other pure liquids: Ethanol ($n_{ethanol} = 1.36$) and Propylene Glycol ($n_{PG} = 1.44$), solid and dashed lines respectively. Against θ for different l/a values (coloured series).

There are other possible ways to measure n including refractometers [79], interferometers [80] and Optical Coherence Tomography (OCT) [81] which may be better suited to single droplet applications.

2.6 Conclusions

A Pattern Distortion technique was developed to measure the absolute volumes of multiple droplets in arbitrary configurations. Matrix transfer theory was developed to make predictions of the magnification of the liquid lenses. Experiments were then conducted alongside a traditional side camera technique to validate its predictions. The matrix transfer theory also allowed for the optimisation of the technique to enhance its sensitivity to different droplet sizes. The technique was also shown to be informative to the design of liquid lenses, as it connects the droplet's shape to the resulting image. The uncertainty

in the technique was also quantified and considerations of how to minimise these were described. Finally, extensions of the technique were discussed including: measuring refractive index of binary liquids, studying bubbles, designing composite lenses and imaging with nonspherical interfaces.

Chapter 3

Diffusive Evaporation

In this chapter the experimental comparisons of multiple droplet arrays to the analytical diffusive theories are made for the first time. Firstly instantaneous flux values for multiple droplet arrays are measured using interferometry and compared to the Wray et al. model (described in section 1.8.4) in section 3.1. The agreement is shown to be very good.

Because of the successful initial comparisons further experiments were conducted capturing the experimental transient volume dynamics using the Pattern Distortion technique presented in section 3.2. One of the assumptions made by the theory is that the vapour transitions quasi-steadily (and the Laplace equation can be used as described in section 1.8.4). This assumption is valid when the vapour field around the droplets develops to a steady state very quickly (in comparison to the overall evaporation) and this is important to validate for multiple droplets. It has been shown that this assumption is acceptable for isolated droplets however for multiple droplets the transient dynamics are likely to take longer initially due to the increased number of droplets having a larger vapour cloud and cases where droplets disappear. In the theory, the interactions of a droplet with its neighbours will disappear sharply when it has completely evaporated, consistent with its vapour cloud turning off like a light bulb. Experimentally there will always be residual vapour and the transition will be smoother. Whether these sharp transitions are important as they accumulate in multiple droplet arrays, needs to be tested. These measurements test the theory's ability to model the dynamic evaporation process including when droplets completely evaporate and the array transitions to a new geometry. Good agreement is found suggesting that the quasi-steady assumption remains valid for the range of arrays tested.

Section 3.2 also gives the first side-by-side comparisons of the Wray et al. and Masoud et al theories, again showing the agreement to be very good within the experimental uncertainties. This agreement for transient arrays is important, as it demonstrates the models can be used to make accurate predictions for the complete evaporation of an array in addition to instantaneous evaporation rates.

The results are also fitted to the Carrier et al. model to demonstrate what is meant by the radius of the so called 'superdroplet'. The comparisons focus on small droplet arrays of $N \leq 21$, initially for monodisperse droplets and finally for a polydisperse array (section 3.3).

3.1 Evaporative flux

I was provided with the experimental data in this section, measured using a Mach-Zehnder interferometer and captured by Dr. Andrew Edwards. The contribution of this thesis consists of the analysis of the recorded images and comparison with theoretical predictions.

To compare the evaporation of multiple droplets to the existing diffusive theory a Mach-Zehnder interferometer was used to capture the change in each droplet height ($\frac{dh}{dt}$), evaporating in CR mode. As droplets evaporate the interference fringes at the apex of the droplet oscillate as the optical path length of the sample arm reduces. The period (Δt) of these oscillations correspond to successive reductions of $\Delta h = \lambda/(n-1) = 1.905\,\mu$m in the path length. By extracting the time between peaks and/or troughs or computing a time windowed FFT, $\Delta h/\Delta t \approx \frac{dh}{dt}$ can be extracted. In order to do this the signal was obtained from the images, by selecting a region over the central fringe at the apex of each droplet. The average intensity in this region was calculated for each droplet in every frame and plotted against time. The MATLAB function `findpeaks` is used to determine corresponding times of the peaks and troughs. The mean time between peaks and troughs was calculated. The signal was analysed between 50 s and 250 s after initial deposition, which allows the interferometer time to stabilise. This 200 s window represents a maximum 13% of the total evaporation time.

The volume (V) of a spherical cap is related to its height, h by eq. 1.11. Differentiating with respect to time gives how the droplet evaporation rate is related to the change in droplet height

$$\frac{dV}{dt} = \frac{\pi}{2}(a^2 + h^2)\frac{dh}{dt}. \tag{3.1}$$

Noting that the surface area of a spherical cap is $S = \pi(a^2 + h^2)$, the change in droplet height can be related to the droplet's interface averaged evaporative flux, J ($\mathrm{m\,s^{-1}}$)

$$J = \left(\frac{dV}{dt}\right)/S = \frac{1}{2}\frac{dh}{dt}. \tag{3.2}$$

Typically evaporation is reported as a volumetric of mass loss however this it difficult to determine from our measurements as interferometers measure changes in height and not absolute heights. To make comparisons to Wray et al, eq. 1.24 must be rewritten in terms of J. The total evaporation rate can be obtained by integrating the flux over the surface of the droplet

$$\left(\frac{dV}{dt}\right) = \int_S j ds = J\pi a^2. \tag{3.3}$$

By substitution of eq. 3.3 into 1.24 and simplifying, remembering that the Wray et al theory is for flat droplets with surface area πa^2, one obtains

$$J_k = J_{0\mathrm{k}} - \frac{2}{\pi}\sum_{\substack{\mathrm{n}=1 \\ \mathrm{n}\neq\mathrm{k}}}^{N}\left(\frac{a_\mathrm{n}^2}{a_\mathrm{k}^2}\right) J_\mathrm{n} \arcsin\left(\frac{a_\mathrm{k}}{s_\mathrm{kn}}\right). \tag{3.4}$$

If the droplet array is monodisperse (ie. $a_\mathrm{k} = a_\mathrm{n} = a$) then this can be further simplified to

$$J_\mathrm{k} = J_{0\mathrm{k}} - \frac{2}{\pi}\sum_{\substack{\mathrm{n}=1 \\ \mathrm{n}\neq\mathrm{k}}}^{N} J_\mathrm{n} \arcsin\left(\frac{a_\mathrm{k}}{s_\mathrm{kn}}\right). \tag{3.5}$$

By experimentally measuring $\frac{dh}{dt}$ with the Mach-Zehnder interferometer, half of this value is J (eq. 3.2), which can be directly compared to calculated theoretical values for the array, by writing in matrix form and inverting the $N \times N$ interaction matrix.

All comparisons assume isothermal evaporation in a constant ambient humidity. Consequently, single values of $D(T)$ and $c_\infty(T)$ are calculated according to eq. 1.4 and 1.15 respectively, where T and ϕ are measured at the beginning of each experiment. These assumptions are valid as the experimental data is analysed over 200 seconds which is much shorter than the timescale for significant changes in the environmental conditions.

For simplicity, we average our interferometric measurements of flux obtained with the peak to peak ($\bar{J}_\mathrm{p}$), trough to trough $\bar{J}_\mathrm{t}$ and FFT (J_FFT) methods, using $J_\mathrm{exp} = \left(\bar{J}_\mathrm{p} + \bar{J}_\mathrm{t} + J_\mathrm{FFT}\right)/3$. This measured flux is then used to colour the left half of each droplet in fig. 3.1. The right half is coloured by the corresponding Wray et al prediction (J_th).

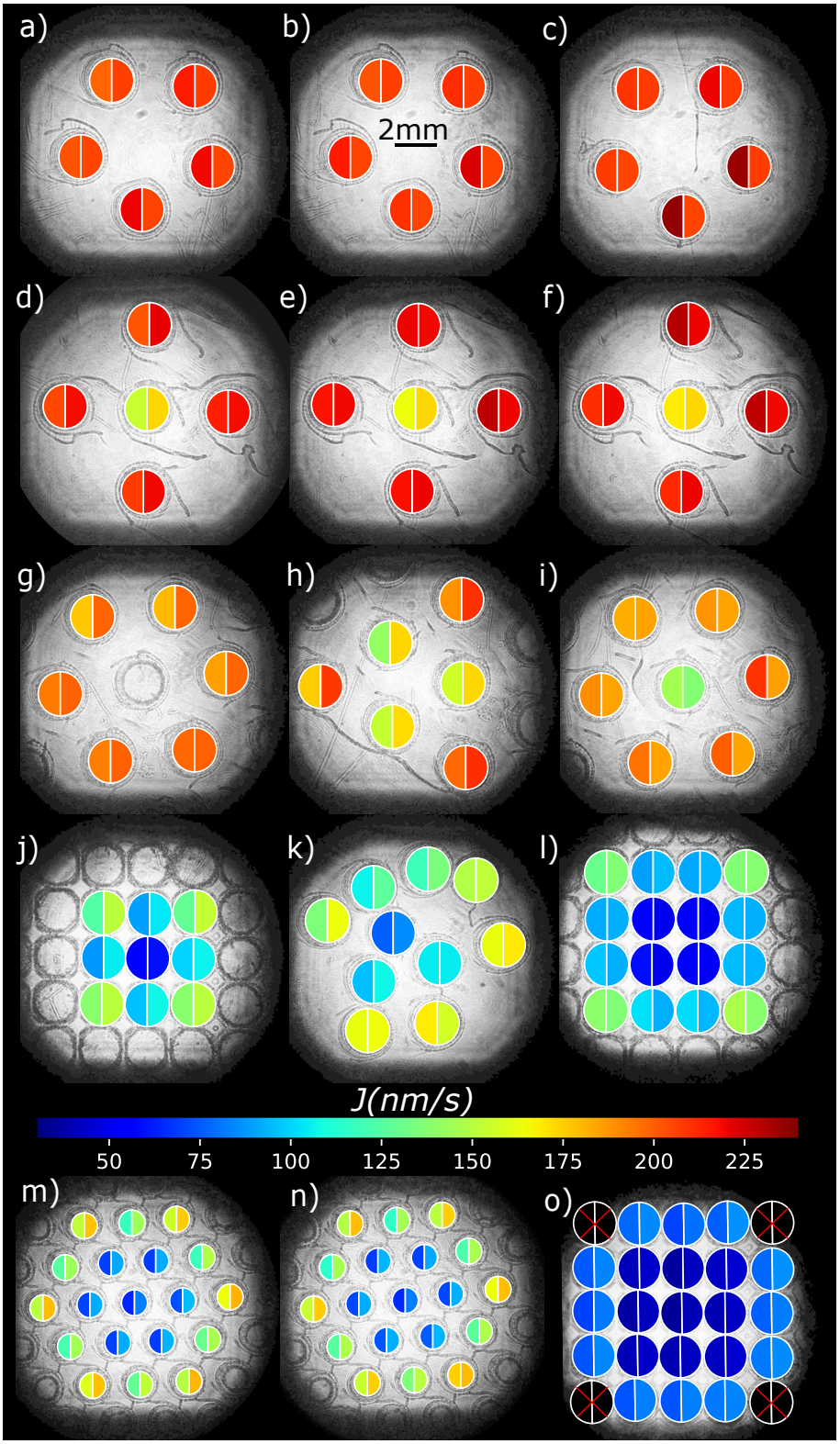

Figure 3.1: Experimental images of evaporating 2-D droplet arrays. Coloured overlays show; measured average evaporation flux (J_{exp}) and Wray et al's theoretically predicted evaporation flux (J_{th}), on the left and right hand semi-circle over each droplet respectively, for between $50\,s$ to $250\,s$ after final droplet deposition. a-c) Pentagon. d-f) Cross. g) Hexagon ring. h) Triangle. i) 7 Hexagon. j) 3×3 Square. k) Random. l) 4×4 Square. m-n) 19 Hexagon. o) 5×5 Square. Images have been histogram equalised. Figure from Edwards et al. [4].

As expected, the effect of shielding on a droplet, and therefore its evaporation flux, is determined by its position within the array, number of neighbouring droplets and their proximity (which we term the droplet's 'confinement'). Droplets in equivalent/symmetric positions have the same confinement and so experience identical shielding effects from neighbouring droplets. Because of this they evaporate at the same rate. Droplets at the corners are the least confined, so evaporate faster than those at the edges, with droplets in the centre evaporating the slowest. Overall the colours of the semi-circles on each droplet are quite similar, indicating good agreement between the Wray et al. theory and the experimental measurements.

Fig. 3.1 a shows the measured evaporation flux for droplets arranged in a pentagon where the average evaporation flux varies by no more than 7% between droplets. This follows from the symmetry of the pentagon providing identical confinement conditions for each droplet. In comparison to an isolated droplet, co-operative shielding reduces the flux of each droplet by approximately 62%. Rearranging the five droplets into a cross formation (fig. 3.1 d-f) creates two confinement conditions: the points and the centre. The points of the cross being the least confined have the highest evaporation flux (a reduction of only $33 \pm 5\%$ compared to an isolated droplet) while the evaporation flux of the centre droplet has reduced by 50%. The triangle formation in fig. 3.1 h illustrates that droplets at the corners of the triangle (two nearest neighbours) are less confined than those on the edges (four nearest neighbours), with the former evaporating approximately 20% faster than the latter.

The dense droplet array configurations in fig. 3.1 l, m and n again show that the evaporation flux is highest from the least confined droplets at the corners and decreases with increasing confinement. Interestingly, within the filled hexagon (fig. 3.1 m and n) we find that the six inner ring droplets evaporate around 50% slower than the outer droplets; however, the centre droplet evaporates only 8% slower than the inner ring. This suggests that the influence of the edge of the pattern only extends a certain distance into the array; further inwards the evaporation rate is almost constant. This is because as the distance to the edge of the array increases the surrounding gas is more and more saturated and diffusion of the vapour around these droplets is predominantly in the vertical direction. Fig. 3.1 k shows a random arrangement of evaporating droplets where each droplet has a unique confinement, similar to a spray pattern.

3.2 Transient dynamics

Furthermore detailed comparisons of the Wray et al. theory can also be conducted by use of the Pattern Distortion technique as well as to the Masoud et al model. The development of this method makes it possible to extract absolute volumes, rather than just flux. In addition, it is easier to make comparisons over a longer period of the array's evaporation time including the situation when droplets begin to disappear and the interaction matrix must be updated. A transient implementation of this theory is written in Python and described in Appendix B.

To determine each droplet's absolute volume we employ the Pattern Distortion technique (described in chapter 2). In the experiments, $2.00 \pm 0.25\,\mu$L droplets of de-ionised water (PURELAB Chorus 1 – ELGA) with surface tension $\gamma = 72.75\,$mN/m were placed into an acrylic box ($W = 722\,$mm, $H = 510\,$mm, $D = 473\,$mm) to prevent air currents influencing the evaporation. Each droplet will evaporate saturating $1.09 \times 10^{-4}\,$m^3 of air, for 9 droplets (the maximum dispensed in this section) this represents an increase in relative humidity of 0.56% for a perfectly sealed enclosure. For an isolated droplet this corresponds to a maximum variation in evaporation of 10%. But, given the enclosure will not be perfectly sealed and the humidity will not increase this much. Selectively hydrophobised soda-lime glass substrates with a thickness of 0.982 mm were prepared for each pattern to pin the contact line of each droplet with a base radius of $a = 0.97 \pm 0.07\,$mm for approximately 80% of the drying time. The initial contact angle of the droplets was $\theta_0 \approx \pi/2$ radians, with $Bo \approx 0.13$. The relative humidity and temperature were recorded with two DHT22 sensors with temperature varying $< 1\%$ and humidity by $< 5\%$ in all cases. The maximum uncertainty in the measurements of temperature and humidity being $\pm 0.5°$C and $\pm 5\%$ respectively. In this section a lot of the experimental data and theoretical results are normalised to make comparisons. The reason the data was not left in standard units is that droplets are very sensitive to their environmental conditions (substrate temperature, ambient humidity and temperature). Therefore unless these quantities are carefully controlled and measured, small variations lead to expected differences in droplet evaporation. Many single droplet studies have been conducted demonstrating that if the ambient environment and substrate temperature are controlled then the theory works very well to capture the evaporation [27]. Therefore to simplify the experiments and to eliminate the variation of these quantities between experiments, normalisation is used.

Fig. 3.2 depicts a time series of experimental images (columns) for four separate droplet configurations (rows). It can be seen that the magnification of the dots monotonically decreases indicating a monotonic decrease in h. By analysing as described in section 2.2 and substitution of $M(t)$ into eq. 2.18, $h_{\mathrm{k}}(t)$ can be obtained and the spherical cap volume is calculated with eq. 1.11. Fig. 3.3 plots the theoretical (lines) predictions for the Wray et al (solid) and Masoud et al (dashed) models for the 'Square' arrangement depicted in the top row of fig. 3.2 and evaporation is assumed isothermal and in a constant humidity environment. In each case the three lines represent the three distinct confinement conditions at the corner, edge and centre. The sharp corners on the theoretical curves are instantaneous changes in evaporation rate when other droplets in the array disappear. Physically these corners are likely to be smoother, their sharpness in the theory is inherent in the assumption of quasi-steady vapour. The experimental data are also plotted (black markers) and represent V averaged across symmetrical confinement for three repeat experiments: corners (twelve droplets), edges (twelve droplets) and centres (three droplets). In both cases V is normalised by its initial value (V_0) and t normalised by the the time (t^*) for the fastest evaporating droplet to reach $V_0/2$. This normalisation ensures that the fastest evaporating droplets in both the predictions and data pass through the point $y = 0.5$ and $x = 1$. Good agreement is obtained with the data falling between the two theoretical models. The data points visually appear to be in closer agreement with the Wray et al model however this will vary with different choices of normalisation. The best way to interpret the graph is to compare the spacing between the lines which capture the position dependant evaporation rates of each of the droplets. In order to accurately compare the two theories comparisons would need to be made without normalisation (absolute values). To achieve this, experiments would need to be conducted in a temperature and humidity controlled environment, due to the sensitivity of their evaporation. Additionally since the difference between the theories is in accounting for the contact angle this could be maximised by improving the pinning technique to allow droplets to have higher initial θ. Alternatively a superhydrophobic substrate could be used such that droplets evaporate in a CA mode. The large value of θ would enhance the difference between the theoretical predictions and comparisons would reveal the extent of the improvement made by inclusion of the interactions dependence on θ. Alternatively experiments could be conducted on droplets with low contact angles which would determine which analytical form performs the best.

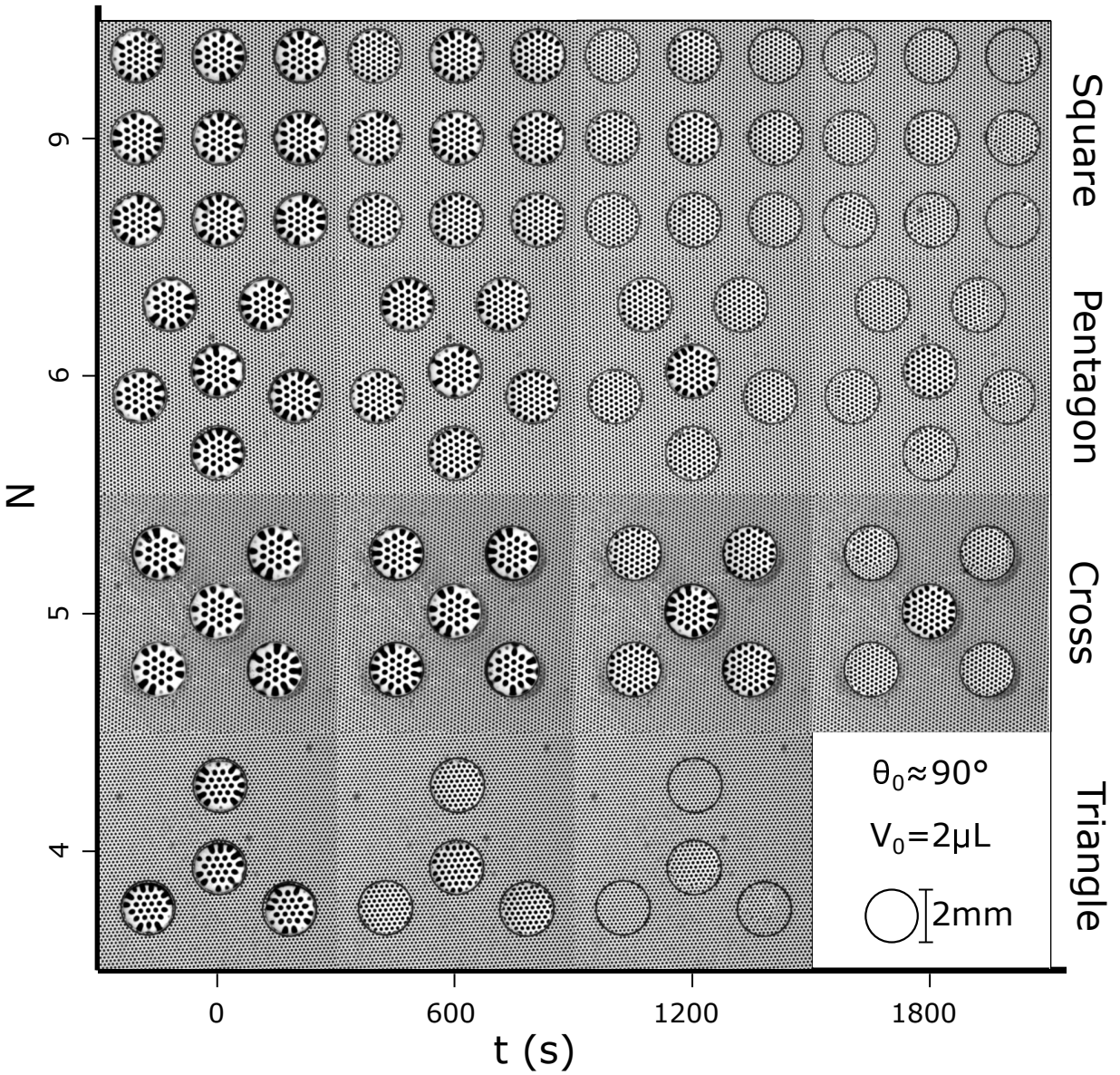

Figure 3.2: Experimental images of droplet arrays magnifying a pattern of dots (ordered vertically by the number of droplets N) as a function of time for the triangle, cross, pentagon and square configurations. The legend indicates the droplet's scale, initial ($t = 0$) contact angle (θ_0), and volume (V_0). The nearest droplets in each arrangement have $s = 3a$. Figure adapted from Iqtidar et al. [6].

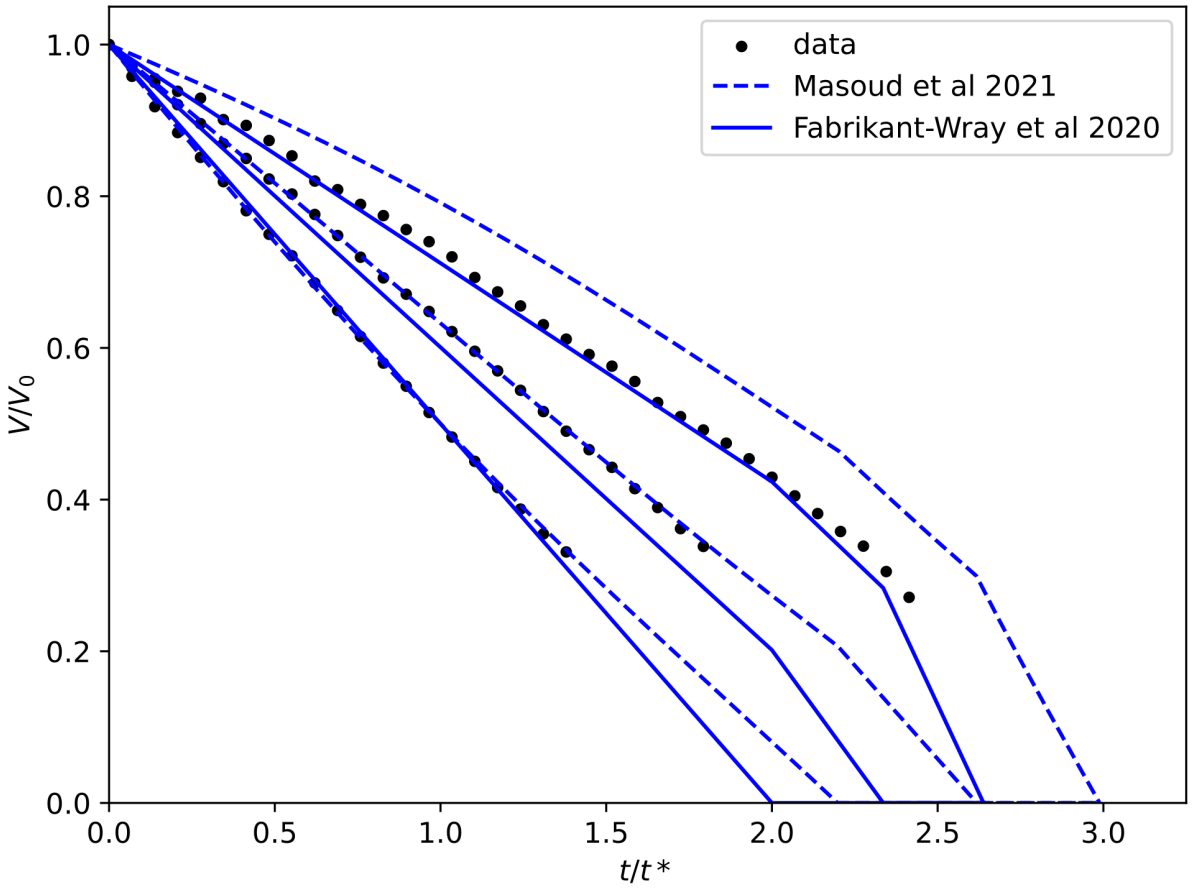

Figure 3.3: Experimental data of a 3×3 square array compared to the predictions of Wray et al. [1] (solid) and Masoud et al. [55] (dashed) of the normalised volume (V/V_0) against normalised time (t/t^*). From Kilbride et al. [5].

The full temporal volume dynamics for the experiments in fig. 3.2 compared to Masoud et al. are plotted in fig. 3.4. In each case the agreement is very good. It can be observed that in general the model predicts that the evaporation rates of droplets in different confinements, are more spread out than measured experimentally. One possible explanation for this is that after the data is truncated because the droplets have de-pinned, a has reduced. This would result in these evaporating slower than assumed by the theory due to the linear dependence of $\left(\frac{dV}{dt}\right)^*$ on a (see eq. 1.18). This de-pinning will also increase the distance between the droplets which will also enhance the evaporation rates. This effect is mostly visible in panels b) and d) as the evaporation rate of the central droplet increases as the surrounding droplets are truncated. Theoretically it is also assumed that the atmosphere is quiescent and that no forced convection occurs. This is difficult to ensure and quantify experimentally as it would require imaging of the airflow around the droplets. Small air flows could exist due to drafts in the surrounding enclosure. Air flows are also generated at the beginning of the experiment by the motion of dispensing and sealing the enclosure which may take time to arrest. Another assumption made by the theory is that the transients times for the vapour field to develop is small in comparison to the total evaporation time. For multiple droplets this assumption may start to break down as the time required to develop the quasi-steady vapour field composed of each of the droplet's individual contributions will be greater. It is also true that the total evaporation time for these multiple droplets is greater, but how the initial transient time and the array's lifetime scale are unknown. Xu et al. [82] detailed how the ratio of the transient time to lifetime (τ_T) scale for isolated droplets in different situations giving the following expression

$$\tau_T = 687.4\frac{(1-\phi)c_{sat}}{\theta\rho_l}, \tag{3.6}$$

which must be $\ll 1$ for the approximation to hold. Calculating the value for a characteristic droplet in this section gives $\tau_T = 0.0033$, which would imply the approximation is reasonable if these droplets were isolated, however eq. 3.6 does not account for more than one droplet and it is not clear how to extend this to their combined vapour field. The level of agreement in fig. 3.3 demonstrates that this approximation is still valid but might explain small discrepancies, indicating this assumption may not hold for larger arrays with more droplets. In addition to the initial transients the theory also assumes the time taken for the vapour to transition to an updated steady state when droplets disappear

is instant. For droplets evaporating in CR mode this transition could take a significant amount of time, increasing and accumulating with the number of droplets which evaporate within the array's lifetime. It is difficult to establish the extent of this effect from the data as the droplets de-pin and are truncated, masking the point they disappear. This de-pinning will also make the transient periods less significant as the evaporation rate of the droplets monotonically decreases to zero and the vapour field naturally transitions to the steady state, when the droplet disappears, as it shrinks. If the droplets remained perfectly pinned the evaporation rate would drop to zero very rapidly and the vapour replenishing the steady-state would too. In this case there would be much more residual vapour at the point of complete evaporation and the time for it to be diffused away as it moves to its new state would be longer. In the theory this residual vapour would vanish instantly.

The diffusive timescale can also be examined to quantify how quickly the vapour can be transported by calculating a characteristic diffusion coefficient for the experiments. From eq. 1.4 for $T = 21°\mathrm{C}$, $D = 2.43 \times 10^{-5}\,\mathrm{m^2 s^{-1}}$ for water vapour in air. The timescale is therefore $\tau_D = L_D^2/D$ where L_D is a diffusive length scale. Over the distance between droplets of $L_D = 0.001\,\mathrm{m}$, it takes $\tau_D = 0.04\,\mathrm{s}$ before the droplets start interacting.

This is the most convincing explanation for the divergences between the theory and data in addition to the measurement uncertainties of the technique. Another possible explanation might be that the experiments are starting to realise non-diffusive effects which are amplified by the presence of multiple droplets. These include thermal interactions through the substrate in which the evaporative cooling of the droplets becomes significant enough that the process cannot be considered isothermal.

The data was also compared to the 'superdroplet' model proposed by Carrier et al. For non-circular arrays it is not clear which radius to use to predict its global evaporation rate, therefore an experimental ($\frac{dV_T}{dt}$) was fit to the data to obtain a predicted R_c in eq. 1.23. Fig. 3.5 shows the linear fit to V_T over t. Eq. 1.23 can be rearranged to

$$R_c = \left(\frac{dV_T}{dt}\right) \frac{\rho_l \pi N R}{4D\pi N R c_s - \frac{dV_T}{dt}\rho_l}. \tag{3.7}$$

The gradient of the fit is then substituted into 3.7. The corresponding 'superdroplet' radius is plotted on top of the array in the inset of fig. 3.5. The contact line aligning well with the outer extent of the array. The same comparisons can be applied to the three other experimental configurations and the resulting R_c values are plotted in fig. 3.6. The two

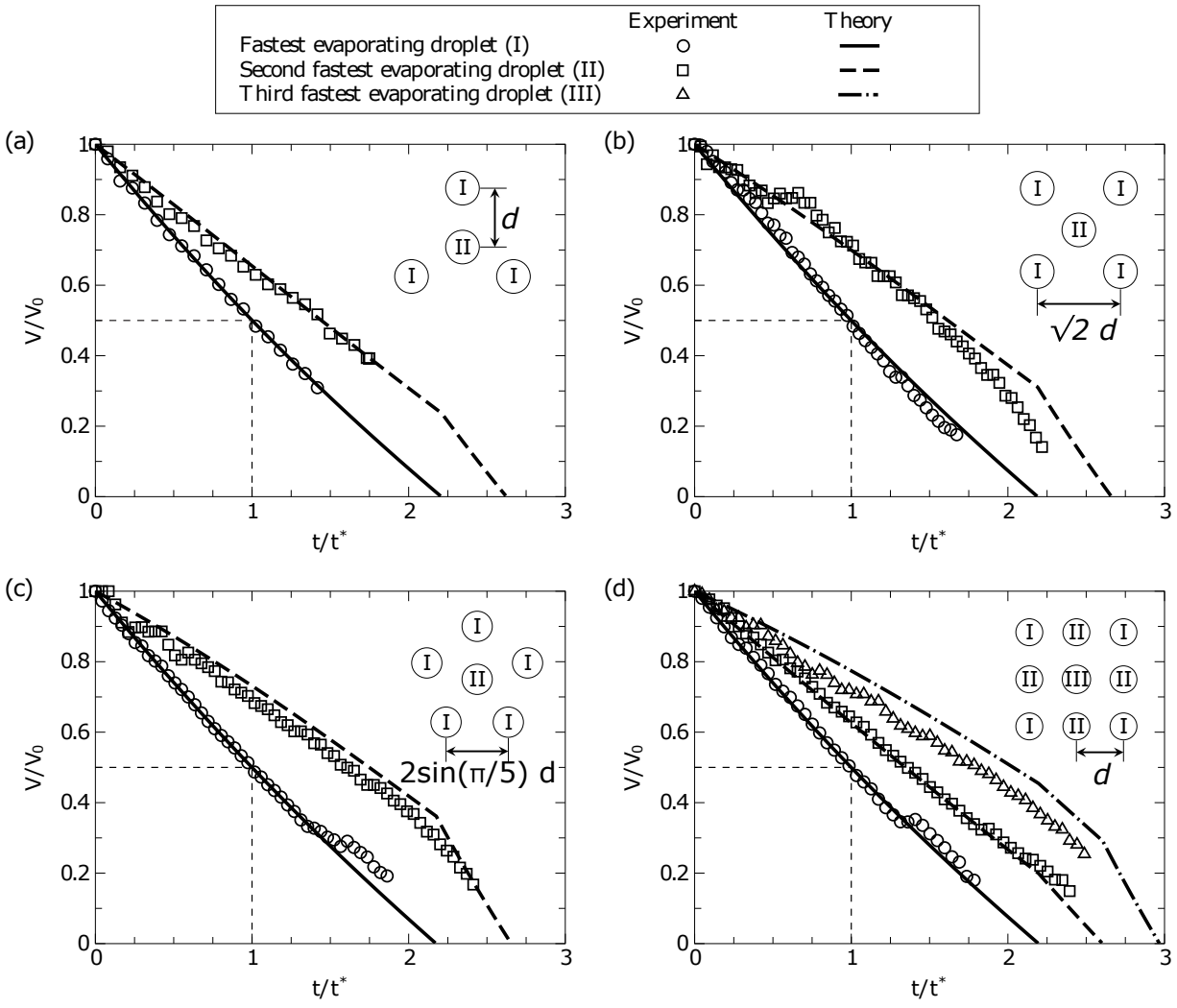

Figure 3.4: Experimental volumes (V/V_0) of the (a) triangle, (b) cross, (c) pentagon and (d) square in fig. 3.2 compared to the predictions of Masoud et al. [55] (dashed lines) against normalised time (t/t^*). Taken from Iqtidar et al. [6].

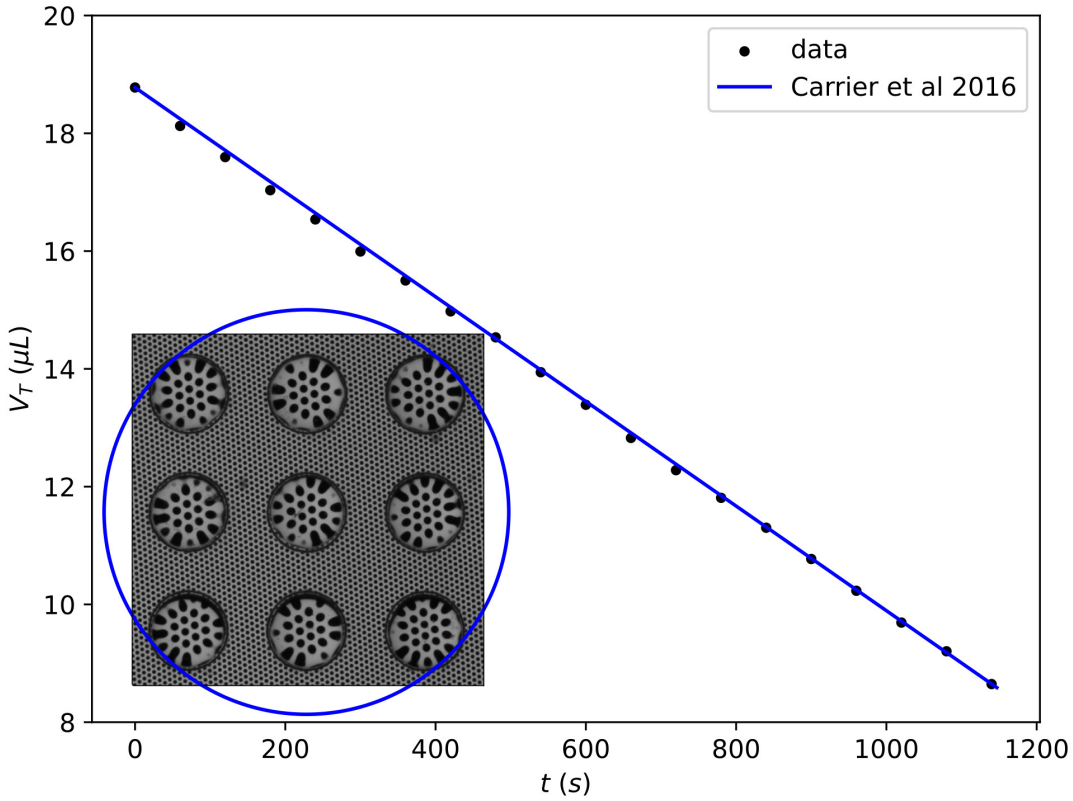

Figure 3.5: Experimental data of a 3×3 square compared to the radius ($R_c = 5.13\,\text{mm}$) of a 'superdroplet' (blue circle) obtained by fitting the total nine droplet volume (V_T) to the theory of Carrier et al. [45].

blue lines in each panel indicate uncertainty from repeated experimental measurements. It can be seen that R_c aligns with the outer extent of the array for each arrangement. In all three cases the minimum radius which encloses all of the droplets is $R = 4\,\text{mm}$ and the radius which passes through the centre of the outer droplets is $R_c = 3\,\text{mm}$. These comparisons argue for selection of R_c somewhere between these two points. The consistency of this across the different arrangements demonstrates that the choice of R_c for making theoretical predictions is not sensitive to the specific positioning of each droplet nor the number of droplets contained within the radius. Therefore 'superdroplet' theory can be used to make predictions for the small arrays in fig. 3.6, however as the arrays become bigger it would be expected that it would only be suited to arrays which have a circular shape.

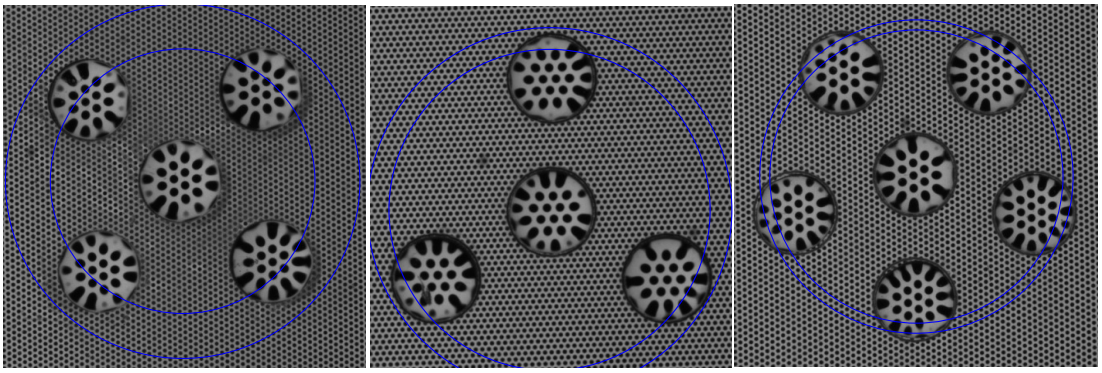

Figure 3.6: The 'superdroplet' radius (R_c) blue circles for the cross ($R_c = 3.89 \pm 0.56\,\text{mm}$), pentagon ($R_c = 3.71 \pm 0.12\,\text{mm}$) and triangle ($R_c = 3.92 \pm 0.25\,\text{mm}$) arrangements. The two lines indicate the maximum and minimum R_c due to the standard error over repeat experiments or uncertainty in experimental measurements.

3.3 Polydisperse Arrays

In addition to testing the theories for the monodisperse case predictions can also be made for polydisperse droplet arrays. In order to generate on demand arrays of different sizes with accuracy, a Liquidyn P-Jet CT jetting dispenser was mounted onto a CNC step motorised translation stage (Zero 4). Dispensing and movement were programmed with Gcode generated by an in-house Python script. A droplet of desired volume could then be dispensed at a desired location approximately every 0.9 seconds. A tempered glass screen protector (4youquality) was used as the substrate, first cleaned with ethanol and dried with an air gun. The substrate has an equilibrium contact angle of $\theta = \pi/2$ and droplets were found to evaporate in a CA mode. The nozzle of the dispenser was positioned approximately 10 mm above the substrate reducing the production of satellite droplets.

A 4×4 square arrangement of droplets with alternating volumes of $1.36 \pm 0.01\,\mu\text{L}$ then $5.40 \pm 0.04\,\mu\text{L}$ with a separation of $s = 5\,\text{mm}$ was printed and left to evaporate. The lifetime of each droplet (τ) was extracted and compared to the predictions of Masoud et al. Fig. 3.7 plots the experimental (τ_{exp}) and theoretical (τ_{th}) lifetimes normalised by the time for the last droplet to evaporate ($\hat{\tau} = \tau/\tau_{max}$). The data falls on the $\tau_{th} = \tau_{exp}$ line (blue) indicating good agreement with the model with only a small amount of scatter. To understand the origin of the scatter the data can be replotted in fig. 3.8 showing the positions of the droplets coloured by normalised lifetime for experiment (left) and theory (middle). Note that grey indicates the droplets with the longest lifetime. The rightmost panel plots the array with the colour indicating the difference between the experiment and theory. The difference demonstrates that one side of the array evaporates 10% faster

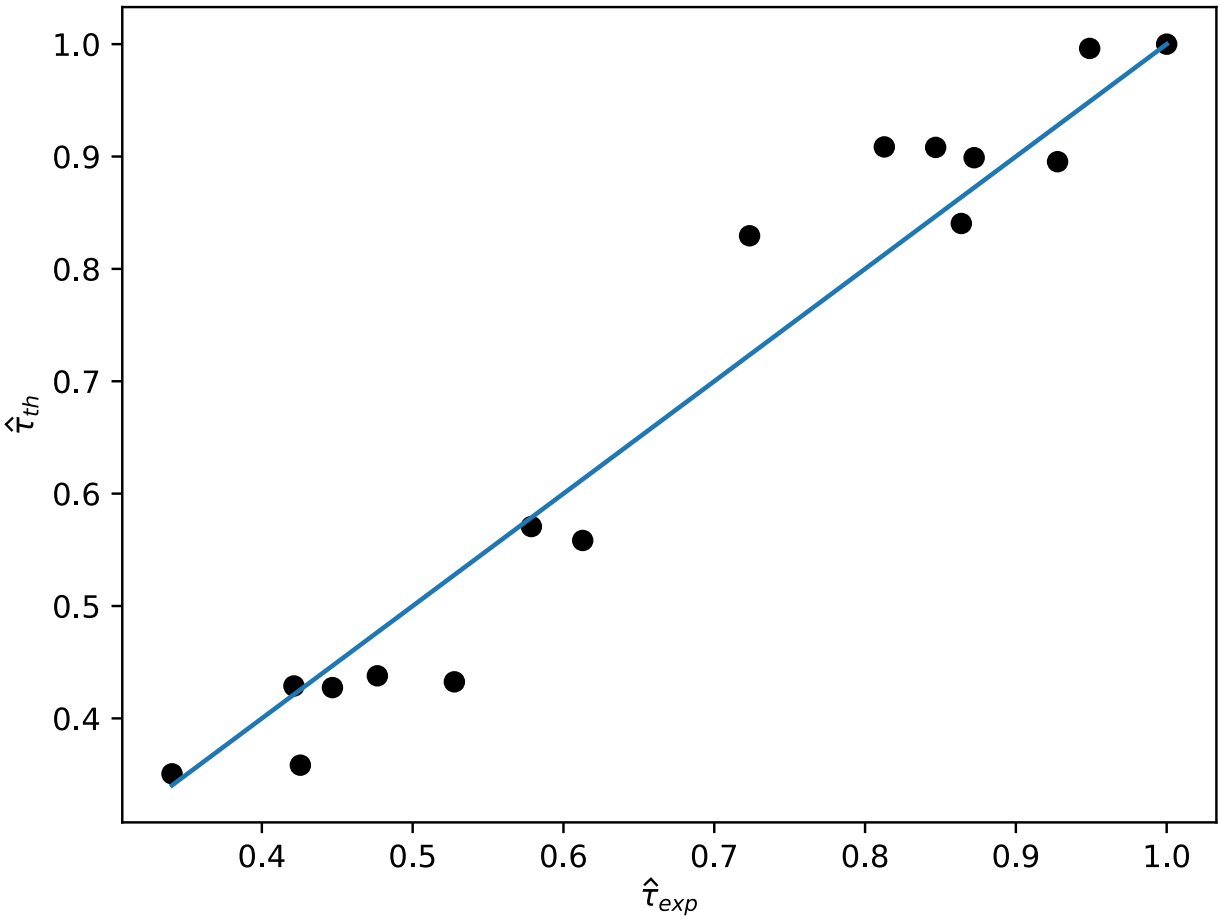

Figure 3.7: Maximum normalised theoretical ($\hat{\tau}_{th}$) and experimental ($\hat{\tau}_{exp}$) lifetimes each droplet in a 4×4 square polydisperse array.

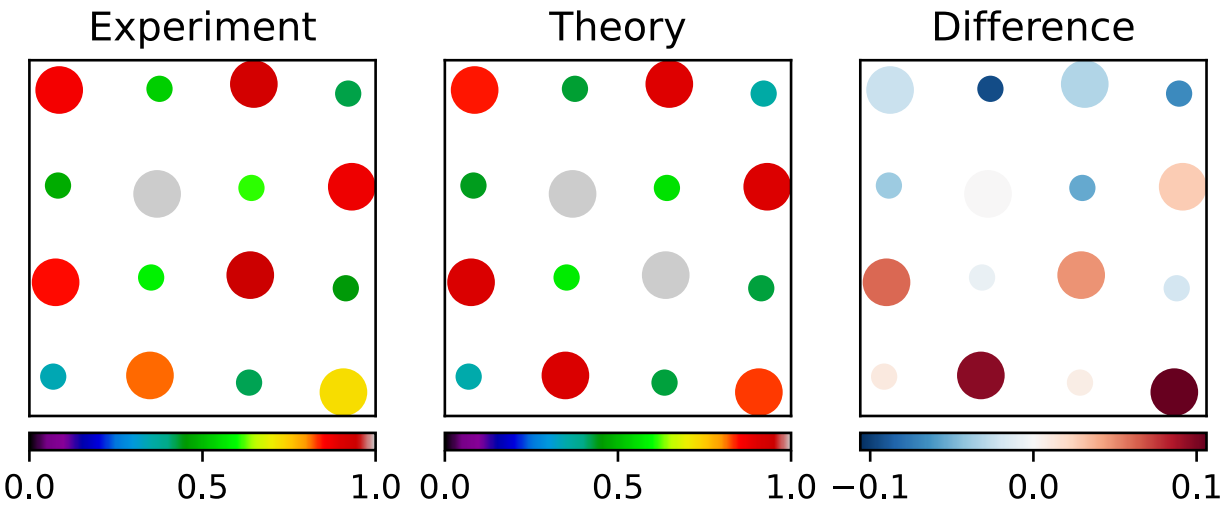

Figure 3.8: 4×4 square polydisperse array. The colourbars indicating the maximum normalised experimental (left panel), theoretical (central panel) and differential (right panel) lifetimes for each droplet.

than the theory and the other 10% slower than the theory, indicating the presence of an external bias limiting and enhancing the diffusion on each side. The origin of this bias is discussed and investigated further in chapter 4 section 4.1.

The normalised lifetimes in fig. 3.7 and 3.8 can be plotted against the radial distance from the centre in fig. 3.9. Both the theory and experiment group together in six clusters on the graph. The reason for this is, there are three distinct radial positions within the 4×4 array and therefore three distinct confinements. In each confinement can either be a big or small droplet, leading to a bifurcation of τ.

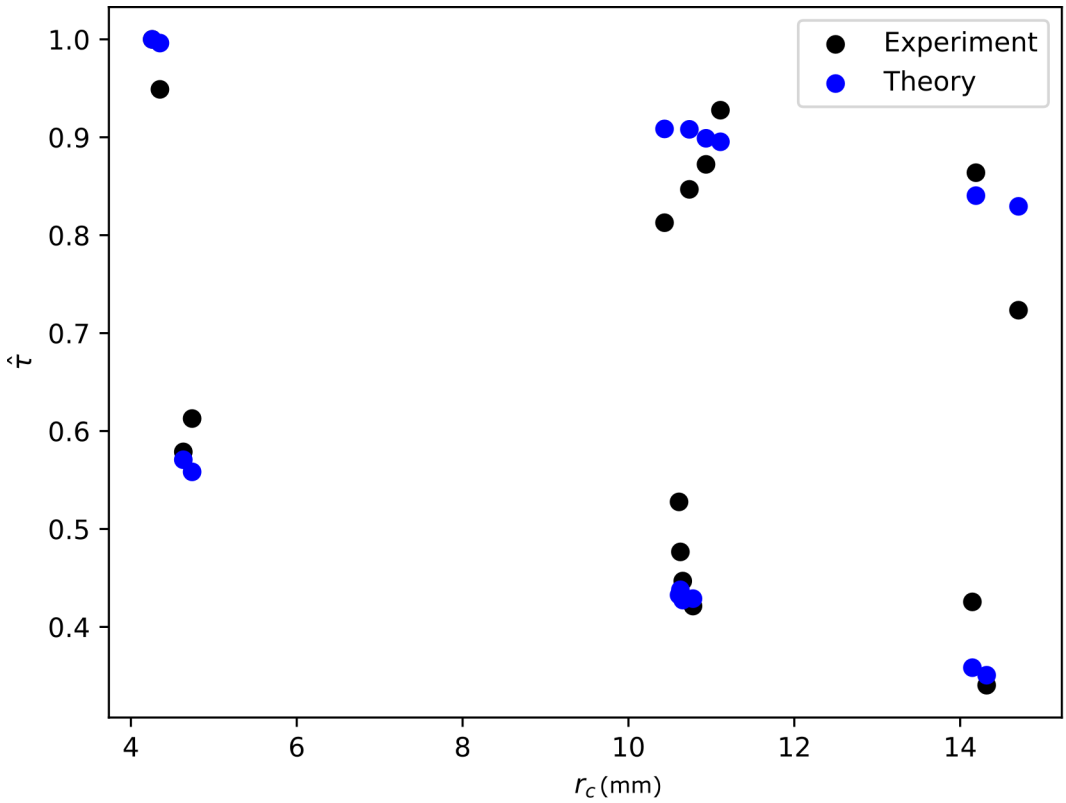

Figure 3.9: The maximum normalised lifetimes ($\hat{\tau}$) for the Masoud et al theory (blue) and experiment (black) for a 4×4 square polydisperse array as a function of radial distance from the centre of the array (r_c).

3.4 Conclusions

In this chapter two experimental methods were implemented to take data from multiple droplet arrays. Flux data measured with a Mach-Zehnder interferometer was found to be in good agreement with the Wray et al diffusive model for a series of small droplet arrays of different shapes. The model was further validated along with the Masoud et al model for volume data measured with the Pattern Distortion technique. The two models are also compared showing similar agreement and performance. Further Pattern distortion experiments again show the Masoud et al model's ability to capture the evaporation dynamics of different shaped small arrays.

The data was also compared with the Carrier et al model and was used to inform the size of the corresponding 'superdroplet' radius.

Finally the lifetimes of an initially polydisperse array of droplets (with different base radii) were compared to the Masoud et al theory. The agreement was also shown to be very good for this array and validates the theory for polydisperse arrangements.

Chapter 4

Non-diffusive dynamics

In chapter 3 the evaporation of small arrays of droplets was shown to agree well with the diffusive theory of Masoud et al. [55]. The arrays considered so far had $N \leq 21$ with $R \lesssim 20\,\text{mm}$ (in section 3.1), $N \leq 9$ with $R \lesssim 6\,\text{mm}$ (in section 3.2) and $N = 16$ with $R \lesssim 11\,\text{mm}$ (in section 3.3). The radius range of the droplets was $0.6 < a < 1.78\,\text{mm}$. The good agreement implies that the dominant method of interactions for these droplet arrays is the diffusive interactions through the vapour. In this chapter the aim will be to find when the limits of the theory and when droplet evaporation begin to diverge from the diffusive theory. It is found that this happens (for millimetre sized droplets) when the array becomes sufficiently large and/or when the array is on a heated substrate.

4.1 Large arrays

In everyday life droplet arrays nearly always extend over larger areas than studied so far in this thesis. The effect of increasing the length scale of the arrays and its impact on the agreement with the diffusive dynamics can be investigated. It is expected that more droplets could result in an amplification of non-diffusive dynamics which may lead to a divergence from the diffusive theory.

4.1.1 Method

To minimise the dispensing time of arrays with many droplets, the droplet printing setup described in section 3.3 was used. For the larger arrays a 12.9 inch iPad screen protector (JETech) was used as the substrate. This was because it provided a large enough clean

continuous hydrophobic surface which prevented the contact line pinning and ensured close to CA evaporation and a circular contact line. The droplets were assumed to evaporate at the equilibrium $\theta = \pi/2$. Evaporation during the dispensing time was further minimised by printing arrays from the centre to the edge such that the first droplets printed were the most confined. Droplets were left to evaporate inside an acrylic enclosure (X=722mm, Y=510mm, Z=473mm) to limit external air currents and maintain a quiescent (still) environment (see fig. 4.1). The screen protector substrates are placed on the base of the box on top of 1 inch sheet of wood. The droplets were illuminated through the top of the enclosure with a LED ring light (Pnitri) with an outer radius of 12.6 inches. Images were taken intermittently through the acrylic roof of the box with a Nikon D750 DSLR camera with an AF-P DX NIKKOR 18-55mm f/3.5-5.6G VR lens. The humidity and temperature inside the box was measured throughout evaporation with two DHT22 sensors wired to and controlled by an external Arduino. All electrical components were kept outside of the box to avoid them thermally influencing the evaporation.

To analyse the videos the droplet lifetime was extracted by the Python program 'Measure_Droplet_Lifetime' (see Appendix C for a description). These droplet lifetimes are then compared to those predicted by the Masoud et al. theory.

The Pattern Distortion technique described in chapter 2 and implemented in chapter 3 section 3.2, was not used in this section due to the challenges associated with the analysis of the magnification inside each droplet with sufficient camera resolution and FOV. In addition to this the droplets evaporate with moving contact lines which would therefore require each of these to be tracked. Despite this, it is possible, and development of analysis code to capture both these quantities for large numbers of droplets would provide valuable information and be the focus of future work. Furthermore smaller sections of the arrays as well as individual droplets could also be studied. Lots of interesting dynamics can be inferred purely from the droplet lifetimes and this will be the focus in this chapter.

4.1.2 Results and Discussion

The data can be plotted against the Masoud et al. predictions for a number of experiments in which the length scale and inter-droplet spacing were varied. But before these experiments were carried out predictions were made using Masoud et al to determine the most suitable array to print to maximise sensitivity to non-diffusive effects.

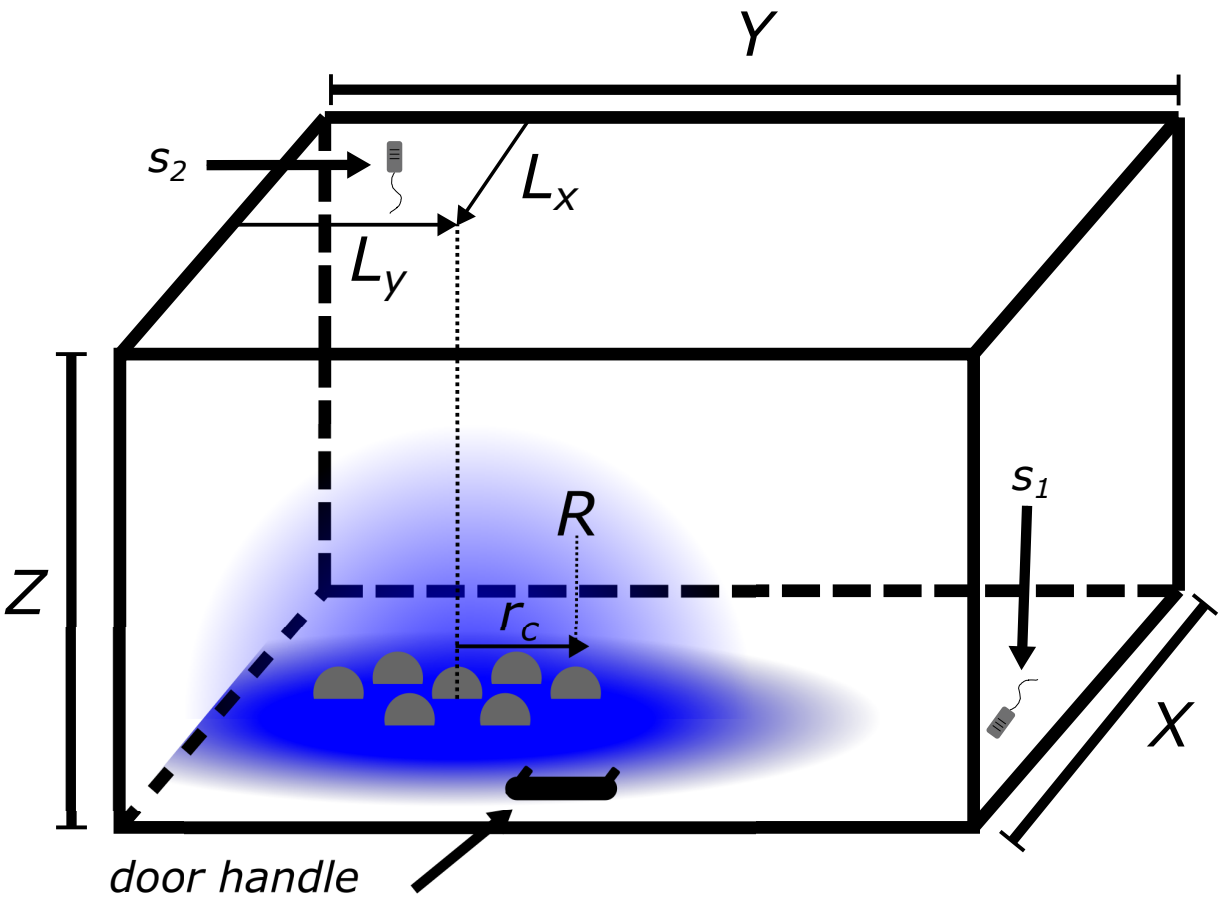

Figure 4.1: Diagram of the experimental setup of the array of radius R evaporating inside the enclosure of dimensions X, Y, Z. The array centre is positioned at distances L_x and L_y from walls of the enclosure. The position of the two temperature humidity sensors are indicated as s_1 and s_2.

4.1.3 Array sensitivity to non-diffusive evaporation

The top panel of fig. 4.2 plots the normalised lifetimes ($\hat{\tau} = \tau/\tau_{max}$) of the droplets in four different array shapes against their radial position from the centre (r_c). These shapes were: circle (black series), triangle (blue) and hexagon (green) (each with hexagonally packed droplets) and a square (red) (with square packing). The length scale of each array was kept approximately the same but was chosen arbitrarily. Fig. 4.2 also presents the $\hat{\tau}$ heat-maps for each array shape in the four lower panels, revealing how $\hat{\tau}$ varies spatially. Due to the diffusive shielding effect the least confined droplets will evaporate first. These are the droplets along the edge of the array with the ones at the corners having the fewest neighbours and therefore evaporating first according to the theory. Because of this, shapes with vertices are slowly rounded off and regularly spaced arrays of mono-disperse droplets like the hexagon, square and triangle in fig. 4.2 become circular. The transition of each array can be seen in the lower panels of fig 4.2, with the different colours showing the corners gradually disappearing with the red and white regions approaching the same circular shape. The top panel demonstrates the perturbation which these vertices make to the smooth $\hat{\tau}(r_c)$ profile, initially very large with droplets evaporating at similar times over a wide r_c range but slowly decaying over time as the array becomes more and more circular. The point in which each array becomes circular is indicated by the coloured arrows. The three non-circular arrays converge to the (black) steady-state circular array which does not have these features because it lacks any vertices and droplets at similar r_c have similar confinement. The shape with the largest perturbation from this steady-state is the triangle as it is the furthest from a circle. The extent to which a certain array will perturb can be quantified by the roundness (o) defined as

$$o = \frac{4\pi A}{P^2}, \tag{4.1}$$

where P is the perimeter of the array and A is the area it covers on the substrate. For a circle $o = 1$ and for all other shapes $o < 1$. The triangle, square and hexagon have roundnesses of $o = 0.698, 0.785$ and 0.907, explaining the decreasing perturbations for the blue, red and green series respectively. To confirm that eq. 4.1 can be used to predict the length of this transition generally, some irregular shaped arrays would need to be tested. In these cases, it is possible that the specific shape of the array outline varies how long it takes for the array to become circular for arrays with the same o. It will also probably

depend on the packing density of the droplets within the array.

For now however, to maximise the sensitivity of the experiments to non-diffusive effects a circular shape array is chosen, as any divergences from it will indicate non-diffusive dynamics. Within this circle the droplets could either be dispensed in a hexagonal or concentric circle arrangement however the former is preferred due to the greater packing efficiency, which provides the possibility for a greater experimental range of droplet density.

4.1.4 Investigating and correcting for array bias

As was observed in section 3.3 larger arrays can start to experience biases with one side of an array evaporating faster than the other. As the arrays begin to increase in droplet number and size this becomes a significant feature of their dynamics. To investigate the origin and effect these biases have on the droplet evaporation lifetimes, an experiment is conducted with an array placed asymmetrically nearer to one side of the enclosure in the X dimension and centred between them in the Y dimension as defined by fig. 4.1. In the asymmetric dimension the array was a distance $L_x = 2.75R = 0.14X$ (from the centre of the array) on one side and $15.6R$ from the other. The $N = 649$ droplets were dispensed hexagonally into a circular array with $R = 40\,\text{mm}$ and left to evaporate. Mathematically diffusion limited theory assumes there are no walls and the concentration approaches the ambient value at infinity. By introducing a wall this boundary condition is no longer satisfied. Effectively droplets can be thought of as evaporating into different ambient conditions depending on their position within the array.

The lifetimes of the droplets can be seen in fig. 4.3 (left panel) with the corresponding Masoud et al. predictions (middle panel). The two panels maintain a reasonably circular evaporation however droplets with the longest lifetimes (coloured white) are shifted and not located at the centre as predicted by the theory. The rightmost panels showing the difference in these lifetimes reveal droplets evaporate faster on one side of the array and slower on the other. This strong bias is due to the asymmetry in the position of the array with the local humidity on one side of the of the enclosure causing a slower evaporation on this side. To visualise the agreement in different ways the data can be plotted as a single series of $\hat{\tau}_{\text{th}}$ against $\hat{\tau}_{\text{exp}}$ for each droplet or as two series against r_c. For the former data points which lie on $y = x$ represent perfect agreement and for the latter the two series should lie on top of each other. These graphs can be seen in fig. 4.4 and in both cases

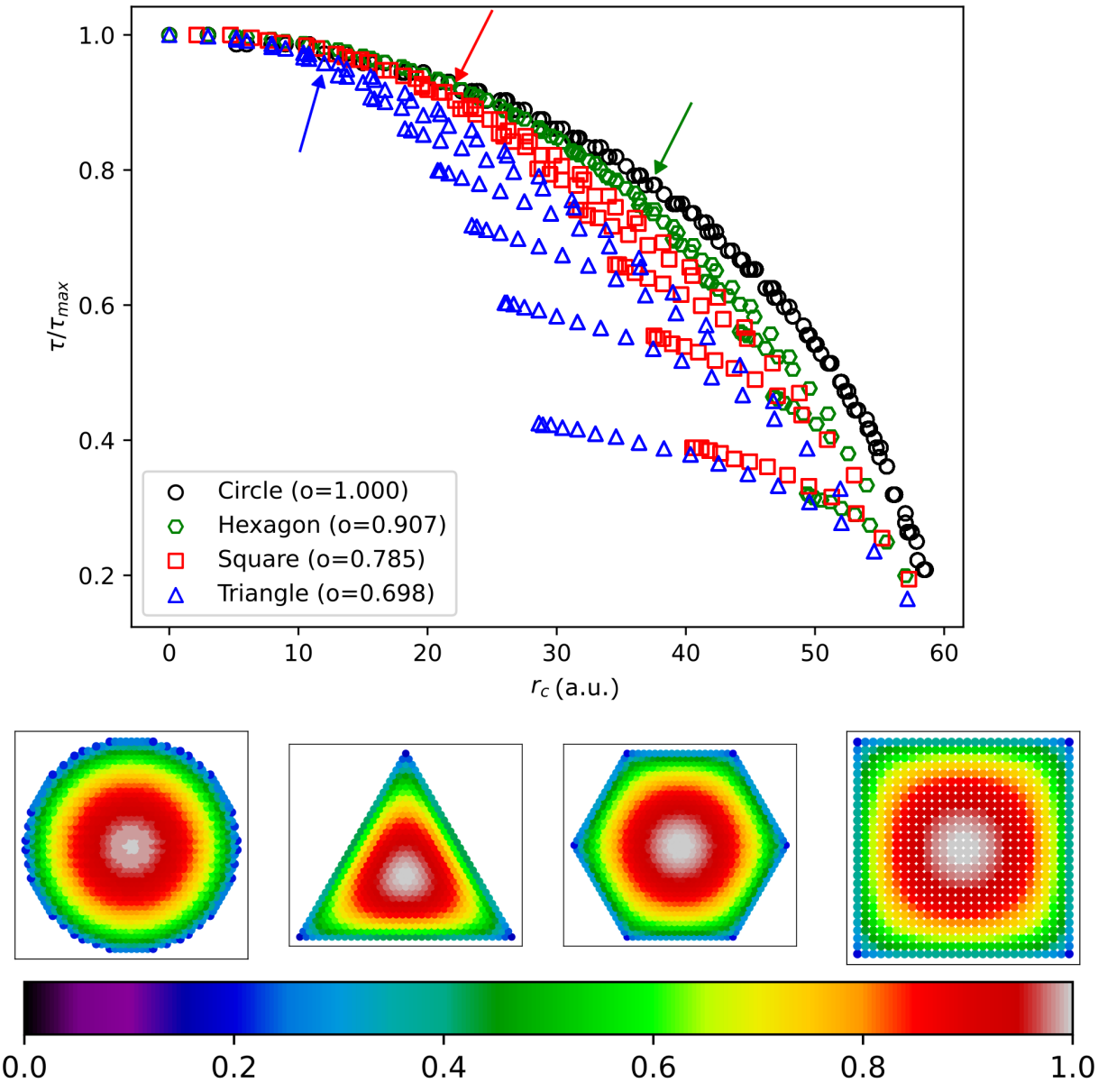

Figure 4.2: Masoud et al. maximum normalised lifetimes ($\hat{\tau}$) for a circle (black), triangle (blue), hexagonal (green) and square (red) array plotted against r_c (top panel). The droplets evaporated in CA mode with $\theta = \pi/2$. The arrows indicate the point in which each array becomes circular. The number in the legend represents roundness (o) define by eq. 4.1. The $\hat{\tau}$ colourmaps for each array plotted in the below panels.

there is poor agreement with large scatter. The origin of the scatter will at least partly be caused by the enhanced bias. This is because experiments without any bias would predict that droplets at a particular radial distance from the centre would evaporate at similar times, as seen previously for the circle in fig. 4.2. The bias however distorts this and in fig. 4.4 introduces a scatter in the $\hat{\tau}$ values for each value of r_c (right panel). It is because of this scatter that there is an offset at $r_c = 0$, as the droplet in the centre of the array is not the one which evaporates last. The limit of the fastest evaporating droplet at any r_c is set by the droplet on the side of the bias where the vapour concentration is lowest. Interestingly this bias is not directly normal to the nearest wall (at $L_y = 0$ in fig. 4.1) but also faster nearer to the door of the enclosure (at $L_x = X$). The side of the array near the wall also evaporates faster, where it would be expected that vapour is stopped by the boundary. This indicates that there are gaps between the base of the container and the walls, leading to small airflows (leaks) which are depleting the vapour on this side. Because of this as the array evaporates the array moves away from the near wall and the asymmetry should reduce. If there were no leaks underneath the walls the edge furthest from the wall would evaporate first and this asymmetry would be maintained. Furthermore, the action of closing the door at the beginning generates a small amount of forced convection, advecting the vapour away from the door. In addition to confinement asymmetries and air currents, thermal gradients in either the substrate or air could also cause biases of this sort.

The biasing is a problem when searching for non-diffusive effects not included in the theory, as it hides their presence. Attempts have been made to minimise this bias experimentally however this is challenging as the droplets appear to be very sensitive to minor asymmetries and the direction in which the bias presents varies between experiments.

To improve the agreement the theory can be modified to account for this directionally dependant bias and improve the agreement. The theoretical values of $\frac{dV}{dt}$ can be enhanced if nearer to one side of the array and reduced if nearer to the other. Since the specific ambient humidity does not affect the agreement (due to normalisation), this should improve the agreement of the normalised lifetime as long as the bias is linear. The magnitude of this correction depends on the component of the radial distance vector (r_c) in the direction of the bias (r_b). To determine the direction of the bias the centre of mass of the last three droplets to evaporate is calculated and labelled the bias point (x_b, y_b). This point is marked with a cross in fig. 4.5 which plots the same array as the asymmetric confinement

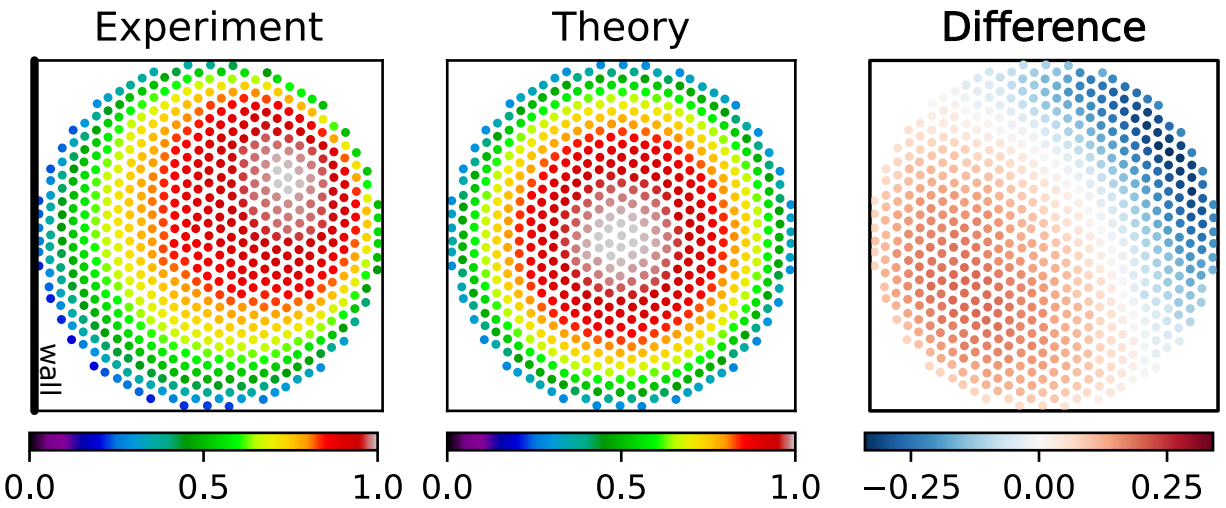

Figure 4.3: 649 droplet hexagonal array within R=40mm. The colourbars indicate the normalised experimental (left panel), theoretical (central panel) and differential (right panel) normalised lifetimes for each droplet. The side of the nearest wall is indicated on the left experimental panel.

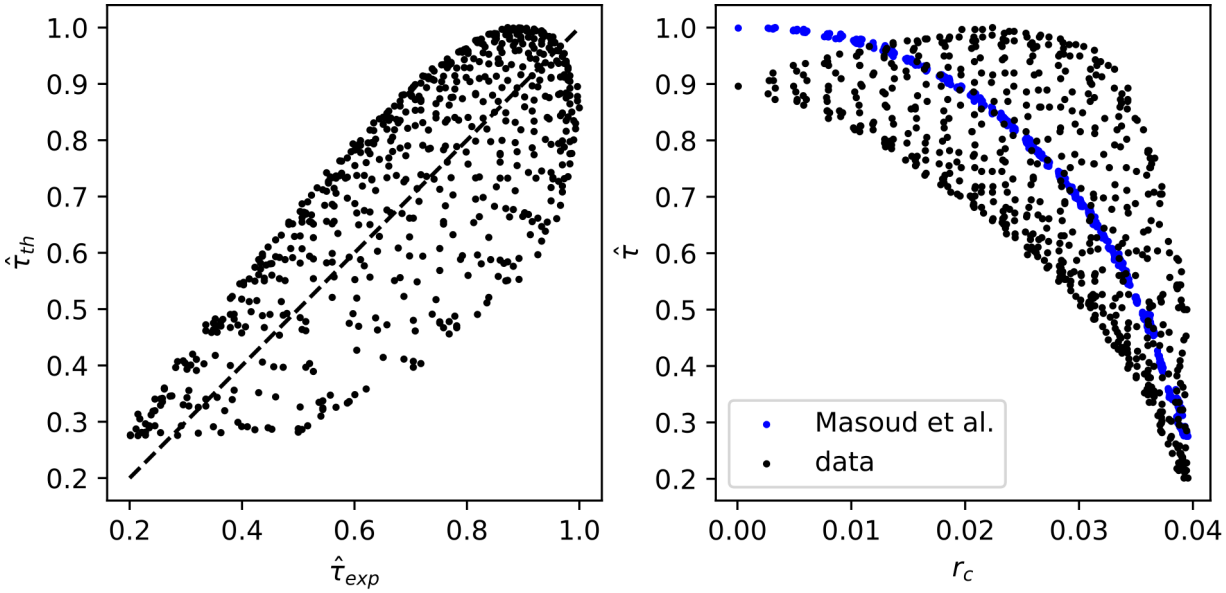

Figure 4.4: Evaporation lifetimes for an $N = 649$ circular array of radius $R = 40$ mm with hexagonal packing spaced $s = 3.0$ mm. The left panel plots theoretical ($\hat{\tau}_{\text{th}}$) against experimental ($\hat{\tau}_{\text{exp}}$) lifetimes with the black dashed line indicating $\hat{\tau}_{\text{th}} = \hat{\tau}_{\text{exp}}$. The right panel plots $\hat{\tau}_{\text{th}}$ (blue) and $\hat{\tau}_{\text{exp}}$ (black) against r_c.

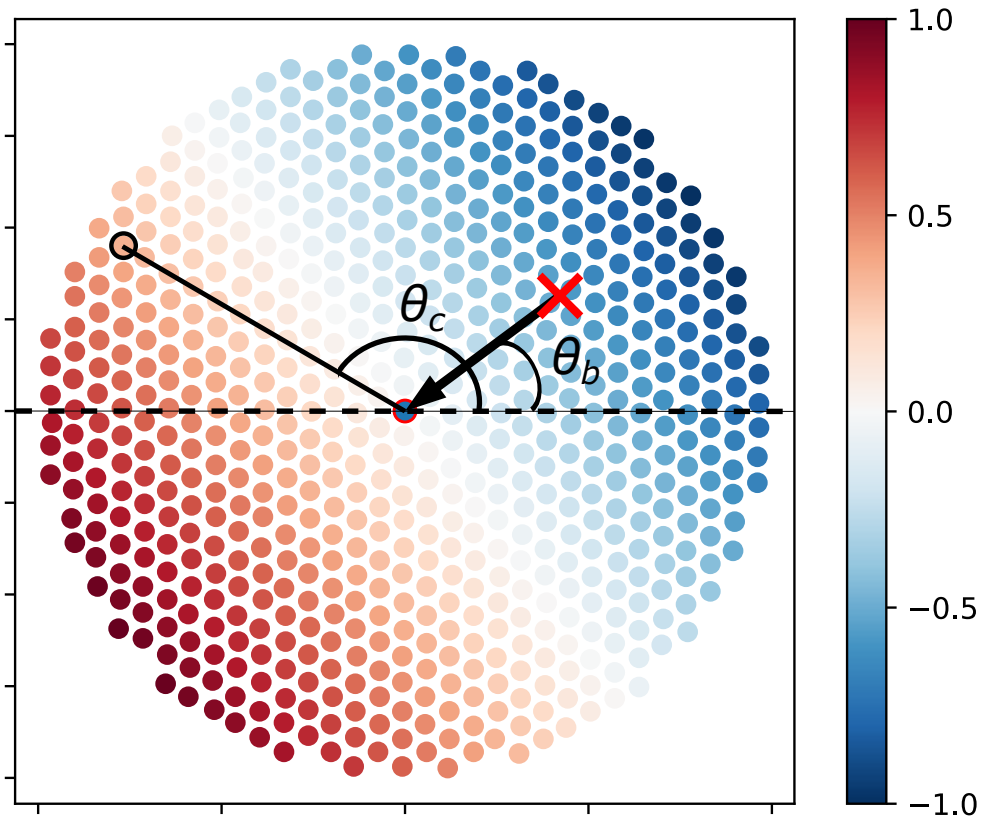

Figure 4.5: Normalised bias ($\hat{b}$) applied to the array in fig. 4.3. The black arrow indicates the direction of the bias. The red cross is the centre of mass of the last three droplets and the red circle is the centre of mass of the full array. Bias angle is labelled θ_b (defined by eq. 4.2). θ_c is an example of the angle to a specific droplet, circled in black here.

experiment discussed above. Without the presence of a bias this point would be at the origin, $x_b = x_0$, $y_b = y_0$ which is marked with a circle in fig. 4.5. The angle of the x axis is set by the arbitrary horizontal direction in the experimental images. The angle between the x-axis and the vector connecting the bias and origin points is given by

$$\theta_b = \text{arctan2}\left(\frac{y_b - y_0}{x_b - x_0}\right) \tag{4.2}$$

and the angle is indicated in fig. 4.5. Where arctan2 represents the two argument arctangent ($-\pi \leq \theta_b \leq \pi$). The same angle can be calculated to any droplet centre (x_c, y_c) in the array for example the black circle indicated in fig. 4.5 shows an example droplet, the angle is given by

$$\theta_c = \text{arctan2}\left(\frac{x_c - y_0}{x_c - x_0}\right). \tag{4.3}$$

The distance along the bias vector for any droplet is then

$$r_b = r_c \cos(\theta_b - \theta_c). \tag{4.4}$$

The normalised value of r_b for each droplet is indicated by the colourbar in fig. 4.5, with the black arrow pointing in the direction of the bias. Eq. 4.4 can then be used to calculate a coefficient (b) which alters the evaporation rates

$$b = 1 - m_b r_b \tag{4.5}$$

where m_b is a positive value having dimensions of $[L^{-1}]$, representing the gradient of the correction bias. b is then used to calculate the corrected evaporation rates $\left(\frac{dV}{dt}\right)_{corr}$ of each droplet from its uncorrected rate $\left(\frac{dV}{dt}\right)$ as

$$\left(\frac{dV}{dt}\right)_{corr} = b\left(\frac{dV}{dt}\right). \tag{4.6}$$

Droplets along the central line of the array perpendicular to the bias direction, have $r_b = 0$ (white droplets in fig. 4.5) and the rate is unchanged $\left(\frac{dV}{dt}\right)_{corr} = \left(\frac{dV}{dt}\right)$ as $b = 1$. The magnitude of b varies linearly with r_b, decreasing when $r_b > 0$ (red droplets) and increasing when $r_b < 0$ (blue droplets) according to eq. 4.5.

Fig. 4.6 demonstrates how increasing m_b (the steepness of the correction) helps reduce the scatter and improves the agreement with the $\hat{\tau}_{th} = \hat{\tau}_{exp}$ indicated by the black dashed line. The bottom panel plots the mean absolute difference ($\delta\hat{\tau}$) of each series from the black dashed line. The choice of m_b has an optimum value ($m_b \approx 10\,\mathrm{m}^{-1}$, green for this experiment) which minimises $\delta\hat{\tau}$. Beyond this the data begins to diverge again (as in the $m_b = 15\,\mathrm{m}^{-1}$, blue).

The lifetime colourmap can be re-plotted (in fig. 4.7) for the bias yielding the best fit in fig. 4.6 ($m_b = 10\,\mathrm{m}^{-1}$) and the theoretical prediction looks qualitatively better with the slowest evaporating droplets (in white) now approximately located at the same non-central position. The rightmost panel showing the spatial difference in the droplet lifetimes has reduced to a maximum of $\sim 15\%$, from $\sim 30\%$ without the correction. It is clear that despite this correction there is still some disagreement. Some of this disagreement may be caused by the limitation in the assumption that the bias is linear. The extent to which this assumption is true is shown by the rightmost panel of fig. 4.3 and fig. 4.5. The white

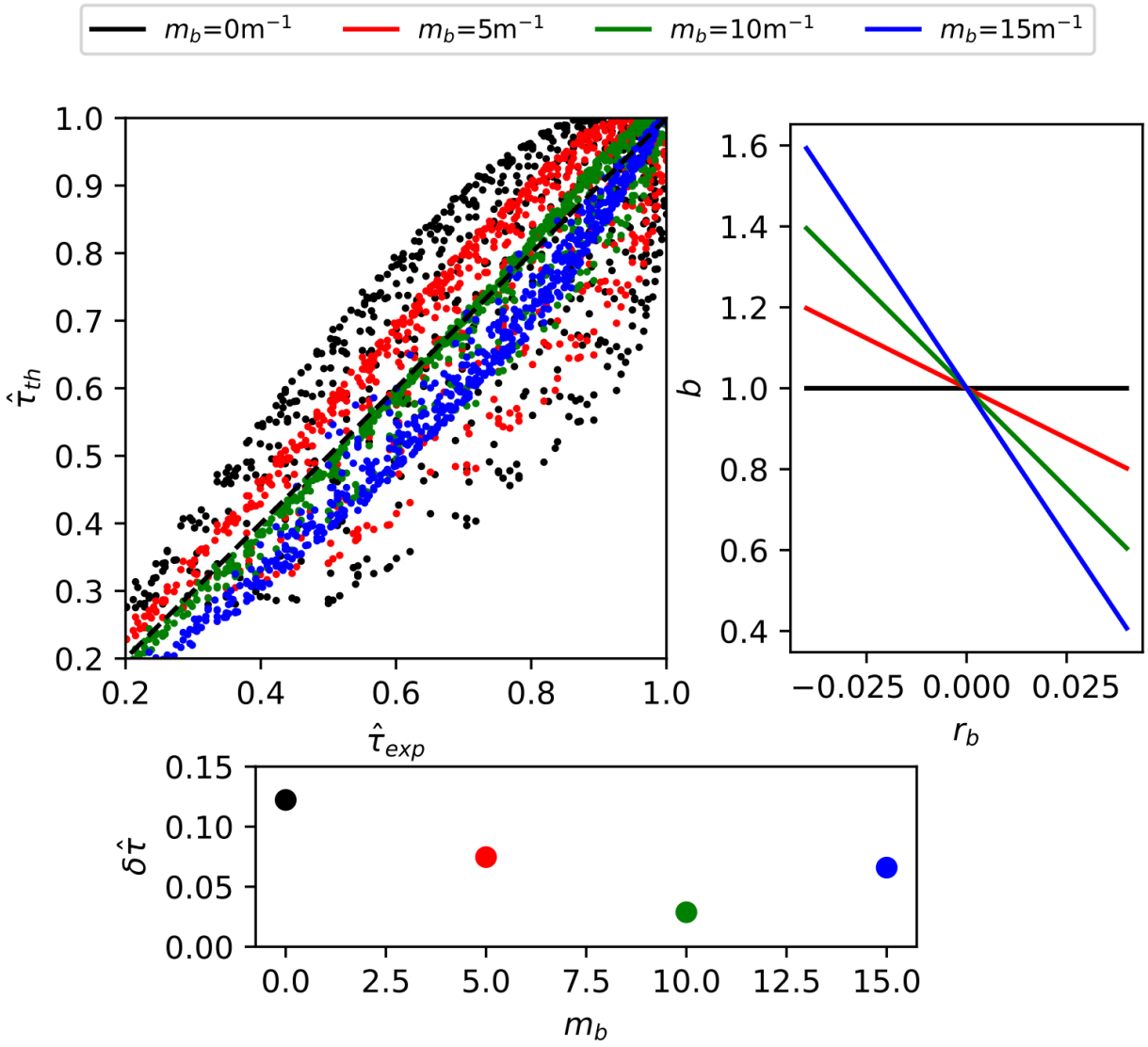

Figure 4.6: Left panel shows the maximum normalised theoretical ($\hat{\tau}_{\mathrm{th}}$) and experimental ($\hat{\tau}_{\mathrm{exp}}$) lifetimes for different bias correction gradients (m_b). The right panel shows the linear bias (b) applied in the direction of the bias. The lower panel indicates the mean absolute difference of the experiment from the theory ($\delta\hat{\tau}$) for each value of m_b.

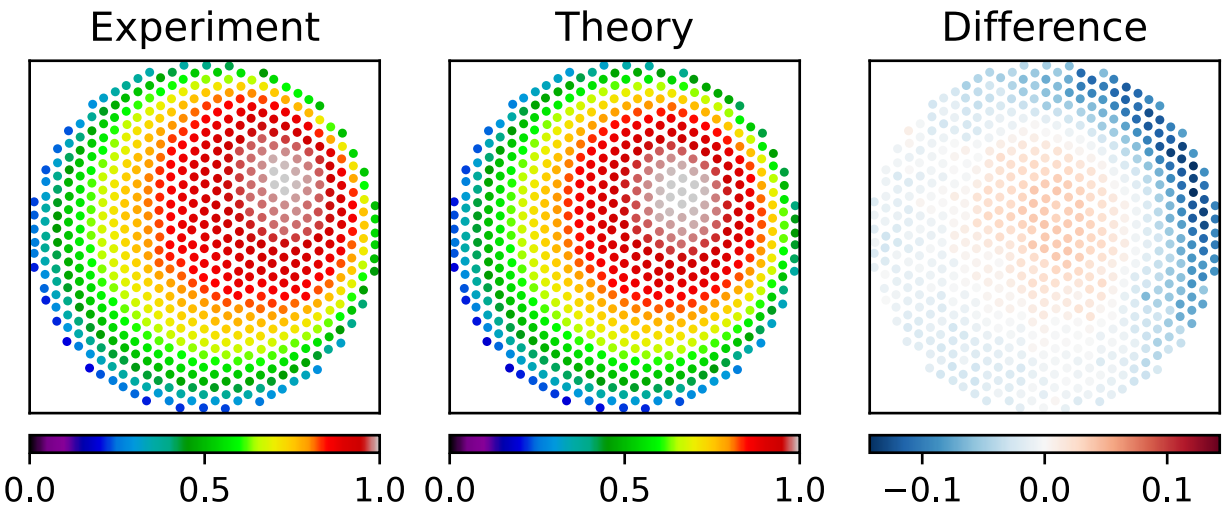

Figure 4.7: Re-plotting fig. 4.3 with the linear bias correction added to the theory panel.

region in the centre of the array is not straight in the former but is completely straight in the latter. This means that there could be an additional dependence on r_c which is not accounted for. The challenge of improving the correction is differentiating between this and other causes of disagreement, namely non-diffusive effects. It is also possible that the non-linearity of the bias and the blue data points in the top left panel of fig. 4.6 are in fact divergences caused by the onset of a length scale dependant non-diffusive effect. This non-linearity is only visible because of the reduced scatter resulting from the imposed correction.

4.1.5 Characterising non-diffusivity

With the knowledge that these biases impose a scatter to the data the origin of the non-linearity in fig. 4.6 is investigated. Three separate experiments of different size arrays are conducted to understand how it influences the non-linearity. For each experiment τ/τ_{mean} is plotted against r_c alongside their corresponding theory in fig. 4.8. The black data represents the experiments and the blue their corresponding Masoud et al predictions. The scatter in these experiments is much reduced as the arrays were centred in the enclosure at $L_x = X/2$ and $L_y = Y/2$ in fig. 4.1 and bias was minimised experimentally as much as possible. In each case you can see the lifetimes decreasing towards the edge of the array ($r_c \to R$), with the longest lifetimes at the centre ($r_c \to 0$) as expected for diffusive evaporation.

For the first (top) panel the agreement is very good and the data and Masoud et al

lifetimes lie on top of each other. For the middle and lower panels however the data points diverge from one another. The largest array (lower panel) having the worst agreement. The divergence of the experimental data suggests the experiments are starting to evaporate with additional non-diffusive effects which depend on the length scale, not captured by the theoretical model and not correctable by introducing a bias. To characterise the non-diffusive profile an equation is fit to the data. The diffusion limited evaporative flux profile over a flat droplet ($\theta = 0$) with $a = R$ (given by eq. 1.17) is

$$\frac{1}{j} \propto (R^2 - r_c^2)^{1/2}. \tag{4.7}$$

Carrier et al. [45] showed that droplet arrays evaporate as flat 'superdroplets', therefore the local flux on the 'superdroplet' interface is inversely proportional to the droplets lifetime ($\tau(r_c) \propto 1/j(r_c)$). This expression can be written into a more general form in order to allow it to fit the different shape of the experimental results, as well as the diffusive theoretical results. The expression used to do this is

$$\tau(r_c) \propto \epsilon(R^n - r_c^n)^{1/n} + \tau_{min}. \tag{4.8}$$

In eq. 4.8 the quantity n captures the profile shape and allows the profile to bend further. When $n = 2$ the profile takes the original diffusive form. As n decreases from 2 the profile flattens reaching a straight line at $n = 1$. For $n < 1$ the profile curves in the other direction. If n is very large the profile approaches a square shape dropping off very quickly close to $r_c = R$. The term $\tau_{min}(= \tau(r_c = R))$ can be varied to shift the profile on the y axis, physically representing the environment's effect on the overall evaporation times as well to correct for the fact that lifetimes do not go to zero at the edge of the array ($R = r_c$). The coefficient $\epsilon = \tau_{min}/\tau_{max}$ varies the difference in lifetime at the edge and centre. When $\epsilon = 0$ the $\tau(r_c) = \tau_{min}$ and the lifetime is independent of droplet position in the array. Physically this would represent when the droplets are not interacting for example when evaporation is completely limited by phase change. The best fit obtained by varying the parameters n, ϵ and τ_{min} for the data and theory in fig. 4.8 are plotted as solid lines in the same colour. Since the Masoud et al theory is purely diffusive, n should equal 2 for the blue data points such that eq. 4.8 reduces to the diffusive eq. 4.7. The optimum n (given in the legend) is found to be slightly less than $n = 2$ for each of the blue

series. This is because eq. 4.7 does not account for the fact that the 'superdroplet' array is effectively evaporating in CA mode and R is decreasing as the edge droplets disappear (note that if the droplets themselves were evaporating in CR mode, the 'superdroplet' would still be evaporating in CA mode). Additionally τ represents a temporally averaged value of the flux from each droplet over the course of its lifetime and not an instantaneous flux. Eq. 4.7 does not account for any changes in flux due to the droplets changing size (*i.e.* becoming smaller towards the edge of the array). This therefore explains why n is not exactly 2. Despite this, the general shape of the Masoud theory is captured well by eq. 4.8 and n being slightly less than 2 is accounting for these limitations.

As previously mentioned, the experimental radial lifetime profiles (black series) show varying levels of agreement, indicating that the diffusive theory is no longer correctly capturing the experimental radial lifetime profiles for these larger arrays. The fit of eq. 4.8 to the experimental data (black lines) is very good in each panel and therefore the parameter n allows the fit to capture the diverging shape of the experimental radial lifetime profile. The three panels show that as the arrays become larger the curvature of the experimental profiles in fig. 4.8 becomes more pronounced. This curvature describes a flattening of the lifetimes in the centre of the array with a sharper decrease in lifetimes near the edge. The fit of eq. 4.8 can be used to measure this curvature with the parameter n allowing the equation to match this curved shaped. The values of $n = 1.60, 2.32$ and 3.50 correspond to arrays of radius $R = 14, 30$ and $55\,\text{mm}$ respectively and so n (the curvature) increases with the length scale of the array. It is also true that the value of n increases for the diffusive theory which may be explained by the aforementioned limitations of eq. 4.7. Despite this, n does not increase as significantly as for the experimental data. This curvature is associated with the extent of the disagreement and therefore the amount of non-diffusivity in each experiment.

It is important to note that, the scatter of the experimental data in fig. 4.8 is largely caused by experimental bias, as observed previously in section 4.1.4. The determination of the fitting parameters are expected to be unaffected by the scatter (experimental bias) as it is symmetric about the centre of the lifetime profile. As such if the bias were reduced and there was less scatter the optimum fitting parameter values would not change significantly.

To establish which explanation is the most convincing a montage of the evaporation behaviour is plotted in fig. 4.9 for the largest array in fig. 4.8 ($R = 55\,\text{mm}$). It can be seen that majority of the evaporation $< 225\,\text{mins}$ (of $339\,\text{mins}$) the droplets evaporate

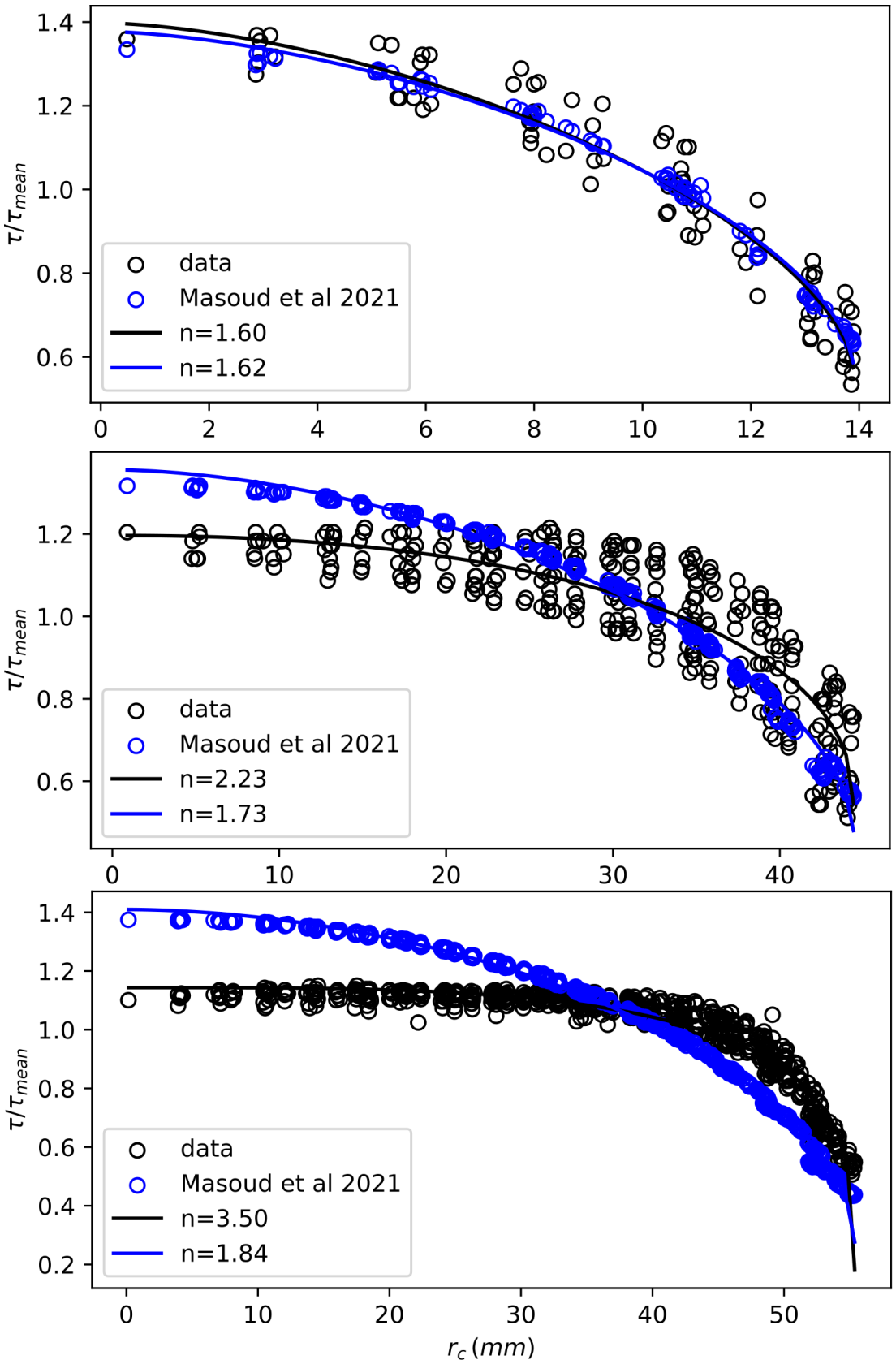

Figure 4.8: lifetime (τ) normalised by mean droplet lifetime (τ_{mean}) against radial distance from the centre of the array (r_c). Black data represents experimental data and blue the corresponding Masoud et al theoretical predictions with the fit to eq. 4.8 represented by lines in the same colour.

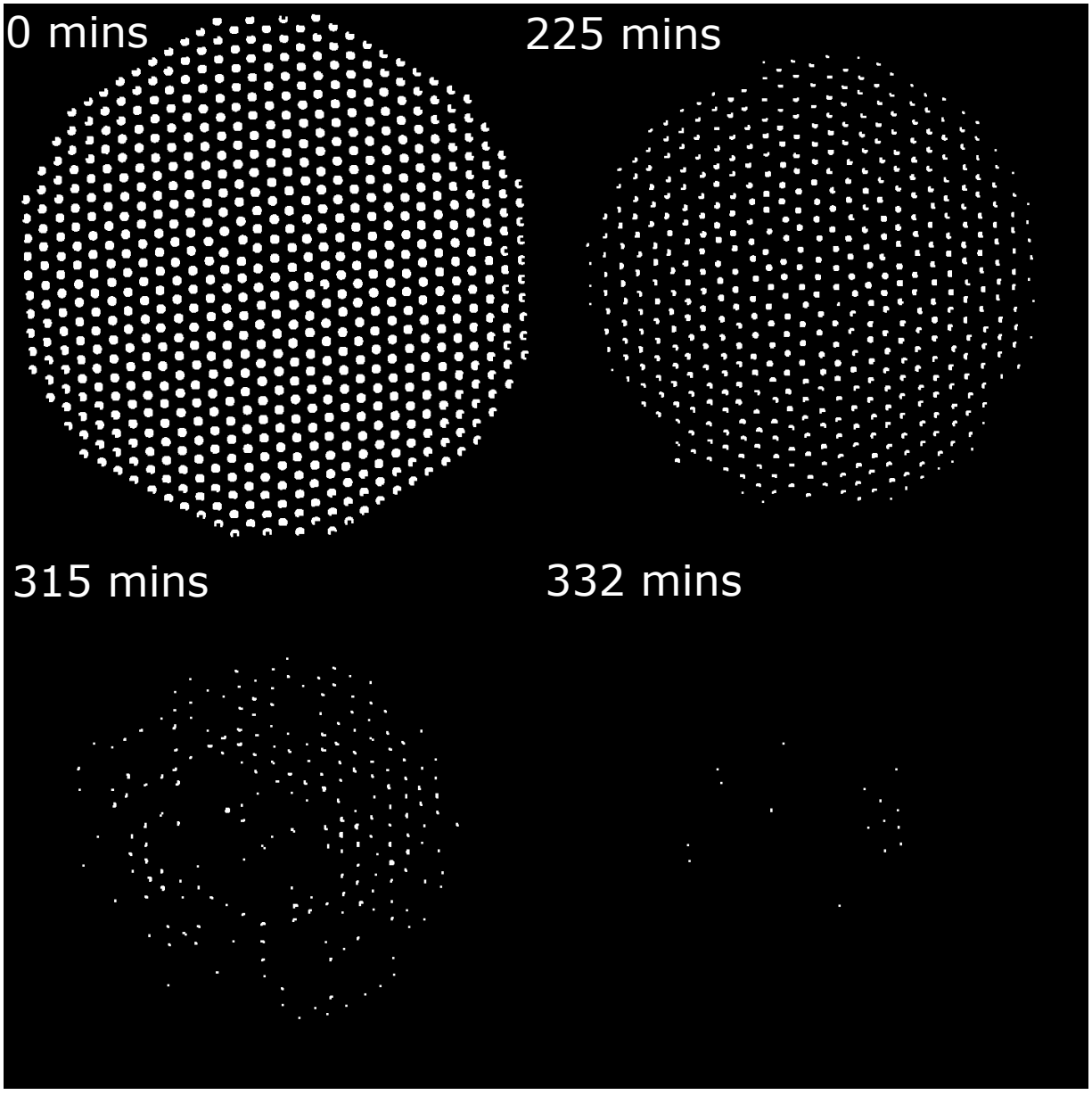

Figure 4.9: Evaporation montage of a $N = 685$ circular array of radius $R = 55$ mm with hexagonal droplet packing separated by $s = 4$ mm. Images have been processed as described in Appendix C for clarity.

in the order expected for diffusion, with the least confined near the edge of the array disappearing first. In the late stages of evaporation this changes and droplets evaporate in a non-diffusive order with the central droplets (the most confined) evaporating before edge droplets. These 'hot spots' could be consistent with natural convection which predicts the development of cells and plumes in the vapour due to the difference in buoyancy between ambient air and saturated air (their formation was described in section 1.2). The convective plumes would transport saturated air away from certain regions effectively decreasing the confinement of the affected droplets. The density of dry air (ρ_{dry}) and water vapour saturated air (ρ_{sat}), differs by $\approx 1\%$ with that of saturated air being less dense than dry air. As a result the saturated air is convected upward away from the droplets and unsaturated parcels of air are convected downward to replace it. These plumes have been observed above pools of water and in droplet dissolution by other authors as described in section 1.8. In each case the work describes the formation of an individual plume at the centre of the array or pool. In fig. 4.9 multiple 'hot-spots' appear and this could indicate the generation of multiple convection cells. These results could therefore be the first observation of convection above evaporating droplets and also the first observation of the formation of multiple convection cells. For comparison a similar montage of the smallest array in fig. 4.8 is plotted in fig. 4.10. These images do not show the same 'hot-spot' evaporation and the array evaporates in the expected circular manner expected for diffusion. These montages therefore indicate that the non-diffusive behaviour depends on the length scale of the array.

To characterise the convection the dimensionless numbers in section 1.2 can be used. Since it is thought that the flow above the droplets is natural convection, it can be characterised by the Rayleigh number (Ra), comparing the relative importance of diffusion and buoyancy driven flow. Ra was preferred to Gr as Sc ≈ 0.6 and diffusion is dominant over viscous dissipation. The Pe number could be considered a more general alternative, also capturing forced convection which other authors have observed changing droplet evaporation rates [83–85]. Despite this, it is not expected that air current velocities are significantly changing for the different experiments in fig. 4.8 and therefore forced convection is ruled out as an explanation for the disagreement. The convective numerator depends on the length scale (L) and Ra predicts that increasing the size of the array promotes convective transport. Convection is also enhanced with an increasing density difference ($\Delta\rho$) between the species. For a pool of liquid this density difference is between ρ_{sat} and

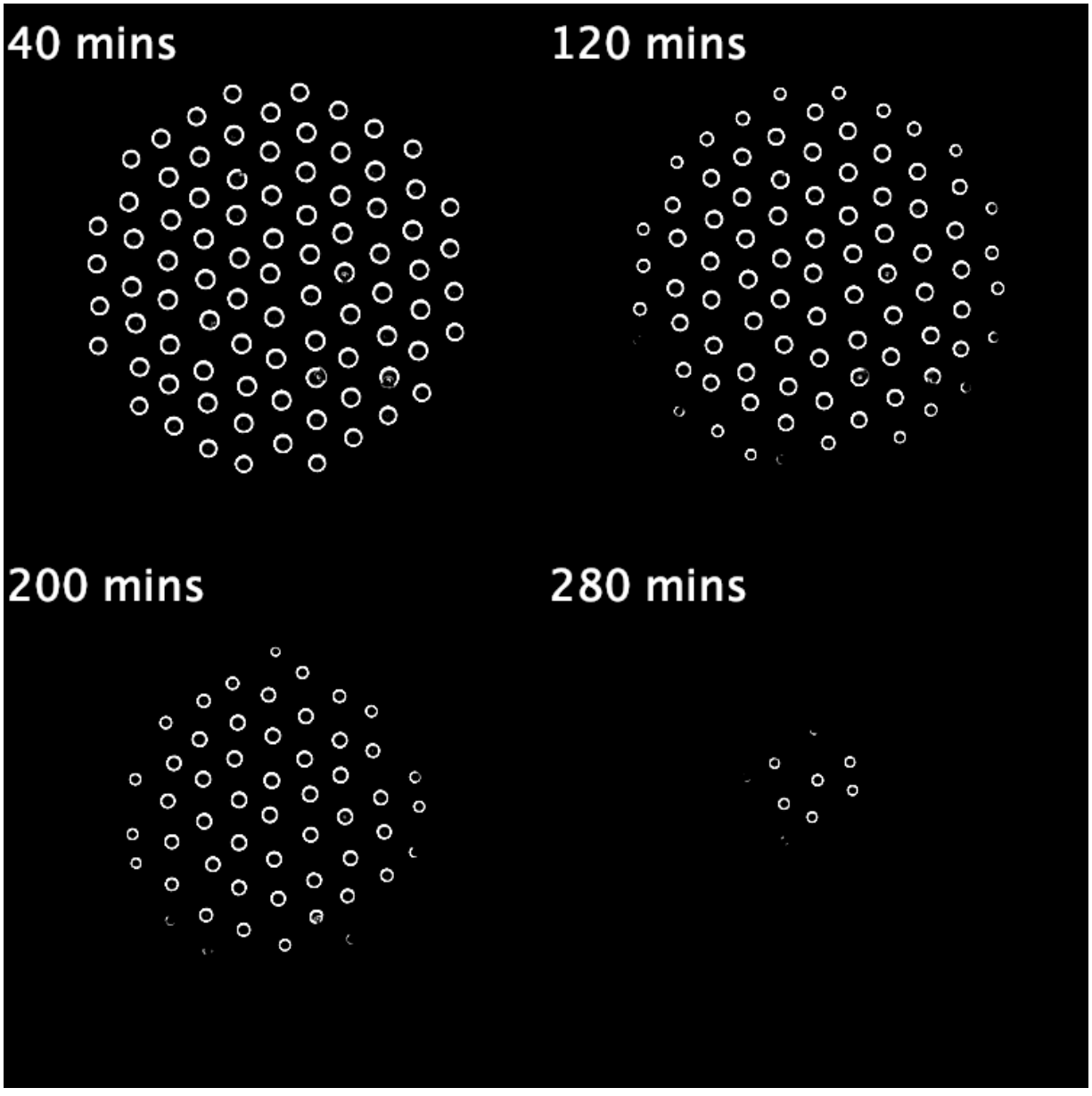

Figure 4.10: Evaporation montage of a $N = 85$ circular array of radius $R = 15$ mm with hexagonal droplet packing separated by $s = 3$ mm. Images have been processed as described in Appendix C for clarity.

ρ_{dry}. For a multiple droplet array of the same size as the pool, the density required for significant convection might be expected to be higher as the area covered by liquid is less. As a result the average vapour concentration above the droplets will be lower due to the increased volume it is able to diffuse into between the droplets. It is therefore proposed here that the standard definition of Ra can be modified from eq. 1.6 to account for this such that the Ra varies with the inter-droplet spacing. In the limit where the inter-droplet spacing tends to zero the modified Ra number (Ra^*) should recover the original definition. Therefore an area fraction (f) is defined as

$$f = \frac{N\pi a^2}{\pi R^2} = \frac{\text{area covered by droplets}}{\text{area covered by array}}. \tag{4.9}$$

For a pool of liquid $f = 1$ and for multiple droplets array $f < 1$, with higher inter-droplet spacing decreasing the value of f. f can then be used to effectively lower the value of $\Delta\rho$ and therefore a higher value of R is required for the onset of convection. Eq. 4.9 can be substituted into the original definition of Ra to give

$$\mathrm{Ra}^* = f \left| \frac{\rho_{sat} - \rho_{amb}}{\rho_{amb}} \right| \left(\frac{gR^3}{\nu D} \right). \tag{4.10}$$

Here Ra^* varies linearly with f which not necessarily true but has been assumed for simplicity as it is not obvious how the average concentration above the droplets varies with the inter-droplet spacing. A series of experiments was then conducted with different R and f values (summarised in table. 4.1). In fig. 4.11 the value of Ra^* for each array is then plotted against the fitting parameter n, from fig. 4.8, to characterise the level of non-diffusivity. The black and blue series represent the value of n for the experimental data and Masoud et al. diffusive predictions respectively. The error bars represent the limits of Ra^* due to the variation in T and ϕ during the experiment. There is a linear relationship between the variables, with a coefficient of determination of 0.877, indicating that as Ra^* increases the value of n increases. The Masoud et al data (blue) demonstrates that the parameter n is not expected to correlate as strongly for pure diffusive evaporation. With this figure it is possible to predict whether droplet arrays will evaporate non-diffusively. For $Ra^* > 10^3$ the value of n rises above that of the diffusive Masoud et al predictions. Therefore this can be considered a critical Ra^* for the onset of non-diffusive evaporation. For thermal Rayleigh-Bernard convection the typical critical Ra is $\sim 2 \times 10^3$ [86], which is

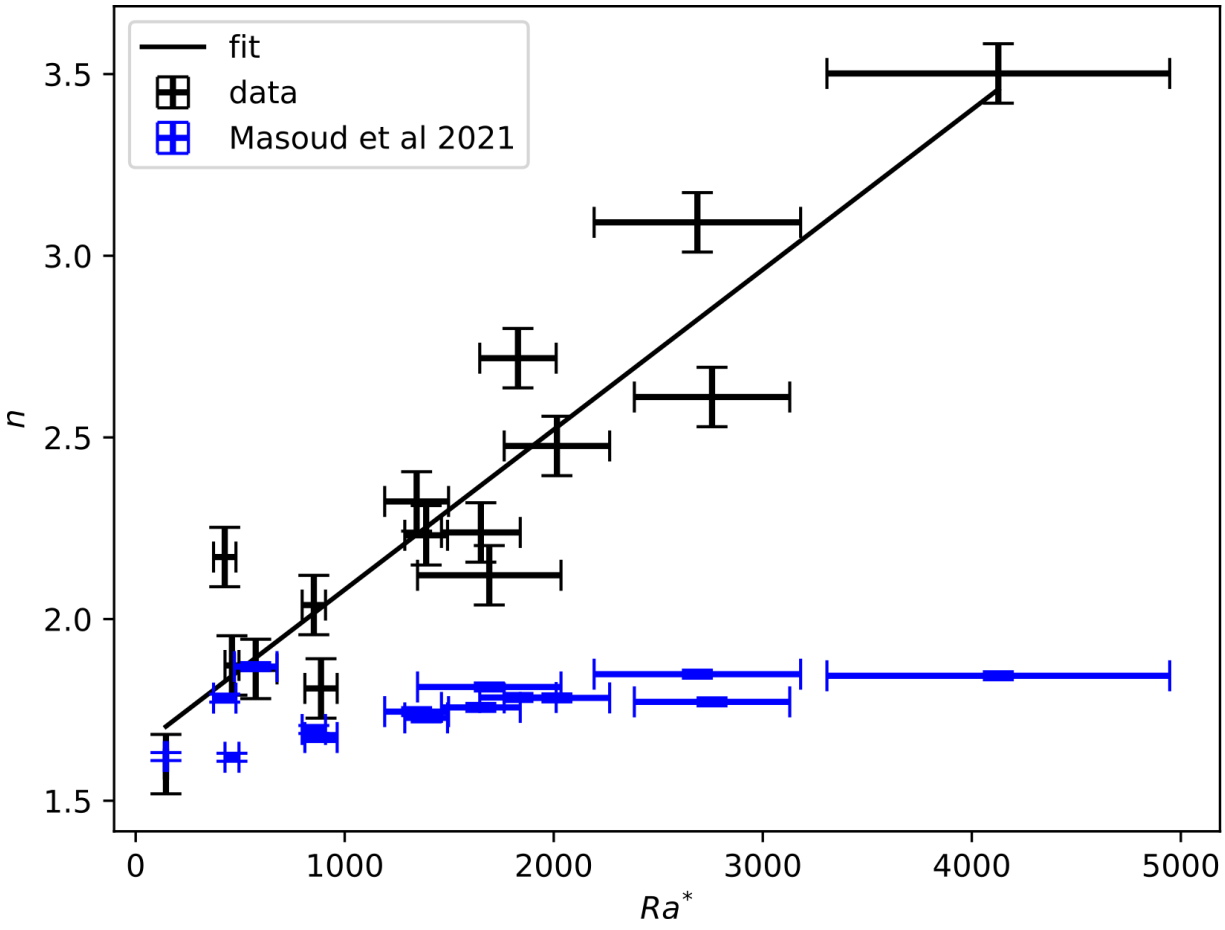

Figure 4.11: Non-diffusive parameter (n) against modified Ra number (Ra*) for the Masoud et al model predictions (blue) and the experimental data (black). Errorbars represent the uncertainty in the fit to n and the experimental variation in T and ϕ for the y and x axes respectively.

s(mm)	R(mm)	N
3.0	40	649
5.0	50	361
6.0	60	361
3.5	30	265
3	30	361
3.5	40	475
5.0	45	295
3.5	40	475
5	30	121
6	40	163
4.0	30	199
3.0	15	85
4.1	40	349
3.1	40	661
4	55	685

Table 4.1: Summary of the droplet separation (s), array radius (R) and number (N) for the data presented in fig. 4.11.

similar to that found from fig. 4.11. A breath figure (like those presented in the upcoming chapter 5) has $\mathrm{Ra}^* \sim 10^{-3}$ and should evaporate diffusively. Conversely a round garden table with a radius of 0.5m covered in rain droplets would have a $\mathrm{Ra} \sim 10^6$ and should evaporate non-diffusively.

The existing convection work does not mention the quantity n and this is the first instance of using it to characterise non-diffusivity. The mechanism which is responsible for this, as shown in fig. 4.9 could be convection. Dollet and Boulogne [61] developed a model containing the evaporative flux over a pool of liquid accounting for convection (see section 1.2 for a description) and also compared to experiment in the same paper. The authors found good agreement between their model and the global evaporation rate of their pool of water. However, they did not compare the prediction of the model to the flux over the surface. This is likely because this quantity is difficult to measure experimentally over a pool of water. Multiple droplets have an advantage when studying flux, as each droplet acts as a sensor with its evaporation providing information about the vapour immediately above it. As above since $\tau \propto 1/j$ the corresponding droplet lifetimes of this convective flux (eq. 1.21) can be compared to the diffusive lifetimes of eq. 4.7 (shown to be applicable to multiple droplets by Carrier et al., see section 1.8.3) in fig. 4.12. It can be seen that the flux accounting for convection (blue) acts to straighten the radial τ profile in comparison to the τ profile for the diffusive flux. It could be that the non-diffusive effects presented

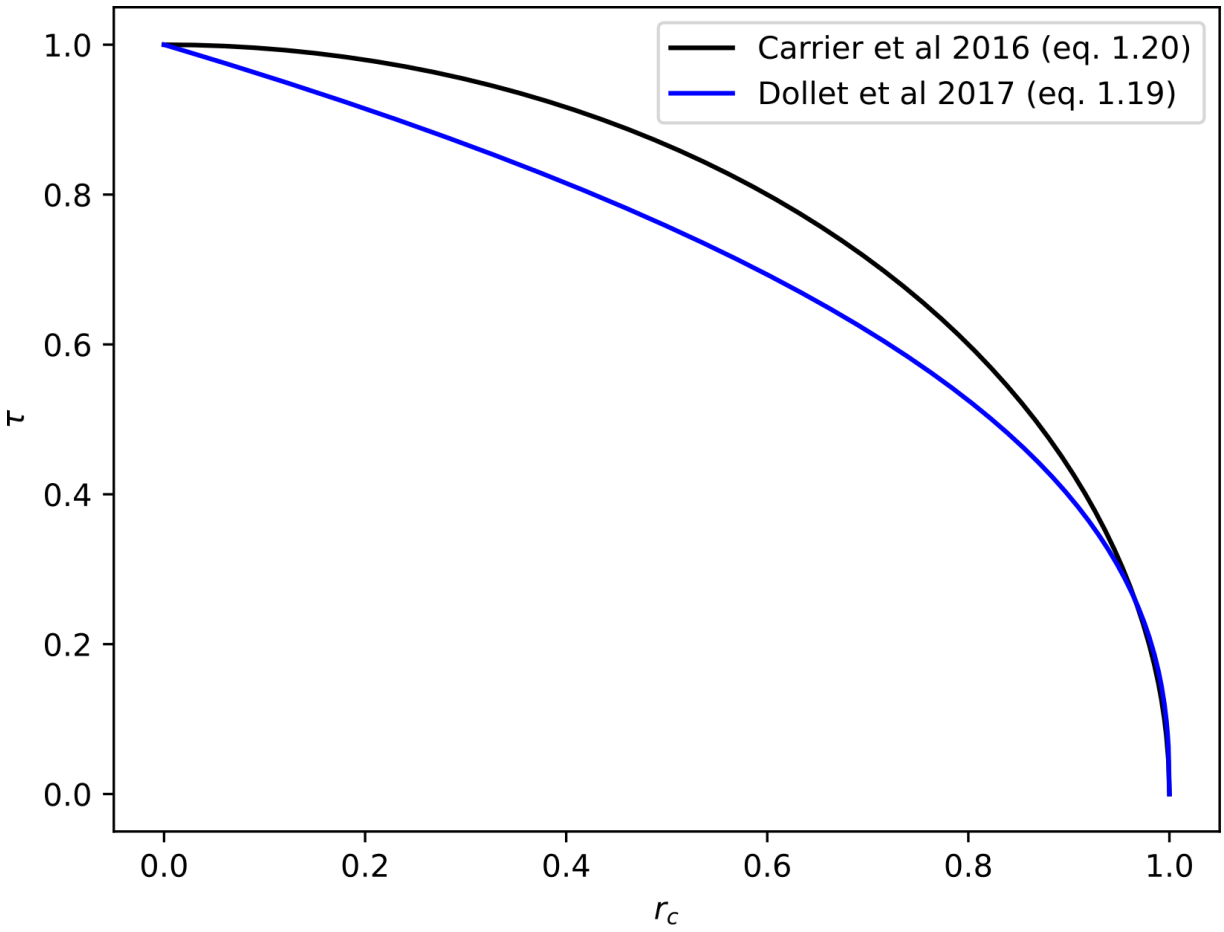

Figure 4.12: The radial lifetimes with a hypothetical 'superdroplet' according to diffusive theory (black series) Carrier et al. [45] and convective (blue series) theory.

in fig. 4.8 are not convection and must be explained by other means. Alternatively the Dollet and Boulogne model may not correctly characterise the convective flux as this was not validated by experiments in their work. Therefore it may need modification.

4.1.6 The effect of box saturation

In addition to convection there is another possible mechanisms which could be responsible for the the disagreement between the theory and experiment; a number of experimental limitations could lead to potential divergences. For example, the theoretical prediction assumes that the droplets evaporate in a semi infinite half space above the droplets and the vapour is unimpeded by any boundaries. Experimentally this means that the walls of the enclosure, preventing externally driven forced convection, must be placed sufficiently far away. To determine if this is being achieved the relative humidity inside the box should not increase significantly as this indicates a build up of vapour concentration at the walls of the enclosure. Inside the same size enclosure this effect would become more significant for larger droplet arrays, due to the increased vapour they generate leading to a higher degree of saturation. The amount of liquid required to saturate the enclosure at temperature T can be calculated by substitution of the saturation vapour pressure (p_{sat}) given by eq. 1.15 and the volume of the acrylic box into the ideal gas law (eq. 1.14). At room temperature ($T = 21°C$) with an initial ambient humidity of $\phi(t = 0) = 0.4$, assuming the box is perfectly sealed, $\approx 1.9\,\text{mL}$ of water must evaporate before $\phi = 1$. One droplet in the experiments for this chapter ($V = 2.72\mu\text{L}$) represents an increase in humidity of 0.085% and therefore ≈ 700 droplets are required for saturation. Measurements of the humidity throughout evaporation indicate that ϕ rises significantly and vapour is increasing above its initial value at the walls. The most extreme rise in ϕ happens for the array with the most droplets ($N = 685$), the bottom panel in fig. 4.8. The measurement of the humidity (bottom panel) and temperature (top panel) throughout evaporation of this array is presented in fig. 4.13 for two sensors s_1 (blue) and s_2 (red) (the positions of which are indicated in fig. 4.1). It can be seen that ϕ does not increase as much as predicted theoretically for a perfectly sealed container and therefore there is an unknown leak in the box. The rate of this leak is likely dependent on the average concentration inside the box, as increases in vapour concentration will increase the internal pressure inside the box. This leak also indicates that air is still permeating the box which could explain the bias

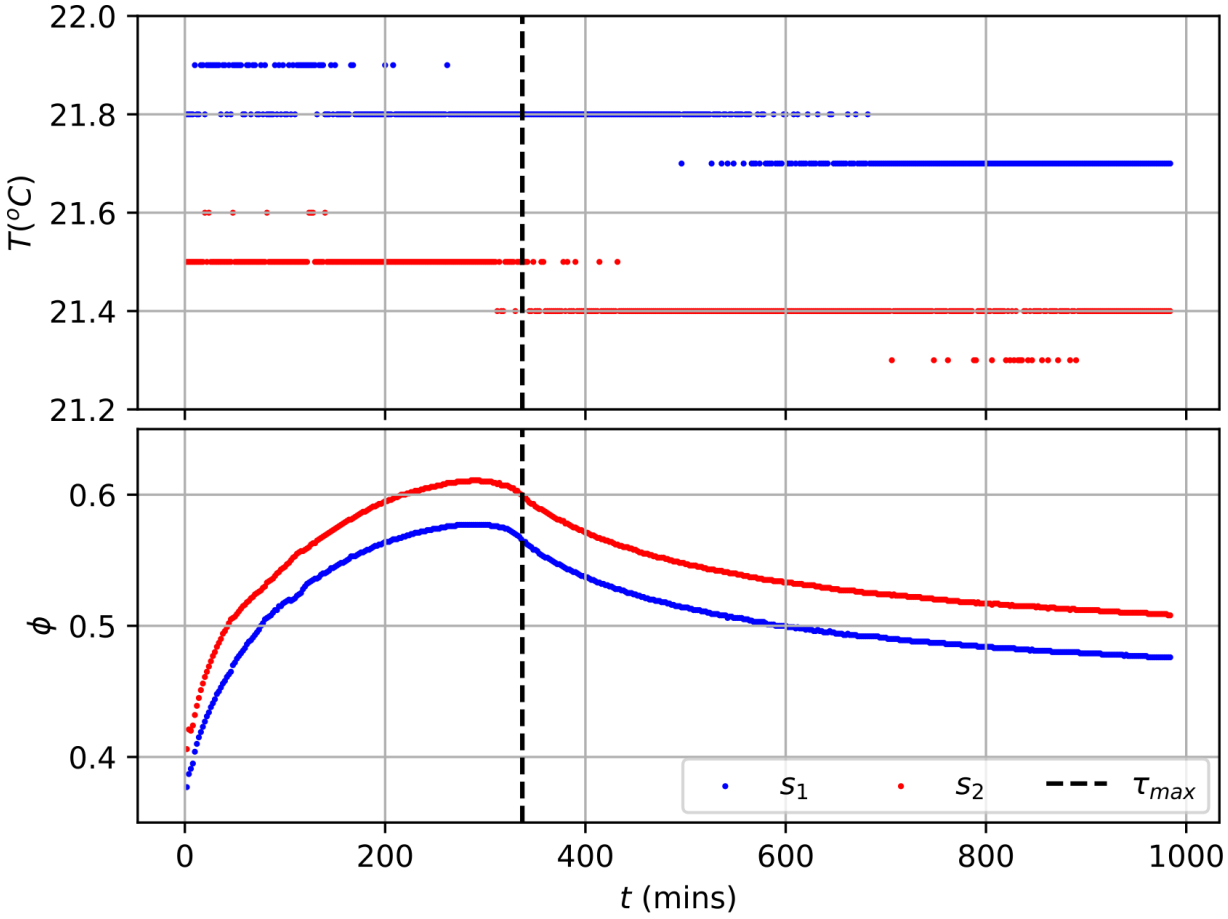

Figure 4.13: ϕ (bottom panel) and T (top panel) as measured by two sensors s_1 (blue series) and s_2 (red series) during evaporation. $t = 0$ is when the camera begins recording. The black dashed line (τ_{max}) represents the total evaporation time of the array.

discussed previously. Saturation of the container would however be expected to increase τ towards the centre of the array as these droplets would be evaporating into a higher ϕ. It would not be expected to cause the curved shape seen in fig. 4.8. To demonstrate the expected shape the value of ϕ can be calculated dynamically in the Masoud et al theory for the $N = 685$ droplet array, increasing the ambient humidity according to the amount of phase change in each timestep. To do this eq. 1.15 is used to calculate p_{sat} and is substituted into eq. 1.14 to give

$$m_{sat} = \frac{p_{sat} V_{box} M_w}{R_g T}. \tag{4.11}$$

This calculates the mass of vapour required to saturate the volume of the enclosure ($V_{box} = 0.174\,\mathrm{m}^3$) into which the droplets evaporated. The ratio of the mass of vapour evaporated in each timestep Δm_{evap} to m_{sat} gives the incremental increase in fractional humidity to be

$$\Delta\phi = \frac{\Delta m_{evap}}{m_{sat}} = \Delta m_{evap} \frac{R_g T}{p_{sat} V_{box} M_w}. \tag{4.12}$$

With an initial $\phi(t = 0) = 0.25$ the concentration rises steadily to $\phi(t = t_{max}) \approx 0.75$. This represents a greater increase that seen experimentally which is expected as the dynamic humidity is modelled assuming the box is completely sealed. Regardless, the resulting τ (red data) can be seen to diverge from the (black) experimental data in fig. 4.14. The constant humidity (blue) data provides a better agreement as the dynamic humidity extends the lifetime of the droplets in the centre of the array. This straightens the dependence of τ on r_c and therefore cannot explain the curving observed in the experimental data.

4.1.7 Droplet volume variations

Another consideration which might explain the curved shape of the experimental curves is the variation in droplet volume due to the increased printing times. As mentioned, droplets are printed from centre to edge such that the droplets which are on the substrate for the longest during printing, are the ones which are most confined. Because these droplets have the slowest evaporation, this minimises their reduction in volume. In the Masoud et al theory the droplets are assumed to have the same volume ($V = 2.09\mu L$) at $t = 0$. If centre droplets are larger at the edge, their lifetimes would be expected to be longer compared with the monodisperse Masoud et al predictions. This is a feature of the

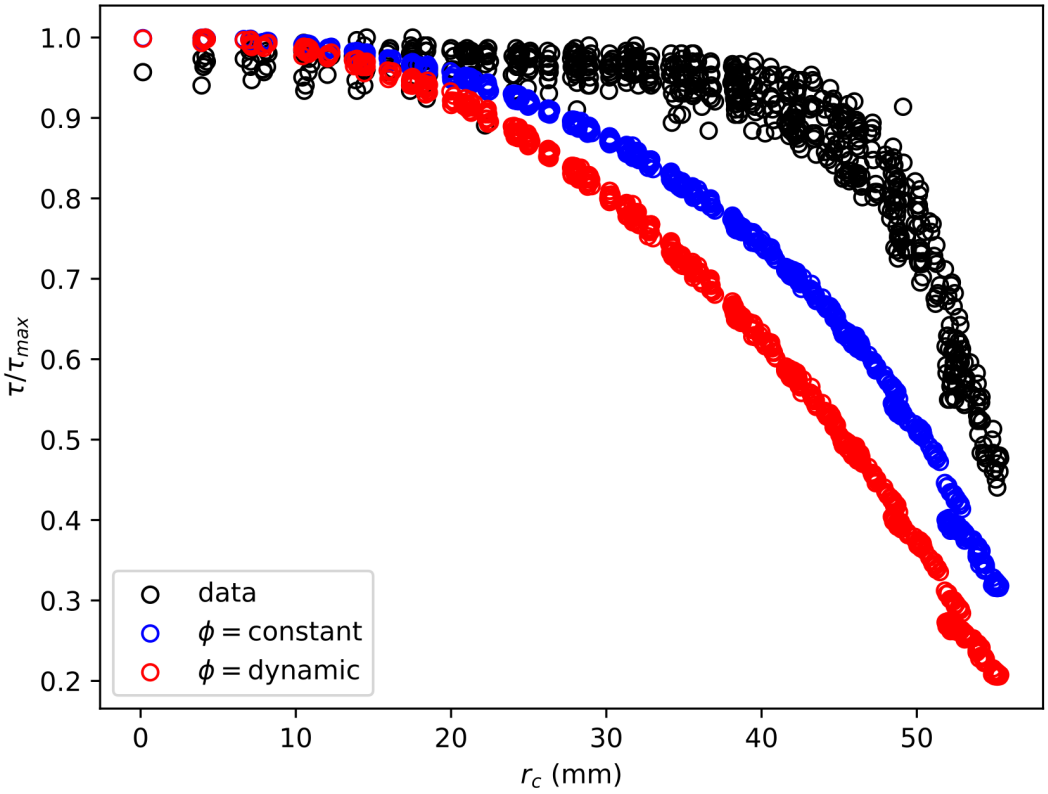

Figure 4.14: The influence of ambient ϕ on the radial dependence of τ/τ_{max}. The black data points show the experimental. The blue and red data plot τ/τ_{max} for a constant ϕ and dynamic ϕ respectively.

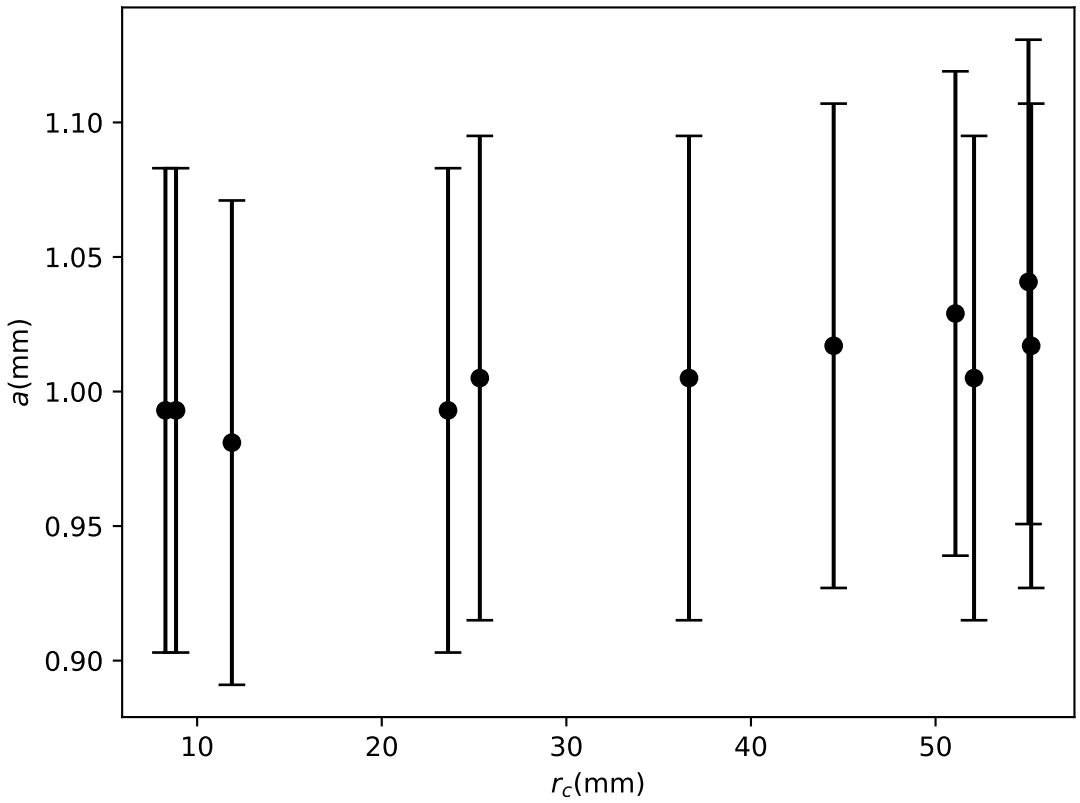

Figure 4.15: Measured base radius (a) of a random selection of droplets at different radial distances from the centre of the array (r_c), for the largest array in table. 4.1. The errorbars represent the uncertainty in determination of the contact line, due to the resolution limits of the camera.

larger arrays (middle and lower panel) of fig. 4.8. To quantify the affect of this, droplets are measured manually from the first frame, for a series of droplets at difference radial positions from the centre, for the largest array in fig. 4.8 ($R = 55\,\text{mm}$). Fig. 4.15 plots these measurements with the data points demonstrating the best subjective measurement of a. The errorbars represent the uncertainty due to the resolution limits of the camera. Despite the errors being too large to statistically prove there is a gradient in the droplet volumes, the data points suggest that droplets near the edge are larger than at the centre. The maximum difference in droplet radius between the centre and edge, accounting for measurement uncertainty is $\pm 0.1\,\text{mm}$. However in reality the discrepancy is likely less than this.

To determine the possible influence of this variation, the droplet size is varied linearly in the Masoud et al predictions between $0.9 \leq a \leq 1.1\,\text{mm}$ ($1.53 \leq V \leq 2.79\,\mu\text{L}$). The droplets at the edge being initialised with the largest radii and the smallest at the centre. The results of these predictions are plotted in fig. 4.16. By comparing this with the monodisperse comparison in the lower panel of fig. 4.8, it can be seen that although this

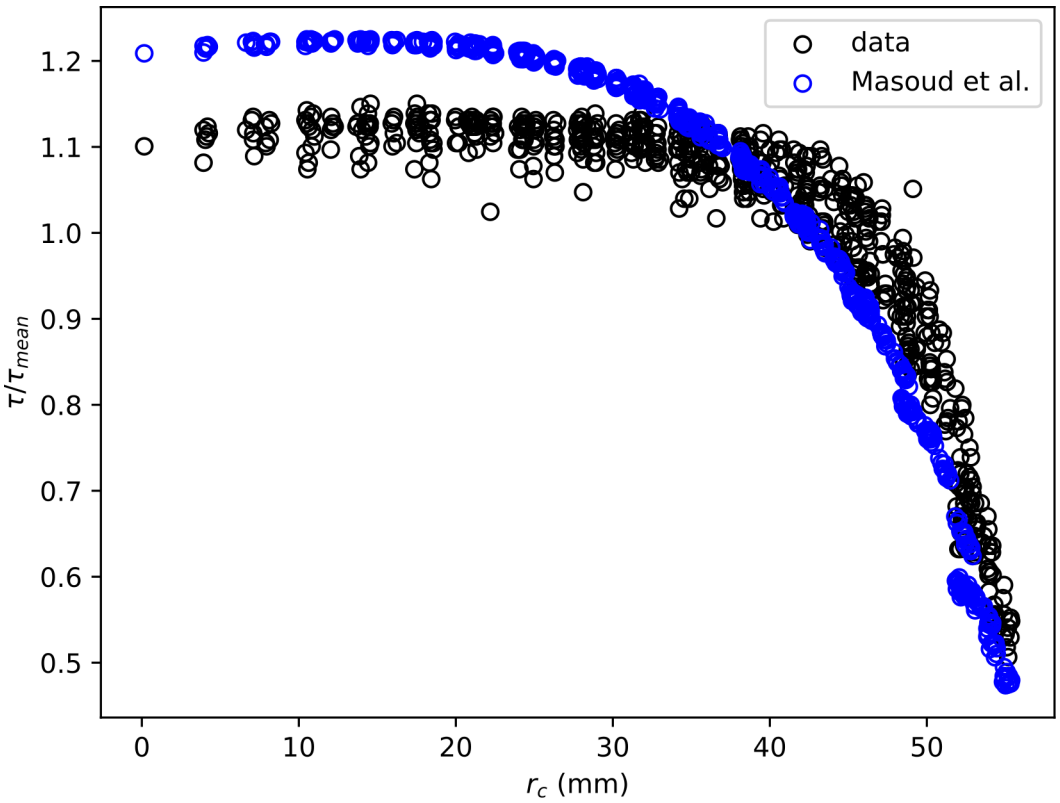

Figure 4.16: The lifetimes (τ/τ_{mean}) of the droplets against their radial positions (r_c). For the experimental (black series) and Masoud et al predictions, accounting for variations in droplet volume.

improves the agreement it is not enough to explain the amount of curving observed. In conclusion variations in droplet volume due to the extended printing times of large arrays are not enough to explain the non-diffusive evaporation observed in section 4.1.5.

4.2 Heated substrates

In this section the evaporation of multiple droplets is studied on heated substrates. It is shown that the dynamics and evaporation again diverges from the diffusive predictions. The evaporation is found to be very sensitive to small temperature differences across the substrate. Other mechanisms are considered for their possible influence on the evaporation including, the presence of thermally driven convection and phase-change limited evaporation.

4.2.1 Methods

To investigate the influence of the substrate temperature on the evaporation of multiple droplets, $N = 469$ droplets of $V = 2.74 \pm 0.02\,\mu$L were dispensed into a hexagonal (13 droplet sided) array with $s = 3.5\,$mm (these values were unchanged for all experiments presented in this section). The substrate was a polished N-type $< 100 >$ silicon (Si) wafer with a radius of 50 mm and thickness of $5 \pm 0.1\,$mm. The equilibrium contact angle is found to be $\theta \approx \pi/2$ radians and the droplets evaporate in a CA mode. The substrate was cleaned before each experiment firstly by wiping with ethanol and then drying with an air gun. Each array was dispensed as described in section 3.3 taking approximately 7 minutes. After dispensing, the silicon wafer and droplets are placed onto an IKA RCT basic hotplate located inside the setup described in section 4.1 and recorded in the same way. The hotplate was preheated to different temperatures prior to placing the droplets on top and has a maximum quoted uncertainty of ± 5°C at 100°C. The Si wafer, initially at room temperature, quickly heats up due to thermal conduction through its contact with the hotplate.

4.2.2 Results and Discussion

The evaporation of the array appeared to be non-circular and therefore non-diffusive. These effects were amplified as T_s was increased. Fig. 4.17 shows a montage of three experiments at different T_s as they evaporate in time. In all cases the outline of the array becomes irregularly shaped, with this irregularity increasing for larger T_s. The diffusive models (as discussed in section 4.1, see fig. 4.2) predicts the hexagonal array will transition to having a circular outline and therefore indicates the presence of other non-diffusive effects. It was observed that experiments at $T_s > 40$°C resulted in condensation forming at the top of the box directly above the array. This condensation did not appear on the closer vertical sides of the box and therefore is not driven by enhanced diffusion, which would be equal in all directions. The presence of this condensation above the array indicates enhanced upward transport of warmer water saturated buoyant air due to thermally driven natural convection, coming into contact with the cooler roof of the box. This condensation obscured the camera's view of the droplets and the dynamics could not be recorded. To remedy this a thin layer of sunflower oil was spread directly under the lens of the camera on the inside roof of the box. This was found to successfully discourage

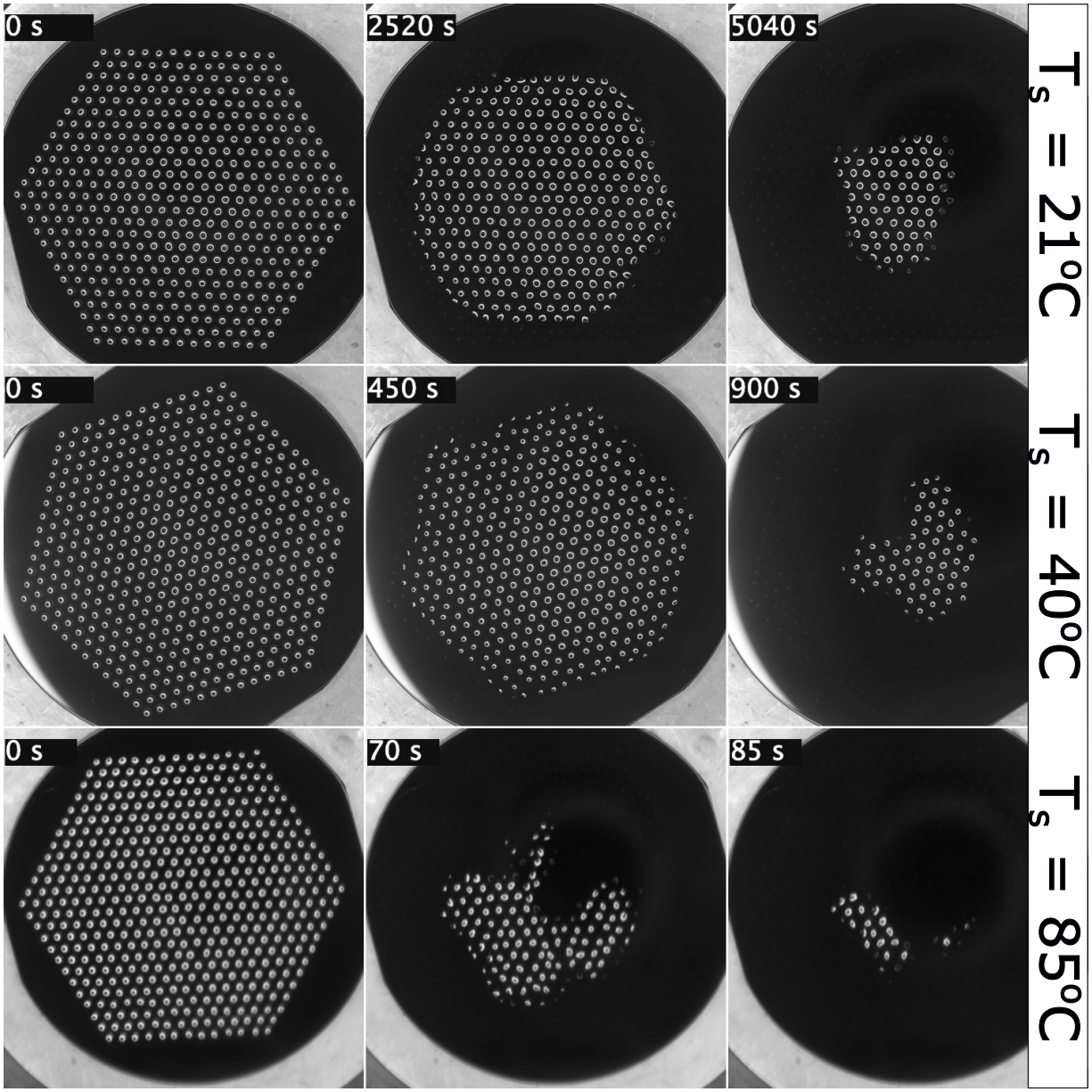

Figure 4.17: Evaporation dynamics montage for three different experiments at $T_s = 21$, 40 and 85°C. Time increases left to right and is indicated in the top left of each image.

condensation. The layer of oil is the reason for the blurring of the images in experiments at $T_s > 40°$C. Convection in the air could explain the irregular evaporation patterns observed as thermally buoyant plumes transport vapour away from certain regions.

One possible other consideration is the homogeneity of T_s over the substrate, which could induce faster local evaporation around hotter parts of the plate. Fig. 4.18 shows a montage of four separate experiments with $T_s = 75°C$ and $T_s = 85°$C at a similar amount of time into their evaporation. It can be seen that the irregular shape is formed repeatably across experiments, with small variations accounted for by the Si wafer and droplets not being placed in exactly the same position with respect to the hot-plate centre. The repeatability of these patterns indicate a consistent inhomogeneous temperature distribution across the hotplate. This could be caused by limitations of the hot-plate's temperature uniformity or internal impurities inside the silicon wafer leading to spatially varying thermal conductivity. This, in addition to natural convection could contribute to the observed irregular patterns, however this repeatability would be surprising in the case of convection. This is because the position of the convection cell is likely to be very sensitive to small perturbations. Despite this, some irregularity can be seen even when the hotplate is at $T_s = 21°$C (unplugged, room temperature) and as such convection cannot be excluded. Where $\mathrm{Ra}^* \approx 3568$ for this array and would be predicted to be non-diffusive by fig. 4.11.

To characterise the variation in temperature across the Si substrate a thermochromic liquid crystal (TLC) sheet (Edmund Optics PN:83-904) with a bandwidth of 35°C to 40°C, was adhered to the surface of the hotplate. The hotplate was place inside an acrylic box to avoid air currents causing temporal variations. The temperature was set on the hotplate to a value within the TLC bandwidth and left to reach an equilibrium. It was found experimentally that the hotplate needed to be set between 35 and 38 °C to completely span its colour spectrum. At each 1°C increment in this range the colour was imaged 5 times. The images were separated into their RGB components and the average intensity over the TLC sheet for each channel was calculated across the five images. The standard deviation was calculated for each image and then averaged to characterise the spatial variation in intensity over the SI wafer at each temperature. In order to establish a relationship between colour and temperature the RGB values were converted to a single Hue value [87]. Fig. 4.19 shows that the Hue value varies monotonically with temperature. The grey shaded region represents the maximum standard uncertainty in the Hue calculated by

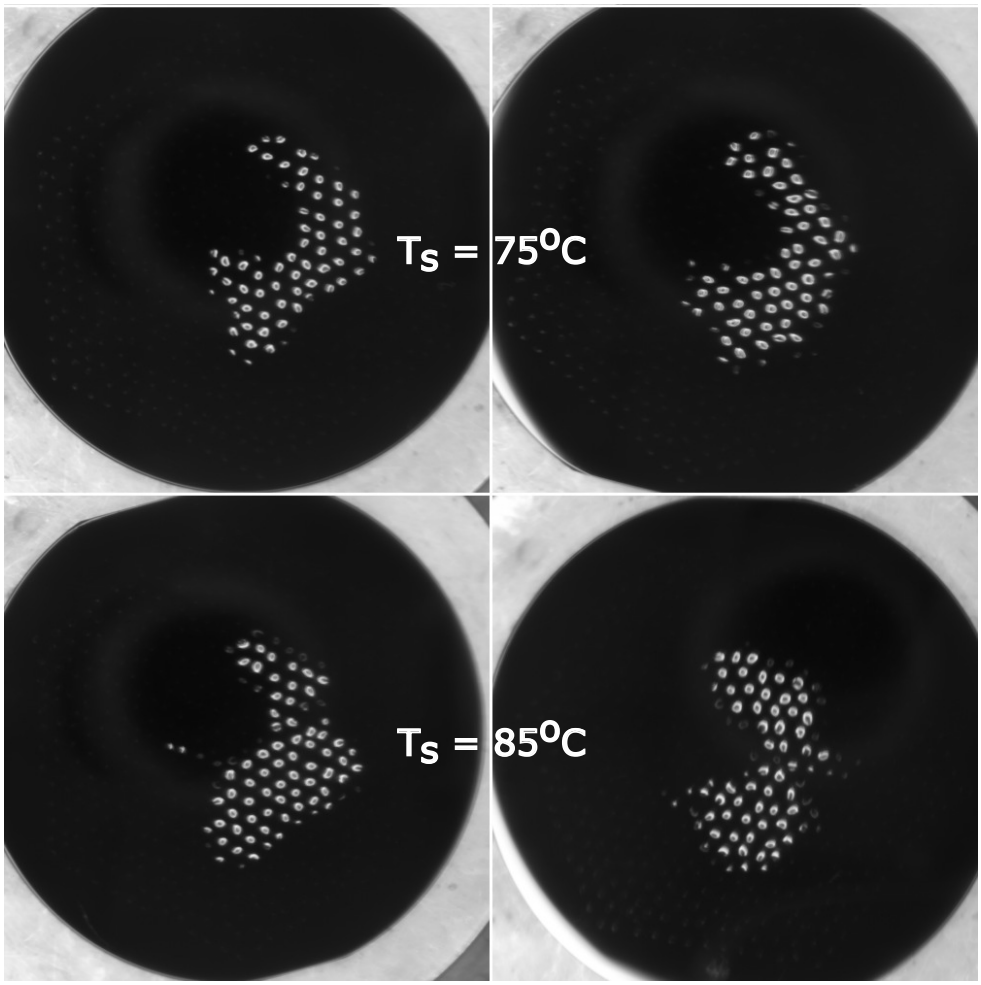

Figure 4.18: Four different experiments at different T_s showing similar and repeatable evaporation patterns.

varying the RGB values over their standard errors and taking the resulting maximum and minimum Hue values. The variation in Hue due to spatial differences across the imaged region is smaller than the difference between consecutive degrees. As a result the spatial difference across the hotplate and by extension the array can be considered to be <1°C. The impact of these small variations presented in fig. 4.17 reveals the sensitivity of the droplet evaporation to T_s and its spatial variation across the hotplate.

The sensitivity of global evaporation to these thermal effects can also be examined. The left panel fig. 4.20 plots τ_{max} for a number of experiments with different T_s. As expected τ_{max} reduces with T_s and becomes much less sensitive. The reason for this is that droplets are initially at T_{amb} and there is a period of time required for them to reach T_s. At elevated T_s it is possible that the transient heating time and τ_{max} is reaching a similar order of magnitude, which would explain the reducing sensitivity to T_s. Eventually it would be expected that the dependence would be completely flat once the droplets were no longer able to heat to T_s within their τ_{max}. If the droplets were initially at T_s the droplets would have greater sensitivity at higher values of T_s. Experimentally this is challenging as preheating the liquid will result in greater evaporation during dispensing and would require a controlled saturated humidity chamber enclosing the droplet dispenser. The temperature dependence predicted by the diffusion limited model over the same temperature range can be investigated. In this isothermal model $\frac{dV}{dt}$ only has temperature dependant properties of the surrounding gas namely c_∞ and D in eq. 1.18. These quantities are assumed to be isothermal in both time and space and therefore do not capture the experiments. Despite this, T_{amb} will be influenced by elevated values of T_s and experimentally so the comparison is nonetheless interesting. The theoretical τ_{max} over the same temperature range is plotted in the right panel of fig. 4.20. The exact values of τ_{max} are not comparable to those measured experimentally for the reason just mentioned, as well as the fact that the droplets were evaporating on a hotplate platform. Because of this τ_{max} would be expected to be shorter even if the temperatures in the gas were equal, as the theory assumes the droplets are evaporating on an infinite plane. The shape of the graphs however appears similar with both having a negative power law dependence. This kind of dependence is similar to that which has been observed in single droplets [88]. The biggest divergences appearing at the extreme temperatures.

Thermal convection in the vapour and larger values of c_{sat} and D in the air due to the elevated T_s will result in evaporated vapour being transported away from the droplet

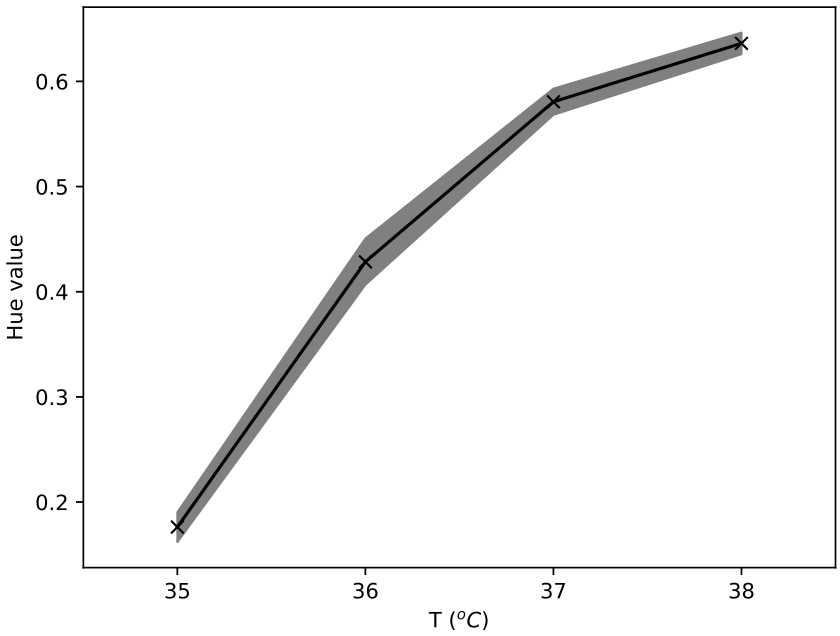

Figure 4.19: Hue value of a thermochromic sheet at different temperatures. The measurements are indicated by the crosses. The grey shaded region represents the maximum uncertainty in the repeated image RGB values.

interface much faster. At some point the rate mass transfer from the liquid will not be limited by the mass diffusion but by the rate of phase change at the interface. The latent heat supplied to the droplet's interface is controlled by its thermal conductivity (κ) which for water is $\kappa_w = 0.586\,W\,\mathrm{m}^{-1}\mathrm{K}^{-1}$ [32]. If the rate of mass transport in the vapour is greater than the rate at which heat can be supplied to the interface the diffusive models will no longer be applicable.

To determine the influence of non-diffusive effects, the ratio of the last to first droplet lifetimes (τ_{max}/τ_{min}) were compared against T_s in fig. 4.21.

For each experiment the system geometry and dispensed array were the same and therefore quasi-steady, purely diffusive, isothermal evaporation would predict no dependence of τ_{max}/τ_{min} on T. This is demonstrated by the blue series in fig. 4.21 which represents Masoud simulations of the same size array with varying ambient temperature, which doesn't depend on T. The same ratio is plotted against T_s for the experimental data (black series) and is found to decrease significantly.

As mentioned previously, changing T (temperature of the gas phase) in the isothermal model (in eq. 1.18) is not the same as experimentally varying T_s as the thermal conductivity

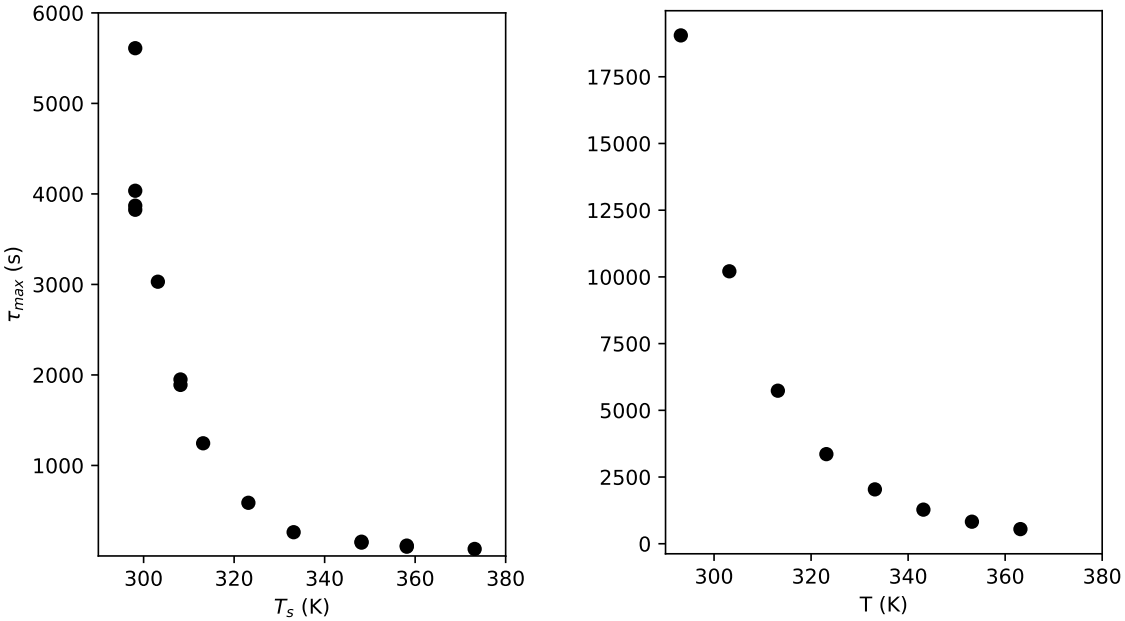

Figure 4.20: Maximum lifetime (τ_{max}) of droplets in array evaporating at different substrate temperatures, (T_s, left panel) and ambient temperatures, (T, right panel). The left panel is experimental data and the right is theoretical calculated according to eq. 1.18.

of air is $\kappa_{air} = 26.23 \times 10^{-3}\, W\, \mathrm{m}^{-1}\mathrm{K}^{-1}$ [30] is low, and will be lower than T_s due to heat loss. Measurements of T at the boundaries of the enclosure were only measured to be < 4K greater than the temperature in the surrounding room. This is why the ratio found for the theory does not intersect the black data points at room temperature, in addition to the platform geometry of the experimental data. Irrespective of this fig. 4.21 provides evidence of whether the isothermal models can still be applied to heated arrays.

One possible reason for the divergence could be that the assumption that the evaporation is quasi-steady. If the timescale for the vapour field to develop around the array becomes significant compared to that of the evaporation time the vapour is not correctly described by eq. 1.16 but by eq. 1.3. Maatar et al. [89] investigated this effect numerically for isolated droplets, finding that the quasi-steady assumption can break down for volatile droplets on substrates with low κ, observing a water droplet evaporating on 4mm thickness aluminium substrate had a transient period of 12% of the lifetime.

Despite this, the difference between their trends demonstrates that the diffusion models assumptions are no longer valid, the decreasing value of τ_{max}/τ_{min} indicates that the evaporation is beginning to have a reduced dependence on position. This would be ex-

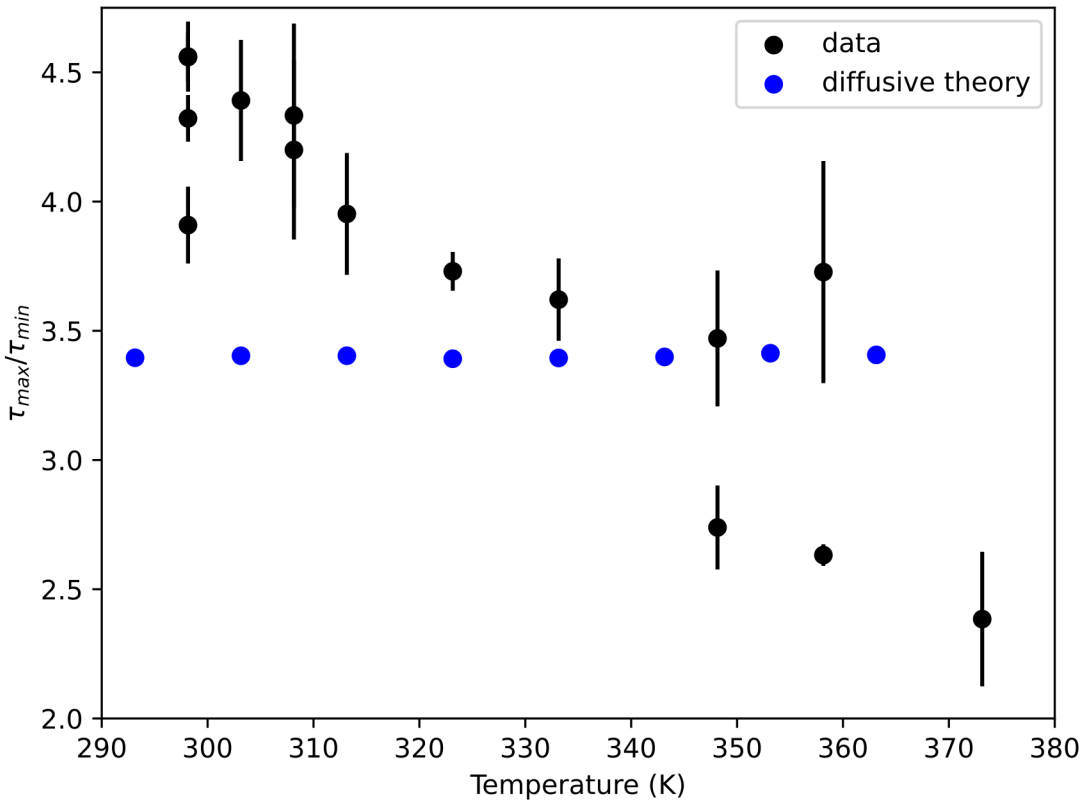

Figure 4.21: Ratio of longest (τ_{max}) to shortest (τ_{min}) droplet lifetimes at different experiments at different T_s (black) and theory at different ambient T (blue). There error bars uncertainty in evaporation times due to the framerate of the camera.

pected as evaporation transitions to being limited by phase change. If the flow of heat to each droplet was equal then the evaporation rate should not depend on position and $\tau_{max}/\tau_{min} = 1$. Experimentally it is likely that there would be a small radial dependence of the heat supplied, as the local heat produced by the hotplate is shared between fewer droplets at the edge of the array. Small perturbations in the evaporation rates of this kind would be amplified, as the timescale for heat conduction to the interface of smaller droplets would be less.

To summarise the divergences of the heated array experiments from standard diffusive theory could be caused by a number of things. Firstly, the droplet evaporated on the elevated platform of the hotplate and not the infinite plane modelled by the theory. Despite this, the ratio τ_{max}/τ_{min} would not be expected to vary with T as this quantity would be dependant solely on the geometry, which did not change. To explain the decrease in τ_{max}/τ_{min} it is expected that the evaporation is transitioning to a non-diffusion limited form of evaporation which may be caused by vapour being transported away from the interface at an accelerated rate. This transport is likely to be a combination of thermally driven convection and enhanced diffusion due to increases in D and c_∞. These effects would then lead to the evaporation being limited by the rate at which heat can be conducted to the droplet's interface to facilitate phase change.

4.3 Conclusions

In this chapter the limitations of the Masoud et al. model is demonstrated for large arrays and heated arrays of millimetre sized droplets. It is shown for large arrays that the evaporation becomes very sensitive to the surrounding environment, with boundaries and air currents leading to biases in the array evaporation. The theory was modified to account for these biases empirically leading to better agreement. It is also shown that larger denser arrays exhibit non-diffusive evaporation. Circular arrays provide the greatest sensitivity to this non-diffusivity and it is argued that natural convection is responsible for generating the local hot spot evaporation within the centre of the arrays. The convection is quantified by fitting to the evaporation lifetimes and a relationship between this parameter and the modified Gr number is shown.

The effect of heating the substrate of the droplet arrays is then investigated. By characterising the temperature across this substrate, multiple droplets are shown to be

very sensitive to small spatial variations. Heating substrates leads to the assumptions of the diffusive evaporation models breaking down. The evaporation can no longer be considered isothermal due to the sensitivity to variations in the substrate and because of the influence the hotplate has on the surrounding air. The order of droplet evaporation also indicates the onset of thermally driven convection meaning the surrounding air cannot be considered quiescent and isothermal. Evaporation also appears to become one-sided, as phase change is limited by heat transport to the droplets interface, rather than diffusion of the vapour around the droplets.

Chapter 5

Breath figures

Droplets are often so small that they cannot be seen without a microscope, for example in breath, clouds and fog. The size of these droplets make it possible for them to carried long distances within the air and transport viruses. The aim of this chapter is to determine whether droplets of micron size, such as those found condensing from breath, evaporate as predicted by diffusive models. Experiments are conducted on breath and the evaporation of the condensed droplets will be examined. It is shown that droplets within the array can grow whilst the whole array is evaporating and the inclusion of the Kelvin effect (described in section 1.7) is required to explain this. The influence of the composition of the breath is discussed and it is shown that the growing also occurs in pure DI water. A simple mean field model is then developed and compared to the data showing excellent qualitative and quantitative agreement. Finally, the applicability of the mean field model is discussed and the length scale over which it is valid is determined.

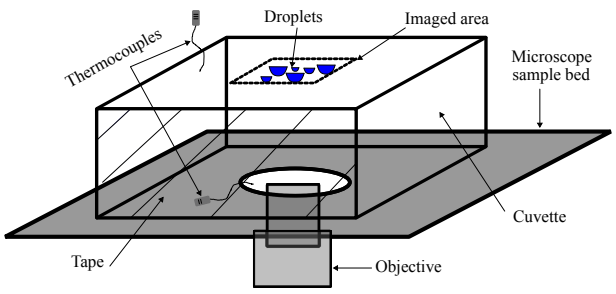

Figure 5.1: Diagram of the experimental setup used to capture the evaporation of confined breath figures.

5.1 Methods

In order to dispense the droplets a container is breathed into from about 5 cm from the opening and the exhaled air causes drop-wise condensation onto the internal walls. The container is chosen to be an optical glass Hellma cuvette container with dimensions 50.13 × 47.52 × 10.17mm (W×H×D) and is subsequently sealed with Scotch tape (see fig. 5.1). The confinement of the container is found to reduce the evaporation rate such that the droplets can be imaged before they have evaporated. The equilibrium contact angle of pure water droplets on the surface of the glass cuvette was found to be $\theta = 1.73 \pm 0.01$. The cuvette was handled through multiple layers of tissue and latex gloves to avoid transferring heat to the walls of the container. The droplets are imaged under an optical microscope (Olympus IX81) with ×10 magnifying lens and a metal lens cage is placed on top of the cuvette to hold it firmly in place. The microscope is focused on the inner top surface and images an 0.61×0.49 mm area of the pendant droplets are taken every 4 seconds, as they evaporate. It was chosen to focus the microscope on the pendant droplets as this side of the cuvette was not in contact with the metal microscope bed. This meant it was the warmest face (measurements in section 5.2.1) and therefore where condensation would be maximally inhibited. The temperature of the upper and lower walls of the cuvette are also measured periodically with two K-type thermocouples. To track the radius of each droplet as a function of time the python script 'DropletTracker' was used. A description of the code is given in Appendix A. It is possible that the droplets arrays are dense enough for coalescence to occur during recording. For simplicity, the imaged region is chosen such that the droplets far enough apart to avoid this.

5.2 Results and Discussion

5.2.1 Evaporation of breath

A selection of images taken of the evaporation are presented in fig. 5.2 and show the number of droplets decreasing over time. The experiment was conducted at an ambient humidity of 57.6±5% and temperature of 25±2°C. The temperatures of the thermocouples during evaporation show the top surface (in contact with the imaged droplets) remains at a constant temperature of 24.3 ± 0.1°C, whilst the bottom surface cools linearly from 24.2°C to 23.7°C during evaporation. The micron size droplets are polydisperse and are

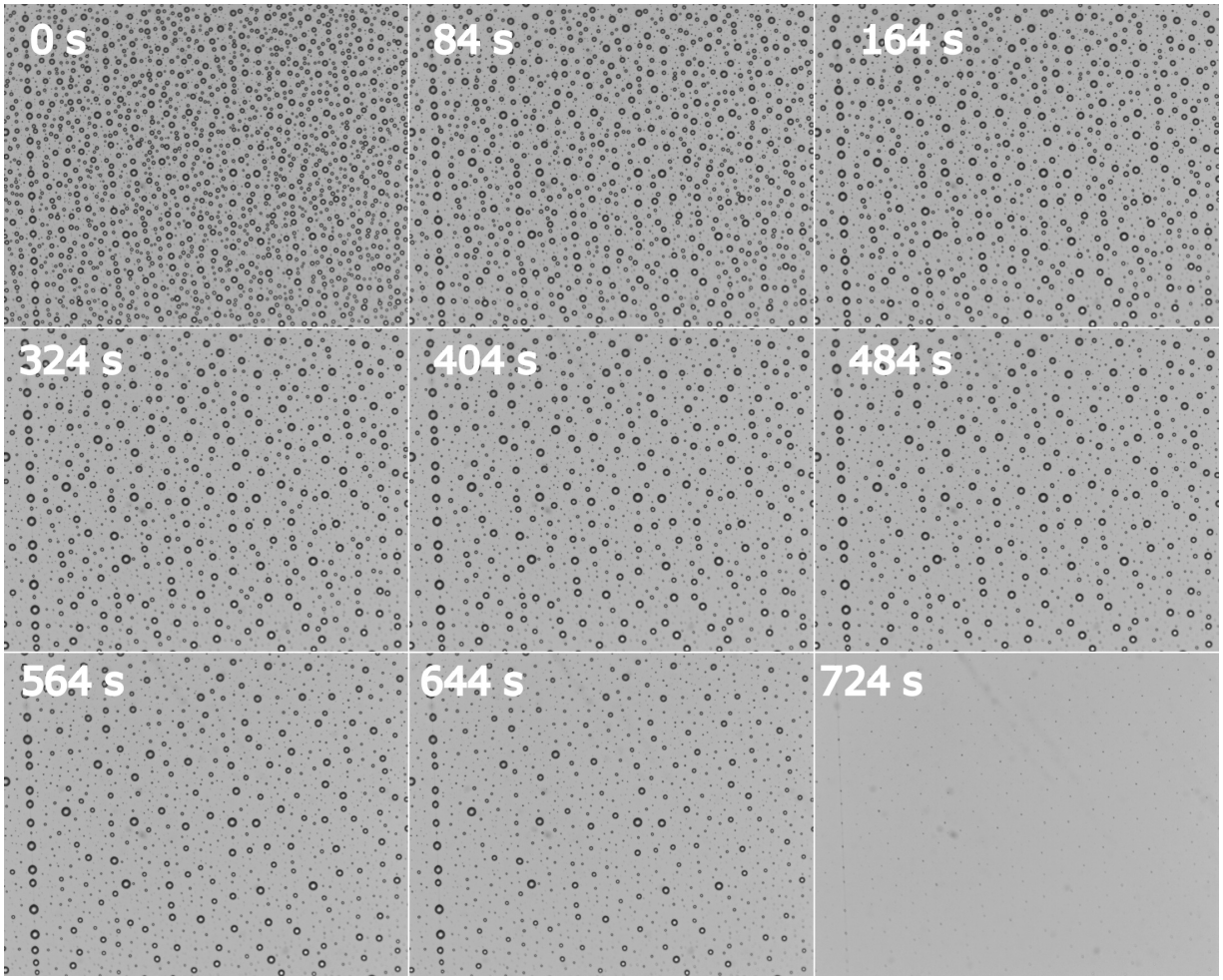

Figure 5.2: Experimental breath figure montage showing their evaporation. Each frame is $0.61 \times 0.49\,\mathrm{mm}$.

relatively evenly distributed within the imaged region. The location in which the droplets condense onto the substrate is controlled by impurities and defects on the surface which act as nucleation sites for the droplets [37]. This is shown in the left of the images as droplets are aligned along a scratch/crack on the substrate, which likely has residual impurities trapped within it.

Fig. 5.3 shows an enlarged region of fig. 5.2. In the image it can be seen that some droplets grow (see red arrow indicating an example) whilst others shrink. By tracking the radius of each droplet (with 'DropletTracker') in fig. 5.4 it can be seen that larger droplets grow and smaller droplets shrink.

The temporal evolution of each droplet's radius is plotted in fig. 5.4 for the 1411 droplets detected initially. The graph clearly shows the larger droplets ($\gtrapprox 4\,\mu\mathrm{m}$) growing whilst the smaller droplets shrink ($\lessapprox 4\,\mu\mathrm{m}$). The radius of the largest droplet increases

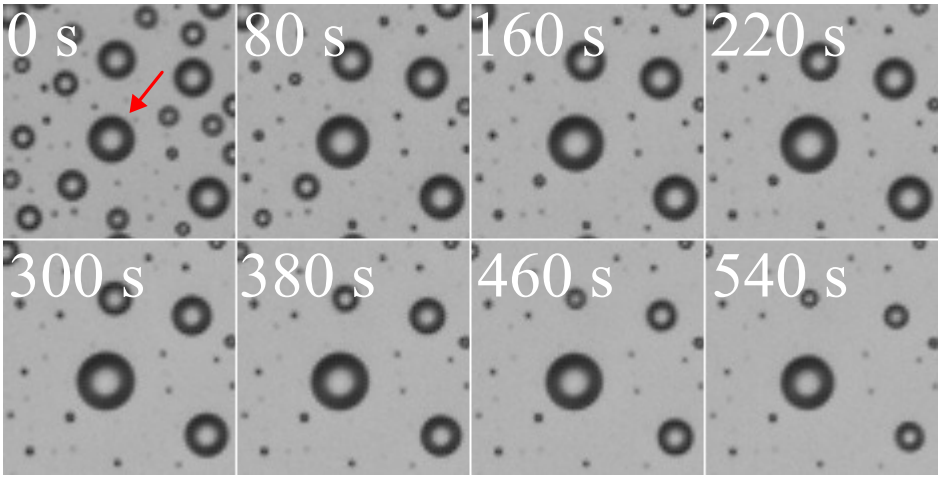

Figure 5.3: Enlarged region ($60 \times 60\,\mu$m) of fig. 5.2 showing a droplet, indicated by the red arrow, growing initially before subsequently shrinking.

by about 17% in 400s.

5.2.2 Evaporation of artificial breath

The growth of droplets is surprising and is not predicted by the implementation of the theory in the thesis to this point. The mechanism responsible for this growth will be investigated in this chapter. It was also considered that the growth might be a phenomenon which is purely a result of the composition of the breath, potentially including components with hygroscopic properties. Other authors have observed saturated salt solutions acting as humidity sinks [90]. To check this possibility, the experiments were repeated with micron-sized droplets of pure water by using a pressure controller to pump air through a chamber of saturated air. This saturated air was directed with plastic tubing to a Petri dish placed underneath a microscope, which was used to observe the droplets. It was found that droplets condensed onto the Petri dish and an artificial breath figure was formed. The resulting evaporation of a $90 \times 90\,\mu$m region is shown in fig. 5.5. It can be seen that the largest droplet grows from $r(t = 0) \approx 14\,\mu$m (indicated by the white lines) to $r(t = 278\text{ s}) \approx 15\,\mu$m. The redistribution of droplet volumes is therefore not due to dissolved components in the breath.

5.2.3 Significance of the Kelvin effect

The mechanisms of this growth could still be diffusive but could require the inclusion of the Kelvin effect. In previous use of eq. 1.18 it was assumed that the droplet's interface

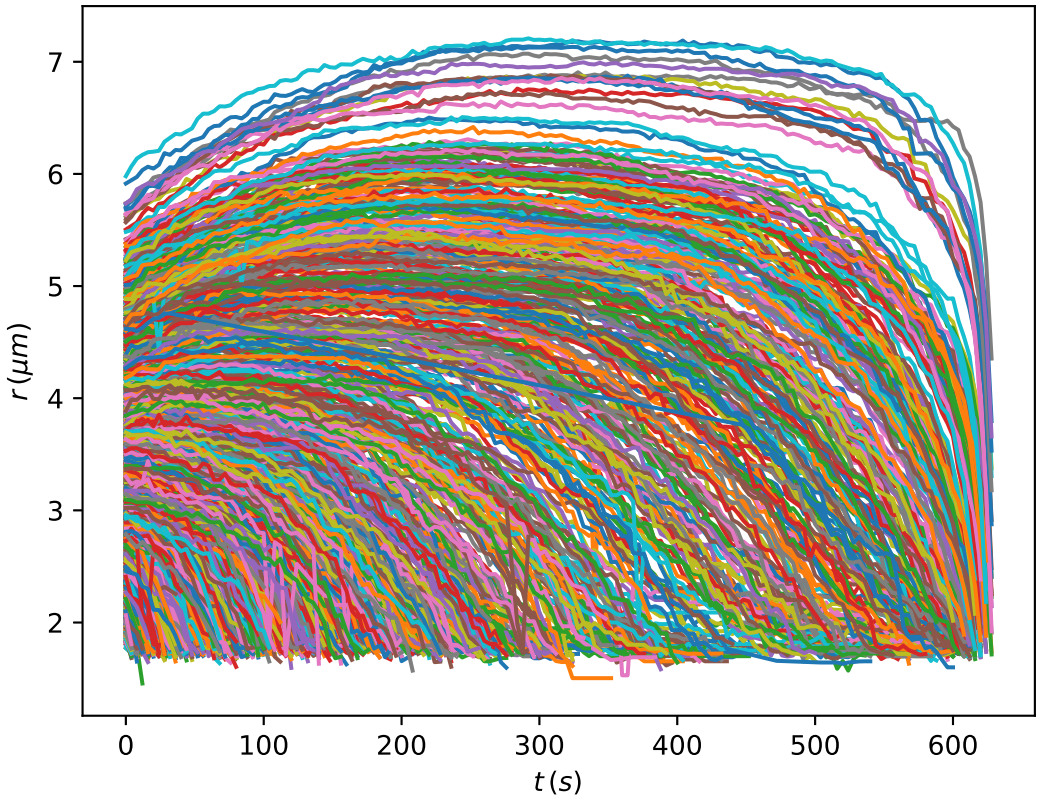

Figure 5.4: Temporal radius of curvature tracking of 1411 droplets in fig. 5.2. Before $t \leq 400\,\mathrm{s}$ the container is close to saturation and evaporation is dominated by neighbouring droplet interactions. After $t > 400\,\mathrm{s}$ the concentration drops rapidly due to the edge of the array moving through the FOV, and the evaporation is dominated by these edge dynamics.

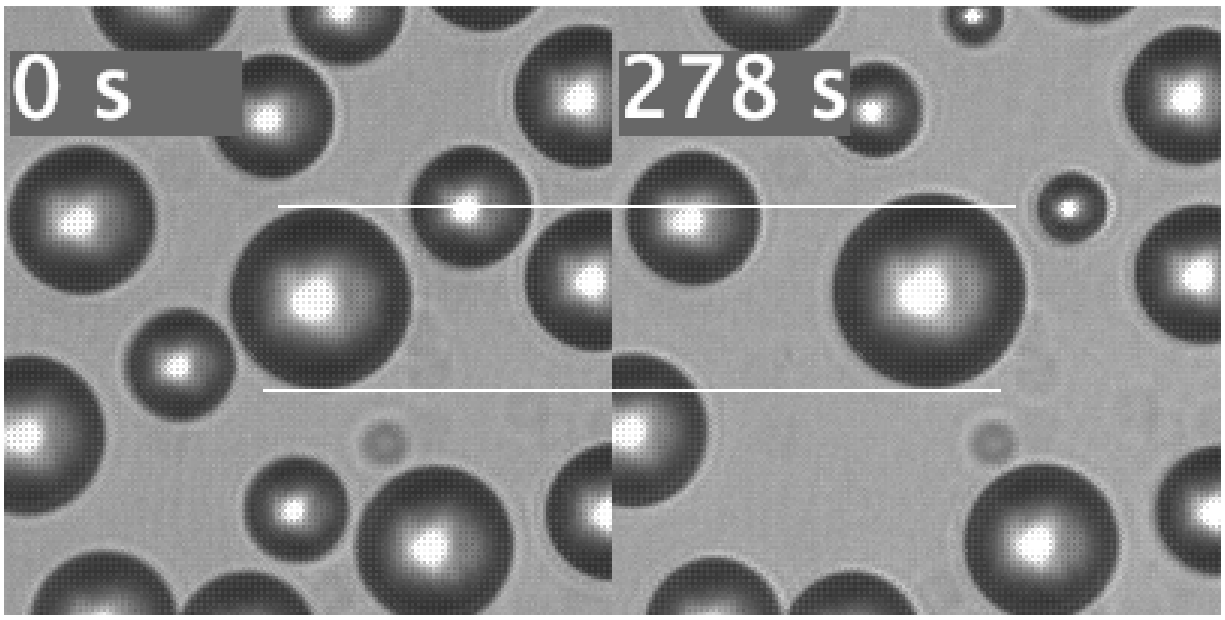

Figure 5.5: $90 \times 90\,\mu$m window showing the growth of a DI water droplet in an artificial breath figure. The white lines show how the initially $r = 14\,\mu$m droplet increases in size after 278 seconds.

is not curved enough for the vapour pressure to be elevated above that of a flat interface and $\phi_{sat} = 1$. At micrometre length scale, the curvature may be sufficient to increase the saturation concentration at the interface, with the smallest droplet having the largest ϕ_{sat} (an explanation of the Kelvin effect is given in section 1.7). These differences could generate concentration gradients between droplets driving condensation. Other authors have observed a similar effect in other multi-phase systems [91], for example gas bubbles inside liquids. The growth of the larger bubbles at the expense of the smaller is named Oswald Ripening. In the case of air bubbles in a liquid the mechanism driving diffusive transport of gas from small bubbles to larger is Laplace pressure. Here it is suggested that is is driven by vapour pressure. Some observations of Oswald ripening have also been observed between droplets in clouds [92], however the mechanism causing the smaller droplets to be less stable is not clearly discussed.

If the Kelvin effect is the mechanism for the growth then the volume of liquid from the neighbouring droplets should be enough to supply the required amount of liquid. Because 'droplet 0' had the lowest curvature it has the lowest value of ϕ_{sat}. As such there will be a concentration gradient towards the smaller droplet (1-4) and a diffusive flux towards 'droplet 0'. To check this, the amount of volume lost from the droplets labelled 1-4 in fig. 5.6 is calculated over a period of 180 seconds, which is the time for them to completely

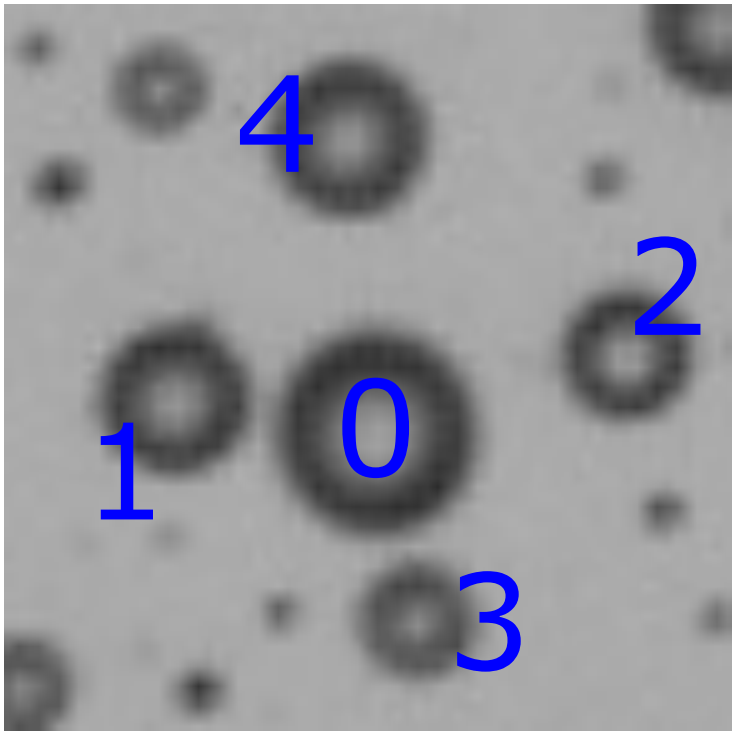

Figure 5.6: Enlarged $40 \times 40\,\mu$m region of fig. 5.2.

evaporate. The volume which 'droplet 0' grew by in this time was then calculated. Droplet 1-4 represented a total loss of $\approx 275\,\mu\text{m}^3$ and 'droplet 0' grew by $\approx 156\,\mu\text{m}^3$. Therefore the shrinking of immediate neighbours represented more than enough volume to account for the observed growth of 'droplet 0'.

Because of this the Kelvin effect could be responsible for the dynamics. Different saturation pressures on the droplet interfaces could be driving a diffusive flux into the larger droplet.

To determine the significance of these differences in pressure/concentration for breath droplets we can look at how much condensation would be driven by these concentration gradients between droplets of different sizes and if this could account for the amount of growth observed. For simplicity the fractional humidity ϕ will be considered a spatially averaged value inside the container. This value will be controlled by the history of droplet evaporation/condensation which has taken place (evaporation increasing ϕ and condensation decreasing ϕ). The value of ϕ itself however influences the evaporation of the droplets in a polydisperse breath figure depending on how it compares to the saturation concentration (ϕ_{sat}) of each droplet. By considering the largest (r_{max}) and smallest (r_{min}) droplet radii in the array, the influence can be divided into three distinct regimes: Firstly, if $\phi < \phi_{sat}(r_{min})$ and $< \phi_{sat}(r_{max})$ then all droplets will be evaporating into the sub-saturated

environment. Conversely, if $\phi > \phi_{sat}(r_{max})$ and $> \phi_{sat}(r_{min})$ then all droplets will be condensing from the supersaturated environment. And finally, if $\phi_{sat}(r_{max}) < \phi < \phi_{sat}(r_{min})$ the droplets will be in a hybrid state, some condensing and some evaporating depending on their size. If the ratio of the amount of liquid to the size of container is large enough then ϕ will be in fact controlled by the droplet dynamics in the container. Inevitably the droplets will bring ϕ to the hybrid state and will depend on the specific size distribution of droplets within the container.

The Kelvin equation [42] (described in section 1.7) can be used to relate the saturation fraction to r as

$$\phi_{sat} = e^{\frac{r_k}{r}} \tag{5.1}$$

and can be substituted into eq. 1.18, giving

$$\rho_l \frac{dV_T}{dt} = a\pi D c_\infty (e^{\frac{r_k}{r}} - \phi) f(\theta). \tag{5.2}$$

The value of $\frac{dV}{dt}$ is calculated and plotted in fig. 5.7 for a range of radii of curvature in different sub-saturated ($\phi < 1$) and super-saturated ($\phi > 1$) ambient environments accounting for the Kelvin effect (solid lines). To demonstrate the requirement of including the Kelvin effect for the prediction of hybrid dynamics (eq. 5.1), $\frac{dV}{dt}$ is also calculated for the original $\phi_{sat} = 1$ (dashed lines). For simplicity $\theta = \pi/2$ radians so that $a = r$ and the evaporation is assumed to be CA, so this is always true. Additionally, the liquid is assumed to be water. It can be seen that without the inclusion of the Kelvin effect (dashed) the sign of $\frac{dV}{dt}$ for a single ambient ϕ is either positive for all possible radii (for $\phi > 1$), all negative (for $\phi < 1$) or all zero (for $\phi = 1$). This is clearly insufficient to explain the dynamics seen in fig. 5.2 and 5.4. With the Kelvin effect (solid lines), $\frac{dV}{dt}$ can have positive and negative sign, giving rise to the possibility of source sink dynamics for polydisperse arrays with ϕ_{sat} distributed across this range. In reality the ϕ is a function of space and the concentration gradients will vary between droplets. It is helpful to define a critical droplet radius

$$r^* = r|_{\dot{V}=0} \tag{5.3}$$

which has unchanging volume ($\dot{V} = 0$) (in equilibrium), indicated by where the lines in fig. 5.7 intersect with the x-axis. Above r^* droplets grow (condense) and below droplets shrink (evaporate). r^* is larger when ϕ is lower and smaller when ϕ is higher. In order

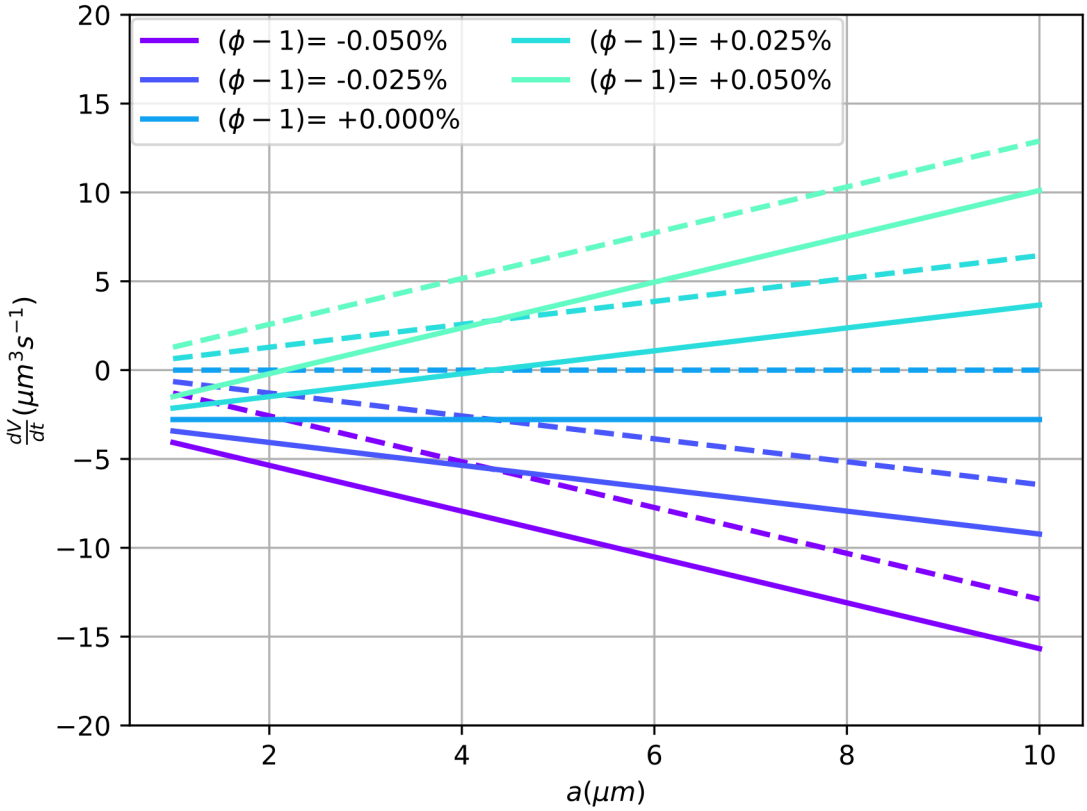

Figure 5.7: Evaporation rates of different radius droplets in different ambient environments (different series), with $\phi_{sat} = 1$ (dashed lines) and ϕ_{sat} set by eq. 5.1 in eq. 5.2 (solid lines).

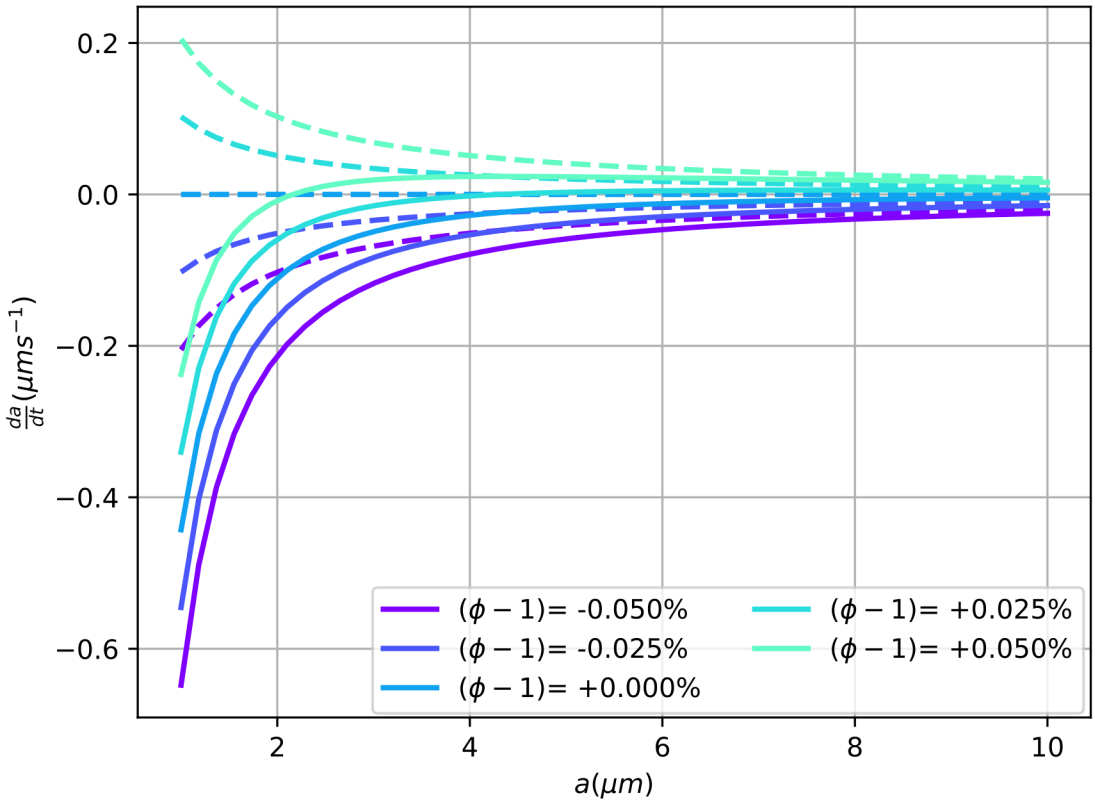

Figure 5.8: Radius of curvature velocity of droplets in different ambient environments (different series), with $\phi_{sat} = 1$ (dashed lines) and ϕ_{sat} set by eq. 5.1 in eq. 5.2 (solid lines).

to better understand the magnitude of these growth rates in relation to the droplet's size fig. 5.7 can be re-plotted to show the contact line velocity $\frac{da}{dt}$ in fig. 5.8. $\frac{da}{dt}$ captures the influence of V on the measured motion of the contact line. Because $V \propto r^3$ a constant condensation rate will result in a reducing contact line velocity as more condensation is required to increase a by the same amount. For this reason it is not expected that droplets with $a \gg 1\mu m$ will experience any significant growth. Indeed no growth is observed in the large droplet experiments presented in chapter 4 section 4.1 which although initially are monodisperse become polydisperse with neighbouring droplets having different radii of curvature. Nor is any growth observed in the large polydisperse droplets in section 3.3.

5.2.4 Mean field modelling of breath evaporation

In order to calculate the collective dynamics for droplet arrays like fig. 5.2 one could take a similar approach to previous chapters by making use of the work of Masoud et al. However this is difficult for breath figures for several reasons. Firstly for these large

numbers of droplets, the interaction matrix (defined previously in eq. 1.26) is 1411×1411 ($\approx 10^6$ elements) and must be inverted at each timestep, which is computationally difficult. Secondly, the droplets in fig. 5.2 only represent a small region of the array and N is much larger than the total visible droplets. Inputting their radii and positions as in previous chapter would assume these droplets were alone, resulting in an artificial edge effect. Initially, a simpler mean field approach is taken. Models of this kind are successfully applied in fields such as magnetism [93]. The model assumes that the region observed is representative of similar surrounding regions on each side and that the edges of the FOV can be considered to have periodic boundary conditions. It also assumes that the interactions between droplets can be replaced by interactions with a single mean field. In this case the mean field is assumed to be the fractional humidity around the droplets and this spatially varying quantity is replaced by a single value. Given that initially droplets are observed growing and shrinking simultaneously, ϕ must lie within the hybrid state described previously. The mean field assumption is that in this hybrid state the droplets do not interact with each other but with the mean field (the growing droplets reducing the mean field ϕ value and the small shrinking droplets increasing it). The net effect of these dynamics will vary ϕ and the droplets will evaporate interacting with this value.

To implement this mathematically eq. 5.2 is rewritten for the k^{th} droplet

$$\rho_l \left(\frac{dV}{dt} \right)_k = a_{\text{k}} \pi D c_\infty (e^{\frac{r_k}{r_{\text{k}}}} - \phi) f(\theta_{\text{k}}). \tag{5.4}$$

Here ϕ is considered the mean field ambient environment experienced by all droplets and the dynamics of any specific droplet will depend on the difference between the saturation concentration on its interface and this mean field value. This approach therefore decouples the specific neighbouring droplet interactions and is much less computationally expensive only requiring a single calculation for each droplet. Formally this value of ϕ comes from the boundary condition that at an infinite radial distance from the droplet's interface the concentration is at an ambient condition. Making ϕ a mean field value inside the container is like saying that the droplets are not evaporating in confinement but their evaporation can immediately effect the ambient environment everywhere, including at infinity.

The use of this diffusive isolated evaporation equation has also been successfully applied to condensation by Sokuler et al. [94] but without including the Kelvin effect.

As discussed previously the value of ϕ will be controlled by the specific distribution

of droplet radii within the container. It will therefore be a function of time ($\phi(t)$) as the distribution of droplets evolves. One way for this value to be time dependant is to make it a function of the distribution of droplet radii. To understand how this could be done, fig. 5.9 shows the temporal evolution of the droplet radii histogram for the redistribution period of the evaporation ($t \leq 400\,\mathrm{s}$). It can be seen that the distribution is initially maximum at $r \approx 3\mu\mathrm{m}$. Over time the smaller droplets evaporate with the larger droplets growing at their expense. At $t \approx 200\,\mathrm{s}$ a peak begins to form at $r \approx 5\,\mu\mathrm{m}$. A helpful way to consider ϕ's connection to the distribution is to think of its corresponding r^*. This critical radius of the droplets in equilibrium (not growing) would be expected to be somewhere in the centre of the distribution. One suitable guess for the dependence of r^* on the distribution it to assume it is the mean ($\bar{r}(t)$). The value of $\bar{r}(t)$ for each series in fig. 5.9 is indicated by the scatter points (of the same colour) under the histograms (at $N = 0$ purely for clarity). The points fall between the initial and final peaks and will therefore result in the desired volume redistribution. The corresponding ϕ for this r^* is $\phi_{sat}(r = r^*) = \phi^*$. Since droplets of this radius cannot be evaporating, $e^{r_k/r^*} - \phi^* = 0$ in eq. 5.4, therefore

$$\phi(t) = \phi^*(t) = \exp\left(\frac{r_k}{r^*}\right) \tag{5.5}$$

and $r^* = \bar{r}(t)$ from the distribution. After $t = 400\,\mathrm{s}$ the resulting histogram drops to zero very quickly for all r and everything completely evaporates. This is caused by the edge of the entire array moving through the camera's FOV. At this point the value of ϕ will no longer be controlled by the distribution and the droplets will be in a sub-saturated environment, all evaporating. Because of this, the edge regime and the redistribution regime will be considered as two separate timescales. The point at which the edge is considered to be dominating the dynamics is determined as the value of t when the largest droplet in the array stops growing and has $\frac{dV}{dt} = 0$. From fig. 5.4 this is at 400 s for this experiment. To test the use of $\bar{r}(t)$ as r^* and the mean field approach eq. 5.4 can be written in terms of the velocity of the radius of curvature by differentiating eq. 1.12 with respect to r and using the chain rule

$$\frac{dr}{dt} = \frac{a_k D c_\infty \left(e^{\frac{r_k}{r_\mathrm{k}}} - \phi(t)\right) f(\theta_\mathrm{k})}{\rho_l r_\mathrm{k}^3 (2 + \cos\theta_\mathrm{k})(1 - \cos\theta_\mathrm{k})^2}. \tag{5.6}$$

Then by using the radius tracking results from fig. 5.4 at $t = 0$ the initial r and positions

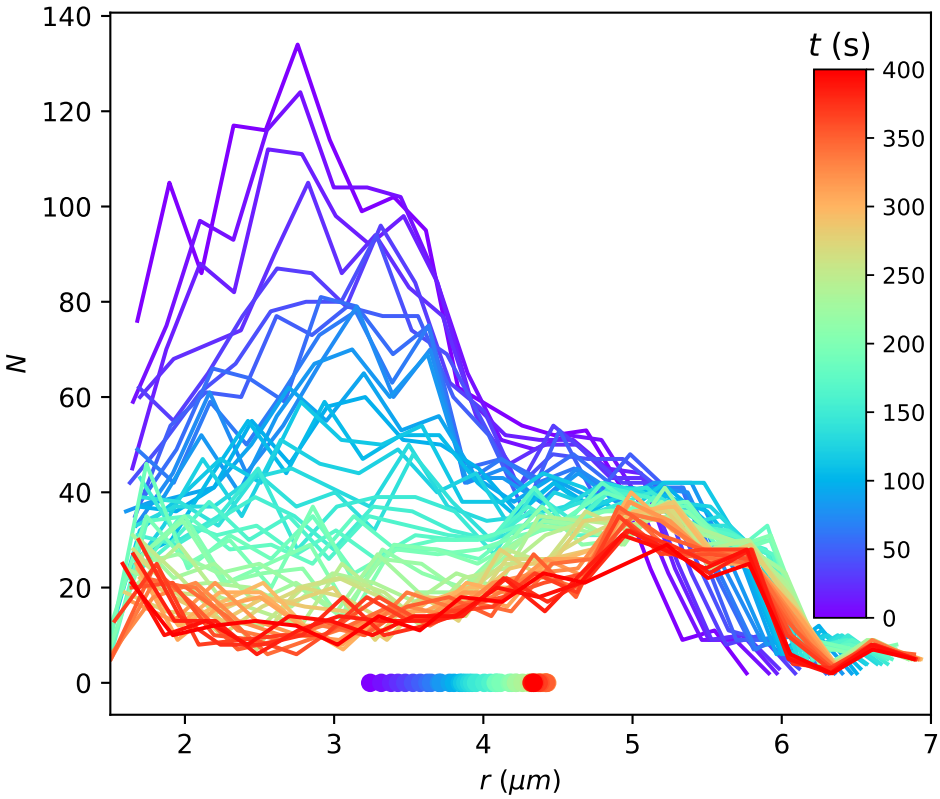

Figure 5.9: Radius of curvature histogram at different times (indicated by the colourbar) for the evaporation of the breath figure. The points represent the corresponding mean radius at each time.

$T\,(^{\circ}\mathrm{C})$	$D\,(\mathrm{m^2 s^{-1}})$	$c_\infty\,(\mathrm{kg\,m^{-3}})$	$M\,(\mathrm{kg\,mol^{-1}})$	$\gamma\,(\mathrm{mN m^{-1}})$	$\rho_l\,(\mathrm{kg\,m^{-3}})$
20	2.417×10^{-5}	0.0172	0.01802	72.75	997

Table 5.1: Constants for water used in eq. 5.6.

can be extracted. The r can then be simulated by advancing eq. 5.6 in time using the standard Euler method, providing mean field predictions for the dynamics. The accuracy of this method is checked by reducing the timestep until the solutions converge. The liquid constants in eq. 5.6 are assumed to be the same as water which is expected to be the main component which condenses on the substrate from the breath. These constants are listed in table 5.1.

The results of the mean field model can then be plotted over the experimental images to compare its ability to capture the redistribution dynamics. The droplet distribution initial condition is plotted over the first image in fig. 5.10. It can be seen that the circles in the image (determined with 'DropletTracker' detection code) align closely with those in the underlying image. As such the mean field theory is initialised within a very close approximation of the initial distribution captured in the image. Fig. 5.11 presents two experimental frames with predicted mean field circles (overlaid and aligned) indicating the size of the droplets after the same amount of time. The colours of the circles classified by the colourbar, indicates the instantaneous value of $\frac{dr}{dt}$. The agreement at 400 s is very good with the size and density of the remaining droplets in each frame looking qualitatively similar. It is worth noting that the small specs represent droplets with high concentrations of solute, which are not accounted for. The agreement begins to deviate $t > 400$ s and the theory overpredicts the size of the droplets at $t = 600$ s. This is because at $t = 400$ s the largest droplet reaches its maximum size (see fig. 5.4) and the edge of the array can be considered to be moving through with ϕ reducing below $\phi_{sat}(r_{max})$. During this time, its value will no longer be set by the droplet distribution but by the dynamics of the edge of the array. It is therefore expected that the agreement diverges after this point. To model the edge, the value of ϕ would have to decay down to the ambient value outside the container. $r^* = \bar{r}(t)$ will not do this and therefore would need to be modified.

To examine the overall quality of the theory's predictions the number of droplets are plotted against time in fig. 5.12, comparing the circle detection of the experiment and the mean field theory. The number of droplets against time is closely predicted indicating the choice of r^* as the mean of the droplet's radius distribution closely captures the temporal

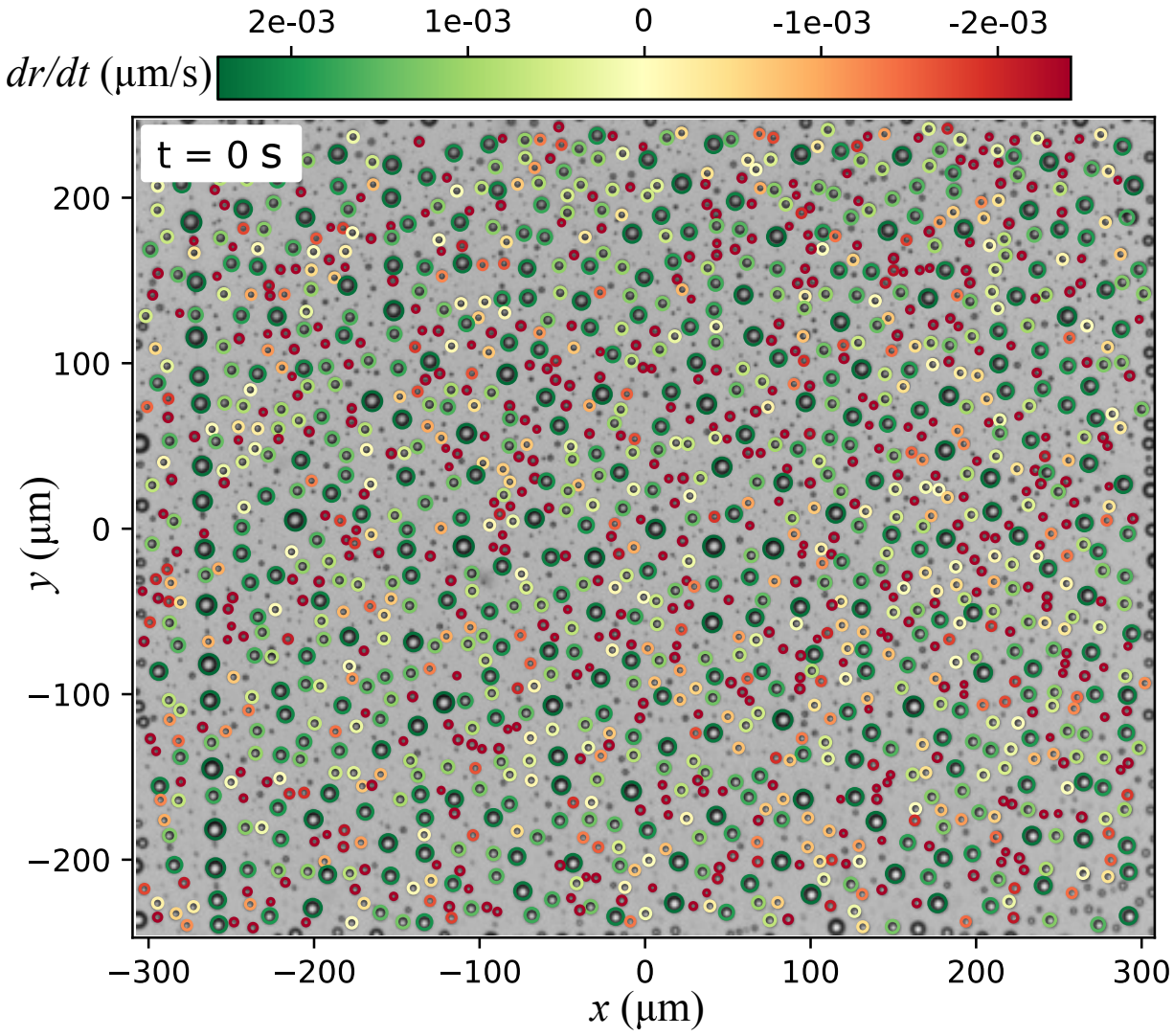

Figure 5.10: Initial droplet distribution of the mean field theory (circles) determined by the 'DropletTracker' detection code. $\frac{dr}{dt}$ of each droplet is indicated by the colourbar. The circles are overlaid and aligned on the first experimental frame.

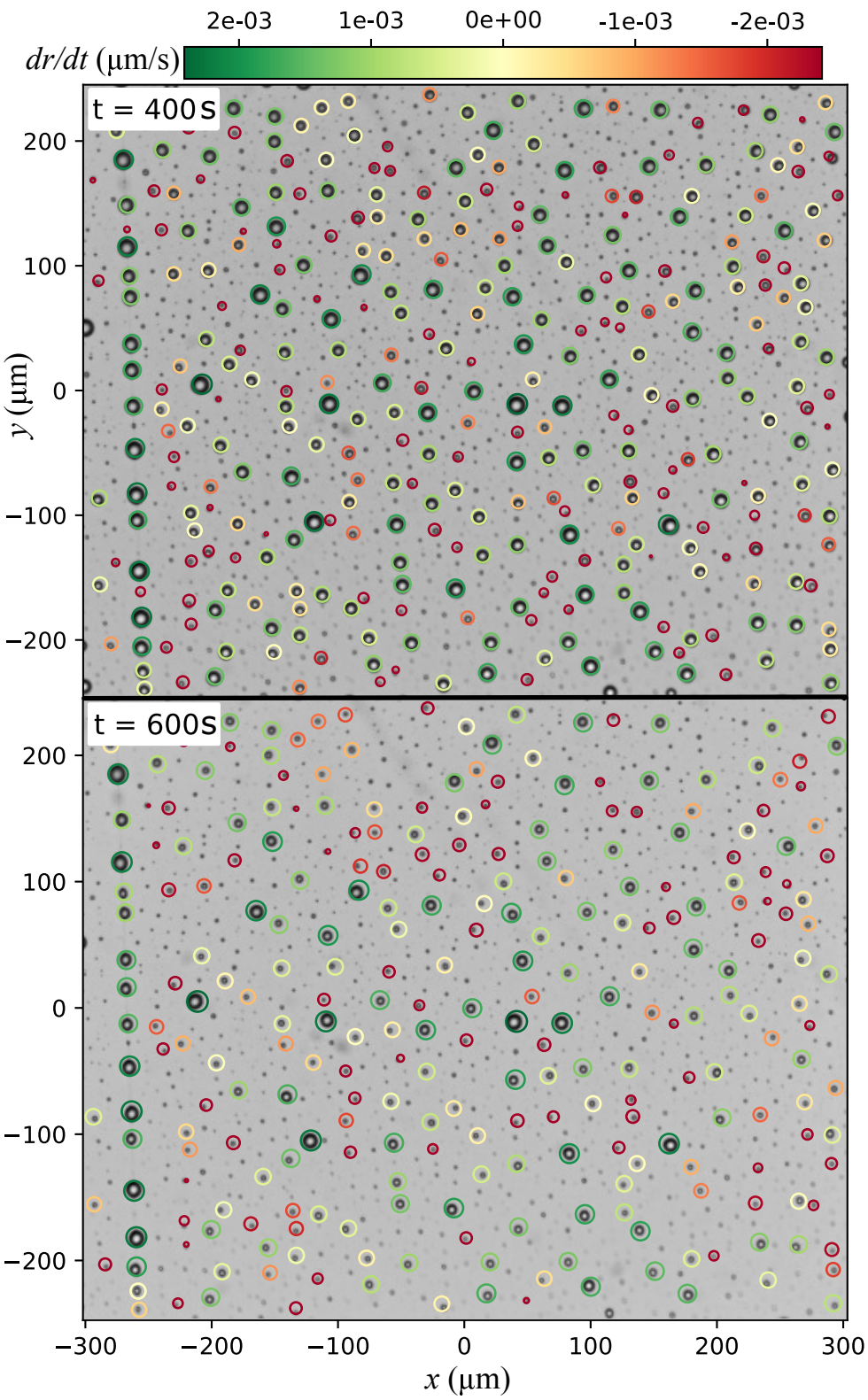

Figure 5.11: Mean field theory predictions (circles) with $r^* = \bar{r}$ at $T = 20°C$ with $\frac{dr}{dt}$ (μm/s) indicated by the colourbar. The circles are overlaid and aligned with the experimental images at 400 s and 600 s.

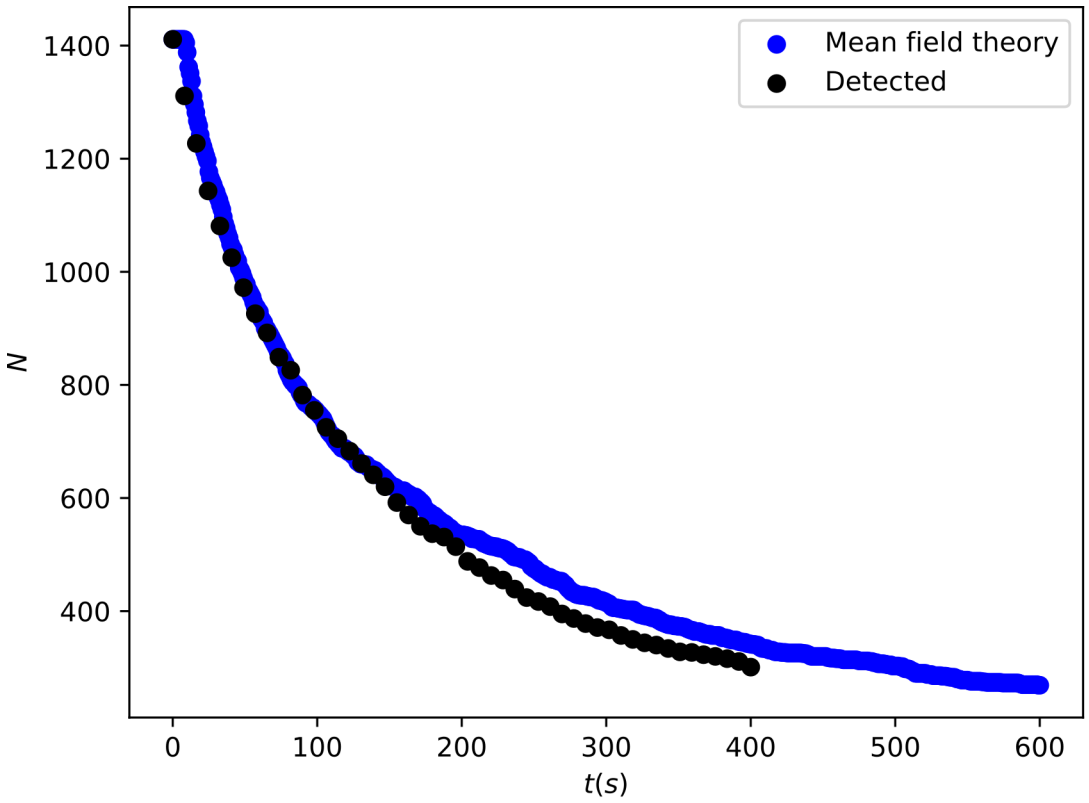

Figure 5.12: The number of droplets in each frame according to the mean field theory (blue) and 'DropletTracker' detection code (black). For data corresponding to fig. 5.11.

dynamics of ϕ up to 400 s.

5.2.5 The Raoult effect

The 400 s panel in fig. 5.11 shows a slight general overprediction of droplet radius. To understand this the radius as a function of time is measured for a number of individual droplets chosen randomly from across the array and are presented in fig. 5.13. In each series, a clear reduction in $\frac{dr}{dt}$ occurs after the droplet evaporates to within a range of r indicated by the black dashed lines. This is because the droplets contain a small amount of solute which begins to have a significant effect on the value of $\frac{dV}{dt}$ when r becomes small. This is known as the Raoult effect which predicts a reduction in the value of ϕ_{sat} with increasing concentration due to the colligative properties of solute [95] (see section 1.7). Due to the reducing volume, the concentration of solute inside the droplets increases during evaporation explaining the persistent small droplets in fig. 5.2. Once evaporation reduces the value low enough, the high solute concentration prevents them from evaporating. At this point they should no longer be contributing to the value of ϕ.

The amount of solute in the droplet can be calculated from the knowledge of when

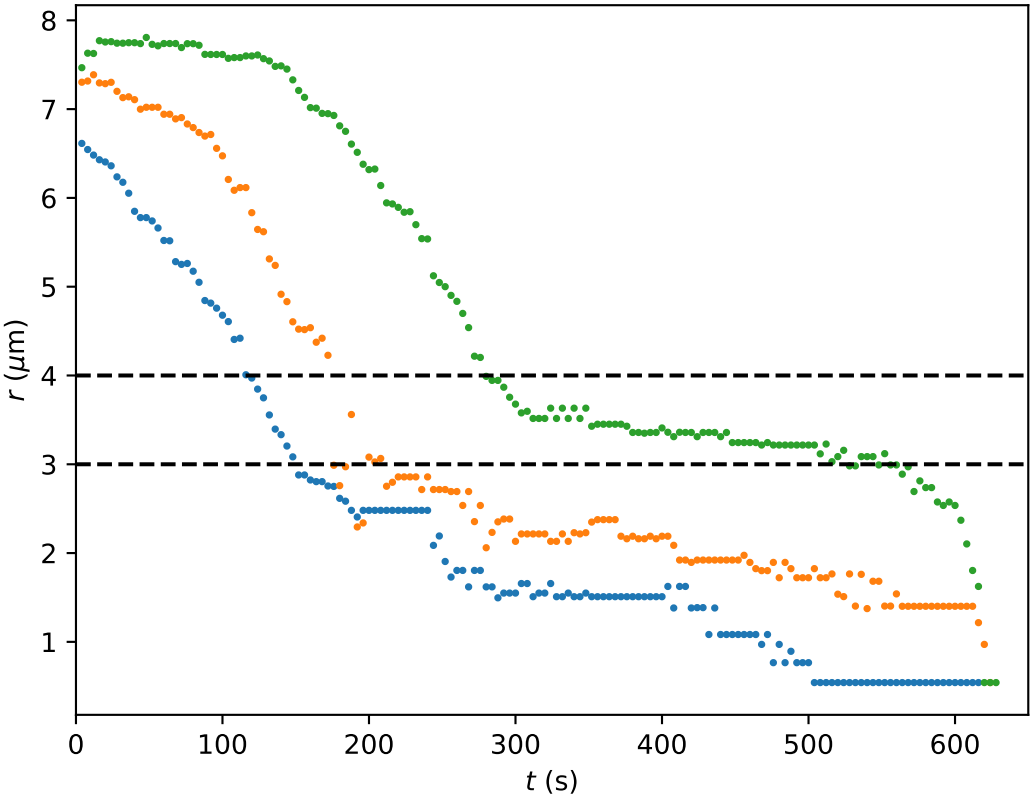

Figure 5.13: Radius of curvature of a selection of three droplets showing their evaporation plateaus as they become small enough (range indicated by the black dashed lines).

the droplet stops evaporating. The Raoult effect states that c_{sat} is reduced by the ratio between molecules of solvent (water) to the total number of molecules (χ) [95], therefore the reduced saturation fraction is

$$\phi_{sat}(\chi) = \chi e^{\frac{r_k}{r}}. \tag{5.7}$$

Because it is known (from fig .5.13) that a droplet has $\frac{dV}{dt} \approx 0$ at $3 \leq r_s \leq 4\,\mu$m the term $\phi_{sat} - \phi = 0$ in eq. 5.2. By substituting eq. 5.7 for ϕ_{sat} and rearranging, χ is given by

$$\chi = \frac{\phi}{e^{\frac{r_k}{r}}}. \tag{5.8}$$

By setting $r = r_s$ and the value of $\phi(t = 400\,\text{s}) = 1.00021$, $(1 - \chi)$ is 0.015% for $r_s = 3\,\mu$m and 0.0060% for $r_s = 4\,\mu$m. This indicates that the droplet's evaporation rate is incredibly sensitive to dissolved solute with only a tiny fraction necessary to make a difference in these saturated conditions for small droplets. These dissolved solutes could either originate directly from the exhaled breath or already be present on the substrate.

For another interesting observation of the Raoult effect see Appendix D.

5.2.6 Correcting for the presence of solute

To include this effect the droplets which are no longer evaporating could be excluded from the calculation of $\bar{r}(t)$ effectively decreasing the value of r^*. This would indeed increase $|\frac{dV}{dt}|$ for evaporating droplets and decrease $|\frac{dV}{dt}|$ for growing droplets and might improve the over-prediction of the radii observed at $t \leq 400\,\text{s}$ in fig. 5.11.

To test this, a cutoff value $r_s = 3.5\,\mu$m is chosen, based on fig. 5.13. If droplets are initially less than or evaporate below r_s then these droplets are not considered. This makes an assumption that all droplets have the same amount of solute contained within them. An alternative assumption might be to assume that the droplets have the same initial concentration, which would determine the size in which they stop evaporating. Fig. 5.14 plots the initial condition of the mean field model (much like fig. 5.10) but without considering the droplets with $r < r_s = 3.5\,\mu$m (indicated by the blue dots). To investigate the success of accounting for dissolved solute, fig. 5.11 is re-plotted with the updated mean field predictions at $t = 400\,\text{s}$ with $r^* = \overline{r(r > r_s)}(t)$ in fig. 5.15. In fig. 5.15, circles are only plotted for droplets with $r(t) > r_s$. It can been seen that the

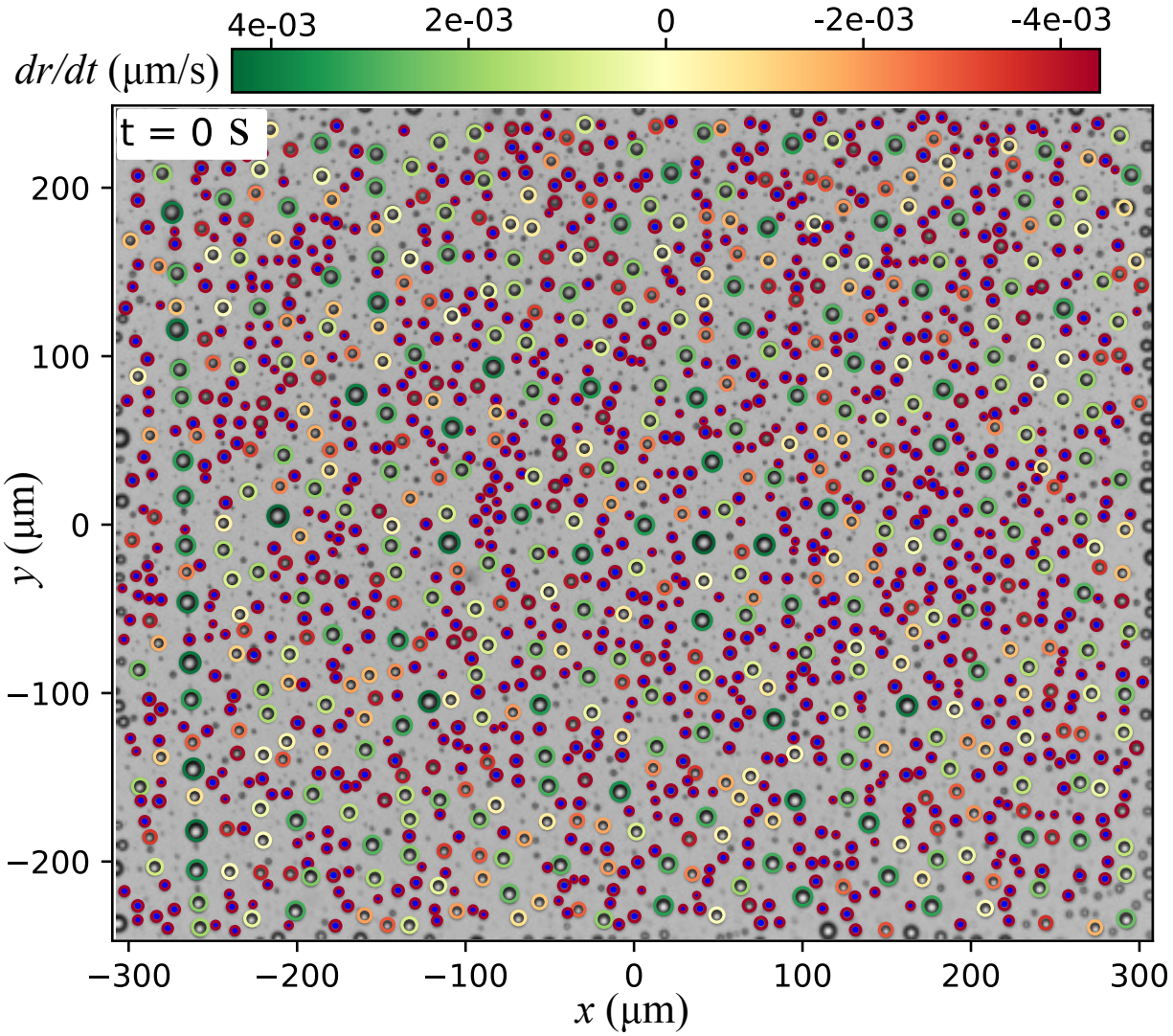

Figure 5.14: Initial droplet distribution of the mean field theory (circles) with $\frac{dr}{dt}$ indicated by the colourbar. The circles are overlaid and aligned on the first experimental frame. Droplets with $r < 3.5\,\mu$m (excluded from the calculation of $\frac{dr}{dt}$) are indicated with blue dots.

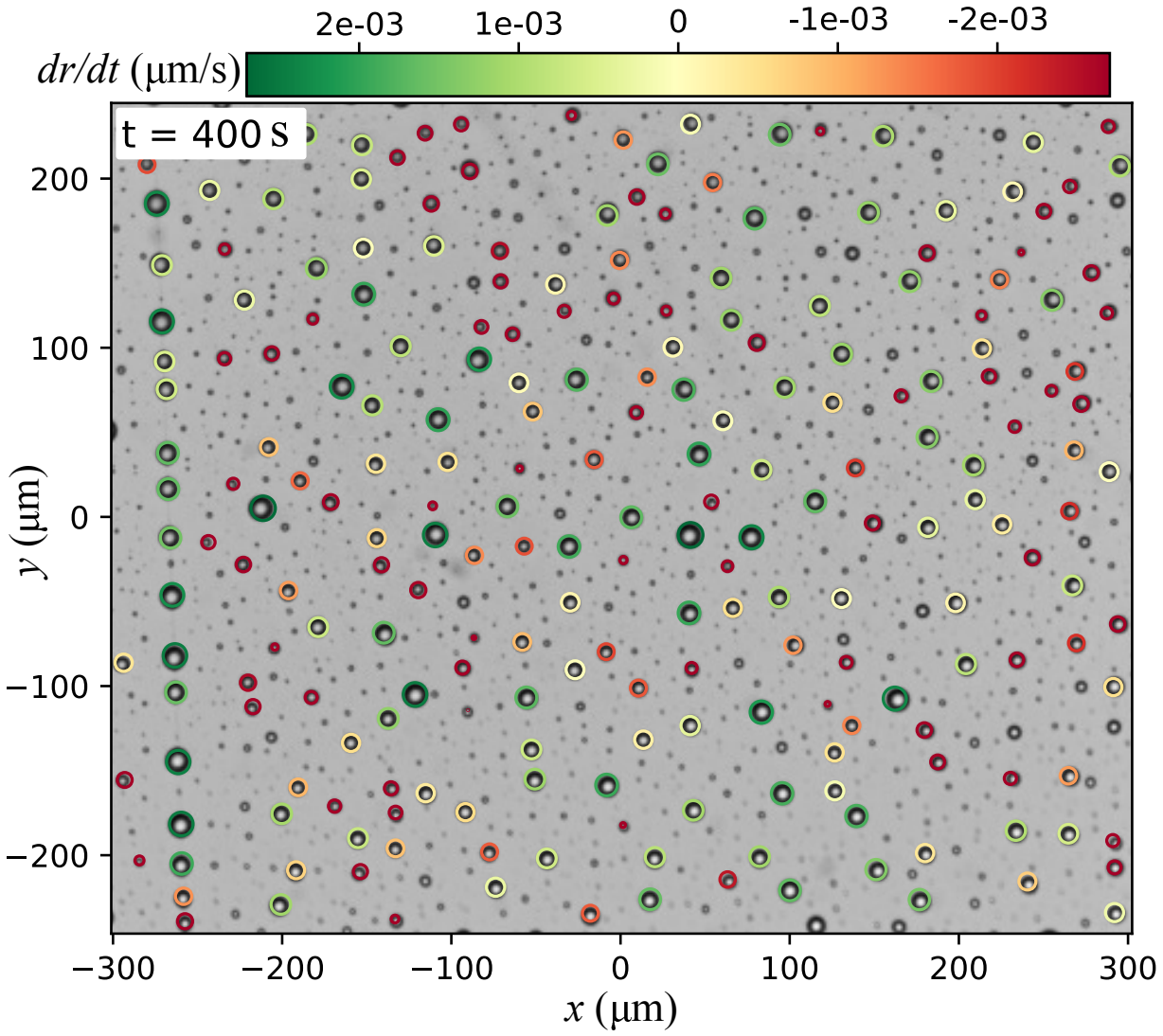

Figure 5.15: Mean field theory predictions (circles) with $r^* = \overline{r(r > r_s)}(t)$ at $T = 20°C$ with $\frac{dr}{dt}$ indicated by the colourbar. The circles are overlaid and aligned on the experimental frame at $t = 400\,\mathrm{s}$.

agreements of the mid sized droplets has qualitatively improved as a result of excluding droplets below r_s. The predictions for the number of droplets can also be compared in fig. 5.16 as before. The value of N is now the number of droplets with $r > r_s$ in both the detected and theory series. The agreement is slightly worse than before with the mean field theory under-predicting the number of droplets when compared to the experiment. There are a number of potential reasons which might explain this, most importantly the limitations associated with mean field theories. The mean field is assumed to represent the inter-droplet interactions on average but does not account for small variations which will occur in the experimental array. For example in a local region which has a large droplet surrounded by small droplets the gradients in ϕ between droplets might be quite different from that assumed by the mean field. Somewhere else in the array is a large droplet surrounded by other large droplets, which would represent a situation where the gradients between droplets might be smaller than predicted by the mean field. The assumption in the model would be that these situations cancel out. In this case the quantity N is particularly sensitive to locally enhanced gradients which would increase evaporation rates and translate into a greater reduction of N. Because $\phi(t)$ is tied to the distribution, variations of this sort might lead to disagreements which will compound, exaggerating differences over time. Despite this, the general shape of the decaying number of droplets is still captured by fig. 5.16 for $t \leq 400\,\mathrm{s}$. Another possible quantity which could be used to evaluate the agreement quantitatively is the total volume, however this also suffers from a similar limitation to N. Whilst N is particularly sensitive to the smaller droplets, the total volume, V_T is disproportionately sensitive to the larger droplets as smaller droplets will not make a significant difference to the value of V_T. The best way to quantitatively evaluate the improvement of excluding droplets less than $r = 3.5\,\mu\mathrm{m}$ is to compare the radius of curvature predicted by the mean field theory (r_{MFT}) and the detected radius of curvature extracted by 'DropletTracker' (r_{detect}). r_{MFT} is plotted verses r_{detect} in fig. 5.17 at $t = 400\,\mathrm{s}$ for when $r^* = \bar{r}$ (black data) and when $r^* = \overline{r(r > r_s)}$ (blue data). The improvement from qualitative judgement of fig. 5.11 is supported by this figure, as the inclusion of droplets influenced by solute did indeed result in a general overprediction of r as can be seen by the black data lying above the $r_{detect} = r_{MFT}$ line. After these droplets are removed from the calculation of r^* the agreement improves and the scatter of this blue data reduces. The mean absolute divergence between r_{MFT} and r_{detect} decreases from $1.53\,\mu\mathrm{m}$ (black data) to $0.31\,\mu\mathrm{m}$ (blue data).

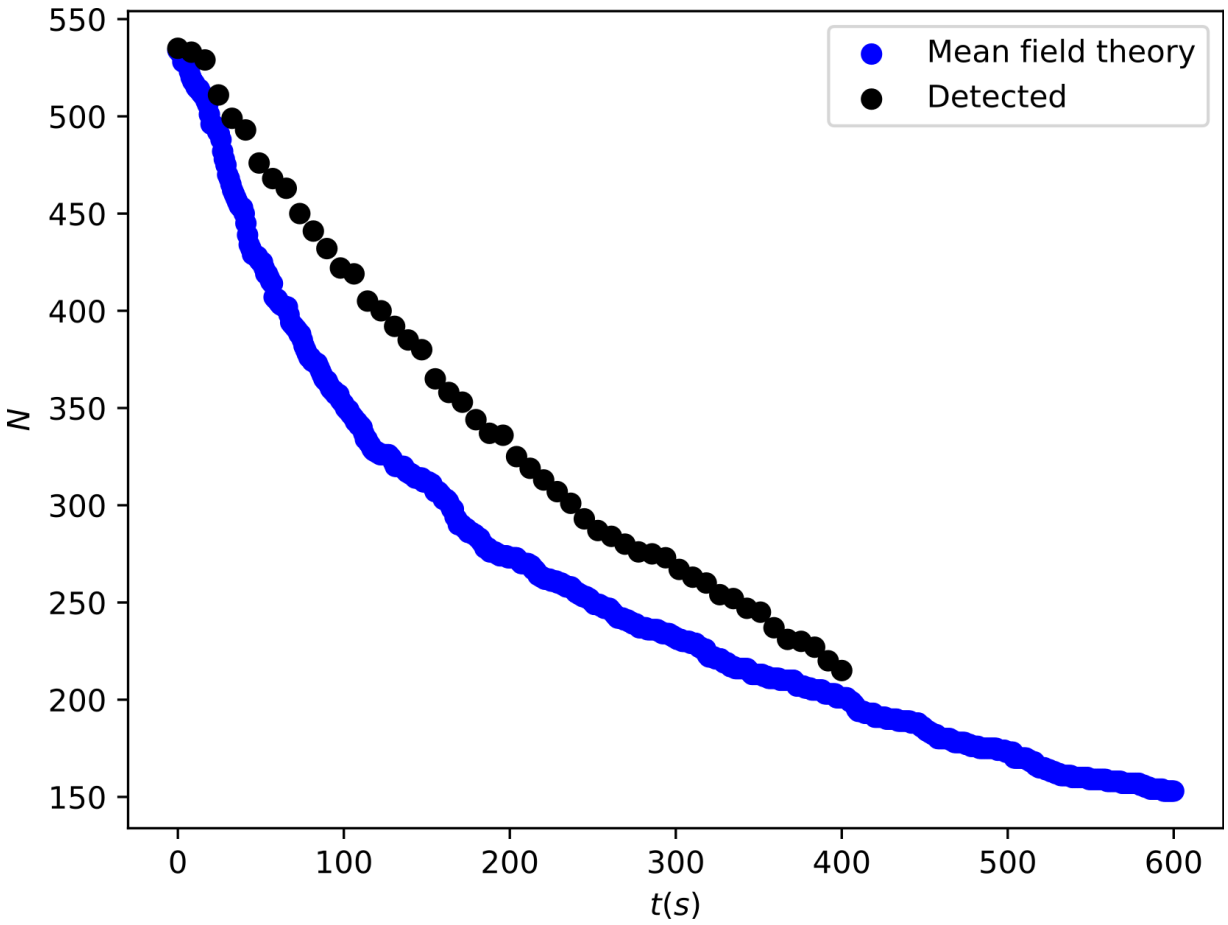

Figure 5.16: The number of droplets in each frame according to the mean field theory (blue) and 'DropletTracker' detection code (black). For data corresponding to fig. 5.15.

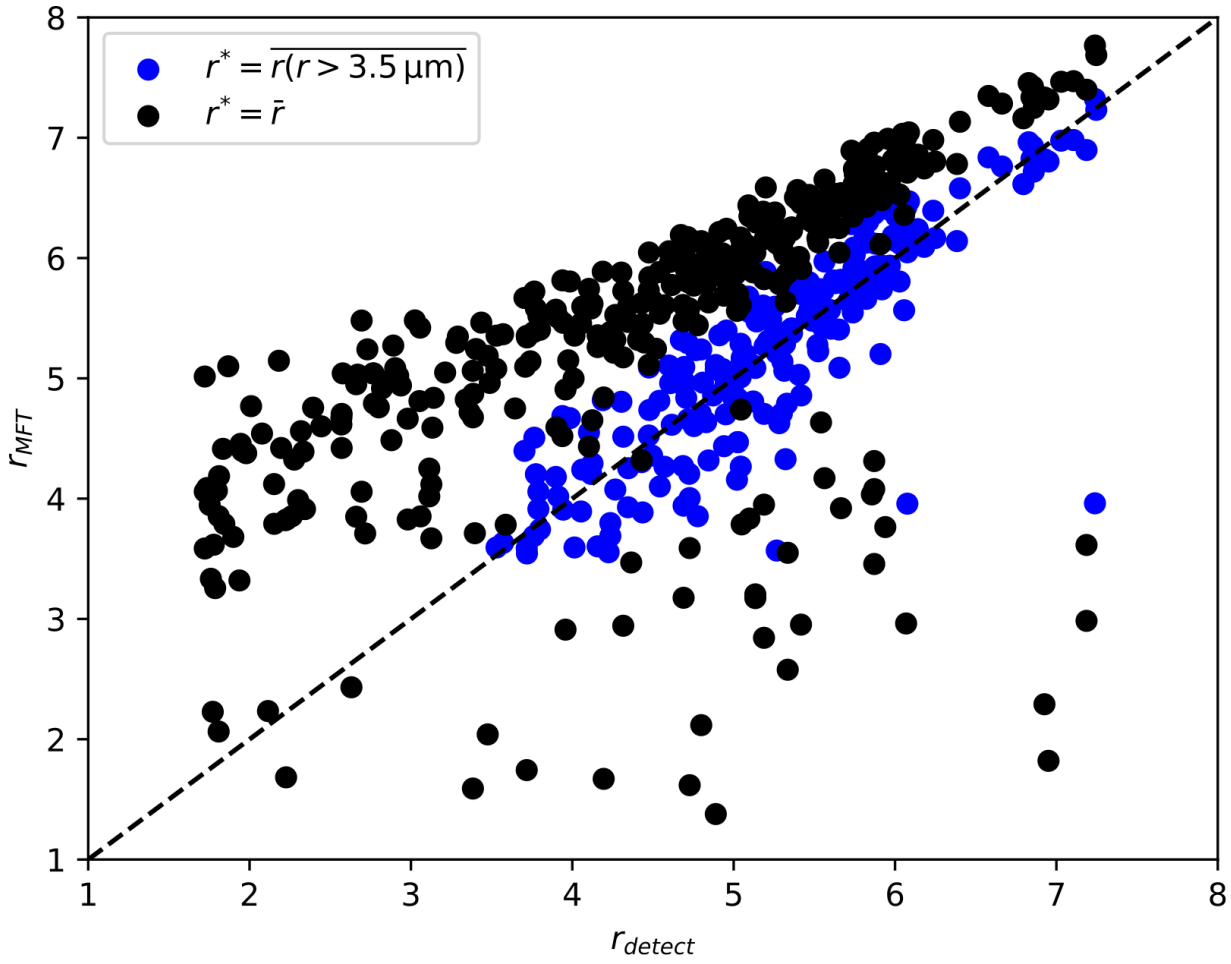

Figure 5.17: radius calculated by the mean field theory (r_{MFT}) against that detected by 'DropletTracker' (r_{detect}) for with (blue) and without the solute correction (black) at $t = 400\,\mathrm{s}$.

The blue data still contains some scatter, some of this will be accounted for by the measurement uncertainty due to the resolution limits of determining the positions of the contact line, as well as 'DropletTracker' misdetections. The resolution uncertainty is measured to be approximately $\pm 1\,\mu$m. Some scatter is expected for mean field models as it assumes each droplet is in the same mean environment which is not true for individual droplets. This is a limitation of mean field models in general. One other explanation for the scatter of the data is the assumption that the liquid exhaled is pure water. The breath may also contain additional components. For example saliva is made up of proteins, mucins, minerals and many others [96], which may be present in the droplets. In addition to the considered of the Raoult effect, these components may change the properties of the liquid (e.g. density). Therefore the constants corresponding to pure water in table. 5.6 will be slightly off. For example the surface tension of pure saliva has surface tension of $\gamma \approx 50\,\mathrm{mNm}^{-1}$ [97] and the density is $\rho \approx 1006\,\mathrm{kgm}^{-3}$ [98]. With these quantities the evaporation rate of an isolated droplet might reduce by $\sim 30\%$. This is of course an absolute limit and the quantities will not diverge this far from water, which will be the component principally condensing from the breath, given that it was the only volatile component.

5.2.7 Length scale applicability of the mean field model

To understand the scale of the local effects and the region size in which droplets can no longer be modelled by a mean field, the array in fig. 5.11 is tiled by a repeating square grid, to divide the droplets up into cells. The overall evaporation rates $\left(\frac{dV}{dt}\right)_k$ of the droplets within each cell are summed up. This value is calculated for all cells of length (L) across the array and divided by the area of the cell to calculate a flux within each. The flux is then plotted as L is varied in fig. 5.18. The variation in flux between each cell reduces with L, when more droplets are included inside each one. From this it can be concluded that the mean field theory will break down when modelling arrays smaller than $L \approx 100\,\mu$m as the variation between cells is large and cannot be considered to be in the same environment.

This value of $L \approx 100\,\mu$m is useful as it defines the minimum size region which needs to be simulated or modelled in order for the results to be general to other places in the array. Using this to inform simulations can reduce computation costs, as it prevents performing calculations on an unnecessarily large number of droplets.

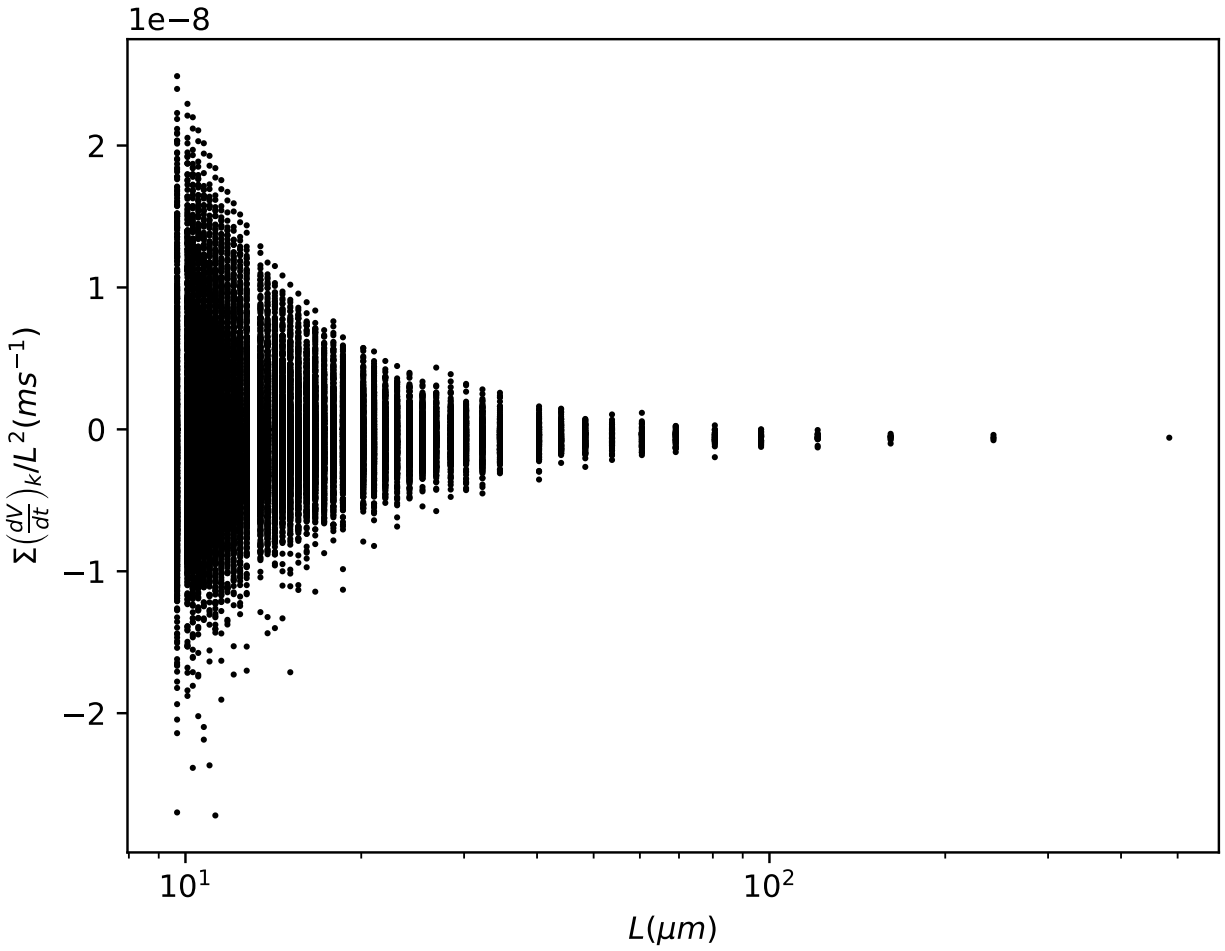

Figure 5.18: The collective flux of the droplets within each $L \times L$ size square square of the grid. The multiple data points at each L represent the summed evaporation in each of these squares $\Sigma \left(\frac{dV}{dt}\right)_{\mathrm{k}}$ divided by L^2 to give a flux.

5.3 Conclusions

In this chapter it has been shown that the big droplets in a micron-sized distribution can grow at the expense of their smaller neighbours. This redistribution of volume, whilst the array is evaporating, seems to be due to the Kelvin effect which drives diffusive fluxes leading to grow/shrink dynamics. This is surprising considering the vapour pressure of a $1\,\mu$m droplet is only 0.08% bigger than a $10\,\mu$m droplet. For comparison, a 1 nm droplet's vapour pressure is 260% bigger than a 10 nm droplet. Because of this its effect is often dismissed for micron droplets [99]. For example Yang et al. [12] also found that the droplet's curvature plays an important role in the growth of droplets in clouds, showing that it leads to a broadening of the radius distribution. This chapter supports the importance of the role of curvature by studying not only global properties of the distribution but by examining the growth of individual droplets. The experimental method used to study the droplet's evaporation, allows the interactions through the vapour to be isolated. In other studies the dynamics of droplet sizes and distributions are governed more significantly by droplet coalescence and due to growth from direct deposition. This is especially true if an airflow is used to initiate condensation. In these cases, the timescale for growth due to the Kelvin effect is often much longer than the previously stated mechanisms and because of this, other studies overlook its importance. Confining evaporating breath in this way represents a method in which it can be studied.

The temporal dynamics of the growth are also connected to the instantaneous droplet distribution and shows that the ambient concentration does not have to be set externally in order to see condensational growth.

The diffusive theories must include the Kelvin effect in order to predict the redistribution dynamics and the standard equation is modified to do this. Using a mean field approach allows for good qualitative predictions to be made and provides an alternative to the Masoud et al model, which is more computationally expensive. Despite the mean field model simplifying the concentration field, it was also able to make quantitative predictions, improved by accounting for solute inside droplets. The evaporation is found to be very sensitive to small concentrations of solute in saturated environments, with them able to completely arrest evaporation. The size of the region over which mean field predictions are applicable are also evaluated and $100\,\mu$m is revealed to be the size of the unit cell.

Chapter 6

Direct numerical simulations

In chapter 4 experimental work was conducted investigating non-diffusive effects and their significance on evaporation. It was shown that droplets are indeed very sensitive to a number of non-diffusive phenomena but characterising them is challenging as their dynamics must be inferred predominantly from the influence they have on the droplet evaporation. In this chapter initial modelling and simulations are conducted to complement experiments and help realise the structures and dynamics of the non-diffusive mechanisms. The intention is to develop a computational model which can simulate multiple droplet evaporation, including the mechanisms which are experimentally difficult to measure/image and are not part of the existing diffusive theory. These include the vapour and temperature fields which surround the droplets. Modelling these allows for the certain mechanisms to be investigated in more detail by solving different equations which include for example the Kelvin effect and/or natural convection. With the ability to visualise the vapour, direct connections can be made between the formation of composition and thermally driven convective plumes, on the evaporation of the droplets. This chapter contains the progress towards testing, validating and developing an existing model for multiple droplet evaporation.

TPLS (Two-Phase Level-Set) is the first diffuse interface (DI) 3D direct numerical simulations (DNS) model of its kind capable of simulating two phase phenomena with heat mass transfer. It was developed by Lennon Ó Náraigh, Prashant Valluri, David Scott, Toni Collis and Iain Bethune and Peter Spelt. TPLS solves the Cahn-Hilliard equation for modelling the dynamics of co-exisiting phases. The model also simulates flow by solving the Navier-Stokes equations in the liquid and gas phases. The name TPLS is

a legacy from when the code used a level-set method to track interfaces between phases. It is now solely a DI model. DI methods treat the interface as unsharp, associating a thickness which allows for interfacial phenomena to be modelled more accurately as it can be shared over multiple grid points. The DI approach is advantageous as it allow for smooth transitions between phases and avoids sharp transitions which are difficult to handle numerically. The DI interface also better captures curved interfaces and doesn't require complex interpolation, or snapping of the interface to square grids which distort its shape. This is especially important when studying interfacial phenomena, such as evaporation (phase change [100]). It is worth noting that this diffuse interface does not correspond in scale or physical sense to modelling the Knudsen layer transition between liquids and gases, which is molecularly thin [101].

TPLS is also highly optimised for large scale simulations and is parallelised for use with multiple processors. It is also supported on supercomputers including Cirrus and Archer2. This computational efficiency is important for multiple droplets because large numbers of grid points are needed to simultaneously resolve the evaporation dynamics at the interface, whilst ensuring a large enough domain. The TPLS code used in this chapter to model multiple droplets can be found at `https://doi.org/10.6084/m9.figshare.26763886`.

All simulations in this chapter were conducted on the Archer2 Cray EX supercomputing system. Information on the architecture used on the system compute nodes can be found at `archer2.ac.uk/about/hardware.html`.

6.1 Methods

As mentioned previously the TPLS model was not written by myself. The changes which have been made to the code which I have contributed to, with the help of Dr David Scott and Prof. Prashant Valluri are limited to the calculation of phase change. Everything else is given as a description of the code for clarity. Further details about the model and its usage can be found in Sáenz et al.[102]. The simulations and corresponding analysis is my own work.

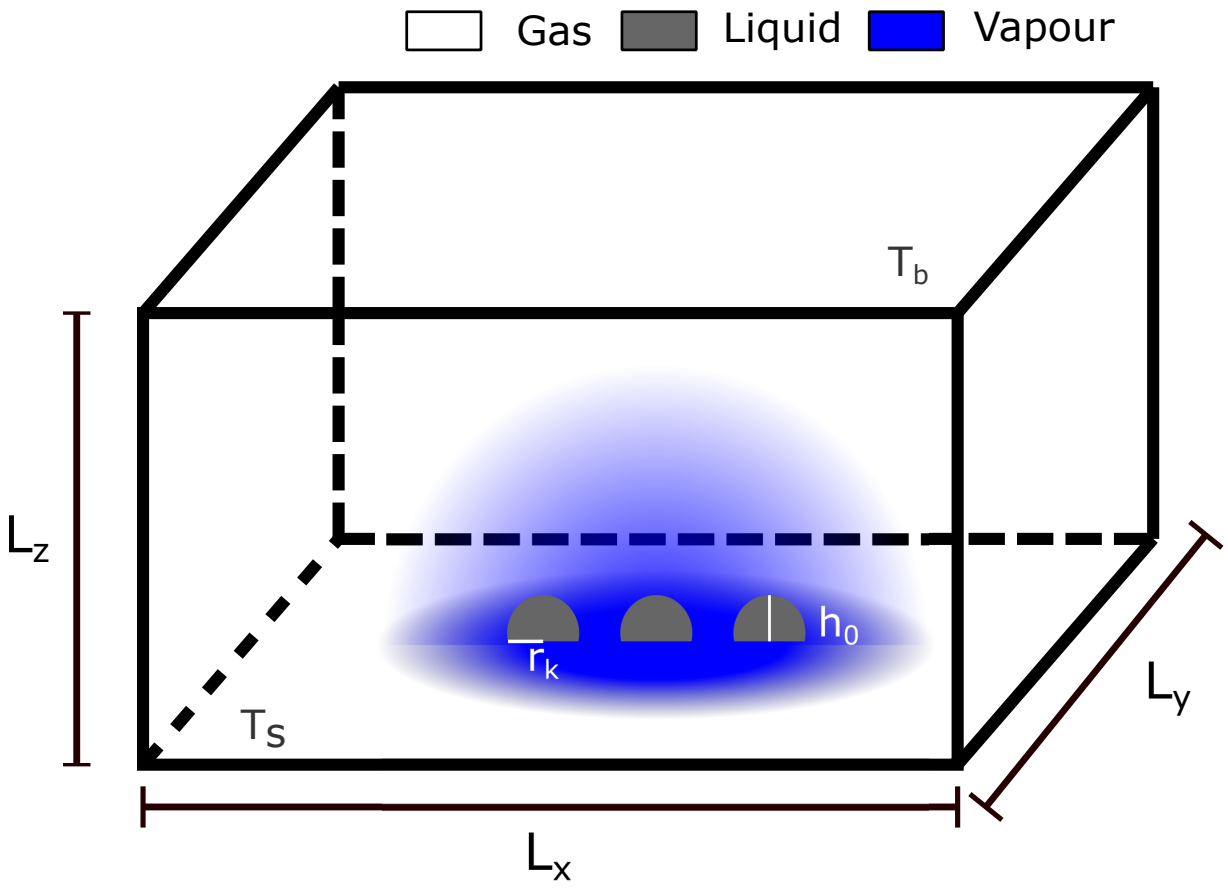

Figure 6.1: Diagram of the simulated domain in TPLS.

6.1.1 Problem statement

The problem to be solved is that of multiple droplets evaporating into a gas at standard temperature and pressure. The model accounts for two phases namely, the liquid phase and a mixed gas phase, containing an immiscible gas and the vaporised water vapour see fig. 6.1. The phases have physical properties of specific heat capacity (c_p), thermal conductivity (κ), dynamic viscosity (μ) and density (ρ) and are simulated with a cartesian domain $\mathbf{x} = (x, y, z)$ with the boundaries spanning $x = [0, L_x]$, $y = [0, L_y]$, $z = [0, L_z]$.

The following variables are made non-dimensional as

$$\mathbf{x} = \frac{\hat{\mathbf{x}}}{\hat{L}_z} \qquad \mathbf{u} = \frac{\hat{\mathbf{u}}}{\hat{U}_c} \qquad p = \frac{\hat{p}}{\hat{p}_0} \tag{6.1}$$

$$T = \frac{\hat{T} - \hat{T}_s}{\Delta\hat{T}} \qquad t = \hat{t}\frac{\hat{U}_c}{\hat{h}_0} \tag{6.2}$$

where hats indicate dimensional values. $\hat{U}_c = \hat{\gamma}\Delta\hat{T}/\hat{\mu}_l \,\mathrm{m\,s^{-1}}$ is the thermocapillarity velocity, $\hat{h}_0$ is the initial height of the droplet, $\hat{T}_s$ is the substrate temperature, $\hat{\mathbf{u}} = (\hat{u}, \hat{v}, \hat{w})$

is the flow velocity vector and $\hat{p}_0$ is the reference atmospheric pressure.

6.1.1.1 Governing equations

In TPLS the Cahn Hilliard equation is solved and the system evolves towards thermodynamic equilibrium, depending on the specific Gibbs free energies of the phases. The two phases are represented by volume fractions in each cell, for the liquid phase (c_l) and the mixed gas (c_g) and vapour (c_v) phase. The volume fractions of each component can be related to each other by considering a control volume V_c containing some fraction of each phase. The volume of the mixed vapour gas phase (V_{mix}) can be calculated as

$$V_{mix} = V_c(1 - c_l). \tag{6.3}$$

This volume is then be separated into the gas and vapour volumes as

$$V_{mix} = c_g V_{mix} + c_v V_{mix} \tag{6.4}$$

and therefore $1 - c_g = c_v$. These volume fractions are evolved by the Cahn-Hilliard equation modelling phase separation, the non-dimensional form is

$$\frac{\partial c_l}{\partial t} + \nabla \cdot (c_l \mathbf{u}) - \frac{1}{\mathrm{Pe_I}} \nabla \cdot (M \nabla \Phi) = -\frac{\dot{m}}{\rho_l} \left[1 + c_l \left(\frac{\rho_l}{\rho_v} - 1 \right) \right], \tag{6.5}$$

where $M = c_l(1 - c_l)$ is the mobility $\mathrm{Pe_I}$ is the interfacial Peclet number set to 2/0.5dz with dz the dimensionless grid spacing. Sc is the Schmidt number defined as

$$\mathrm{Sc} = \frac{\mu}{\rho D} \tag{6.6}$$

where c_l is an order parameter defining the volume fraction of the liquid phase. The species equation modelling the vapour component of the mixed gas phase is given by

$$\frac{\partial c_v}{\partial t} + \mathbf{u} \cdot \nabla c_v - \nabla^2 c_v + \frac{1}{\mathrm{Pe_I}} c_l \nabla \Phi \cdot \nabla c_v - \frac{1}{\mathrm{ReSc}} \frac{\nabla (1 - c_l) \cdot \nabla c_v}{(1 - c_l)} = \frac{c_g}{(1 - c_l)} \frac{\dot{m}}{\rho_v}. \tag{6.7}$$

In both eq. 6.5 and 6.7 $\dot{m}$ is a source/sink term controlling the amount of phase change, which will be discussed in section 6.1.1.2.

The energy equation in dimensionless form is

$$\frac{\partial(\rho c_p T)}{\partial t} + \nabla \cdot (\rho c_p T \mathbf{u}) = \frac{1}{\mathrm{RePr}} \nabla \cdot (k \nabla T) - \frac{1}{\mathrm{Ja}} \dot{m}. \tag{6.8}$$

Where Re is the Reynolds number,

$$\mathrm{Re} = \frac{\rho U L}{\mu} \tag{6.9}$$

Pr is the Prandtl number,

$$\mathrm{Pr} = \frac{\mu c_p}{k} \tag{6.10}$$

and Ja is the Jakob number,

$$\mathrm{Ja} = \frac{c_p \Delta T}{\Delta h}. \tag{6.11}$$

Conservation of momentum is governed by the Navier-Stokes equation which describes the bulk flow in the fluids,

$$\frac{\partial \rho \mathbf{u}}{\partial t} + \nabla \cdot (\rho \mathbf{u}\mathbf{u}) = -\nabla p + \frac{1}{\mathrm{Re}} \nabla \cdot [\mu(\nabla \mathbf{u} + \nabla \mathbf{u}^T)] + \frac{1}{\mathrm{We}} \Phi \nabla c_l - \frac{1}{\mathrm{Re}} (\nabla T - \mathbf{n}(\mathbf{n} \cdot \nabla T)) |\nabla c_l| + f_b \tag{6.12}$$

here $\mathbf{n} = \nabla c_l / |\nabla c_l|$ and We is the Weber number defined as

$$\mathrm{We} = \frac{\rho U^2 L}{\gamma}. \tag{6.13}$$

$\mathbf{f_b}$ is a body force term accounting for buoyancy as a result of density differences due variations in temperature, defined as

$$\mathbf{f_b} = -\rho \left(\frac{1}{\mathrm{Fr}^2} - \frac{\mathrm{Bd}}{\mathrm{Re}} \beta T \right) \mathbf{e}_k. \tag{6.14}$$

Where β is the coefficient of thermal expansion, $\mathbf{e}_k$ is a vertical unit vector and Fr is the Froude number defined as

$$\mathrm{Fr} = \frac{U}{\sqrt{gL}} \tag{6.15}$$

and Bd is a bond number defined as

$$\mathrm{Bd} = \frac{\rho \beta g L^2}{\gamma}. \tag{6.16}$$

In the momentum equation the Boussinesq approximation is made and density of pure components only vary with temperature in terms involving g (*i.e.* eq. 6.14).

Conservation of mass is enforced by the continuity equation

$$\frac{\partial \rho}{\partial t} + \nabla \cdot (\rho \mathbf{u}) = -\dot{m} \left(\frac{1}{\rho_l} - \frac{1}{\rho_v} \right) \rho \tag{6.17}$$

noting that outside the interface $\dot{m}$ is zero and the term on the RHS becomes nil.

6.1.1.2 Phase change

Phase change is an interfacial phenomenon [103] and is therefore only allowed to occur in the diffuse interface of the droplet which is identified by the grid points which lie between a gaseous phase contour at $c_l = 0.3$ and liquid phase contour at $c_l = 0.7$. These values are chosen as they are found to always enclose at least one grid point across the interface, which is important to allow phase change to be calculated at each timestep at all points on the droplet's interface. The rate of this phase change ($\dot{m}$), is the rate at which c_l is converted to c_v for evaporation and vice versa for condensation. The value of $\dot{m}$ is calculated with a two step iterative procedure. Firstly, the Cahn-Hilliard equation is solved from the current timestep (i), for c_v in the next timestep ($i+1$) with $\dot{m} = 0$, giving $c_v^{(0)}$. The amount of phase change for diffusion limited evaporation, according to Maxwell's assumption [21] is proportional to the difference between c_v and its saturation value (c_v^s). $\dot{m}$ is therefore given the following form

$$\dot{m} = V_0 \left(\frac{\rho_v}{\Delta t} \right) (c_v^s - c_v) \tag{6.18}$$

which has dimensions of $[ML^{-3}T^{-1}]$, with the second term capturing Maxwell's assumption and V_0 is a vaporisation coefficient. A first approximation for the phase change ($\dot{m}^{(1)}$) is then calculated with eq. 6.18 with $c_v = c_v^{(0)}$. The Cahn-Hilliard equation is then solved a second time with $\dot{m} = \dot{m}^{(1)}$, giving $c_v^{(1)}$. Eq. 6.18 is recalculated for the updated $c_v = c_v^{(1)}$ to give an $\dot{m}$ correction ($\dot{m}^{(2)}$) which either reduces or enhances phase change depending on if $c_v^{(1)}$ is greater or less than c_v^s in the interface. The final value is then

$$\dot{m} = V_0 \left(\frac{\dot{m}^{(1)}}{V_0} + V_2 \dot{m}^{(2)} \right) \tag{6.19}$$

where V_2 is a weight for the size of the correction. It was found that calculating $\dot{m}$ in this way, maintained $c_v = c_v^s$ in the interface with $V_0 = 2/3$ and $V_2 = 0.1$. These are heuristic values determined by trial and error.

In each calculation of eq. 6.18, $\dot{m}$ is prevented from exceeding the amount of vapour available to be condensed such that if

$$\frac{|\dot{m}|\Delta t}{\rho_v} > (1 - c_l)c_v \tag{6.20}$$

then condensation is limited to

$$\dot{m} = -\left(\frac{\rho_v}{\Delta t}\right)(1 - c_l)c_v \tag{6.21}$$

and also prevented from exceeding the amount of liquid available to be evaporated. Such that if

$$\frac{|\dot{m}|\Delta t}{\rho_v} > c_l \tag{6.22}$$

then evaporation is limited to

$$\dot{m} = \left(\frac{\rho_l}{\Delta t}\right)c_l \tag{6.23}$$

6.1.1.3 Numerical method

TPLS uses a marker in cell grid with scalar quantities (e.g. c_l, c_v, T) stored at the centre of the cell and vector quantities stored on the faces (e.g. u, v, w). The Cahn-Hilliard equation (6.5) is solved numerically with an implicit-explicit scheme (solving one term explicitly and the other term implicitly) with a semi backward difference formula (SBDF) [104]. The convective term is evaluated using a weighted essentially non-oscillatory scheme (WENO) [105, 106]. The momentum equation (eq. 6.12) is solved with a projection method comprising two steps: the first calculates the velocity field neglecting pressure and the second enforces incompressability to calculate the final field. The energy eq. 6.8 is solved using a Crank Nicholson-Adam Bashforth scheme [107].

6.1.1.4 Boundary and initial conditions

The top surface of the domain ($z = L_z$) has an open Dirichlet boundary condition for $c_v = 0$ and $T = 0$ and Neumann boundary conditions for $\frac{\partial \mathbf{u}}{\partial z} = 0$ and $\frac{\partial c_l}{\partial z} = 0$. On the base of the domain at $z = 0$ there is a no slip and no penetration condition such that

$\mathbf{u} = 0$, $\frac{\partial c_l}{\partial z} = 0$ and $\frac{\partial c_v}{\partial z} = 0$. The base is the droplet substrate and is held at a constant temperature $T = T_s$. On the walls of the domain the boundary conditions are periodic taking the $x = 0$, L_x as an example, $q(x = 0) = q(x = L_x)$ where q is c_v, T, $\mathbf{u}$ and c_l. The equivalent boundary conditions are applied on the $y = 0$, L_y walls in the y direction.

The initial condition of the c_l field is generated by first specifying the centre locations $x = x_\mathrm{k}$, $y = y_\mathrm{k}$ and radius $r = r_\mathrm{k}$ of the N droplets, where the subscript k represents the droplet index and r is the radial distance to the nearest droplet centre. Inside the droplet $c_l = 1$ and outside the droplet $c_l = 0$ and should smoothly but quickly transition between these values in the interface with $c_l = 0.5$ at $r = r_\mathrm{k}$. One such function which achieves this is

$$c_l(x, y, z) = 0.5 - 0.5 \tanh\left(\frac{r(x, y, z)}{2\sqrt{2}\epsilon}\right) \tag{6.24}$$

which is the 1D solution to the Cahn-Hilliard equation and will satisfy the above conditions providing a reasonable initial guess. The benefit of modelling the interface with a smooth continuous function is that it avoids the problem of representing sharp interfaces on finite grids, such as in finite element codes such as COMSOL.

For initialising the vapour phase the interface should be initially saturated ($c_v = c_v^s$). In order to avoid sharp gradients leading to potential numerical problems, c_v is set to c_v^s inside the droplet too. Although physically there is no vapour inside the droplet, numerically this volume will tend to zero and saturating these regions will have little influence on the simulation. Again to avoid sharp gradients outside the droplet and within the interface $c_v = c_v^s$ is extended such that the transition occurs at the largest value of r_k (r_{max}) away from each interface. A similar expression is used to initialise the transition from c_v^s to a lower ambient value, with the constants chosen to reduce its sharpness as

$$c_v(x, y, z) = c_v^s \left[0.6 - 0.4 \tanh\left(\frac{r(x, y, z) - r_{max}}{5(2\sqrt{2})\epsilon}\right)\right]. \tag{6.25}$$

The values 0.6 and 0.4 mean the term inside the square brackets varies between 1 and 0.2 and so $0.2c_v^s \leq c_v \leq c_v^s$, where 0.2 is chosen as an arbitrary ambient value. The temperature is initialised homogeneously in x and y and varies in the z dimension. To satisfy the boundary conditions on substrate ($z = 0$) and top ($z = L_z$) of the domain the

temperature varies from T_s to T_b respectively. The profile is given by

$$T(z) = (T_s - T_b)\,\mathrm{erf}\left(\frac{5(r_{max} - z) + 1}{2}\right) + T_b. \tag{6.26}$$

The constants are chosen to avoid large initial variations in temperature within the interface. The velocity fields are initialised as $\mathbf{u} = 0$ everywhere in the domain.

These conditions are found to represent a good enough initial estimate for the simulations to progress.

6.2 Results and Discussion

Initially a computational efficiency test is conducted in a domain of $400 \times 800 \times 800$ grid points. For each number of nodes (128 CPU's per node) the simulation is run for 10 timesteps and the average time taken per iteration is reported. 16 nodes were chosen for the simulations as it is found that it provided the maximum computational efficiency, taking 1.76 seconds per iteration. A timestep of $\Delta t = 1 \times 10^{-5}$ is tested and found to be smaller than the timescales of the relevant physical processes and maintain numerical stability.

Due to the number of grid points in the domain and the intensive computation being carried out, the amount time and resources needed to capture a significant amount of evaporation is prohibitively large. In order to overcome this challenge, c_v^s is increased by a factor of 10. This allows more phase change to be permitted from the droplet before saturation is reached and enhances the concentration gradients surrounding the droplets leading to a greater diffusive flux away from the interface.

With this addition the larger of the two domains in the computational efficiency test was chosen ($400 \times 800 \times 800$) which provides finer resolution and also allows for the boundaries to be placed further away from the edge of the array. A multiple droplet simulation was run with a 5×5 sessile droplet array. Each droplet had an initial contact angle of $\theta = \pi/2$ radians and a base radius of $a = 20$ grid points. The domain had $400 \times 800 \times 800$ grid points in each dimension, with the array centred at $x = L_x/2$, $y = L_y/2$ on the substrate at $z = 0$. The liquid was chosen to be water and the dimensional values were: $c_p = 4180\,\mathrm{J\,kg\,K^{-1}}$, $\kappa = 0.623\,\mathrm{W\,m^{-1}\,K^{-1}}$, $\mu = 0.000646\,\mathrm{Pa\,s}$ and $\rho = 997\,\mathrm{kg\,m^{-3}}$. The dimensionless values for the vapour, gas and liquid are given in table. 6.1 noting that the

Property	Liquid	Gas	Vapour
$\hat{c_p}$	1	0.2488	0.4471
$\hat{\kappa}$	1	0.0429	0.0316
$\hat{\mu}$	1	0.0279	0.0163
$\hat{\rho}$	1	0.0011	0.0007

Table 6.1: The physical non-dimensional constants for the simulated liquid, gas and vapour phases.

Re	Pr	We	Ja	Sc	Fr
1838	4.334	2.293	0.0079	0.0228	114.6

Table 6.2: Summary of the non-dimensional numbers for the simulations conducted.

liquid phase quantities are chosen as the characteristic value used to non-dimensionalise. These values represent water vapour and Nitrogen (at $40°C$ at 1 atmosphere).

6.2.1 Interfacial dynamics

The calculated dimensionless numbers in the governing equations are summarised in table. 6.2. Fig. 6.2 shows the position of the contact line during evaporation with t indicated by the different coloured lines in the legend.

The droplets appear to evaporate at different rates with the final contact lines (black) receding to a smaller area at the corners and edge of the array. This indicates that the model captures the diffusive shielding effect observed experimentally in previous chapters.

The droplets also seem to be distorted and do not retain their spherical cap shape. The origin of these distortions could be physical however their scale is likely to be accentuated artificially. To reduce these artefacts the number of grid points would need to be increased such that surface tension can be properly resolved in the droplet's interface. For the regular grids used in TPLS, increasing the number of grid points in the interface means increasing the total number of grid points in the entire domain significantly. Simulations of larger numbers of grid points are currently not possible due to current limitations of TPLS. The development of the code to allow for larger domains is discussed further in section 7.6. Another interesting observation of the droplets is the direction in which the droplets depin. The four droplets at the corners evaporate with the contact line nearest the centre of the array receding outwards, however the twelve edge droplets recede in the opposite direction, with the contact line at the edge of the array receding inwards. The reason for this is unknown and is not expected experimentally. It may also be a numerical artefact

of not resolving the interface with high enough resolution.

To test whether these distortions and the lack of smoothness of the interface are indeed of numerical origin, an isolated droplet can be simulated with the same size domain (to ensure the evaporation rate is consistent), both for the same grid point density as the droplets presented in fig. 6.2 and for a greater density. The results of these simulations are presented in fig. 6.3. The left column shows the results for a droplet with an initial base radius, $a = 20$ grid points equivalent to that for the 5×5 array. The right column shows an equivalent size droplet with $a = 40$ grid points resulting in a greater number and density of grid points in the droplet's interface (both after evaporating until $t = 0.05$). By comparing these two columns for a profile slice through the centre of the droplet (first row) and top view slice through the droplet's substrate contact area (second row), it can be seen that the interface becomes smoother for the higher grid point density, when viewed from both directions. This demonstrates the requirement for finer meshes in order to eliminate these distortions. To check if these distortion would be expected at very early times experimentally the timescale for capillarity ($\tau_\gamma = \sqrt{\rho_l r^3/\gamma}$) can be compared to the timescale of evaporation (controlled predominately by diffusion) ($\tau_D = r^2/D$). For water at standard temperature and pressure, $\tau_D \sim 10^{-2}$ and $\tau_\gamma \sim 10^{-7}$ and therefore these distortions would be expected to be smoothed out by surface tension as $\tau_\gamma \ll \tau_D$. This further indicates the origin of these distortions are numerical.

6.2.2 Evaporation rates

Despite this limitation, the evaporation rates of each droplet can be examined to determine if they correspond to their local confinement within the array, as observed experimentally in previous chapters. Fig. 6.4 plots the droplet volumes normalised by their initial values against time. For square arrays the droplets in symmetric confinement can be distinguished as they all have unique radial distances from the centre of the array. By calculating this radial distance the droplets can be coloured by their distinct confinements with droplets of the same colour expected to evaporate at the same rate. These colours are indicated by the inset image and correspond to the same colour scatter points in the graph. Generally the least confined at the corners and edges of the array evaporate the fastest consistent with diffusive theory. Interestingly the light green droplets immediately adjacent to the corners begin to overtake these yellow droplets. This is likely caused by variations in

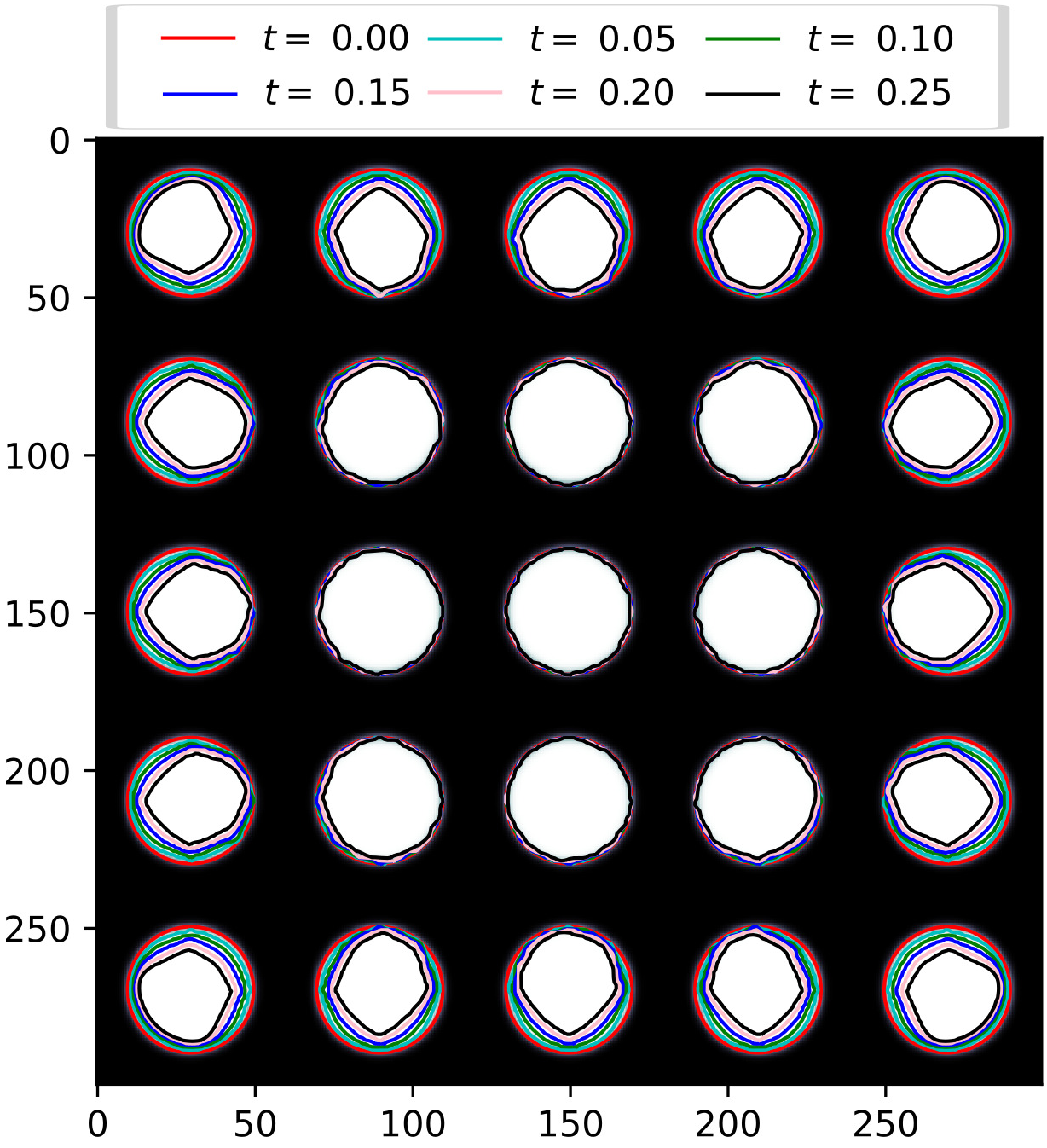

Figure 6.2: Position of the droplet contact lines of a 5×5 droplet array at different dimensionless times t, indicated by the different colours in the legend. The axes are labelled by the number of grid points.

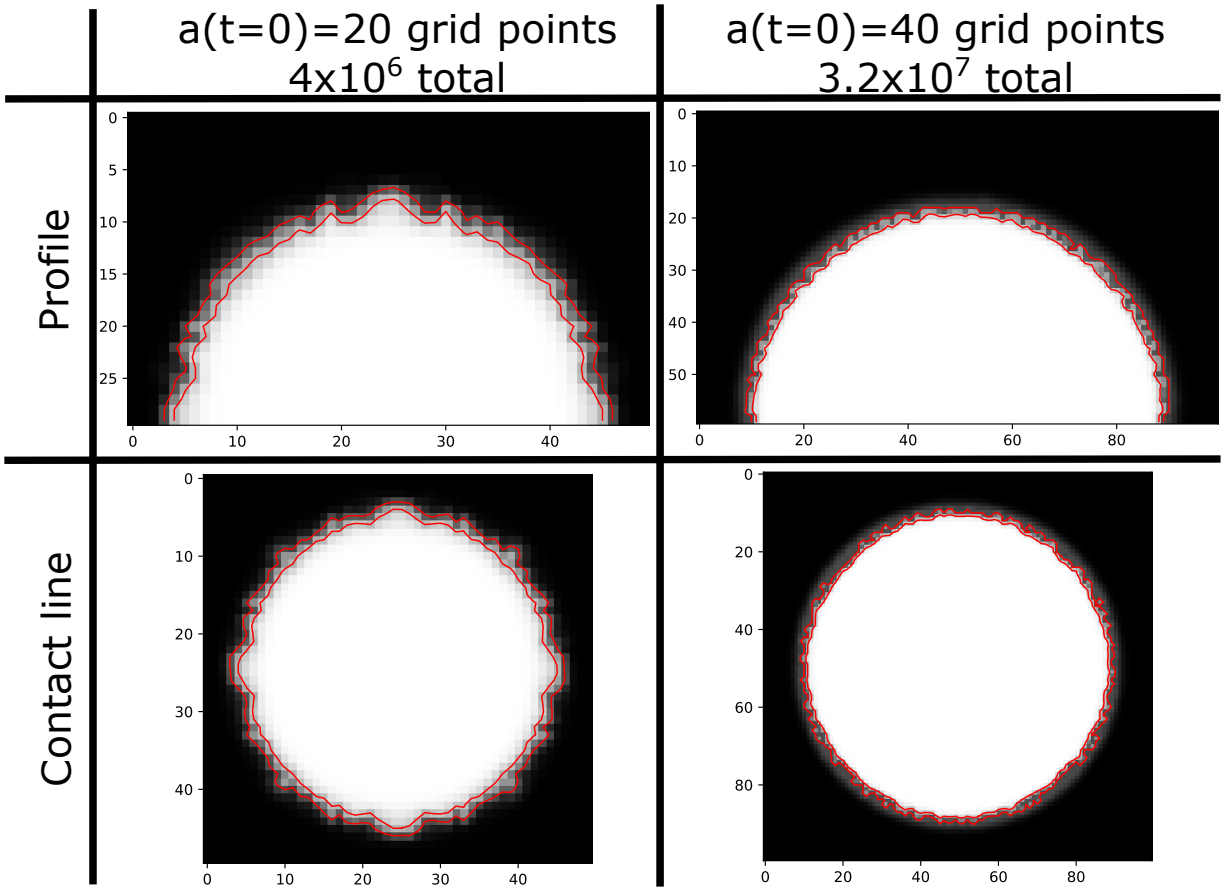

Figure 6.3: Comparison of the interface fluctuations for an isolated droplet with an initial base radius of 20 grid points (left column) and 40 (right column), both in a $200 \times 400 \times 400$ domain. The profile (top row) and contact base (bottom row) slices of the droplets are shown with red lines indicating the $c_l = 0.3$ and 0.7 contours. The axes of the inner figures represent the number of grid points.

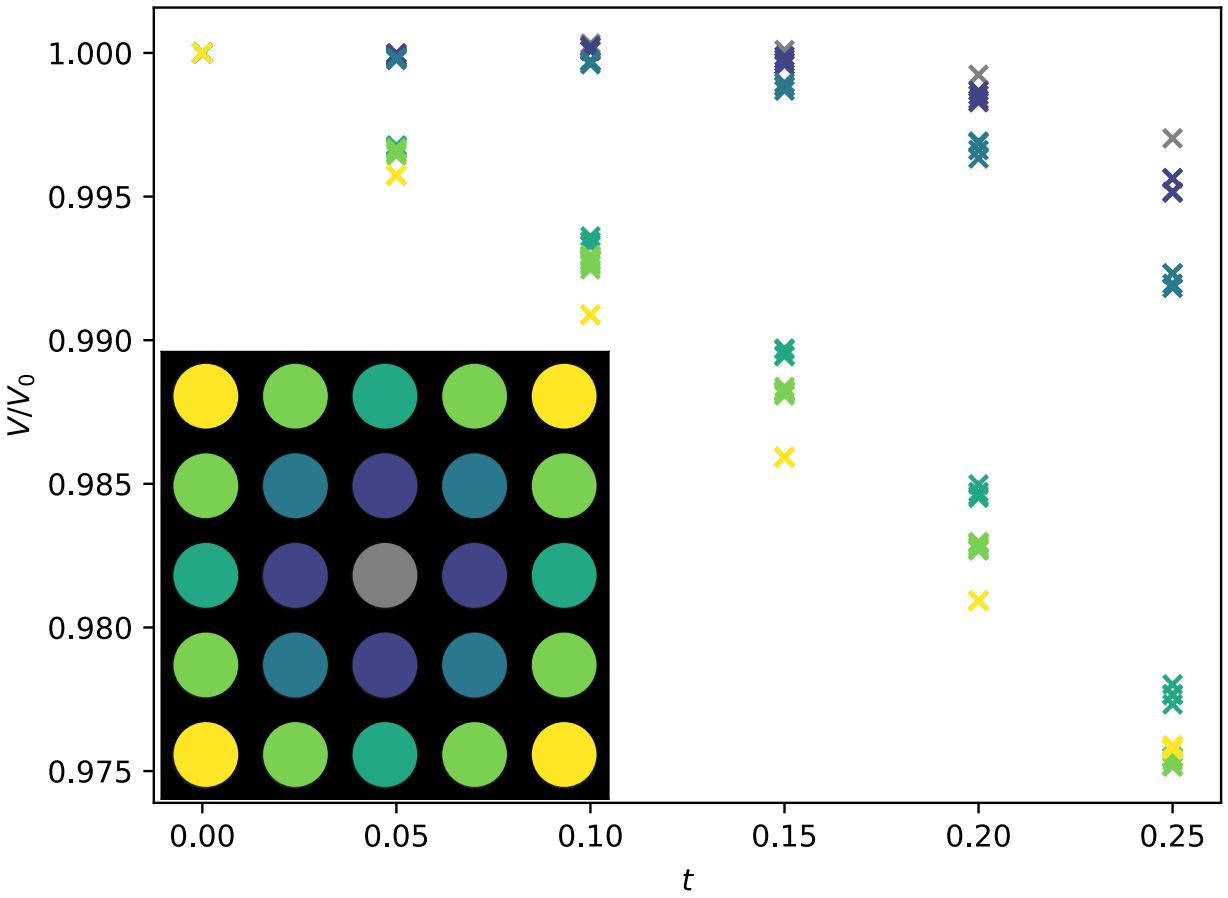

Figure 6.4: Normalised volume of each droplet in the 5×5 array against dimensionless t. The droplets are coloured in the inset by their radial position in the array indicating droplets in distinct confinements. The corresponding data points on the graph are also coloured according to the inset.

temperature in this early stage evaporation, with the fastest evaporating droplet initially cooling the most. At these early times each field is still adapting from its initial condition, it would be expected that if the simulation was run for longer the yellow droplets would return to being the fastest. It is worth noticing that the amount of volume evaporated is only at maximum 2.5% of the initial value.

One consideration for ensuring droplet evaporation is comparable to experiment, as shown by previous single droplet studies [35], is to prevent the droplets interacting with the boundaries. To achieve this the boundary must be placed sufficiently far away from the droplet to avoid significant removal or accumulation of vapour (depending on the choice of boundary conditions). Due to limitations on the number of grid points which can be simulated this cannot be achieved and there is accumulation of vapour at the boundaries. This is also the reason why the simulations cannot be easily compared to the existing

diffusive theoretical models as in previous chapters.

In order to check that the differential evaporation rates are not numerical artefacts which are caused by being in close proximity to the boundaries, a similar simulation is conducted for a 3×3 array of droplets with the boundaries placed a distance $s/2$ from the edge of the array ($400 \times 180 \times 180$ grid points). Because the boundary conditions are periodic this simulates nine droplets of an infinitely repeating droplet grid. Therefore all should evaporate at the same rate, as each droplet will be in symmetric confinement, as the array has no edge. The results of the periodic domain are presented in fig. 6.5 with the V/V_0 range on the y-axis set to the same as fig. 6.4. It can be seen that the evaporation rates of the droplets are much lower which is expected as the droplets at the edge no longer have additional space to evaporate into. The evaporation is purely due to vertical vapour transport, as the space between droplets is saturated. There is no clear difference between the droplets (the data points overlap), consistent with the droplets now being in equivalent confinements, experiencing the same vapour shielding effect.

It is also interesting to investigate whether the asymmetric distortions observed in fig. 6.2 are related to the boundaries or are due to droplet-droplet interactions. Fig. 6.6 shows the contact lines of each droplet in time for the same simulation. There is minimal change in their position and the lines lie over the top of one another. Additionally there is also no evidence of asymmetry in their shape. If the distortions were caused by proximity to the boundaries the edge droplets should still have become asymmetric. Therefore it can be concluded that the droplet distortions in the 5×5 simulation above are caused by their reduced confinement and faster evaporation. The previous asymmetries are caused by inhomogenous phase change ($\dot{m}$) on the droplet's interface, due to the local vapour shielding effect. This diffusive shielding interaction is present within the model even at early times. The results qualitatively show that which was observed experimentally in chapter 3 (and by other authors, discussed in chapter 2 section). 1.8).

A further set of $N \times N$ simulations of droplet arrays are conducted for $N = 7, 9$ and 11, with the same size domain as the 5×5 array above. The droplets are centred in the domain and the spacing between them remained $s = 3r$. A top-down image of the initialised droplets within the domain for each simulation is given in fig. 6.7. The results of these simulations can be compared for the total amount of evaporation. The average reduction of volume of each droplet ($\Delta V/N^2$) for each simulation after $t = 0.25$ is plotted verses coverage fraction of the base of the domain ($N^2\pi r^2/L_x L_y$). Fig. 6.8 shows that the average

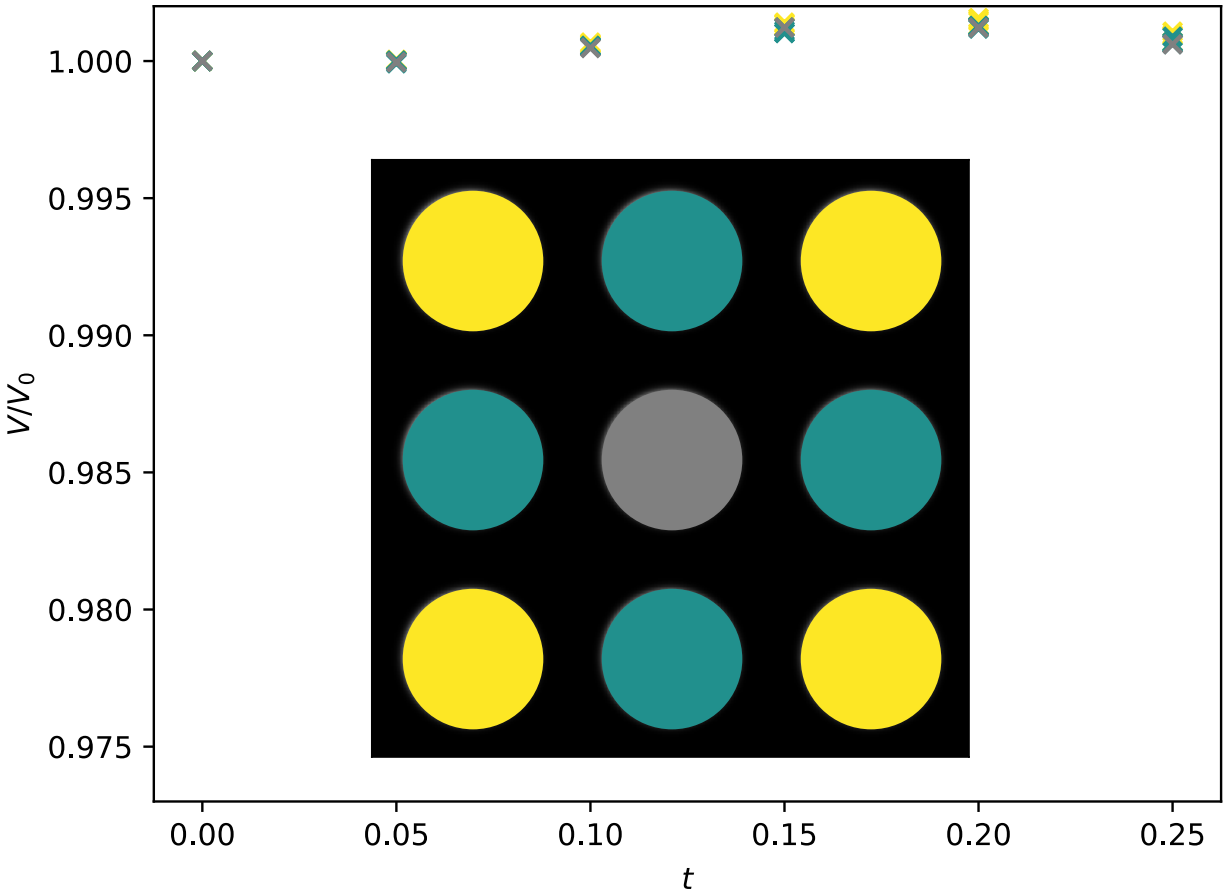

Figure 6.5: V/V_0 of each droplet in the 3×3 periodic array against dimensionless t. The y axis range is set to the same as fig. 6.4 for comparison. The droplets are coloured in the inset by their radial position in the array indicating droplets in distinct confinements. The corresponding data points on the graph are also coloured according to the inset.

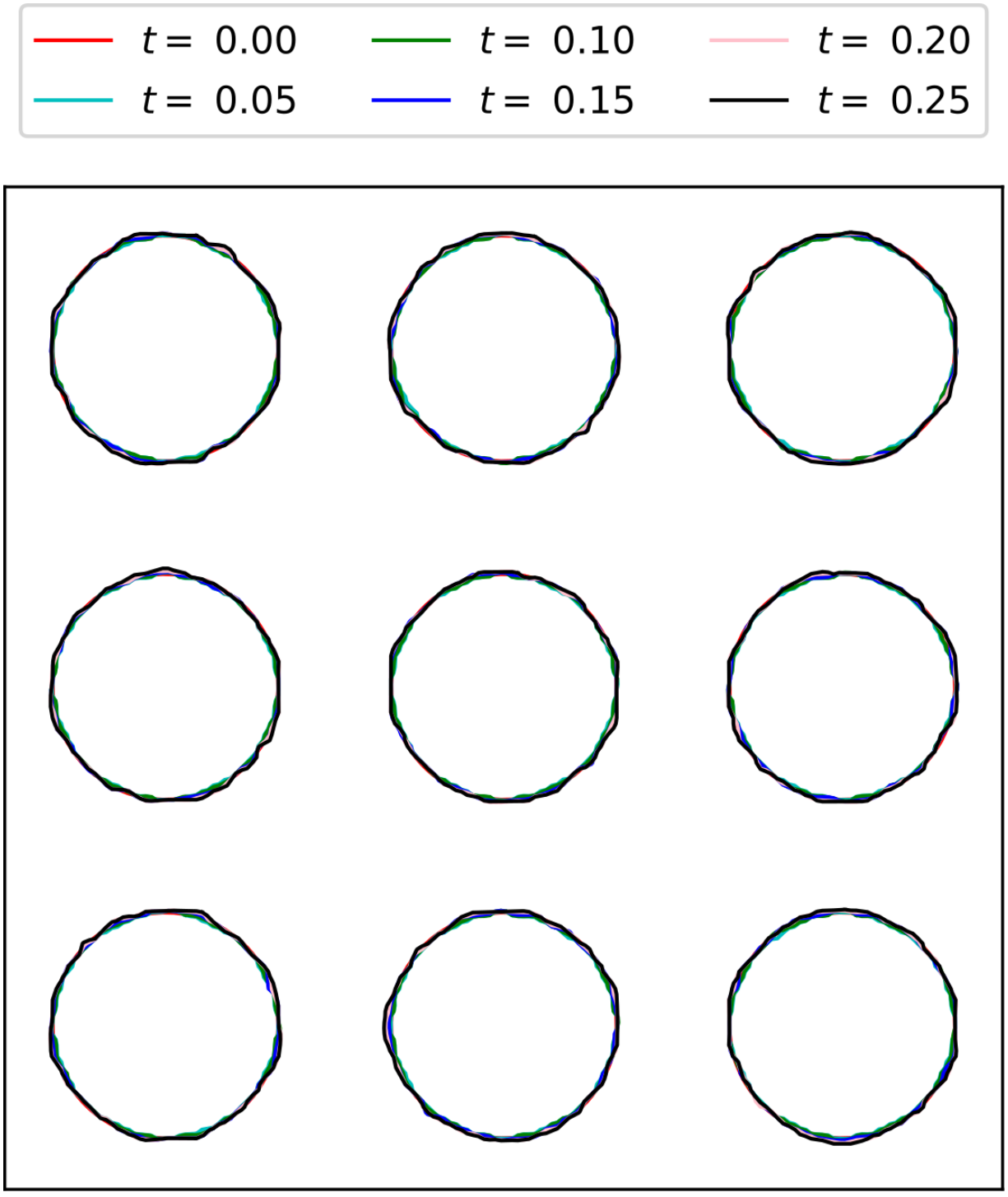

Figure 6.6: Contact line positions against dimensionless t of the 3×3 periodic simulation in fig. 6.5.

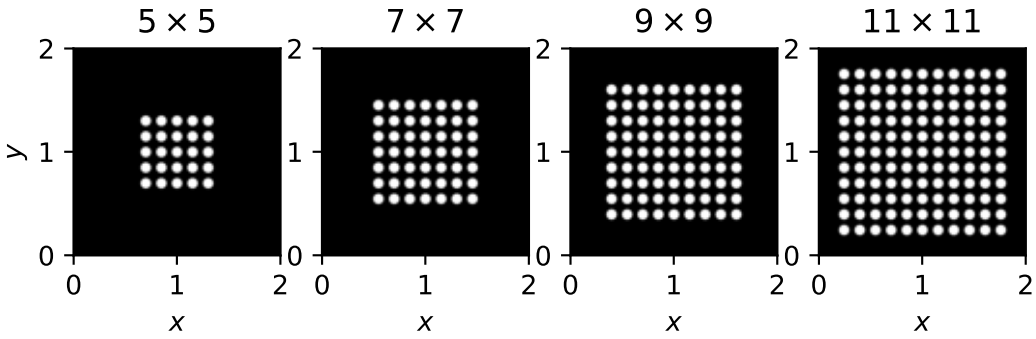

Figure 6.7: $N \times N$ initialised droplet arrays within the simulated domain. The white circles indicate the position of each droplet.

evaporation of each droplet decreases as the number of droplets increases. This is because the amount of free space for the vapour to diffuse into is reducing as N increases because the droplets are approaching the periodic boundaries. The red data point represents the 3×3 array with the periodic boundaries placed $s/2$ from the edge of the array on both sides, with the height of the domain kept the same. This gives the evaporation of the droplets due purely to the vertical diffusion away from the substrate. The value of $\Delta V/N^2$ for this point is 2.07×10^{-12} indicating that the additional space around the edge of the array contributes most of the evaporation.

6.2.3 Maintaining interface saturation

A method to calculate the amount of phase change at each grid point in the interface was described in section 6.1.1.2. It is important that this phase change calculation maintains stable saturation in the interface throughout time. For the simulations conducted in this chapter the average volume fraction of vapour across all points on the interface ($\bar{c_v}$) is divided by the average saturation volume fraction in the interface ($\bar{c_v^s}$). These values are plotted against time (t) in fig. 6.9. It can be seen that eq. 6.19 reliably calculates the correct amount of phase change to saturate the interface for all of the simulations. The black dashed lines show that it achieves this to within $\pm0.3\%$ of perfect saturation (indicated by the solid black line).

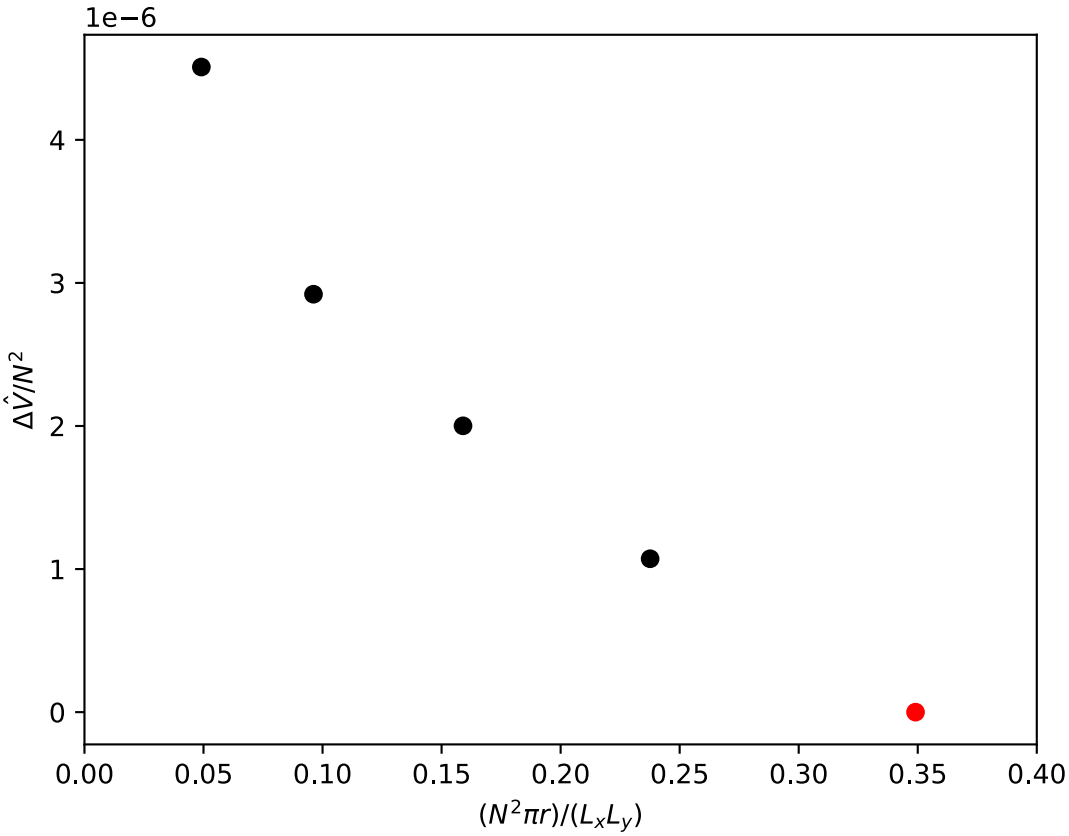

Figure 6.8: The average reduction of volume of each droplet $\Delta V/N^2$ after $t = 0.25$ verses coverage fraction of the base of the domain $(N^2\pi r^2)/(L_xL_y)$. Each data point represents a simulation of an $N \times N$ array of droplets where $N = 5, 7, 9$ and 11 (black data). The red data point represents $N = 3$ with the boundaries of the domain positioned such that the array is infinitely repeating.

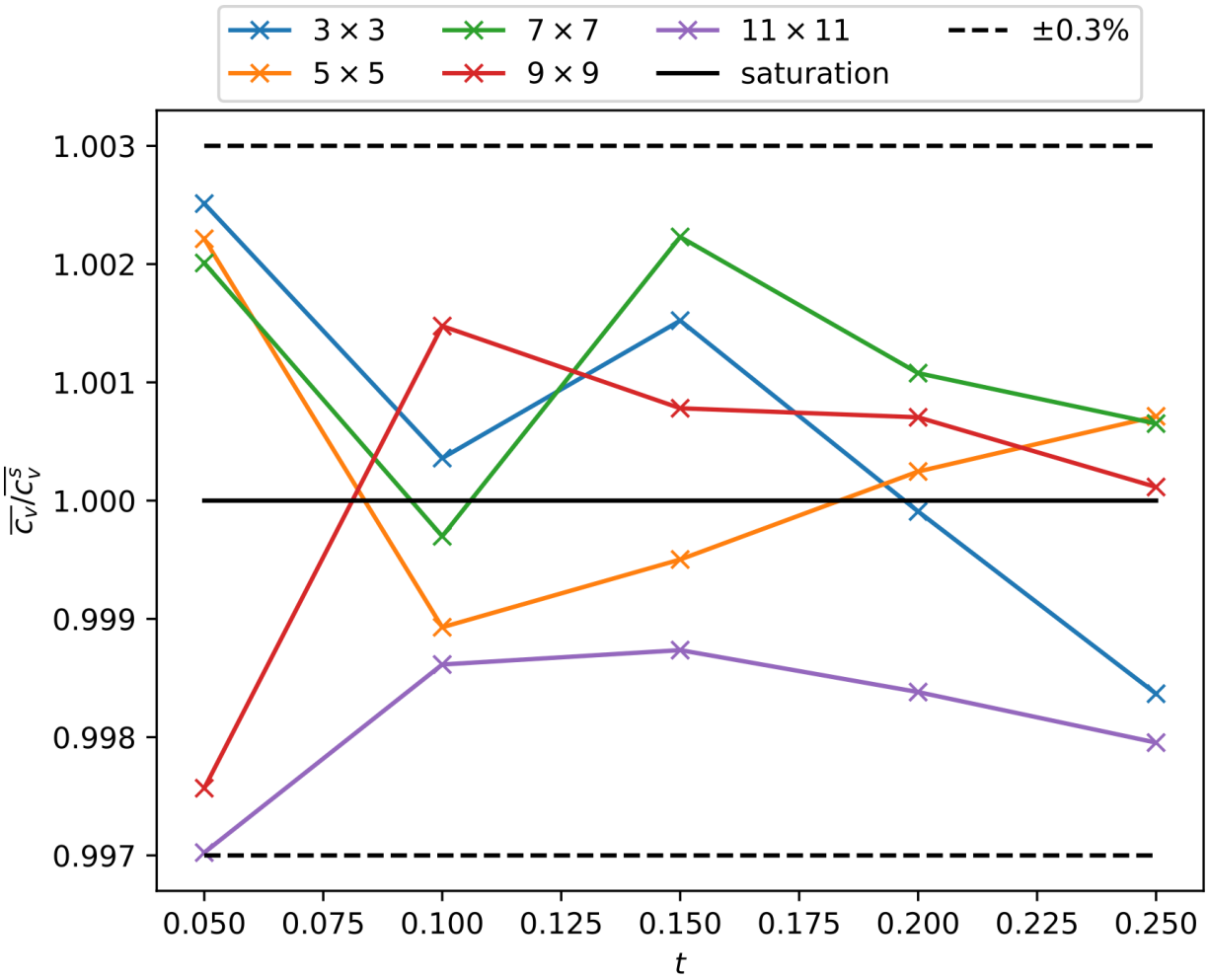

Figure 6.9: Mean saturation in the droplet interfaces maintained by eq. 6.19 verses time, for the simulations presented in this chapter.

6.3 Conclusions

In this chapter direct numerical simulations of multiple droplets were conducted using a diffuse interface model called TPLS. The phase change at the interface was successfully modelled, constraining phase change to the interface and maintaining it at the saturation concentration. The diffusive shielding effect was observed to be captured by the model and droplets were shown to evaporate at different rates depending on their confinement and proximity to the edge of the array. $N \times N$ droplet arrays were simulated and the influence of edge and the vertical diffusion above the droplets were investigated. It was shown that the amount of evaporation due to reduced confinement at the edge is responsible for most of the reduction in volume.

Chapter 7

Conclusion and future work

7.1 Conclusion

In this thesis the evaporation of multiple droplets has been investigated experimentally and numerically. In order to facilitate these experiments a new technique needed to be developed, to make capturing the volumes from arbitrary arrays of droplets possible. This was named the Pattern Distortion technique and uses the droplet's lens-like nature to image a pattern of dots. The magnification was then measured and used to infer the droplet's geometry. Experiments exploiting this technique were compared with existing recent theoretical models and their validity has been tested. The comparisons have shown that the models work well for small arrays of millimetre-sized droplets, capturing the diffusive dynamics which dominate the evaporation. It has also be shown that the diffusive theoretical models begin to break down and can no longer make successful predictions. This indicates the presence of non-diffusive dynamics becoming more significant and it is shown that these are amplified by increasing the length scale of the array. The possible non-diffusive candidates are discussed, the most likely being natural convection in the vapour above the droplets.

In addition to this it is shown that heated arrays are also not captured by the diffusive theories. The reason for this is again discussed, with phase change potentially becoming the rate limiting evaporation process.

Breath figures have also been investigated containing ~ 1000, micrometre-sized droplets evaporating in confinement. The size and dynamics of these droplets are successfully tracked and analysed. It was shown that these droplets interact and can even redis-

tribute their volumes through the vapour. This redistribution is explained to be caused by the Kelvin effect, which results in concentration gradients from the smaller to the larger droplets. These concentration gradients lead to a diffusive flux, with big droplets growing at the expense of their smaller neighbouring droplets. The redistribution dynamics in these arrays were then modelled using a simple mean field theory (MFT) model. The MFT couples the collective evaporative flux from each of the droplets and the ambient vapour concentration inside the container. The rates at which the droplets grow or shrink therefore depend on the interactions of each of these droplets, with this ambient concentration. Comparisons of the MFT and the experimental data captured the general redistribution behaviour well, both qualitatively and quantitatively.

Finally, direct numerical simulations have been conducted using the TPLS model. Multiple droplet evaporation was successfully simulated with droplet volumes reducing. The amount of phase change in the interface was modelled, maintaining saturation during evaporation. It is shown that the model contains the diffusive shielding effect which is present experimentally and droplets evaporate at different rates due to their local confinement in the array.

To summarise the evaporation mechanisms investigated in this thesis, the approximate regimes in which they are dominant have been plotted in the phase diagram in fig. 7.1. The diagram should be interpreted as relating the evaporation of water droplets (or arrays) on thermally conductive surfaces. The labelled horizontal arrows indicate the mechanism(s) which are significant over each length scale. The solid horizontal lines indicates how higher and lower temperature regimes (compared with room temperature, $T \approx 21^{\circ}\mathrm{C}$) alters the mechanisms controlling the evaporation. Of course the diagram is very approximate and the exact values defining the high and low temperature regimes are unknown.

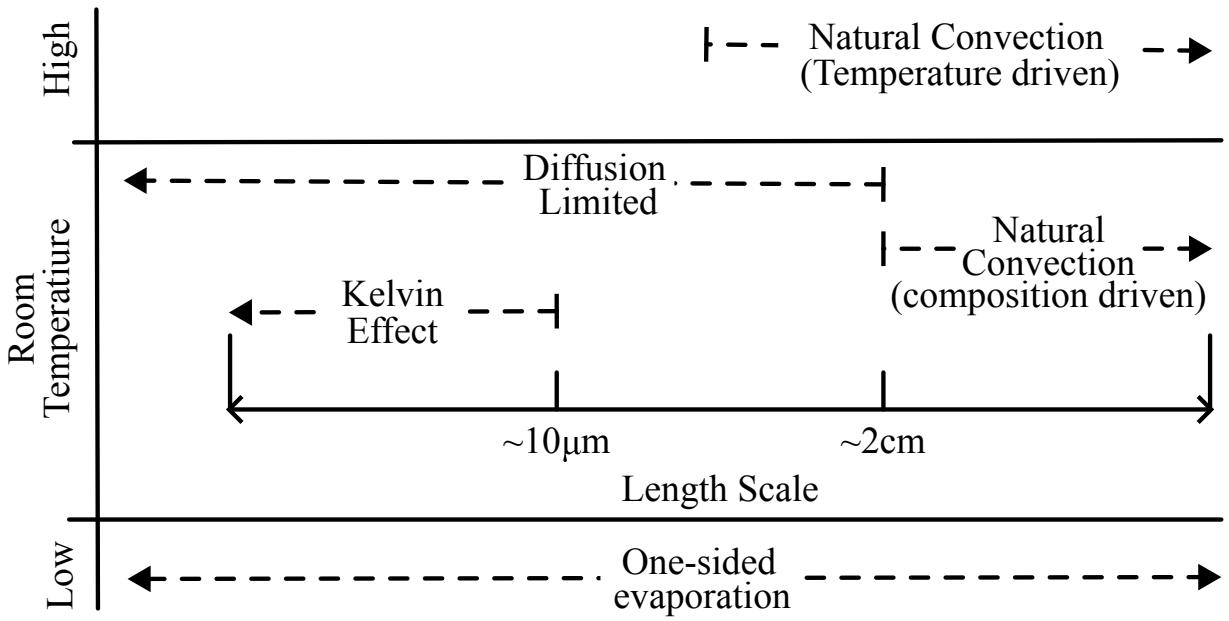

Figure 7.1: Evaporation phase diagram indicating the dominant physical mechanisms for different length scales (x axis) at low, room and high temperatures.

7.2 Future work

This thesis will hopefully lead to future work in many different directions. The work contained within the thesis contains experimental work on multiple droplet evaporation and has begun to reveal the areas in which more research is needed. These experiments indicate where the current theories no longer correctly predict the evaporation. Future work is needed to determine the origin of the non-diffusive mechanisms which lead to the disagreement. The results for experiments and simulations can be combined and help guide theoretical development of the models to account for these effects.

In the below sections specific future work both experimentally and numerically are discussed. Each section refers to the future work which might follow each of the chapters in this thesis.

7.2.1 Pattern Distortion technique

There are many ways in which the Pattern Distortion technique could be developed so it can be used for different applications. These include: liquid lenses, composite lenses, non-spherical interfaces and measuring composition of binary mixtures. These ideas are discussed in detail in chapter 2 section 2.5.

The Pattern Distortion technique was developed to capture arbitrary arrays of evaporating droplets, in either evaporation mode (CA or CR). For CR mode the technique worked very well, however for even larger arrays of droplets, pinning the contact lines reliably proved difficult. Because of this the droplets evaporated in CA mode and ensuring a circular contact line and tracking it, was not attempted. Future work could focus on developing a pinning technique for large numbers of multiple droplets. There are several methods which could be used to do this. For example, lithography could be used to create hydrophilic rings onto a hydrophobic substrate and droplets could be placed on these rings. The contact line of the droplet would want to stay inside the ring at all times. Because the droplet would not want to spread outside the ring it would potentially be able to take on very high initial contact angles. Additionally close to the end of evaporation, the droplet would not want to recede into the hydrophobic centre and would therefore have a very low receding angle. With this ability the droplets base radius would be well known, which is an important parameter for determining its volume with Pattern Distortion and for controlling its evaporation rate. An alternative approach would be to extend the measurements to CA evaporation. As mentioned before, this would require contact lines to be tracked and remain circular. In order to ensure this circularity, low hysteresis substrates could be used to prevent the contact line experiencing asymmetric pinning. These substrates include slippery liquid infused (SLIP) surfaces [108] or slippery omniphobic covalently attached liquid (SOCAL) surfaces [109].

Precise knowledge of the droplet's contact base radius would allow better evaluation of the resolution limits which can be achieved using the Pattern Distortion technique. If these limits are very high it might present a better approach to the traditional side imaging as it measures a contact angle value from all points on the contact line. Side cameras can only see two points on this line at any one time, making it more susceptible to uncertainty. Development of the contact line control would then make it possible to measure the droplet volumes from large arrays of multiple droplets. As proof of principle of this, demonstrating the technique's ability to extend to large arrays but without further analysis, a $96 \times 96\,\mathrm{mm}$ square array with $N = 1089$ droplets with a separation of $s = 3\,\mathrm{mm}$ was dispensed. An image of the array was taken and is presented in fig. 7.2. The zoomed in inset shows the resolution is high enough to capture the magnified dots within each droplet. It is therefore possible to conduct Pattern Distortion experiments of droplet arrays of this size and extract not just lifetimes but also droplet volumes.

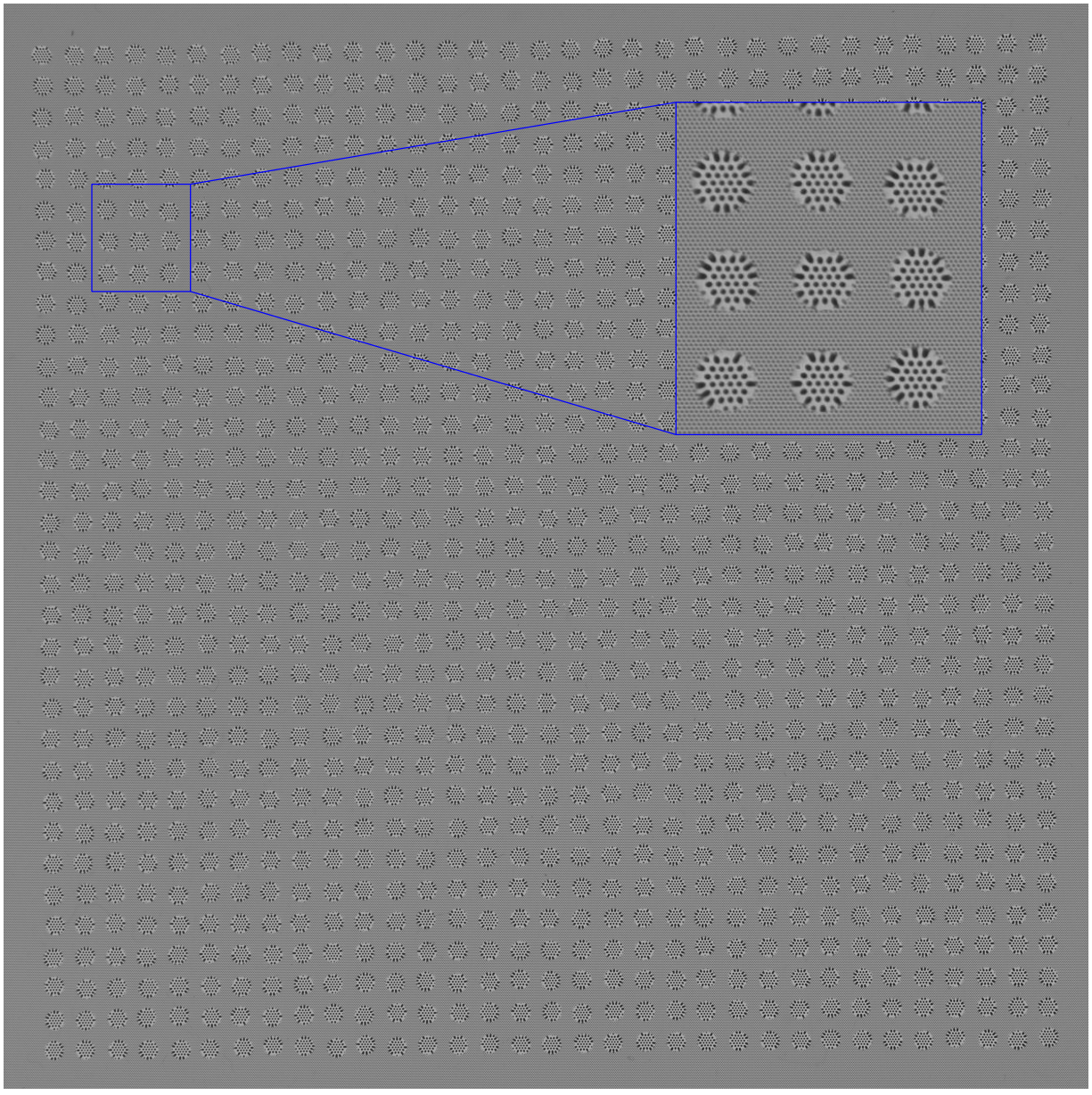

Figure 7.2: First frame of a $N = 1089$ square array of droplets on a hexagonal dot pattern. The magnification of the dots in each droplet can be resolved by the camera, demonstrating extracting Pattern Distortion data from large arrays.

7.3 Diffusive evaporation

The results of chapter 3 showed that the diffusive models work well to make predictions of the evaporation of small arbitrary droplet arrays. Within this diffusive regime other comparisons can be made to test the applicability of the model. One such comparison is the evaporation of droplets which are non-spherically capped, either distorted by gravity or taking on different contact line shapes such as triangles or ovals. Droplets which take on these shapes are more realistic, for example rain droplets tend to have non-circular contact lines and be greater than the capillary length in size. To do this the contact lines can be pinned into different shapes and larger droplets can be dispensed.

In addition to this, droplet evaporation models in this thesis have been compared by normalising the data to remove the influence of changing ambient conditions. To compare if the models can make accurate predictions of the evaporation in physical units, experiments could be conducted within controlled environments in which the humidity and temperature were fixed.

7.4 Non-diffusive evaporation

In chapter 4 it was observed that arrays began to evaporate with non-diffusive dynamics. Future work should be focused on determining the origin of these non-diffusive effects and which assumptions made by the current diffusive models are no longer valid. It was suggested that one such candidate was natural convection. More investigation into the formation of convective plumes above the droplets is needed. This could be done by rotating the experiment upside down which would reverse the direction in which gravity advects the saturated air. In both cases it is important that the vapour concentration is imaged and methods exist in order to achieve this. These imaging methods would allow the formation of plumes and the distribution of vapour to be coupled with the evaporation rates of each droplet. Previous work has shown that Mach-Zehnder interferometers [110] are capable of measuring the concentration of vapour above evaporating liquids as well as Schlieren imagining techniques [111].

In this chapter it was also shown that heating arrays leads to non-diffusive evaporation. Experimental studies which vary the substrate thermal conductivity in which the droplets evaporate from could be conducted. The transition from diffusion limited evaporation

and one-sided evaporation could then be determined for multiple droplets. For complete one-sided evaporation, droplets should stop experiencing the vapour shielding effect and should therefore begin to evaporate homogeneously.

7.5 Breath figures

In chapter 5 the redistribution dynamics were attributed to the Kelvin effect. Future work could determine the size and distribution of droplets in which no growth is observed. This would inform when it is important to include the Kelvin effect in the theories.

As discussed previously in section 1.8.1 the sessile droplet literature seems to has made little connection to the fuel droplet research which already exists. Fuel combustion literature has developed Point Source Methods (PSM) of characterising evaporation of fuel droplets. Comparisons of these models to the diffusive models of Wray et al. [1] and Masoud et al. [55] are necessary. If PSM can accurately capture the evaporation rates of sessile droplets, they represent an avenue for theorists to explore the extension of the models to 3D multiple droplet evaporation [64]. Also in this chapter, the importance of the Raoult effect to the evaporation was shown, as well as by the spider in Appendix D. Experiments which investigated droplets with multiple components would be interesting as the diffusive shielding effect and the Raoult effect would compete. In this case, the least confined droplets would evaporate the fastest, reducing in volume and as this happens the concentration of solute would increase and the Raoult effect would act to slow its evaporation. Different concentrations could be used to control the dynamics of these two effects and could be used to stabilise the differential evaporation rates and control their dynamics.

7.6 Direct numerical simulations

In chapter 6 simulations which contained the diffusive shielding effect were shown. Future development of the model to allow these simulations to match the current experiments would provide valuable insights into quantities which are difficult to measure experimentally.

With access to these fields the flow in the surrounding vapour due to natural convection can be visualised and connected to the droplet's evaporation. The formation of the

plumes which form at different Ra could be investigated and compared to the experimental observations. Additionally, the temperature field would allow for the cooling effect of the droplets to be monitored. The changing temperature could be quantified and used to determine when droplet evaporation can no longer be considered isothermal. The velocity field inside the droplet could also be used to investigate how multiple droplets influence the internal flow.

To do this the model needs to be developed. Firstly, to allow for Dirichlet (fixed value) boundary conditions on the walls of the domain. This feature would enhance the droplet evaporation rates and allow for simulations to be run longer into the array's evaporation lifetime. Secondly, to allow for larger domains to be simulated. Further separating the droplets from the boundaries would also enhance evaporation rates. This is important for making quantitative comparisons with experiments and the diffusive theories. One of the challenges of doing this is that as the arrays become bigger the domain has to increase in size too. As the grid point resolution in the interface must be maintained, the total number of grids points becomes prohibitively costly to simulate. One possible extension of the model is to allow for adaptive grids. These grids would allow for high resolution near the interface, required to resolve the phase change as well as the surface tension, but sparser resolution far from the droplet where there are low concentration gradients [112]. The challenge with dynamic grids is that they require additional computation to manage the adaption, which could be prohibitive.

Bibliography

[1] A. W. Wray, B. R. Duffy, and S. K. Wilson. "Competitive evaporation of multiple sessile droplets". *Journal of Fluid Mechanics* 884 (2019). DOI: 10.1017/jfm.2019.919.

[2] H. Masoud and J. D. Felske. "Analytical solution for Stokes flow inside an evaporating sessile drop: Spherical and cylindrical cap shapes". *Physics of Fluids* 21.4 (2009). DOI: 10.1063/1.3112002.

[3] L. M. Skinner and J. R. Sambles. "Vapour pressure over curved surfaces-the Kelvin equation". *Contemporary Physics* 12.6 (1971). DOI: 10.1080/00107517108205661.

[4] A. M. Edwards, J. Cater, J. J. Kilbride, P. Le Minter, C. V. Brown, D. J. Fairhurst, and F. F. Ouali. "Interferometric measurement of co-operative evaporation in 2D droplet arrays". *Applied Physics Letters* 119.15 (2021). DOI: 10.1063/5.0064924.

[5] J. J. Kilbride, K. E. Fagg, F. F. Ouali, and D. J. Fairhurst. "Pattern-Distortion Technique: Using Liquid-Lens Magnification to Extract Volumes of Individual Droplets or Bubbles within Evaporating Two-Dimensional Arrays". *Physical Review Applied* 19.4 (2023). DOI: 10.1103/PhysRevApplied.19.044030.

[6] A. Iqtidar, J. J. Kilbride, F. F. Ouali, D. J. Fairhurst, H. A. Stone, and H. Masoud. "Drying dynamics of sessile-droplet arrays". *Physical Review Fluids* 8.1 (2023). DOI: 10.1103/PhysRevFluids.8.013602.

[7] H. Y. Erbil. "Evaporation of pure liquid sessile and spherical suspended drops: A review". *Advances in Colloid and Interface Science* 170.1-2 (2012). DOI: 10.1016/j.cis.2011.12.006.

[8] R. Bhardwaj and A. Agrawal. "Likelihood of survival of coronavirus in a respiratory droplet deposited on a solid surface". *Physics of Fluids* 32.6 (2020). DOI: 10.1063/5.0012009.

[9] R. D. Deegan, O. Bakajin, T. F. Dupont, G. Huber, S. R. Nagel, and T. A. Witten. "Capillary flow as the cause of ring stains from dried liquid drops". *Nature* 389.6653 (1997). DOI: 10.1038/39827.

[10] T. K. Pradhan and P. K. Panigrahi. "Deposition pattern of interacting droplets". *Colloids and Surfaces A: Physicochemical and Engineering Aspects* 482 (2015). DOI: 10.1016/j.colsurfa.2015.07.013.

[11] A. W. Wray, P. S. Wray, B. R. Duffy, and S. K. Wilson. "Contact-line deposits from multiple evaporating droplets". *Physical Review Fluids* 6.7 (2021). DOI: 10.1103/PhysRevFluids.6.073604.

[12] F. Yang, P. Kollias, R. A. Shaw, and A. M. Vogelmann. "Cloud droplet size distribution broadening during diffusional growth: Ripening amplified by deactivation and reactivation". *Atmospheric Chemistry and Physics* 18.10 (2018). DOI: 10.5194/acp-18-7313-2018.

[13] J. Wang, X. Huang, X. Qiao, D. Ju, and C. Sun. "Experimental study on evaporation characteristics of single and multiple fuel droplets". *Journal of the Energy Institute* 93.4 (2020). DOI: 10.1016/j.joei.2020.01.009.

[14] A. R. Pati, A. Panda, Lily, B. Munshi, A. Kumar, A. Sahoo, S. Ghosh, and S. S. Mohapatra. "Dropwise evaporative cooling of hot water: A novel methodology to enhance heat transfer rate at very high surface temperatures". *International Journal of Thermal Sciences* 127 (2018). DOI: 10.1016/J.IJTHERMALSCI.2018.01.028.

[15] A. Fick. " V. On liquid diffusion ". *The London, Edinburgh, and Dublin Philosophical Magazine and Journal of Science* 10.63 (1855). DOI: 10.1080/14786445508641925.

[16] J. L. Monteith and M. H. Unsworth. Transport of Heat, Mass, and Momentum. Academic Press, 2013, pp. 25–35. ISBN: 978-0-12-386910-4. DOI: 10.1016/B978-0-12-386910-4.00003-2.

[17] B. D. Storey and O. College. "Fluid dynamics and heat transfer: An introduction to the fundamentals". *MIT Open Course* (2015).

[18] T. E. Faber. "Instabilities". *Fluid Dynamics for Physicists*. Cambridge University Press, (2012), pp. 289–342. DOI: 10.1017/cbo9780511806735.010.

[19] J. Safarian and T. A. Engh. "Vacuum evaporation of pure metals". *Metallurgical and Materials Transactions A: Physical Metallurgy and Materials Science* 44.2 (2013). DOI: 10.1007/s11661-012-1464-2.

[20] R. P. Feynman, R. B. Leighton, and M. Sands. The Feynman Lectures on Physics -The New Millennium Edition (Volume I). 2010.

[21] E. S. Benilov. "Does Maxwell's hypothesis of air saturation near the surface of evaporating liquid hold at all spatial scales?" *Journal of Fluid Mechanics* 971 (2023). DOI: 10.1017/jfm.2023.667.

[22] R. A. Silverman and N. N. Lebedev. Special Functions and Their Applications. Dover Publications, 1972. ISBN: 0-486-60624-4.

[23] J. D. Jackson. Jackson - Classical Electrodynamics. John Wiley and Sons, 1962, pp. 89–93. ISBN: 9780471309321.

[24] J. M. Stauber, S. K. Wilson, B. R. Duffy, and K. Sefiane. "Evaporation of droplets on strongly hydrophobic substrates". *Langmuir* 31.12 (2015). DOI: 10.1021/acs.langmuir.5b00286.

[25] R. G. Picknett and R. Bexon. "The Evaporation of Sessile or Pendant Drops in Still Air" (1977). DOI: 10.1016/0021-9797(77)90396-4.

[26] C. Bourges-Monnier and M. E. R. Shanahan. *Influence of Evaporation on Contact Angle*. Tech. rep. 1995, pp. 2820–2829. DOI: 10.1021/la00007a076.

[27] H. Hu and R. G. Larson. "Evaporation of a sessile droplet on a substrate". *Journal of Physical Chemistry B* 106.6 (2002). DOI: 10.1021/jp0118322.

[28] D. Hu, H. Wu, and Z. Liu. "Effect of liquid-vapor interface area on the evaporation rate of small sessile droplets". *International Journal of Thermal Sciences* 84 (2014). DOI: 10.1016/j.ijthermalsci.2014.05.024.

[29] A. Wray and M. Moore. "A novel asymptotically consistent approximation for integral evaporation from a spherical cap droplet". *Journal of Engineering Mathematics* 146.1 (2024). DOI: 10.1007/s10665-024-10355-1.

[30] K. Stephan and A. Laesecke. "The Thermal Conductivity of Fluid Air". *Journal of Physical and Chemical Reference Data* 14.1 (1985). DOI: 10.1063/1.555749.

[31] M. Simoncelli, F. Mauri, and N. Marzari. "Thermal conductivity of glasses: first-principles theory and applications". *npj Computational Materials* 9.1 (2023). DOI: 10.1038/s41524-023-01033-4.

[32] I. Dinçer and C. Zamfirescu. "Appendix B Thermophysical Properties of Water". *Drying Phenomena*. (2015). DOI: 10.1002/9781118534892.app2.

[33] Y. O. Popov. "Evaporative deposition patterns: Spatial dimensions of the deposit". *Physical Review E - Statistical, Nonlinear, and Soft Matter Physics* 71.3 (2005). DOI: 10.1103/PhysRevE.71.036313.

[34] W. D. Ristenpart, P. G. Kim, C. Domingues, J. Wan, and H. A. Stone. "Influence of substrate conductivity on circulation reversal in evaporating drops". *Physical Review Letters* 99.23 (2007). DOI: 10.1103/PhysRevLett.99.234502.

[35] C. Diddens. "Detailed finite element method modeling of evaporating multi-component droplets". *Journal of Computational Physics* 340 (2017). DOI: 10.1016/j.jcp.2017.03.049.

[36] A. M. Edwards, P. S. Atkinson, C. S. Cheung, H. Liang, D. J. Fairhurst, and F. F. Ouali. "Density-Driven Flows in Evaporating Binary Liquid Droplets". *Physical Review Letters* 121.18 (2018). DOI: 10.1103/PhysRevLett.121.184501.

[37] T. S. B. Quang, F. Y. Leong, H. An, B. H. Tan, and C. D. Ohl. "Growth and wetting of water droplet condensed between micron-sized particles and substrate". *Scientific Reports* 6 (2016). DOI: 10.1038/srep30989.

[38] J. Rodríguez-Hernández and E. Bormashenko. Breath figures: Mechanisms of multi-scale patterning and strategies for fabrication and applications of microstructured functional porous surfaces. 2020. DOI: 10.1007/978-3-030-51136-4.

[39] C. M. Knobler and D. Beysens. "Growth of Breath Figures on Fluid Surfaces". *Europhysics Letters* 6.8 (1988). DOI: 10.1209/0295-5075/6/8/007.

[40] R. N. Leach, F Stevens, S. C. Langford, and J. T. Dickinson. "Dropwise Condensation: Experiments and Simulations of Nucleation and Growth of Water Drops in a Cooling System". *Langmuir* 22.21 (2006). DOI: 10.1021/la061901.

[41] G. Mao, B. Zhao, and K. Wang. "Condensation distribution and evolution characteristics of water vapor in annulus of flexible riser". *Journal of Petroleum Exploration and Production Technology* 13.8 (2023). DOI: 10.1007/s13202-023-01648-9.

[42] W. Thomson. "On the Equilibrium of Vapour at a Curved Surface of Liquid". *Proceedings of the Royal Society of Edinburgh* 7 (1872). DOI: 10.1017/s0370164600041729.

[43] F. M. Raoult. "Loi générale des tensions de vapeur des dissolvants". *CR Hebd. Seances Acad. Sci* 104 (1887).

[44] H. Köhler. "The nucleus in and the growth of hygroscopic droplets". *Transactions of the Faraday Society* 32 (1936). DOI: 10.1039/TF9363201152.

[45] O. Carrier, N. Shahidzadeh-Bonn, R. Zargar, M. Aytouna, M. Habibi, J. Eggers, and D. Bonn. "Evaporation of water: evaporation rate and collective effects". *Journal of Fluid Mechanics* 798 (2016). DOI: 10.1017/jfm.2016.356.

[46] L. Bansal, S. Hatte, S. Basu, and S. Chakraborty. "Universal evaporation dynamics of a confined sessile droplet". *Applied Physics Letters* 111.10 (2017). DOI: 10.1063/1.4996986.

[47] S. Hatte, K. Pandey, K. Pandey, S. Chakraborty, and S. Basu. "Universal evaporation dynamics of ordered arrays of sessile droplets". *Journal of Fluid Mechanics* 866 (2019). DOI: 10.1017/jfm.2019.105.

[48] F. G. Schofield, A. W. Wray, D. Pritchard, and S. K. Wilson. "The shielding effect extends the lifetimes of two-dimensional sessile droplets". *Journal of Engineering Mathematics* 120.1 (2020). DOI: 10.1007/s10665-019-10033-7.

[49] S. Michelin, E. Guérin, and E. Lauga. "Collective dissolution of microbubbles". *Physical Review Fluids* 3.4 (2018). DOI: 10.1103/PhysRevFluids.3.043601.

[50] J. H. Weijs and D. Lohse. "Why surface nanobubbles live for hours". *Physical Review Letters* 110.5 (2013). DOI: 10.1103/PhysRevLett.110.054501.

[51] G. Laghezza, E. Dietrich, J. M. Yeomans, R. Ledesma-Aguilar, E. S. Kooij, H. J. Zandvliet, and D. Lohse. "Collective and convective effects compete in patterns of dissolving surface droplets". *Soft Matter* 12.26 (2016). DOI: 10.1039/c6sm00767h.

[52] X. Zhu, R. Verzicco, X. Zhang, and D. Lohse. "Diffusive interaction of multiple surface nanobubbles: Shrinkage, growth, and coarsening". *Soft Matter* 14.11 (2018). DOI: 10.1039/c7sm02523h.

[53] K. L. Chong, Y. Li, C. S. Ng, R. Verzicco, and D. Lohse. "Convection-dominated dissolution for single and multiple immersed sessile droplets". *Journal of Fluid Mechanics* 892 (2020). DOI: 10.1017/jfm.2020.175.

[54] V. I. Fabrikant. "On the potential flow through membranes". *Zeitschrift für angewandte Mathematik und Physik ZAMP* 36.4 (1985). DOI: 10.1007/BF00945301.

[55] H. Masoud, P. D. Howell, and H. A. Stone. "Evaporation of multiple droplets". *Journal of Fluid Mechanics* 927 (2021). DOI: 10.1017/jfm.2021.785.

[56] I. O. Ucar and H. Y. Erbil. "Use of diffusion controlled drop evaporation equations for dropwise condensation during dew formation and effect of neighboring droplets". *Colloids and Surfaces A: Physicochemical and Engineering Aspects* 411 (2012). DOI: 10.1016/j.colsurfa.2012.07.002.

[57] J. E. Castillo and J. A. Weibel. "A point sink superposition method for predicting droplet interaction effects during vapor-diffusion-driven dropwise condensation in humid air". *International Journal of Heat and Mass Transfer* 118 (2018). DOI: 10.1016/j.ijheatmasstransfer.2017.11.045.

[58] S. Zheng, F. Eimann, C. Philipp, T. Fieback, and U. Gross. "The interaction effects between droplets condensing from moist air using a distributed point sink method". *E3S Web of Conferences*. Vol. 128. EDP Sciences, 2019. DOI: 10.1051/e3sconf/201912801005.

[59] P. L. Kelly-Zion, C. J. Pursell, G. N. Wassom, B. V. Mandelkorn, and C. Nkinthorn. "Correlation for sessile drop evaporation over a wide range of drop volatilities, ambient gases and pressures". *International Journal of Heat and Mass Transfer* 118 (2018). DOI: 10.1016/j.ijheatmasstransfer.2017.10.129.

[60] E. Dietrich, S. Wildeman, C. W. Visser, K. Hofhuis, E. S. Kooij, H. J. Zandvliet, and D. Lohse. "Role of natural convection in the dissolution of sessile droplets". *Journal of Fluid Mechanics* 794 (2016). DOI: 10.1017/jfm.2016.158.

[61] B. Dollet and F. Boulogne. "Natural convection above circular disks of evaporating liquids". *Physical Review Fluids* 2.5 (2017). DOI: 10.1103/PhysRevFluids.2.053501.

[62] D. Khilifi, W. Foudhil, K. Fahem, S. Harmand, and S. B. Jabrallah. "Study of the phenomenon of the interaction between sessile drops during evaporation". *Thermal Science* 23 (2019). DOI: 10.2298/TSCI180406188K.

[63] V. I. Fabrikant. "Diffusion through perforated membranes". *Journal of Applied Physics* 61.3 (1987). DOI: 10.1063/1.338127.

[64] K. Annamalai, W. Ryan, and S. Chandra. "Evaporation of multicomponent drop arrays". *Journal of Heat Transfer* 115.3 (1993). DOI: 10.1115/1.2910742.

[65] K. Miyasaka and C. K. Law. "Combustion of strongly-interacting linear droplet arrays". *Symposium (International) on Combustion* 18.1 (1981). DOI: 10.1016/S0082-0784(81)80034-3.

[66] J. P. Burelbach, S. G. Bankoff, and S. H. Davis. "Nonlinear stability of evaporating/condensing liquid films". *Journal of Fluid Mechanics* 195 (1988). DOI: 10.1017/S0022112088002484.

[67] A. M. Cazabat and G. Guéna. "Evaporation of macroscopic sessile droplets". *Soft Matter* 6.12 (2010). DOI: 10.1039/b924477h.

[68] N. Murisic and L. Kondic. "On evaporation of sessile drops with moving contact lines". *Journal of Fluid Mechanics* 679 (2011). DOI: 10.1017/jfm.2011.133.

[69] S. Luster and B. Batchelor. *Machine Vision Handbook*. Tech. rep. 2012, pp. 259–281. DOI: doi.org/10.1007/978-1-84996-169-1{_}6.

[70] G. P. Zhu, J. F. Yao, S. H. Wu, and X. D. Zhang. *Actuation of adaptive liquid microlens droplet in microfluidic devices: A review*. 2019. DOI: 10.1002/elps.201800297.

[71] S. Nagelberg et al. "Reconfigurable and responsive droplet-based compound microlenses". *Nature Communications* 8 (2017). DOI: 10.1038/ncomms14673.

[72] S. Sharma, S. J. Rao, N. K. Chandra, A. Kumar, S. Basu, and C. Tropea. "Depth from defocus technique applied to unsteady shock-drop secondary atomization". *Experiments in Fluids* 64.4 (2023). DOI: 10.1007/s00348-023-03588-w.

[73] M. L. Timm, E. Dehdashti, A. Jarrahi Darban, and H. Masoud. "Evaporation of a sessile droplet on a slope". *Scientific Reports* 9.1 (2019). DOI: 10.1038/s41598-019-55040-x.

[74] E. Yariv and O. Schnitzer. "Shape of sessile drops in the large-Bond-number 'pancake' limit". *Journal of Fluid Mechanics* 961 (2023). DOI: 10.1017/jfm.2023.243.

[75] M. R. Moore and A. W. Wray. "Gravitational effects on coffee-ring formation during the evaporation of sessile droplets". *Journal of Fluid Mechanics* 967 (2023). DOI: 10.1017/jfm.2023.493.

[76] S. Wildeman. "Real-time quantitative Schlieren imaging by fast Fourier demodulation of a checkered backdrop". *Experiments in Fluids* 59.6 (2018). DOI: 10.1007/s00348-018-2553-9.

[77] O. Sijilmassi, P. García-Parejo, and A. Álvarez-Herrero. "Evaluation of the refractive indices of pure organic dyes using binary mixture models". *Journal of Molecular Liquids* 384 (2023). DOI: 10.1016/j.molliq.2023.122221.

[78] S. O. Isehunwa, E. B. Olanisebe, O. O. Ajiboye, and S. A. Akintola. "Estimation of the refractive indices of some binary mixtures". *African Journal of Pure and Applied Chemistry* 10.4 (2015). DOI: 10.5897/ajpac2015.0613.

[79] M. A. Rahman, Q. Galand, M. Soliman, S. Van Vaerenbergh, and M. Z. Saghir. *Measurement of refractive indices of binary mixtures using digital interferometry and multi-wavelength Abbemat refractometer*. 2013. DOI: 10.1016/j.optlaseng.2013.01.002.

[80] T. Schubert, N. Haase, H. Kück, and R. Gottfried-Gottfried. "Refractive-index measurements using an integrated Mach-Zehnder interferometer". *Sensors and Actuators, A: Physical* 60.1-3 (1997). DOI: 10.1016/S0924-4247(97)01380-0.

[81] S. R. Uhlhorn, D. Borja, F. Manns, and J.-M. Parel. "Refractive index measurement of the isolated crystalline lens using optical coherence tomography". *Vision Research* 48.27 (2008). DOI: 10.1016/J.VISRES.2008.09.010.

[82] L. Xu, L. Ma, X. Xu, and J. Luo. "The transients in the evaporation of sessile liquid droplets and the applicability of the steady-state approximation". *International Journal of Heat and Mass Transfer* 169 (2021). DOI: 10.1016/j.ijheatmasstransfer.2021.120946.

[83] A. L. Ljung and T. Staffan Lundström. "Evaporation of a sessile water droplet subjected to forced convection in humid environment". *Drying Technology* 37.1 (2019). DOI: 10.1080/07373937.2018.1441866.

[84] A. E. Korenchenko and A. A. Zhukova. "Sessile droplet evaporation in the atmosphere of different gases under forced convection". *Physics of Fluids* 34.4 (2022). DOI: 10.1063/5.0084830.

[85] H. W. Fung, M. A. Mahmud, and B. D. MacDonald. "Experimental investigation of forced convection on evaporation of continuously-fed sessile droplets". *International Journal of Thermal Sciences* 175 (2022). DOI: 10.1016/j.ijthermalsci.2022.107459.

[86] E. Bodenschatz, W. Pesch, and G. Ahlers. "Recent developments in rayleigh-bénard convection". *Annual Review of Fluid Mechanics* 32 (2000). DOI: 10.1146/annurev.fluid.32.1.709.

[87] V. U. Kakade, G. D. Lock, M. Wilson, J. M. Owen, and J. E. Mayhew. "Accurate heat transfer measurements using thermochromic liquid crystal. Part 1: Calibration and characteristics of crystals". *International Journal of Heat and Fluid Flow* 30.5 (2009). DOI: 10.1016/J.IJHEATFLUIDFLOW.2009.04.007.

[88] S. Dash and S. V. Garimella. "Droplet evaporation on heated hydrophobic and superhydrophobic surfaces". *Physical Review E - Statistical, Nonlinear, and Soft Matter Physics* 89.4 (2014). DOI: 10.1103/PhysRevE.89.042402.

[89] A. Maatar, S. Chikh, M. Ait Saada, and L. Tadrist. "Transient effects on sessile droplet evaporation of volatile liquids". *International Journal of Heat and Mass Transfer* 86 (2015). DOI: 10.1016/j.ijheatmasstransfer.2015.02.077.

[90] J. Guadarrama-Cetina, R. D. Narhe, D. A. Beysens, and W. González-Viñas. "Droplet pattern and condensation gradient around a humidity sink". *Physical Review E - Statistical, Nonlinear, and Soft Matter Physics* 89.1 (2014). DOI: 10.1103/PhysRevE.89.012402.

[91] A. Kabalnov. "Ostwald ripening and related phenomena". *Journal of Dispersion Science and Technology* 22.1 (2001). DOI: 10.1081/DIS-100102675.

[92] R. Wood, S. Irons, and P. R. Jonas. "How important is the spectral ripening effect in stratiform boundary layer clouds? Studies using simple trajectory analysis". *Journal of the Atmospheric Sciences* 59.18 (2002). DOI: 10.1175/1520-0469(2002)059<2681:HIITSR>2.0.CO;2.

[93] D. A. Sakthivadivel. "Magnetisation and mean field theory in the Ising model". *SciPost Physics Lecture Notes* 35 (2022). DOI: 10.21468/SciPostPhysLectNotes.35.

[94] M. Sokuler, G. K. Auernhammer, C. J. Liu, E. Bonaccurso, and H. J. Butt. "Dynamics of condensation and evaporation: Effect of inter-drop spacing". *Europhysics Letters* 89.3 (2010). DOI: 10.1209/0295-5075/89/36004.

[95] M. H. Ambaum. Thermal Physics of the Atmosphere. 2010. DOI: 10.1002/9780470710364.

[96] S. P. Humphrey and R. T. Williamson. "A review of saliva: Normal composition, flow, and function". *Journal of Prosthetic Dentistry* 85.2 (2001). DOI: 10.1067/mpr.2001.113778.

[97] A. Sarkar, F. Xu, and S. Lee. *Human saliva and model saliva at bulk to adsorbed phases – similarities and differences*. 2019. DOI: 10.1016/j.cis.2019.102034.

[98] C. Z. Zhang, X. Q. Cheng, J. Y. Li, P. Zhang, P. Yi, X. Xu, and X. D. Zhou. *Saliva in the diagnosis of diseases*. 2016. DOI: 10.1038/ijos.2016.38.

[99] S. P. Fisenko, W. N. Wang, I. Wuled Lenggoro, and K. Okyuama. "Evaporative cooling of micron-sized droplets in a low-pressure aerosol reactor". *Chemical Engineering Science* 61.18 (2006). DOI: 10.1016/j.ces.2006.05.028.

[100] D. M. Anderson, G. B. McFadden, and A. A. Wheeler. "Diffuse-interface methods in fluid mechanics". *Annual Review of Fluid Mechanics* 30 (1998). DOI: 10.1146/annurev.fluid.30.1.139.

[101] A. V. Gusarov and I. Smurov. "Gas-dynamic boundary conditions of evaporation and condensation: Numerical analysis of the Knudsen layer". *Physics of Fluids* 14.12 (2002). DOI: 10.1063/1.1516211.

[102] P. J. Sáenz, K. Sefiane, J. Kim, O. K. Matar, and P. Valluri. "Evaporation of sessile drops: A three-dimensional approach". *Journal of Fluid Mechanics* 772 (2015). DOI: 10.1017/jfm.2015.224.

[103] B. Rana, D. J. Fairhurst, and K. C. Jena. "Investigation of Water Evaporation Process at Air/Water Interface using Hofmeister Ions". *Journal of the American Chemical Society* 144.39 (2022). DOI: 10.1021/jacs.2c05837.

[104] V. E. Badalassi, H. D. Ceniceros, and S. Banerjee. "Computation of multiphase systems with phase field models". *Journal of Computational Physics* 190.2 (2003). DOI: 10.1016/S0021-9991(03)00280-8.

[105] X. D. Liu. "Weighted essentially non-oscillatory schemes". *Journal of Computational Physics* 115.1 (1994). DOI: 10.1006/jcph.1994.1187.

[106] H. Ding, P. D. Spelt, and C. Shu. "Diffuse interface model for incompressible two-phase flows with large density ratios". *Journal of Computational Physics* 226.2 (2007). DOI: 10.1016/j.jcp.2007.06.028.

[107] T. Zhang, J. J. Jin, and Y. G. HuangFu. "The Crank–Nicolson/Adams–Bashforth scheme for the Burgers equation with H2 and H1 initial data". *Applied Numerical Mathematics* 125 (2018). DOI: 10.1016/j.apnum.2017.10.009.

[108] M. Pelizzari, G. McHale, S. Armstrong, H. Zhao, R. Ledesma-Aguilar, G. G. Wells, and H. Kusumaatmaja. "Droplet Self-Propulsion on Slippery Liquid-Infused Surfaces with Dual-Lubricant Wedge-Shaped Wettability Patterns". *Langmuir* 39.44 (2023). DOI: 10.1021/acs.langmuir.3c02205.

[109] H. Barrio-Zhang, É. Ruiz-Gutiérrez, S. Armstrong, G. McHale, G. G. Wells, and R. Ledesma-Aguilar. "Contact-Angle Hysteresis and Contact-Line Friction on Slippery Liquid-like Surfaces". *Langmuir* 36.49 (2020). DOI: 10.1021/acs.langmuir.0c02668.

[110] M. Kuk, J. Pyeon, and H. Kim. "Vapor distribution changes evaporative flux profiles of a sessile droplet". *Journal of Colloid and Interface Science* 652 (2023). DOI: 10.1016/j.jcis.2023.07.209.

[111] P. L. Kelly-Zion, C. J. Pursell, N. Hasbamrer, B. Cardozo, K. Gaughan, and K. Nickels. "Vapor distribution above an evaporating sessile drop". *International Journal of Heat and Mass Transfer* 65 (2013). DOI: 10.1016/j.ijheatmasstransfer.2013.06.003.

[112] P. J. Coelho and J. Argain. "A local grid refinement technique based upon Richardson extrapolation". *Applied Mathematical Modelling* 21.7 (1997). DOI: 10.1016/S0307-904X(97)00037-1.

Appendix A

DropletTracker

DropletTracker (dTrack) is a Python script designed to be used in conjunction with FIJI (ImageJ V1.54f) to track circular features (breath droplets in this thesis) between video frames. The code is accessible from `https://doi.org/10.6084/m9.figshare.26587513`. To reduce noise and misdetections of the features, the frames are first processed with the following sequence:

1. Otsu threshold: making the image binary.
2. `Fill Holes`: removing backlight image from centre of each droplets.
3. `Watershed`: ensuring droplets remain separated.

To track the dynamics of the features (droplets), the processed images are analysed with the function `Analyse Particles` and ellipses are fit to each of the droplets in every image recording the centres and major and minor axes. dTrack is used to identify and track the droplets through each frame. To do this the closest coordinates in consecutive frames are assumed to be the same droplet. The droplet is considered to have evaporated if the closest centre is more than the initial radius of the droplet.

Appendix B

Multiple-Droplet-Theory-Models

The analytical diffusive theories of Wray, Duffy, and Wilson [1] and Masoud, Howell, and Stone [55] were implemented to model multiple droplet evaporation in a Python script called Multiple-Droplet-Theory-Models (DTM). These theories make predictions for the evaporation dynamics of arbitrary droplet arrays (see chapter 2 1.8). The code is accessible from `https://doi.org/10.6084/m9.figshare.26587516.v1`. The code requires the initial conditions for the array, including the droplets array geometry such as the initial centre coordinates and radii. By specifying additional environmental constants like temperature and ambient humidity, eq. 1.18 can be evaluated to obtain the isolated evaporation rates for each droplet. The aforementioned matrix eq. 1.29 can then be solved, modifying the isolated evaporation rates to account for the diffusive vapour interactions of each droplet with their neighbours.

To implement this the theories are iterated in time by solving eq. 1.29 for the Wray et al. and Masoud et al models. The initial $\left(\frac{dV}{dt}\right)_{\mathrm{k}}$ values are calculated for the initial radii and centres of the droplets. The calculation can then be progressed in time by the Euler method, decrementing the volume according to,

$$\Delta V_{\mathrm{k}} = \Delta t \left(\frac{dV}{dt}\right)_{\mathrm{k}} \tag{B.1}$$

where Δt is a small timestep. As the volume reduces the geometry of the droplets are updated depending on their evaporation mode. Since $\left(\frac{dV}{dt}\right)^{*}$ depends on the in-situ droplet geometry, the mode will influence its value differently. For a CR mode the initial base radius ($a_{0,\mathrm{k}}$) remains constant and the new volume calculated as $V_{\mathrm{k}}(t+\Delta t) = V_{\mathrm{k}}(t) - \Delta V_{\mathrm{k}}$ can be used to calculate the new $\theta_{\mathrm{k}}(t+\Delta t)$. Alternatively, if droplets are evaporating in CA mode the initial contact angle (θ_0) is constant and can be used with $V_{\mathrm{k}}(t+\Delta t)$ to calculate $a_{\mathrm{k}}(t+\Delta t)$. Eq. 1.18 is a function of a and θ and therefore in both cases must be updated after each Δt. If after any of the reductions, $V_{\mathrm{k}} \leq 0$, the interaction matrix Ψ must be recalculated and inverted for the remaining droplets. Repeating this process until all droplets have evaporated provides a piecewise theoretical prediction for the volume evaporation dynamics.

The fastest and most stable method of recalculating the evaporation in Python is found to be the Scipy module's implementation of LU factorisation (`scipy.org`). This is particularly important for large arrays of droplets.

The numerical error in the above implementation comes from Δt inexactly capturing the point in which $V_{\mathrm{k}} = 0$. If Δt is too large ΔV_{k} will significantly overshoot an amount δV such that $V_{\mathrm{k}} = \delta V < 0$. In this time the array is incorrectly evaporating as if the

droplet(s) remain(s). The size of δV will increase with Δt however the computation time will decrease. The number of times $V_\mathrm{k} = 0$ is overshot will depend on the number of symmetric confinements in the array (number of distinct times in which droplets evaporate). In each case δV will augment as evaporation transitions through droplets disappearing. For example, a circular ring of droplets contains only one confinement condition (all droplets should evaporate at the same time) and therefore minimises the error due to overshooting. In general, as droplet evaporate $\frac{dV}{dt}$ will increase, so overshooting will artificially prolong evaporation.

Hexagonal arrays have an increased number confinement conditions (recalculations of eq. 1.29) with increasing N. The influence of this overshooting will also depend on the difference in evaporation rate before and after the interactions have been updated. Hexagons maximise this difference in evaporation rate as the number of droplet in each confinement condition is large and transitioning between them represents a significant reduction in confinement for the adjacent droplets. For these reasons a hexagonal array is a good choice for establishing a maximum numerical error. The size of the transitions is also enhanced by choosing a minimum separation. A number of predictions are made with different values of Δt for a 61 droplet hexagonal array (nine confinement conditions) with $s_\mathrm{kn} = 2a$ (touching droplets). Fig. B.1a) plots the effect of the timestep size on the average volume overshoot for each confinement. The average volume is normalised by the initial volume of one droplet and plotted for both CA (blue) and CR (black) modes. For increasing timestep size (decreasing number of timesteps) the error in both cases grows faster for the CR mode. This is expected as the evaporation rate of the droplets as $V \to 0$ is larger and therefore so is the overshoot. In the CA mode the evaporation decreases smoothly to zero as $a \to 0$ and the extent of the overshoot will therefore be reduced. Additionally the error associated with the Euler method will also be reduced as $\frac{dV}{dt}$ will change less rapidly as droplets evaporate, again, due to $\frac{dV}{dt}$ slowly reducing to zero. As a result of the overshoot the array lifetime (τ_{max}) also increases for larger Δt. This is shown in panel b) which plots the array lifetime normalised by calculation with the greatest number of timesteps ($\hat{\tau}_{max}$). Panel a) and b) both plateau for large numbers of timesteps, increasing the number further provides diminishing improvements in accuracy. The time taken for these calculations to be run must be considered. The calculation run time is plotted in panel c). It can be seen that above 10^3 timesteps the accuracy is not significantly improving however the computation time is continuing to grow linearly.

Fig. B.1 shows that in general, the accuracy of this implementation depends on the size of Δt. In one special case however, more accurate results can be obtained for the Wray et al model in CR mode. Recalling that the predictions are for flat droplets, $\left(\frac{dV}{dt}\right)^*$ does not depend on θ and as a result are independent of time. Because of this the rates are linear with the gradient only changing when droplets disappear. And so the amount of time (Δt) required for the kth droplet to evaporate its entire volume (ΔV_k) is given by

$$\Delta t_\mathrm{k} = \Delta V_\mathrm{k} \left(\frac{dV}{dt}\right)_\mathrm{k}^{-1} \tag{B.2}$$

The droplet with the smallest evaporation time (Δt_{min}) can be selected as Δt and the uncertainty associated with overshooting can be eliminated.

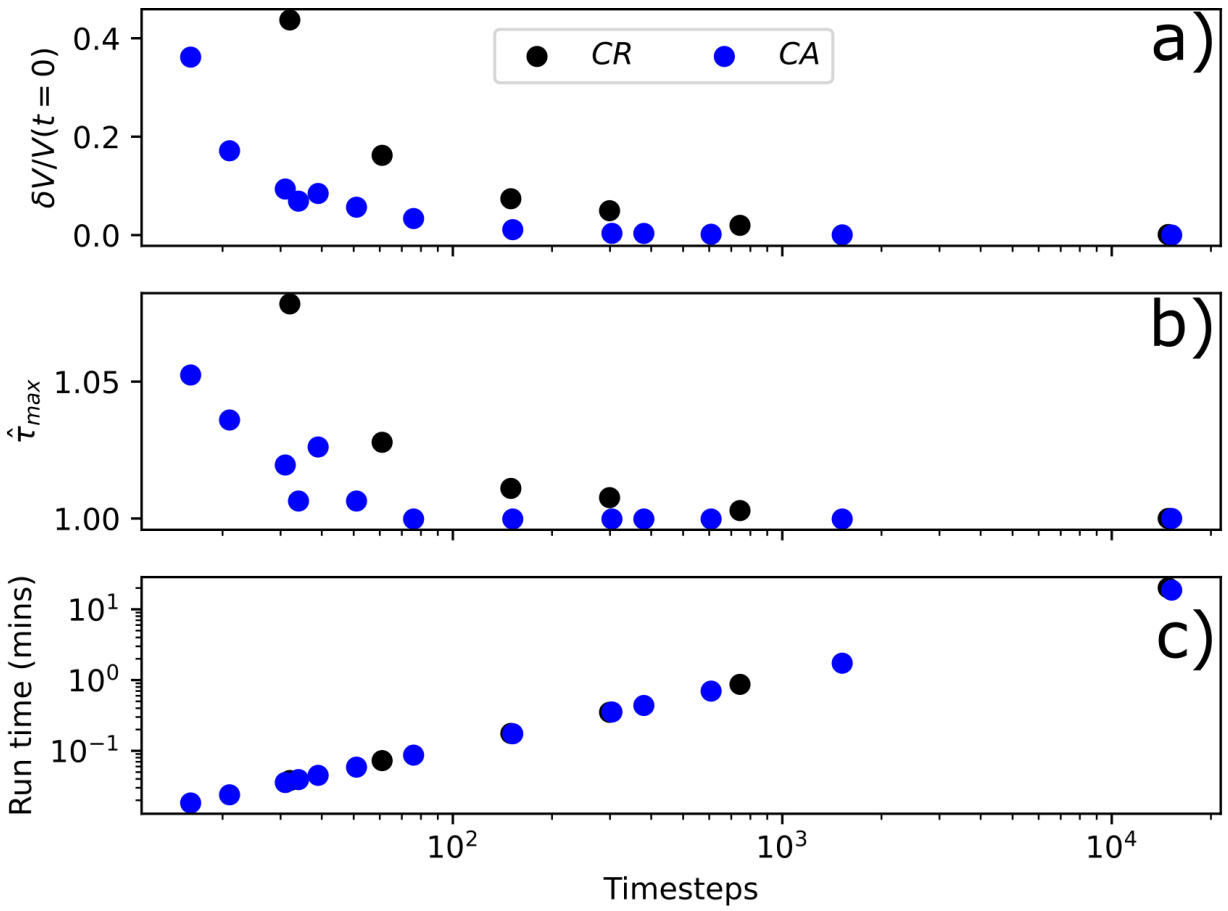

Figure B.1: Computational uncertainty in the DTM implementation. a) is the average volume overshoot for the number of confinements in the array (δV), compared to the initial volume of a single droplet ($V(t = 0)$), b) temporal overshoot normalised by the most accurate ($\hat{\tau}_{max}$) and c) the computational run time. Each against the total number of timesteps in the simulation. The blue series represents CA and the black CR evaporation modes.

Appendix C

Measure_Droplet_Lifetime

Measure_Droplet_Lifetimes (MDL) is a Python program written to extract experimental drying times from multiple droplet arrays. The code is accessible from `https://doi.org/10.6084/m9.figshare.26587519.v1`. The code requires the image coordinates of the droplets and then processes the video to determine the individual droplet lifetimes for the specified coordinates. The coordinates can be determined with any method (including manually) and simple functions can be written to format the data correctly as an input to the code. Currently a function (`read_imageJ_coords`) exists to interpret the text data output by FIJI (ImageJ). The FIJI software's function `Analyze Particles` was used to establish the coordinates from the first frame. The centres could be determined natively in Python however a general image processing algorithm would require high contrast videos with an appreciable signal to noise ratio. The benefit of establishing the droplet centres separately is it allows for manual user manipulation to correct for misdetections and artefacts. Additionally, once these ROIs are specified the videos can be processed automatically to enhance the contrast in these regions without concern for potential amplification of noise outside these regions. Once the coordinated are specified the program performs a series of image processing steps on the specified video frames:

1. For each frame a difference image is calculated from the final frame, which removes the background and enhances the droplet contrast.

2. The difference image is Otsu thresholded to create a binary image with white pixels representing liquid and black representing background.

3. The binary image can then be dilated a number of times specified by the user to enhance the pixel signal around each droplet.

After the images are processed, binary masks are created over the image each capturing a circular ROI centred on each specified coordinate. The masks are iterated over and the mean greyscale (I) is calculated in the region for each frame. The lifetime is determine by reversing the array of greyscale values and establishing the first frame in which the mean greyscale increases above a user specified threshold (I_t). This frame is then recorded as the drying time for that specific droplet. The drying time can also be determined by not reversing the array and finding the first frame in which I falls below I_t. The method of choice depends on the video itself, if there is not a strong droplet to background contrast when droplets become very small then the former method gives more accurate results as the greyscale value likely oscillates above and below the threshold when $a \to 0$. This method prevents erroneously early drying times. However if the background in the images is noisy (often caused by slight movement of the substrate underneath the droplets during

evaporation being amplified by the difference image) the latter gives better drying time estimates as it avoids late noise being interpreted as liquid presence in the reversed array.

The choice of the threshold marking the presence of liquid can be determined in FIJI prior to running the code and often is only required once for an experimental setup with specific lighting and background. This is because the drying time is not very sensitive to the selection of the threshold as $\frac{dI}{dt} \ll 0$ towards the end of the droplets lifetime. As a result slight increases or decreases in I_t do not traverse very far on the time axis.

Appendix D

Spider "spit" in droplets

During an experiment from the chapter 4 section 4.1 a spider was caught drinking from one of the droplets at the edge of the array as it evaporated. The array was $N = 361$ droplets hexagonally arranged within a circle of radius $R = 60\,\text{mm}$ and spaced $6.0\,\text{mm}$ apart.

Fig. D.1 shows a montage of the frame before (left, 22 mins), whilst (middle, 24 mins) and after (right, 26 mins) the spider was present. On the right frame, after the spider had departed the radius of the droplet has shrunk (as can be seen from the enlarged droplet in the bottom right of the panel) from $a = 1.00 \pm 0.05\,\text{mm}$ (blue circle) to $0.773 \pm 0.05\,\text{mm}$ (red circle), a 22.7% reduction. Assuming a contact angle of $\theta = 90°$ this corresponds to the spider drinking $\approx 1.13\,\mu\text{L}$ of DI water. The same droplet then took 3.88 ± 0.09 times longer to evaporate with a 27% lower volume than the two droplets immediately adjacent also at the edge of the array, in almost exactly the same confinement at the same radial distance from the centre. Furthermore its volume was 43% of the largest (most confined) droplets in the centre of the array, but took 2 times longer to evaporate. This is likely because the spider introduced some impurities and other components into the droplet, here colloquially referred to as "spit". The slowing of the evaporation due to these impurities can be explained by the Raoult effect decreasing the droplet's volatility (see chapter 2 section 1.7).

It is therefore clear that the presence of small amounts of dissolved substances in the droplets can have a significant effect on their evaporation. Droplets are so sensitive to this that the normal diffusive order of evaporation due to confinement and droplet volume can be overcome and even reversed.

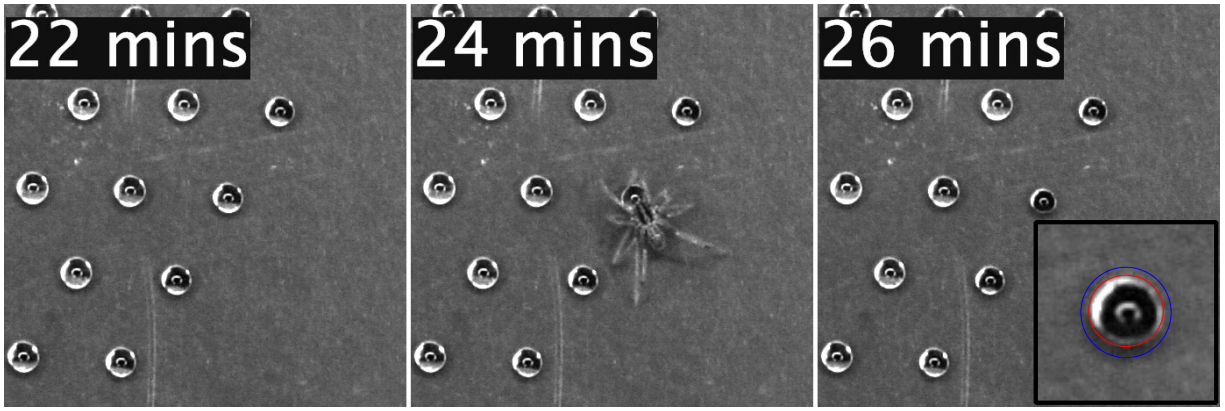

Figure D.1: Zoomed in region at the edge of the droplet array for three consecutive frames before (left panel), during (middle panel) and after (right panel) a spider is drinking from a droplet. The inset in the right frame shows an enlarged view of the affected droplet, with the blue and red circles showing the position of the contact lines for the frame before (left panel) and after the spider has drank respectively. The blue circle corresponds to a base radius of $a = 1.00 \pm 0.05\,\mathrm{mm}$ and the red $0.773 \pm 0.05\,\mathrm{mm}$.